Radiation-induced alterations in mesoporous silicas : The effect of electronic processes involving ions and electrons

Jun Lin

To cite this version:

Jun Lin. Radiation-induced alterations in mesoporous silicas : The effect of electronic processes involving ions and electrons. Material chemistry. Montpellier, Ecole nationale supérieure de chimie, 2022. English. NNT : 2022ENCM0006 . tel-03880560

HAL Id: tel-03880560
https://theses.hal.science/tel-03880560v1

Submitted on 1 Dec 2022

THESE POUR OBTENIR LE GRADE DE DOCTEUR DE L'ECOLE NATIONALE SUPERIEURE DE CHIMIE DE MONTPELLIER

En Chimie des Matériaux

École doctorale ED-459

Unité de recherche ICSM – UMR 5257

Radiation-induced Alterations in Mesoporous Silicas: The Effect of Electronic Processes Involving Ions and Electrons

Présentée par **Jun LIN**
le 18/03/2022

Sous la direction de **Dr. Xavier DESCHANELS**

Devant le jury composé de

André AYRAL, Professeur, UM / IEM Montpellier	Président du jury
Marie-France BARTHE, Directrice de Recherche, CEMHTI Orléans	Rapporteur
Emmanuel BALANZAT, Directeur de Recherche Emérite, CIMAP Caen	Rapporteur
Antonino ALESSI, Docteur, LSI Polytechnique Palaiseau	Examinateur
Clara GRYGIEL, HDR, CIMAP Caen	Examinatrice/Co-Encadrante
Xavier DESCHANELS, Directeur de Recherche, ICSM Marcoule	Directeur de thèse
Sandrine DOURDAIN, HDR, ICSM Marcoule	Invitée/Co-Encadrante
Guillaume TOQUER, Maître de conférences, ICSM Marcoule	Invité/Co-Encadrant

Abstract

Materials used in nuclear energy (fuel, packaging matrix, structural materials...) are subject to significant stresses due to the creation of defects that modify their properties. Several studies[1] have shown that interfaces can act as a sink for defects caused by irradiation, which suggests that nanomaterials could have a higher resistance to irradiation than materials with a "micrometric" structure. Simultaneously, mesoporous silica materials have grown in popularity in recent years and are becoming more involved in the domain related to radiation conditioning[2], such as the prospective use of conditioning for nuclear waste. While research has begun to focus on the behavior of non-porous silica materials when exposed to radiation, no extensive investigations have been conducted on the behavior of mesoporous silica when exposed to radiation, particularly at electronic irradiation regime.

This thesis aims to comprehend and explain the radiation-induced changes in mesoporous silicas under electronic regimes. This work quantified the evolution of physical (pore volume, pore diameter and distribution...) and structural (polymerization of the network, creation of defects...) properties of mesoporous silica irradiated with high-energy ion beams with stopping powers ranging from 1 keV/nm to 12 keV/nm, and with electron beams (10 - 200 keV and 0.6 - 2.4 MeV). Post-irradiation characterization methods (X-ray reflectivity, gas adsorption, SAXS, FTIR, etc.) have been used, as well as in-situ pore structure monitoring using electron microscopes. The experimental findings indicated that pore structures were susceptible to a certain degree of irradiation-induced shrinking. In contrast, evidence shows that the silica network itself does not alter much in porous silica compared to non-porous silica. Meanwhile, a 3DTS (3D thermal spike) model has been successfully applied to describe and explain the observed pore contraction behavior in response to ionic irradiation. Additionally, the mechanism of pore contraction under electron irradiation has been delineated according to the domain of incident electron energies. When compared to non-porous silica, this research has demonstrated that the existence of nanoscale pores reduces the accumulation of damage induced by irradiation. In conjunction with this effect, the pore contracts until it completely disappears under the impact of irradiation. This characteristic could, from an applicative point of view, be of interest to practitioners in the context of new methods of treating radioactive effluents, such as through the use of a "separation/conditioning" strategy, or in the context of the self-healing of porous gel layers formed on the surface of vitrified waste packages whose final destination is deep geological disposal.

Keywords: mesoporous silicas, heavy-ion irradiation, electron irradiation, structural behavior, compaction

---

[1] Bringa, E. M. *et al.* Are nanoporous materials radiation resistant? Nano Lett. 12, 3351-3355 (2012).

[2] Makowski, P. *et al.* Mesoporous materials in the field of nuclear industry: applications and perspectives. New J. Chem. 36, 531-541 (2012).

Résumé

Les matériaux utilisés dans le nucléaire (combustible, matrice de conditionnement, matériaux de structure…) sont soumis à des contraintes importantes liées à la création de défauts qui modifient leurs propriétés. Plusieurs études[1] ont montré que les interfaces peuvent agir comme un puits pour les défauts causés par l'irradiation, ce qui suggère que les nanomatériaux pourraient avoir une plus grande résistance à l'irradiation que les matériaux présentant une structure « micrométrique ». Par ailleurs, les silices mésoporeuses ont gagné en popularité ces dernières années[2] et sont envisagées pour le traitement des effluents radioactifs (séparation, conditionnement…). Bien que de nombreuses études aient été réalisées sur le comportement de silices non poreuses sous irradiation, très peu de travaux s'intéressent à celui de la silice mésoporeuse en particulier lorsqu'elle est irradiée en régime d'électronique.

Le but de cette thèse est de comprendre et d'expliquer les modifications induites par irradiation dans les silices mésoporeuses en régime électronique. Ce travail a permis de quantifier l'évolution de propriétés physico-chimiques (polymérisation du réseau, création de défauts…) et structurales (volume poreux, diamètre et distribution des pores…) de la silice mésoporeuse irradiée par des faisceaux d'ions de haute énergie dans une gamme de pouvoirs d'arrêt variant entre 1 keV/nm et 12 keV/nm, ainsi que par des électrons (10 - 200 keV et 0.6 - 2.4 MeV). Des méthodes de caractérisation post-irradiation (réflectivité des rayons X, adsorption de gaz, SAXS et FTIR, etc.) ont été utilisées, ainsi que le suivi in situ de la structure des pores à l'aide de microscopie électronique. Les résultats expérimentaux ont indiqué que la structure des pores était sensible à l'irradiation conduisant dans certaines conditions à son effondrement, tandis que le réseau de silice lui-même évolue peu par rapport à la silice non poreuse. Parallèlement, un modèle TS3D (modèle de pointe thermique 3D) a été utilisé avec succès pour décrire et expliquer le comportement de contraction des pores observé en réponse à l'irradiation ionique. De plus, le mécanisme de contraction des pores sous irradiation par des électrons a été délimité en fonction du domaine des énergies incidentes des électrons et de la dose. Cette recherche a montré que par rapport à une silice non poreuse, la présence de pores nanométriques réduit l'accumulation des dommages causés par les irradiations. Conjointement à cet effet bénéfique, le pore se contracte jusqu'à disparaitre sous l'impact de l'irradiation. Par conséquent, d'un point de vue applicatif cette caractéristique pourrait être mise à profit pour imaginer de nouvelles voies de traitement des effluents radioactifs, par une stratégie de type « séparation/conditionnement » ou pour l'autoguérison des couches de gel poreux formées à la surface des colis de déchets vitrifiés dont l'exutoire envisagé est le stockage géologique profond.

Mots clés : silices mésoporeuses, évolution structurale, densification, irradiation par ion, irradiation par électron

---

[1] Bringa, E. M. *et al.* Are nanoporous materials radiation resistant ? Nano Lett. 12, 3351-3355 (2012).

[2] Makowski, P. *et al.* Mesoporous materials in the field of nuclear industry : applications and perspectives. New J. Chem. 36, 531-541 (2012).

Acknowledgements

Throughout my PhD work, I've had a lot of help and encouragement. This is a wonderful chance for me to pursue my PhD studies in ICSM / CEA-Marcoule and CIMAP / GANIL. I thoroughly appreciated the friendly working environment, as well as the resources and assistance offered by the laboratory. I am immensely grateful to EMIR&A network, for provision of irradiation beamtime on several irradiation facilities that help realize this project.

My first and most heartfelt thanks go out to my supervisors, Dr. Xavier DESCHANELS, Dr. Clara GRYGIEL, Dr. Sandrine DOURDAIN and Dr. Guillaume TOQUER, for all the enthusiastic supervision and helps. Especially for their open-ended guidance and supervision, which allowed me to explore a wide range of possibilities within my PhD framework. It has been a pleasure working with you over the last four years.

A special thanks to my jury members, Prof. André AYRAL, Dr. Marie-France BARTHE, Dr. Emmanuel BALANZAT and Dr. Antonino ALESSI, for their participation and advice on this thesis. It is an honor to defend my PhD in front of them.

I owe a debt of gratitude to Dr. Christian Dufour for his kind support, especially for the technical help on the use and development of the 3DTS code. Special thanks to Dr. Emmanuel Gardés and Dr. Mamour Sall for their tremendous assistance and resource on electron microscopy-related topics. My sincere thanks go out to my colleagues who have assisted me in any way. Particularly, Dr. I.Monnet, Dr. Y.Ngono-Ravache, Dr. T.Sauvage, Dr. B.Boudeau, Dr. D.Baux, Dr. B.Boizot, Dr. O.Cavani, Dr. R.Grasset and Dr. N.Ollier for their help and support during my stay in different irradiation facilities.

Thanks to my colleagues of LNER and ICSM, Mrs. Cyrielle REY, Dr. Jérémy CAUSSE and Dr. Diane REBISCOUL for their contributions to this thesis. I'd like to thank the technicians, engineers of ICSM without whom it would never have been possible to carry out most of the work of this thesis. I also acknowledge the administrative staff of the institute and especially Mrs. Vainina RUSSELLO and Mrs. Véronique HAON for their help in administrative formalities during my PhD studies.

Thanks to present and former PhD students and Postdocs of LNER, for the lunch time, jokes and laughs and occasional complaints during these years. A special thank you goes out to all my Chinese friends for spending time after work with me and feeding me some of the greatest Chinese food I've ever tasted.

Last but not least, many thanks to my family for their support, especially during the difficult period of Covid-19. We begin our lives with our families and our affection never fades away.

Contents

I Introduction and Rationale 3

List of Abbreviations

3DTS	3-dimensional thermal spike model
ATR	Attenuated total reflection
CEMHTI	Conditions extrêmes et matériaux : haute température et irradiation
CIMAP	Centre of research on ions, materials and photonics
CIRIL	Centre for interdisciplinary research with heavy ions
CL	Cathodoluminescence
DFT	Density functional theory
FIB	Focused ion beam technique
FTIR	Fourier-transform infrared spectroscopy
GANIL	Grand accélérateur national d'ions lourds
HLW	High level waste
ICc	Silica thin film synthesized with CTAB surfactant
IPc	Silica thin film synthesized with P123 surfactant
LSI	Irradiated solids laboratory
MAS	Magic angle spinning
MC	Monte carlo
NBOHC	Non-bridging oxygen hole center
NLDFT	Non-local density functional theory
NMR	Nuclear magnetic resonance
NPc	Silica thin film synthesized with sol-gel process
PL	Photoluminescence
POR	Peroxy radical
PSD	Pore size distribution
SAXS	Small-angle x-ray scattering
$\mathbf{S_e}$	Electronic stopping power
SEM	Scanning electron microscope
SHI	Swift heavy ion
$\mathbf{SiO_2}$ **therm**	Non-porous silica thin film synthesized with thermal process
SIRIUS	Système d'irradiation pour l'innovation et les utilisateurs scientifiques
$\mathbf{S_n}$	Nuclear (ballistic) stopping power
STEM	Scanning transmission electron microscope
TEM	Transmission electron microscope
TGA	Thermal gravimetric analysis
TO	Transverse optical mode
XRD	X-ray diffraction
XRR	X-ray reflectivity

General introduction

Radiation damage and radiation resistance have long been a question of great interest in a wide range of fields. Not only do spacecraft subjected to long-term or high dose rates of radiation, such as trips to Mars or the inner solar system, demand consideration in this field, but so do the various components of sophisticated nuclear energy systems and nuclear power plants (fuel, cladding internals, and pressure vessels). Parallel to this, the storage and disposal of all types of nuclear waste poses a significant challenge to current materials in terms of durability, and the change in their characteristics with dose accumulation has long been a major issue for the related scientific community.

In general, three of the main types of radiation are alpha rays, beta rays and gamma rays. Research shows that ion irradiations could provide a reasonable simulation of radiation effects in solids, i.e. α -disintegration in HLW glasses, neutron in reactor vessel, fission products in nuclear fuel. Electron irradiations have also been proven to be a feasible method to simulate and study the effects of ionization and electronic excitations from β -particles and γ -rays.[1, 2]

When energetic particle penetrates a solid, it progressively transfers its energy mainly by two types of interaction: the elastic collision which is an interaction between the nuclei of the projectile and that of the target atom (also called the ballistic effect or the nuclear effect) and the inelastic collision which is an interaction between the electron procession of the incident particle and that of the target atoms (also called the electronic effect). It is now relatively well established how the ballistic process causes damage and effects on the material, and the modeling to anticipate changes in the structure. Kinchin's article[3] entitled "The displacement of atoms in solids by radiation" was a precursor by introducing the atomic displacement (dpa). Since then, other formalisms have been developed to calculate the irradiation damage. However, the influence of electronic effect on materials has remained unclear due to the great complexity of describing defect creation processes involving in electronic processes, compared to purely elastic processes. During the inelastic collision, the kinetic energy of the system is modified, which leads to the ionization or excitation of the collision partners. The process is more complex than the elastic collision because many physical phenomena are involved (e^- capture by the ion, ionization followed by Auger processes or photon emission, etc.).

The aim of this study was to examine the behavior of the mesoporous silicas under electronic region irradiation. Two reasons, which may seem antagonistic, have led us to study the behavior of these materials under these irradiation conditions. First, some cross-sectional investigations indicate that surfaces are associated with the behavior of radiation. A simplistic explanation for this effect is to say that the surface / interface act as sinks for defects created by irradiation, therefore nanomaterials might have improved resistance to irradiation compared to micrometrics. Many studies have investigated this effect for nanostructured materials, ceramics[4–7] or metal[8, 9] but only a few report results on porous or rather mesoporous materials : metallic foams[10] or mesoporous oxide[11]. To investigate this effect, it could be interesting to change the size and the organization of the mesoporosity. Therefore, mesoporous silicas are a good model compounds because these parameters can be easily tuned via the sol-gel process.

Second, around the late 1970s, research and case studies began to emerge linking the use of high-silica glasses to nuclear waste management. The work of Simmons[12] in 1979 has demonstrated that the fixation of radioactive wastes is feasible in high-silica porous glasses of good chemical durability. With the discovery of numerous extraction agents, the concept of "separation/conditioning process" was brought up as the optimization of the Simmons process in which all porous materials can be used. Later, since the discovery of ordered mesoporous silica material, more recent attention has focused on its potential application as an alternative process for treating radioactive effluents containing actinides and fission products. In this way, a precise knowledge of the damage induced due to the radiation in silica-based materials is then required. Recent studies[13–18] have highlighted the collapse of the porous network of silica-based materials induced by the ballistic or electronic radiation damage. These effects could be favorable to the encapsulation of radionuclides in the porosity of the silicas in order to obtain a wasteform matrix.

External irradiation methodologies involving both ion and electron beams were used in this thesis, and materials were adapted to these irradiations in two different forms (thin film and pellet) in order to examine changes in both structural and chemical properties. This manuscript is composed of three main parts consisting of seven chapters.

- Part I, which includes chapters 1 and 2, will present the fundamental concepts of ion-matter interaction, mesoporous silica, and the experimental methodologies and procedures employed in this study. Additionally, the distinctiveness of the modifications generated by irradiation will be spotlighted.

- Part II, which consists of chapters 3 - 5, will discuss the results of ion beam irradiations. A simulation model will be used to study the underlying mechanism.

- Part III, including chapters 6 and 7, will explorer the results of electron beam irradiations.

Finally, the findings reported in the preceding chapters will be compared to those documented in the literature in order to acquire a comprehensive understanding of radiation-induced perturbations in mesoporous silicas involving ions and electrons.

Part I

Introduction and Rationale

Chapter 1

Theoretical framework and methodology

1.1 Ion-solid interactions and ion beam modification of materials

The fundamental principles and the rationale for current investigations of electronic regime irradiation, the selection and the usage of the materials and characterization technologies are briefly presented in this section.

1.1.1 Ion-solid interactions

1.1.1.a Stopping power

The stopping power (dE/dx) describes the capacity to slow down an ion (projectile) during its contact with a target, as indicated by the name. It is commonly defined as the average energy loss <ΔE>, transferred by the ion to the target, over a sufficiently small ion path δx at a given time.

$$S = \frac{\mathrm{dE}}{\mathrm{dx}} = -\frac{< \Delta E >}{\delta \mathrm{x}}$$

The cross section d$\sigma(E, T)$ determines the probability dP(E, T) for a collision in a medium with atoms dispersed randomly with a density N, i.e. dP$(E, T) = N\delta x \; d\sigma(E, T)$. Many theoretical and experimental investigations have been conducted on the effective cross section and it is a function of the transferred energy T. The average energy loss <ΔE> in a number of collisions is given by

$$< \Delta E > = \int \mathrm{T \; dP} = -N \; \delta x \; \int_{T_{\min}}^{T_{\max}} \mathrm{T \; d}\sigma$$

where $T_{\min}$ and $T_{\max}$ are the minimum and maximum transferred energy, respectively.

Under the assumptions of nuclear and electronic stopping powers are independent, total stopping power is split into two parts.

$$\frac{\mathrm{dE}}{\mathrm{dx}} = \left(\frac{\mathrm{dE}}{\mathrm{dx}}\right)_n + \left(\frac{\mathrm{dE}}{\mathrm{dx}}\right)_e = S_N(E) + S_E(E)$$

$\mathrm{S_N}$: Nuclear stopping power, also called ballistic or elastic stopping power. This term corresponds to the elastic interaction between the projectile and the nucleus of the atom in the medium.

S_E: Electronic stopping power, also called inelastic stopping power. This term corresponds to the inelastic interaction between the projectile and the electrons of the atom in the medium.

The relative importance of these two stopping capabilities in a particular material is determined by the incoming ion's kinetic energy (velocity). The nuclear (ballistic) stopping power predominates in the low velocity phase, whereas the electronic stopping power predominates in the higher velocity regime.

It's important to note that this PhD thesis focuses on the electronic regime of projectile transport - in other words, a situation where $S_e \gg S_n$ is guaranteed during our experiment (see figure 1.1 for an example). Previous work [13, 16] focused more particularly on the study of the damage to mesoporous silicas by heavy ions of low energies (Au 0.5 MeV) inducing ballistic effects.

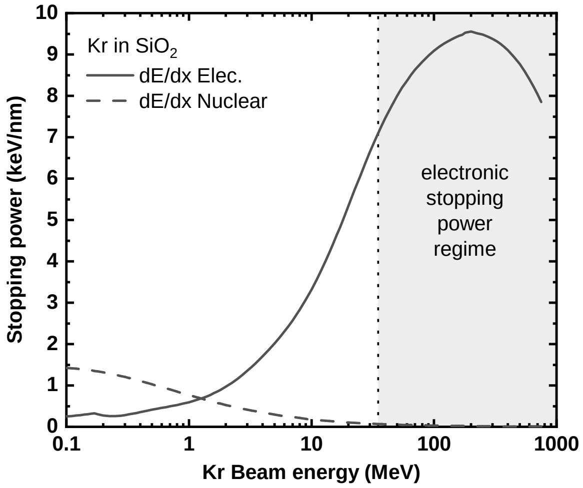

FIGURE 1.1: Calculated stopping power for Kr in SiO_2 at density of 2.2 g/cm^3.

1.1.1.b Calculations with SRIM / TRIM

The most widely used program for calculating S_n and S_e for ions irradiations is the TRIM/SRIM code created by J.F.Ziegler and J.P.Biersack [19, 20]. The calculation's theoretical foundation is briefly described here.

Electronic stopping of heavy ions

Electronic stopping is the main source of energy loss for ions moving faster than Bohr velocity v_b. At ion velocities where relativistic effects can be ignored, there are numerous processes that contribute to the electronic stopping. The electronic stopping takes place both during the collision of the ion and atom and between these collisions. Between the collisions, a constant slowing force acts on the ion owing to momentum exchange between the ion and a free electron in the target material. The stopping during a close collision of the ion and atom is connected to electron exchange between them (excitation of the ion and excitation of a target atom). In addition to these frozen-charge energy losses, there are charge-exchange events (ionization of the ion, capture of an electron by the ion, and ionization of a target atom) and collective effects such as polarization and plasmon excitation. The relative prominence of the various contributions to overall electronic stopping power is determined by ion velocity [21].

There are three velocity regions: the low-velocity region for $v_I < v_B$, where the upper limit is the Bohr velocity of the target electrons or, in the electron gas theory, the Fermi velocity v_F, in this velocity region, the energy loss is generally proportional to the ion's velocity; the high-velocity region for $v_I > 3\, v_F$, where heavy ion stopping can be calculated by scaling proton stopping powers using Thomas-Fermi scaling rules; and the intermediate velocity region for $v_F < v_I < 3\, v_F$.

In SRIM/TRIM, the three velocity intervals mentioned above will be roughly (1) 25keV/amu, (2) >200 keV/amu, and (3) 25-200keV/amu, since the Fermi velocity v_F of metals is about equal to the Bohr velocity, v_B.

The detailed calculation procedure used in SRIM/TRIM is shown in the appendix A.

Ballistic stopping

The electron clouds that screen the ion and target nuclei complicate the computation of energy loss in elastic collisions. It is a product of the Coulomb potential Q_1/r and the screening function spherically symmetric. Using an appropriate screening function, the nuclear stopping of any ion in any target material can be evaluated analytically [22]. It was shown by J.F. Ziegler [19] and confirmed in ICRU report [23] that it is possible to describe the nuclear stopping power using a universal parameterization for reduced ion energy ε:

$$\varepsilon = \frac{32.53 M_2 E_0}{Z_1 Z_2 \left(M_1 + M_2\right) \left(Z_1^{0.23} Z_2^{0.23}\right)}$$

And the universal reduced nuclear stopping power $S_n(\varepsilon)$ is calculated in the framework of Thomas-Fermi potential [24]:

$$for\, \varepsilon \leq 30: \qquad S_n(\varepsilon) = \frac{\ln(1 + 1.1383\varepsilon)}{2\left[\varepsilon + 0.01321\varepsilon^{0.21226} + 0.19593\varepsilon^{0.5}\right]}$$

$$for\, \varepsilon > 30: \qquad S_n(\varepsilon) = \frac{\ln(\varepsilon)}{2\varepsilon}$$

And finally to transform the nuclear stopping power from reduced units to eV/(atom/cm^2) the following formula is used:

$$S_n\left(E_0\right) = \frac{8.462 \times 10^{-15} Z_1 Z_2 M_1 S_n(\varepsilon)}{\left(M_1 + M_2\right)\left(Z_1^{0.23} Z_2^{0.23}\right)} \text{eV/}\left(\text{atom/cm}^2\right)$$

Theoretical electronic stopping powers of common ion beam in silica

Our predicted stopping power of common particle beams operating on non-porous amorphous silica with an average density of 2.2 g/cm^3 was determined with the use of SRIM/TRIM based on the above theoretical basis.

Figure 1.2 shows the result of the calculations and based on the calculations and the availability of research facilities (see section 1.3), we have chosen a series of particle sources for this thesis project. The selected experimental parameters are listed in the table, along with the calculated data for S_n and the R, projection range (discussed in the next section). Comparing the theoretical values of S_n and S_e, we ensure that the criterion $S_n \ll S_e$ is satisfied in all cases.

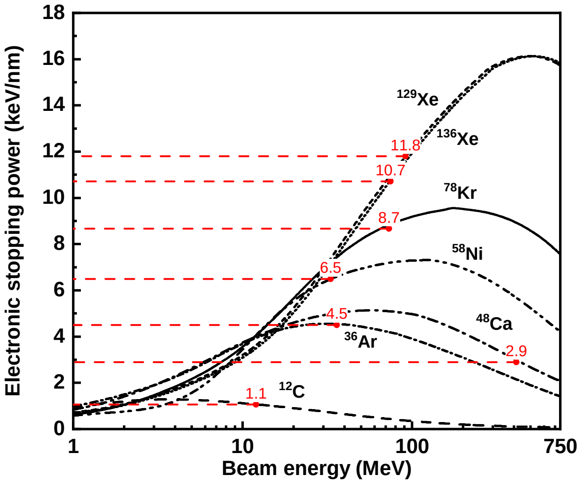

FIGURE 1.2: Calculated stopping powers in SiO_2 at density of 2.2 g/cm^3.

1.1.2 Electron-matter interactions

According to recent studies, electron beam damage is mostly generated by three processes:

- When an incoming electron collides with an atom, ionizing and exciting the atoms, this is referred to as "radiolytic" damage process or collision stopping power. This is comparable to what is referred to as electronic stopping power in heavy charged particle irradiation.

- When energy is transferred from a electron to atoms and atomic electrons via bremsstrahlung quanta-emitting collisions, the process is referred to as radiative stopping power, which is important only for electrons with energy greater than several dozen MeV. In the presented study, this process will not be discussed.

- When energy transfer to recoiling atoms in elastic (ballistic) collisions, the process is referred to as "knock-on" damage or nuclear stopping power.

The calculation of electronic and nuclear stopping powers for electrons can be realized using database ESTAR and SR-NIEL, respectively (see Figure 1.3). ESTAR calculate the collision stopping powers and radiative stopping powers with the help of methods described in ICRU Reports 37 and 49 [25]. Nuclear stopping powers were estimated using the SR-NIEL calculator ver.7.7.1[26] with the displacement energy of 9 eV for silicon ions and 20 eV for oxygen ions[27].

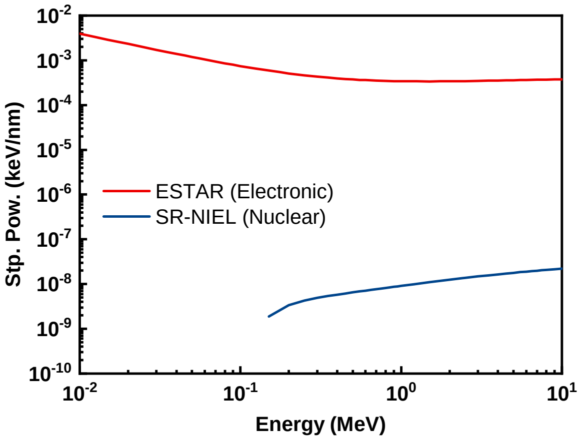

FIGURE 1.3: Electronic and nuclear stopping power of electrons in silicon dioxide at density of 2.2 g/cm^3.

1.1.3 Projected range

The energetic particle progressively loses its energy by the processes presented above. The outcome of these processes is the stopping (implantation) of the ion in the solid, if it is thick enough. The stopping power allows to calculate the path of the ion from the following expression :

$$R = \int_0^{E_I} \frac{\mathrm{dE}}{S(E)}$$

R - Stopping range of the ion

E_I - Initial kinetic energy of the ion

The path of the ion is not always straight, especially in ballistic regime. This results from the fact that, especially at low speed, the fluctuations of energy loss are no longer negligible compared to the average energy loss defined by the stopping power. This phenomenon leads to a diffusion of the ion called "struggling" in English. The projected path and angular distribution due to the statistical fluctuation can be calculated. The average projected path is that of the ion along its initial direction. It is noted R_p.

Note that the ion beam can have a variable angle of incidence with respect to the surface of the sample. In this work, we always work at normal incidence. Consequently, the value R_p corresponds to the depth of implantation of the ion with respect to the surface of the sample.

TABLE 1.1: Average projected R_p calculated by SRIM/TRIM

Particles	Energie MeV	$dE/dx_{Elec.}$ keV / nm	$dE/dx_{Nucl.}$ keV / nm	Projected Range µm	Longitudinal Straggling µm	Lateral Straggling µm
^{12}C	12.0	1.1	1.1E-03	11.0	0.4	0.4
^{36}Ar	36.0	4.6	1.0E-02	11.0	0.4	0.4
^{48}Ca	412.8	3.0	1.7E-03	106.0	3.2	0.9
^{58}Ni	33.1	6.5	3.3E-02	10.4	0.5	0.7
^{78}Kr	54.6	8.4	4.4E-02	11.3	0.5	0.6
^{129}Xe	91.6	11.8	9.2E-02	13.5	0.5	0.6
^{1}H	16.0	5.7E-03	2.7E-06	1590.0	63.6	58.6

Table 1.1 shows the average projected R_p calculated by SRIM/TRIM for ion beam. To make sure that energy deposition can be considered homogeneous for the entire specimen under the experimental condition, we have synthesized and prepared two different forms of mesoporous silica - the thin films and the pellets.

1.2 Studied materials and state of the art of their irradaition

Because of radiation penetration depths, we choose the appropriate material shape for different practical experimental needs, namely thin films for ions beam irradiation (R_p ~ dozen µm) and pellets for electron beam irradiation (R_p ~ many thousands of microns). In this subsection we will briefly outline the principles of the synthesis method used, and specific detailed synthesis parameters will be given later with the discussion of the actual experiments. The literature review on the defects of the survey material will also be discussed.

1.2.1 Ordered mesoporous silica

Although mesoporous silicas were obtained before the 1990s [28], mesoporous silica with a highly organized structure was first synthesized in 1992 by scientists at Mobil Oil Company [29]. These materials are part of the M41S family. This family of materials is said to be "revolutionary" since it has highly structured pores with sizes up to 10 nm, which is far larger than conventional porous materials such as zeolite (<1.5 nm). This increase in pore size offered new application prospects. This family consists of materials of very varied pore morphologies, of which MCM-41 (cylindrical mesopores of hexagonal stacking, P6mm), MCM-48 (tubular mesopores of cubic symmetry, $Ia\bar{3}d$), and MCM-50 (cylindrical mesopores of laminar structure, P2) are the best known (see figure 1.4).

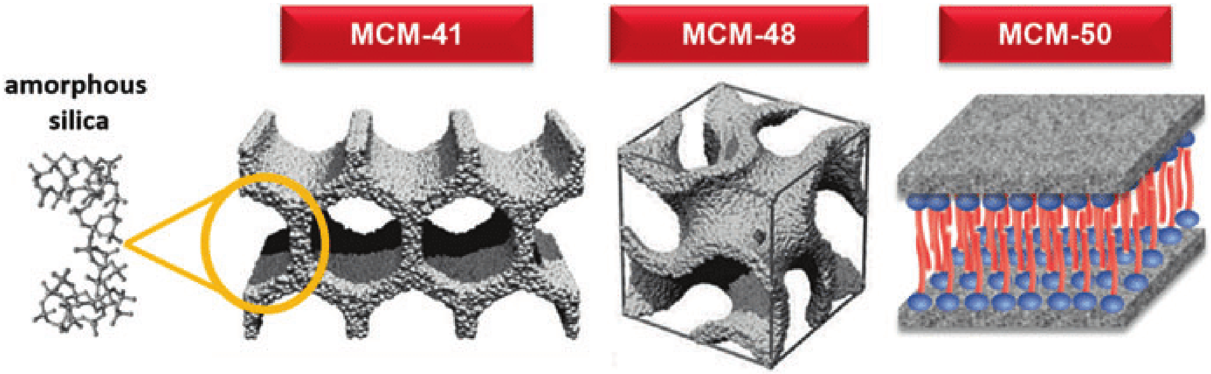

FIGURE 1.4: Members of the M41S family. MCM-41 (hexagonal), MCM-48 (cubic), and MCM-50 (lamellar with the presence of surfactant molecules between lamellae). Figure from reference [30].

A few years after the discovery of the M41S family, another team at the University of California Santa Barbara synthesized another family of mesoporous silica, named SBA after their university [31]. The particularity of these materials is that the pore size could reach 30 nm.

The process of mesoporous structure formation is based on the use of a structuring surfactant and a silica precursor. The surfactant aggregates and leads to the formation of organized micelles which can be lamellar, cylindrical or spherical, depending on the operating conditions (concentration, pH). The silica precursor cross-links, also called polycondensate, around the micelles called "template", which leads to the formation of the silica skeleton (wall) which fixes the structure. Finally, the surfactant can be removed by rinsing or pyrolysis (annealing at high temperature) leaving a pore network. At the same time, the silica network can be further stiffened by natural aging or additional thermal annealing.

1.2.1.a Surfactants

Surfactants, also called tensioactives, are amphiphilic molecules. They have a hydrophilic part and a hydrophobic part, or lipophilic. There are four types of surfactants depending on the nature of their hydrophilic part: a) Anionic surfactant, b) cationic surfactant, c) zwitterionic surfactant and d) nonionic surfactant. SBA-15 and MCM-41 have reasonably well-established synthesizing methods, therefore we'll adopt the same validated surfactant, namely P123 and CTAB.

The triblock copolymer Pluronic P123 is used to synthesize the SBA-15 powder which has 2D-hexagonal stacking cylindrical pores (P6mm) with a diameter in the range of 7 nm and the thin film which has 2D-hexagonal stacking cylindrical pores (P6mm) with a diameter of 4 nm. P123 is a surfactant nonionic made of a hydrophobic poly(propylene glycol) block surrounded by two hydrophilic poly(ethylene glycol) blocks. We often find the writing PEO-PPO-PEO with EO= CH_2CH_2O and PO = $CH_2CH(CH_3)O$. The nominal chemical formula of P123 is $HO(CH_2CH_2O)_{20}(CH_2CH(CH_3)O)_{70}(CH_2CH_2O)_{20}H$.

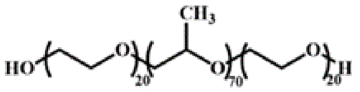

The cationic surfactant cetyltrimethylammonium bromide CTAB is used to synthesize the famous MCM-41 structure of the M41S family and the thin film with diameter of about 2 nm. CTAB is composed of a hydrophilic ammonium head and a hydrophobic tail of hexadecyl type. The chemical formula of CTAB is $[(C_{16}H_{33})N(CH_3)_3]Br$.

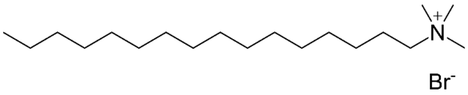

1.2.1.b Silica precursor

The polymerization of the silica network is the result of a sol-gel process, also known as "soft chemistry," in which the solid is produced at low temperature from a liquid silica precursor. The sol is a colloidal dispersion of particles in a liquid. The formation of this solution necessitates the use of a precursor consisting of a metallic or metalloid atom surrounded by a ligand [32]. The most widely used precursor for silica is TEOS (Tetra Etoxy Ortho Silicate, $Si\text{-}(OCH_2CH_3)_4$). This precursor can hydrolysis by adjusting the pH as follows:

$$\mathrm{Si} - (\mathrm{OR})_4 + x\mathrm{H_2O} \rightarrow (\mathrm{HO})_x - \mathrm{Si} - (\mathrm{OR})_{4-x} + x(\mathrm{ROH})$$

Several hydrolyzed precursors combine to form dimers, trimers, or polymers, which result in the formation of consecutive covalent bonds.

$$(\mathrm{OR})_3 - \mathrm{Si} - \mathrm{OH} + \mathrm{HO} - \mathrm{Si} - (\mathrm{OR})_3 \rightarrow (\mathrm{OR})_3 - \mathrm{Si} - \mathrm{O} - \mathrm{Si} - (\mathrm{OR})_3 + \mathrm{H_2O}$$

This condensation results in the formation of colloidal particles, which make up the sol. During this process, the formation of colloidal particles causes the sol to become increasingly viscous until a macroscopic network forms. As a result, a gel is formed.

At this stage, the gel still contains a significant portion of the sol, non-hydrolyzed and non-condensed groups. An aging stage leads to a shrinking of the gel and its densification, called syneresis, by the continuous formation of covalent bonds and the exclusion of water. This stage contributes to the mechanical strengthening of the material.

1.2.1.c Structure of mesoporous silica

It has been discovered that the structure of the silica network in mesoporous silica is comparable to the structure of nonporous silica that has been generated by sol-gel under similar circumstances. The relevant structural information was explored and proved to be characterized by IR, RMN, and other methods [33–36]. The approaches used to characterize the silica structure using these techniques, as well as the strategies used to monitor the structural changes generated by irradiation, are detailed in the sections 1.4 and chapters devoted to the experiments.

1.2.2 Mesoporous a-SiO_2 thin film

Mesoporous thin film preparation needs specific coating processes such as spray coating, meniscus coating, spin coating and dip coating [35]. We have simply employed dip-coating in this thesis, and the first structured mesoporous thin films were created by C.J. Brinker *et al.* using the same method [37].

Dip-coating exploits the mechanism of Self Assembly induced by the evaporation of the solvent: Evaporation-Induced Self Assembly (EISA). A very dilute solution of silica precursor and surfactant is prepared beforehand. The substrate is soaked in the solution and pulled at a constant speed and under a controlled humidity level. Evaporation of the solvent triggers a gradual increase in surfactant concentration. When the critical micellar concentration (CMC) is reached, the micelles form and organize (see figure 1.5).

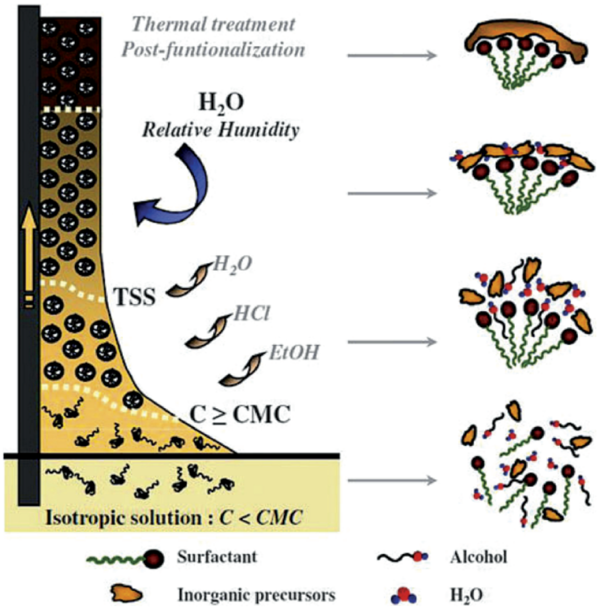

FIGURE 1.5: Schematic representation of the evaporation-induced self-assembly (EISA) mechanism via dip-coating (CMC = critical micellar concentration; TSS = tunable steady state). Figure from reference [38].

In addition to mesoporous silica films, we have also investigated nonporous silica thin films, which are thermally grown on silicon wafer or synthesized by sol-gel dip-coating method.

1.2.3 Mesoporous a-SiO_2 pellet

The mesoporous silica powders of SBA-15 and MCM-41 were prepared by adapting the sol-gel procedure used by Zhao *et al.*[31] and Kumar *et al.*[39] To achieve a homogenous irradiation throughout the volume, the as-synthesized SBA-15 and MCM-41 powders must be compressed into pellets.

The powders are shaped by uniaxial pressing at room temperature under a pressure of a pressure of about 250 MPa (the details of this choice will be discussed later in 2) in a tri-shell die (figure 1.6). The pelleting pressure was carefully selected such that the mesoporous structure would not be adversely impacted. In this study, we adopted 250 MPa, and a discussion of the pressure selection will be provided in a subsequent section.

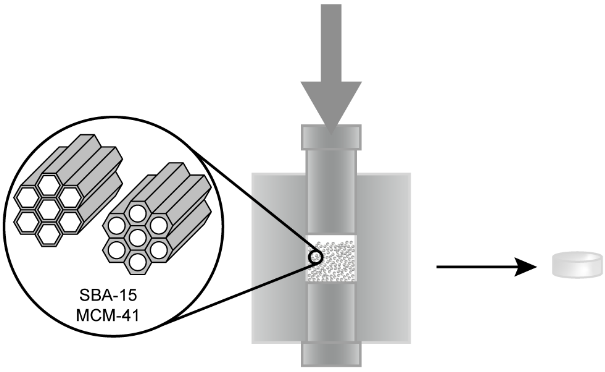

FIGURE 1.6: Schematic diagram of the die pellet press used to produce silica pellets from silica powder.

The pelletization of the powders also allows to limit the sputtering under the beam and facilitates the maintenance of the sample during the irradiation, since the beam arrives horizontally in the chamber, and perpendicular to the sample.

1.2.4 Bombardment-induced defects in silica

Silica holds a prominent position in the class of inorganic oxides since it is an inorganic polymer that may be formed in either amorphous or crystalline form. Furthermore, because a number of applications of this material (nuclear waste conditioning, optoelectronics, etc.) necessitate that it is subjected to particle irradiation (photons, electrons, alpha, neutrons, etc.), many studies have concentrated on the defects that are created under these conditions. In the following paragraphs, we will briefly summarize the most important contributions of those researches.

1.2.4.a Structure of pure silicon dioxide

As shown in figure 1.7, vitreous silicate and SiO_2-glasses are composed of the SiO_4 tetrahedron as its structural unit [40–42]. These fundamental tetrahedral units are connected by oxygen bonds, and the arrangement of these connections defines the silicate's categorization. The materials is classed as a Nesosilicate when the tetrahedra are not connected together, as each exists in isolation. The material is classed as a Sorosilicate if it consists of two tetrahedra bonded together. If all of the tetrahedra connect back onto one other to create a closed ring, then the material is a Cyclosilicate.

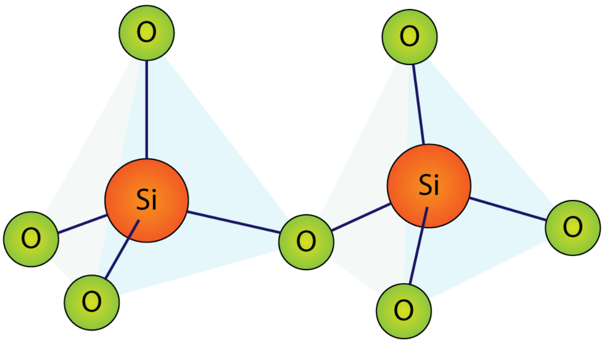

FIGURE 1.7: SiO_4 tetrahedron.

1.2.4.b Intrinsic point defects

A variety of defect structures (figure 1.8) are known to exist in silica materials [43–45]. Many aspects regarding the nature of the defects and their correlated properties are still controversial and not yet completely understood. Quite a lot of defect types have been discussed in the literature and many reproduction models have been proposed for each one. In this part we will review only the three main defects in the silica network.

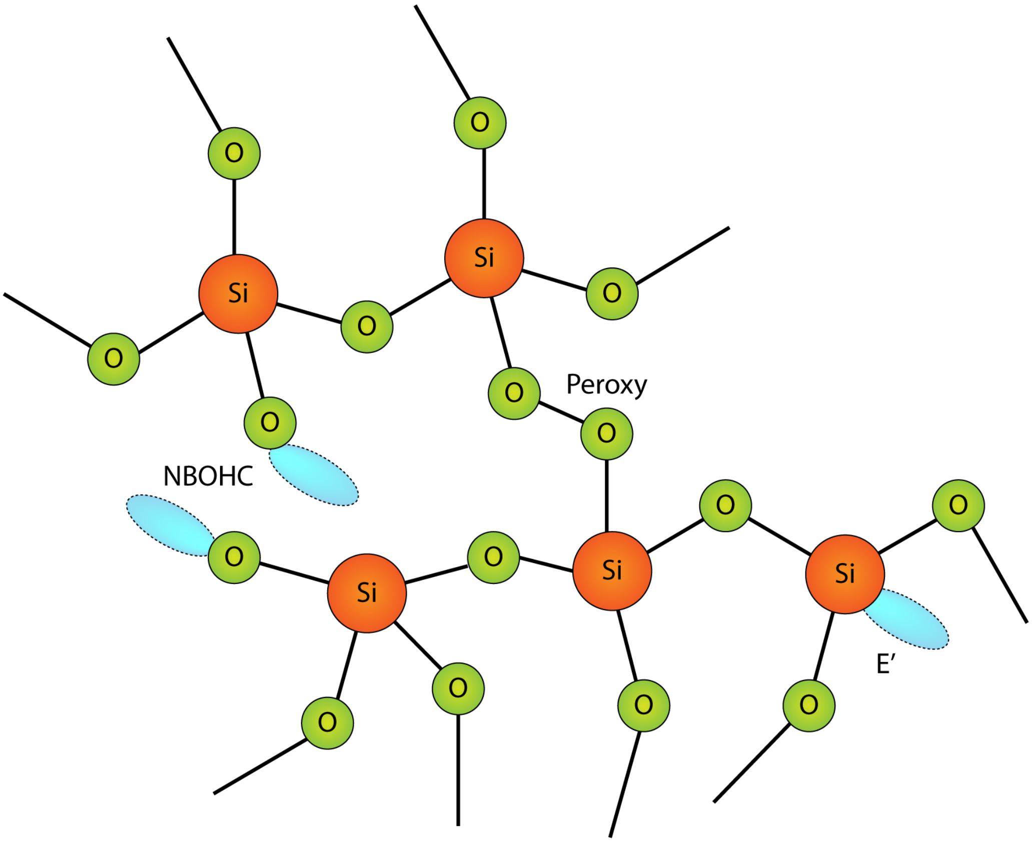

FIGURE 1.8: Defect structures in silicon oxide. Hydrogen atoms are not shown.

E'-center

Perhaps the most well-known paramagnetic defect in all types of SiO_2 is the E'-center, originally discovered by EPR spectroscopy in the late 1950s [46–49]. Griscom, Isoya *et al.* [50, 51] have studied the hyperfine structure in the EPR spectrum and found that the E'-center can consist of an unpaired electron in a dangling tetrahedral (sp3) orbital of a single silicon atom, which is linked to just three oxygens in the glass network. In figure 1.9, a generic E'-center is depicted as $\equiv$ Si•, where the three parallel lines indicate three distinct oxygen connections to one silicon atom and the dot represents the unpaired electron.

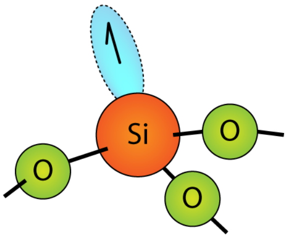

FIGURE 1.9: Generic E'-center

Non-bridging oxygen hole center (NBOHC)

This center can be represented as the oxygen portion of a broken bond (figure 1.10). It is both electrically neutral and paramagnetic, and it is the most basic oxygen-related inherent defect in silica. The NBOHC is thought to be formed when hydrogen atoms are released radiolytically from one of a pair of -OH groups in wet silica [52].

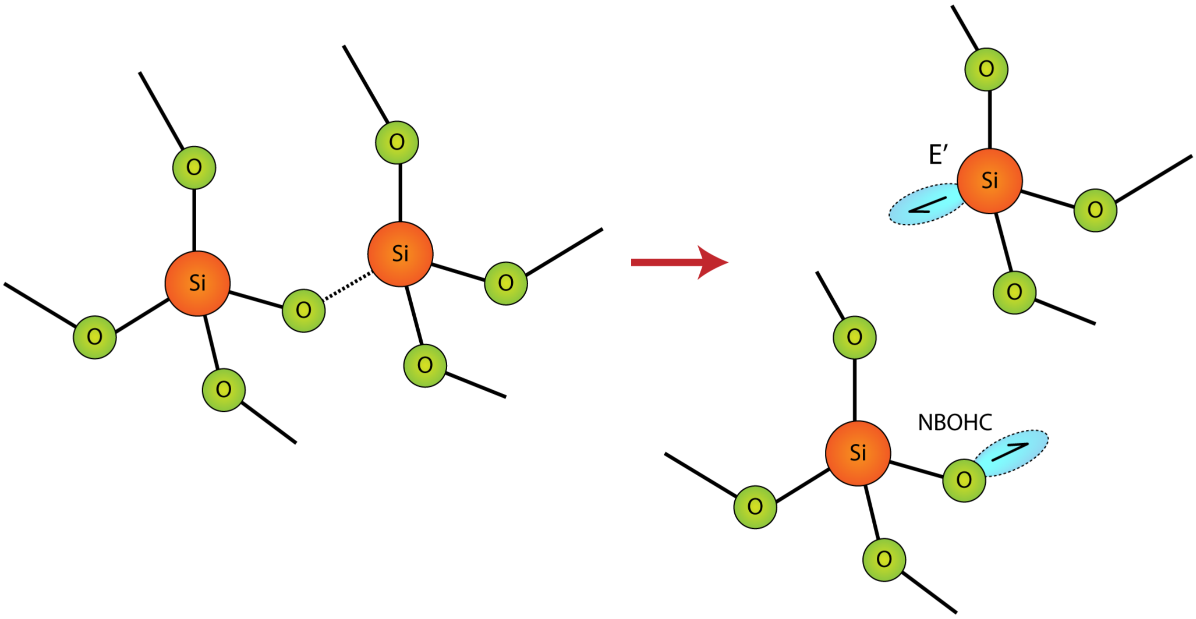

FIGURE 1.10: Schematic representation of the structure of the NBOHC center in a-SiO_2.

Peroxy radical (POR)

Silica's Peroxy Radical (POR) (figure 1.11) is an antibonding π-type orbital defect with a hole delocalized over the O - O bond. The peroxide radical defect was confirmed by Friebele *et al.* [53]. Using the diffuse reflectance method, the optical absorption spectrum for peroxy radicals on SiO_2's surface was estimated in the region around 5.4 eV with FWHM 1.3 eV, and with an oscillator strength of $f \approx 0.067$ [54].

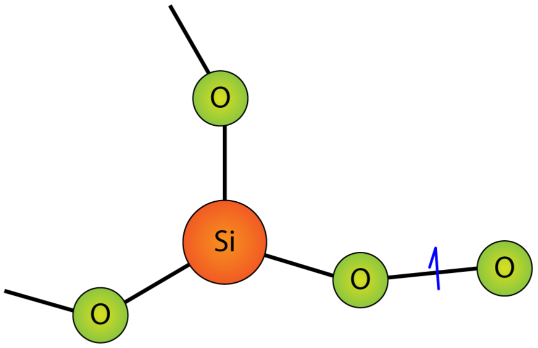

FIGURE 1.11: Schematic representation of the structure of the Peroxy center in a-SiO_2.

Irradiation-induced point defects

The creation of all the defects mentioned above was observed after irradiation by neutrons and ions of intermediate energy producing ballistic effects [55]. The mentioned E' center creation was also observed after irradiation with γ-rays and electron beams whose effect is purely electronic [56, 57]. It has also been observed after irradiation by heavy ions for high energies. Dooryhee *et al.* [58] irradiated amorphous silica with the following ions: O 93.5 MeV/amu, Ar 76 MeV/amu, Kr 43 MeV/amu, Xe 27 MeV/amu and U 16.5 MeV/amu whose effect is purely electronic. They found that the production of E' center defects depends, non-linearly, on the stopping power.

1.2.4.c Radiation-induced phase changes: amorphization and crystallization

At low doses (<10^{13} ions/cm^2), one almost just needs to deal with the creation of single point defects (or clustered defects). But when the doses go higher, damage includes amorphization and crystallization are much more essential. The radiation-induced phases changes effects of intermediate- and high-energy radiation on non-oxide materials have been evaluated in two studies. Inui *et al.* [27] found that, when attacked with 2-MeV electrons, only 7 of the 42 ceramic materials were amorphized. In their experiments, they found that the susceptibility of materials to beam-induced crystallization was closely connected to their location on the temperature-crystallinity phase diagrams. According to a previous study [59] on 72 nonmetallic materials bombarded with heavy ions, two factors may be used to determine whether an amorphous or crystallized outcome is achieved. The ratio of a material's crystallization temperature to melting point is the first indication, while ionicity is the second.

Temperature-ratio criterion

The temperature-ratio criterion is a phenomenological criterion proposed by Naguib and Kelly [59] based on experimental observation of bombardment-induced structural changes in non-metallic solids. It was discovered that if the T_c/T_m value was more than 0.30, an amorphous product would result. This value is 0.57 for silica, suggesting that an amorphous outcome is expected.

Ionicity criterion

The same authors [59] explore how well one can explain the response of solids to ion impact on the basis of bond type, i.e. of ionicity. If the ionicity of the irradiated material is $\leq$0.47, an amorphous result is predicted and seen. The ionicity has the form of Pauling's equation: [60]

$$\text{ionicity} = 1 - \exp\left\{-0.25\left(X_A - X_b\right)^2\right\}$$

with X_A and X_b the suitable electronegativity value of atom.
Considering SiO_2 has an ionicity of 0.47, an amorphous result is predicted.

The case of mesoporous silicas

Since the silica architecture of the materials examined in this thesis is naturally amorphous, analyzing atom disruptions or rearrangements from their lattice locations is difficult. However, a change in the volume of the pores is feasible, and so is the metamorphism of an ordered amorphous structure with a periodic pattern of pores into a disordered, nonporous structure.

1.2.5 Ion-Beam-Induced deformation in a-SiO_2

When compared to crystalline silica, amorphous silica exhibits a number of unique characteristics under irradiation, one of which is irradiation-induced deformation. In the following paragraphs, we will highlight three of the most relevant findings.

1.2.5.a Anisotropic plastic deformation in non-porous silica - hammering effect

In 1989, Benyagoub and Klaumünzer *et al.* [61, 62] observed ion-beam-induced anisotropic plastic deformation in silica and a wide variety of amorphous materials, which is not found in crystals. Under irradiation with a high energy heavy ion beam, the so-called ion harmmering effect is defined as the apparent increase of the sample dimensions perpendicular to the ion beam and the shrinking of the sample dimensions parallel to the ion beam. Their investigation is mostly focused on a non-porous sample with a high depth to surface ratio. Following that, numerous investigations [63–65] corroborated and expanded on this observation to colloidal particles. Furthermore, research has indicated that ion hammering exhibits several characteristics: it represents the volume-conserving anisotropic deformation; the hammering is only dominant at high fluences (approximately 4×10^{12} ions/cm^2 in silica under 200 MeV Xe irradiation); and the hammering is only induced at S_e greater than ~2 keV/nm. There are, to our knowledge, no studies of this effect in mesoporous materials that have been conducted under irradiation at the present time.

1.2.5.b Isotropic shrinkage of non-porous silica matrix

Particle or ionizing radiation, according to Primak and EerNisse *et al.* [66, 67], generates a densification in a-SiO_2 that approaches a constant value of ~3% to the relaxed network In both the ballistic and electronic regimes, this phenomenon has been observed. It has been reported that the 3% limit can be reached when the density of energy deposited is greater than 3×10^{23} eV/cm^3 in the ballistic regime and greater than 2×10^{26} eV/cm^3 in the electronic regime, respectively. In 1993, Devine examined this isotropic compaction (densification) of amorphous silica caused by keV-ion irradiation. The overall densification is shown to be caused by a reduction in the bond angle as well as the simultaneous production of both small and large rings in the amorphous silica network. Despite this, the majority of the research has focused on the nonporous silica network rather than porous silica.

1.2.5.c Deformation of porous silica

Klaumünzer[17, 18] previously bombarded amorphous nanoporous Vycor glass (%m_{SiO2}>96%) with track-generating ions (70 MeV Ar, 260 MeV Kr, 340 MeV Xe) and observed pores progressively shrink and vanish. Pore shrinkage and lateral shift are assigned to pressure and shear stress relaxation in the hot and fluid ion tracks, respectively. The effect of pores on the chemical stability of Vycor when exposed to radiation, on the other hand, has not been investigated.

Lou's work [16] was the impetus for a renewed interest in the behavior of ordered mesoporous silica under irradiation. He demonstrated that, in the ballistic regime, a 100 % compaction owing to the collapse of mesopores may be detected with a dose of around 10^{22} keV/cm^3 (~1.4 dpa). A analysis using conventional Molecular Dynamics modeling for ballistic effect was carried out. Despite the presence of certain parametrical incoherence, it is possible to effectively replicate mesopores collapse and to give early mechanistic explanations in the case of ballistic regime. In the electronic regime, two sets of S_e were investigated: one at 1 keV/nm and another at 5 keV/nm. Initial results appear to indicate that ions with S_e around 1keV/nm have no noticeable influence on the evolution of the mesoporous structure. However, a considerable collapse impact was found at S_e around 5 keV/nm, but no complete compaction was detected until the highest tested dose ($E_{elec.}$ = 10^{21} keV/cm^3).

An in-depth and comprehensive investigation will be conducted in the present thesis for the electronic regime, which will, on the one hand, greatly widen the range of the examined Se and, on the other hand, give a more in-depth knowledge of the structural alterations and mechanisms.

1.3 Experimental facilities

In this section, we will present the irradiators involved in this work. These facilities are part of the national network EMIR&A, which is is the French national accelerator network dedicated to the studies of irradiation of materials and molecules and/or to their analysis by using ion beams. It gathers 15 advanced ion and electron accelerators and in situ instruments with unique performances, installed on 11 platforms, distributed over 6 sites (Caen, Orléans, Orsay, Palaiseau, Paris, Saclay). We used the SME and IRRSUD lines at CIMAP/GANIL (Caen), the Pelletron accelerator at LSI (Saclay) and the Cyclotron at CEMHTI (Orléans). These instruments are available through an annual call for projects.

1.3.1 CIMAP/GANIL

CIMAP (**C**entre of research on **I**ons, **MA**terials and **P**hotonics) is a laboratory that directs interdisciplinary research at the GANIL (**G**rand **A**ccélérateur **N**ational d'**I**ons **L**ourds) facility. It was developed from the CIRIL (**C**entre for **I**nterdisciplinary **R**esearch with **H**eavy **I**ons) platform. It provides an ideal platform for the international scientific community whose objective is to investigate the processes of ion - atom collisions, their implications on atomic arrangements, and their effects on physical and chemical characteristics. The target consist of atoms, molecules (biologic or not), clusters, surfaces and materials of all types. These investigations are primarily concerned with the impacts of the electronic excitations created by multi-charged ions, whatever it is at high- or low-velocity.

Most of the irradiations involving ions interacting by electronic processes have been performed at SME and IRRSUD beamline of CIMAP/GANIL. At IRRSUD beamline, the available ions from Carbon to Uranium are accelerated by one of the injector cyclotrons (C01 or C02) at energy from 0.25 to 1 MeV/A with a continuous measurement of the ion flux during irradiation. At D_1-SME beamline, it receives ion beams accelerated by CSS1 cyclotron for the medium-energy beams and by CSS2 cyclotron for the high-energy-ion beams. This accelerator allows the production of ions with energies up to a few tens of MeV/A. The schematic of the CIMAP/GANIL installations is shown in figure 1.12.

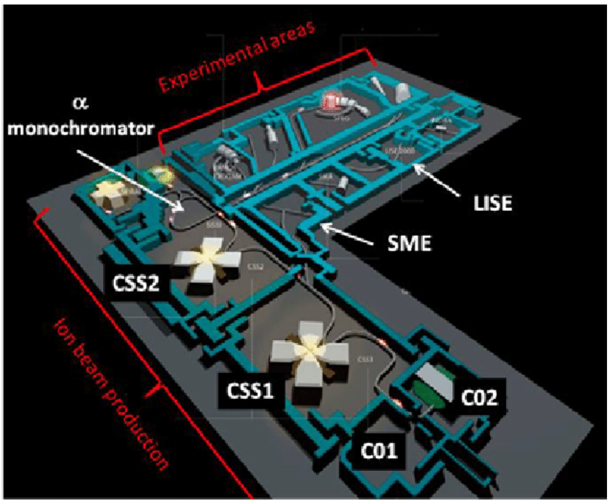

FIGURE 1.12: CIMAP/GANIL installations at Caen. Figure extracted from reference [68].

1.3.2 SIRIUS

The SIRIUS (**S**ystème d'**IR**radiation pour l'**I**nnovation et les **U**tilisateurs **S**cientifiques) facility, at the (LSI) Irradiated Solids Laboratory (UMR 7642 CEA-CNRS-Ecole polytechnique), is an irradiation platform with high energy electrons consisting of an electron accelerator and two irradiation stations (having the possibility of carrying out irradiations at high currents and at low temperatures). The SIRIUS facility is open to a large community of users nationally and internationally and is part of the national network of accelerators for the study of irradiated materials EMIR&A.

Most of the irradiations involving electron beam have been performed at Pelletron accelerator (figure 1.13) of SIRIUS, which delivers electrons of energy from 150 keV to 2.5 MeV. Electron beam current is measured using pico-ammeters at the output of the accelerator and along the irradiation line. The electrical charge passing through the sample section is, in turn, measured via a digital current integrator.

FIGURE 1.13: The SIRIUS facility, at the Irradiated Solids Laboratory (UMR 7642 CEA-CNRS-Ecole polytechnique).

1.3.3 CEMHTI

The CEMHTI (**C**onditions **E**xtrêmes et **M**atériaux : **H**aute **T**empérature et **I**rradiation) laboratory is equipped with a fairly unique variable energy cyclotron. Its versatility and the very high degree of competences of associated technicians and scientists make it an extremely multidisciplinary machine and efficient instrument with applications in various fields (solid state physics, materials properties under irradiation, archeology, production of radionuclides…). The cyclotron is part of the national network EMIR&A.

1.4 Experimental characterization techniques

In this paragraph, the main post-irradiation analysis techniques used are presented. Detailed parameters of the characterization will be given in the subsequent practical experimental sections. We will also address common (irradiation-induced) damage and defects that may be identified by the relevant characterization techniques in silica materials.

1.4.1 Nitrogen adsorption/desorption isotherms

A frequent method for characterizing the pore characteristics of a solid material is to use gas adsorption/desorption. Probe gas molecules can pass through and adsorb on the surface of the target. The link between the quantity of adsorbed gas and the gas pressure at a constant temperature allows for the calculation of the specific surface area, the pore volume, and the pore size distribution of the adsorbent. Depending on the type of isotherm generated and the nature of the materials under investigation, a variety of models of gas adsorption on solid surfaces can be used for this purpose. Non-local density functional theory (NLDFT) models [69–72] were used to characterize mesoporous materials in this work, and their advantages over other conventional approaches will be explored briefly in this section.

BJH, DR, HK, and other [73–76] commonly used classic approaches involving a specific pore filling process underpins the foundation for so-called classical macroscopic, thermodynamic theories. The BJH (Barrett-Joyner-Halenda) method is based on the Kelvin equation (also known as the Young-Laplace equation), which ties pressure to the radius of curvature (pore size) of a liquid meniscus while taking into account the thickness of the adsorbed layer of adsorbate. However, in tiny mesopores (such as the material known as MCM-41), the accuracy of this fundamental model can be significantly reduced. Additionally, it is absolutely incompatible with micropores (where no liquid meniscus occurs). The Dubinin-Radushkevich technique, as well as semiempirical approaches such as those of Horvath and Kawazoe (HK) and Saito and Foley, are devoted to characterizing micropore filling, but they are unable to be applied to the study of mesopore size. A consequence of this is that, in the case of a material that contains both micro- and mesopores, it is necessary to utilize at least two approaches in order to determine the size distribution(s) of the pores from an adsorption/desorption isotherm. The accuracy of such thermodynamic, macroscopic approaches is further limited since the pore fluid is considered to have thermophysical properties that are equal to those of the bulk fluid. According to a recent theoretical and experimental investigation, the thermodynamic features of a confined fluid can differ dramatically from those of a bulk fluid in certain situations (shifts in critical point, freezing point, and triple point etc.)

Comparatively to these macroscopic techniques, methodologies such as the Density Functional Theory (DFT) or methods of Monte Carlo simulation give not only a microscopic model of adsorption but also a more accurate description of the thermodynamic parameters of the pore fluid. They are based on statistical mechanics and link macroscopic features to molecular behavior in a way that is not possible with conventional theories. These methods take into account the direct interaction of the adsorbate with the adsorbent surface, the micropore filling process (which is not a condensation process), the development of the adsorbed film thickness, and capillary condensation (adsorption) and capillary evaporation (desorption), and they allow for the calculation of equilibrium density profiles of a fluid adsorbed on surfaces and in pores. Regarding the type of pore filling (for example, first order phase transition or continuous pore filling), no assumptions are required. DFT and MC calculations are capable of directly deriving the equilibration density profiles of the confined fluid at a given temperature and pressure. By employing a single approach that incorporates DFT or MC techniques, it is possible to provide pore size analyses over the whole micro- and mesopore diameter range.

1.4.2 Small-angle X-ray scattering (SAXS)

Small-angle X-ray scattering (SAXS) is non-destructive and provides information on the structure of mesoporous silicas with excellent statistical precision owing to averaging over a microscopic sample volume.

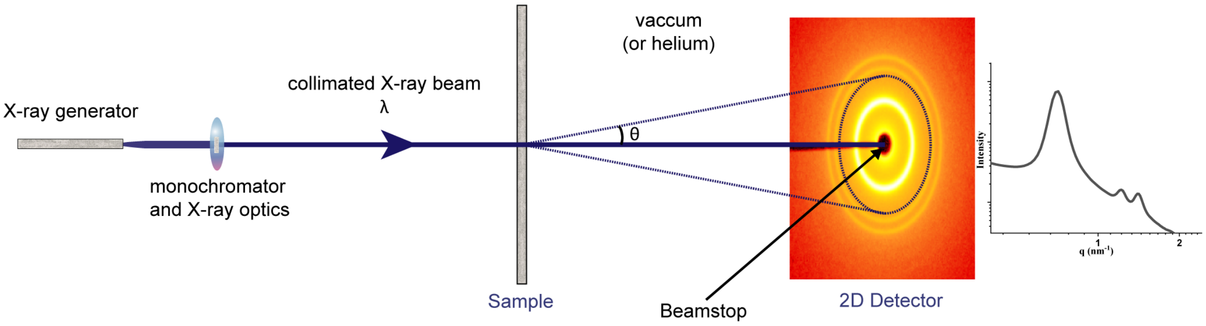

FIGURE 1.14: Scheme of the experimental setup for recording the scattering patterns.

Small-angle X-ray scattering (SAXS) experiments were conducted using a Guinier-Mering set-up with a 2D image plate detector. The X-ray source was a molybdenum anode, delivering a highly collimated and monochromatic X-ray beam (Λ = 0.71 Å, E = 17.4 keV). The region between the sample and the image plate was purged with flowing helium to avoid air absorption. Figure 1.14 shows the scattering geometry of a typical SAXS experiment set-up showing the incident, scattered, and transmitted beams; the 2D detector; and the beamstop. The 2D detector records the scattered intensity in the forward direction, which is the number of photons dispersed as a function of the scattering angle. A beamstop in front of the detector blocks the transmitted X-ray beam. Because scattering at short angles is entirely elastic, the magnitudes of incident and scattered wave vectors (k_i and k_s respectively) are equal to $2\pi/\lambda$. The magnitude of scattering vector $q = k_s - k_i$ can be calculated by vector transfer (momentum transfer) as

$$q = \frac{4\pi}{\lambda} \sin\frac{\theta}{2}$$

A simple integration may be used to express radially symmetrical 2D patterns as a 1D profile.

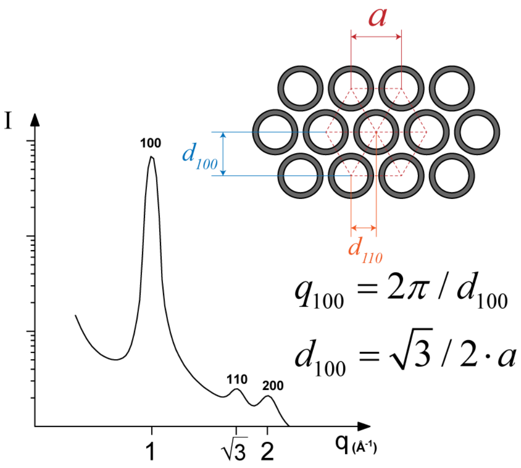

FIGURE 1.15: Small angle X-ray scattering (SAXS) pattern of 2D hexagonal structure.

As shown in the figure 1.15, ordered mesoporous silicas with hexagonal lattices, such as SBA-15 and MCM-41, have a diffractions peak position ratios of 1, $\sqrt{3}$, 2, $\sqrt{7}$, 3, ... For 2D hexagonal structure, the lattice parameter is given by $a_0 = 2d_{100}/\sqrt{3}$, where $d_{100} = 2\pi/q_{100}$

1.4.3 Pycnometry

Skeletal density is defined as the ratio of a solid material's mass to the sum of the solid material's volume and closed (or blind) pores within the material. A pycnometer estimates the skeletal volume of a material by gas displacement using the volume-pressure relationship of Boyle's Law. The displacement medium is an inert gas, generally helium. The sample is placed in a sealed cup with a known volume. After that, the cup is deposited into the sample chamber. The sample chamber is filled with gas, which is then expanded into a second chamber with a known volume. The pressure in the sample cell after filling and the pressure in the expansion chamber after filling are measured, and then the volume is determined based on the analysis. "Helium density" refers to the density determined using Helium Pycnometry, which excludes open pores from the calculations. Since Helium can't get to closed pores, they're included in the overall volume of the system. The density is calculated by dividing the sample weight by the volume.

$$\rho_{\text{ skeletal}} = \frac{m_{\text{pellet}}}{V_{\text{pycno}}}$$

The pellets were considered cylindrical, and the apparent volume (V_{apparent}) of pellets was measured by vernier caliper. The closed porosity of the sample was deemed insignificant when the skeletal density and the theoretical density of amorphous silica are extremely near. In this case, total open porosity will be used as a measure of total porosity in the discussion that will follow. It was based on:

$$\varepsilon_{\text{ total}} = 1 - \frac{\frac{m_{\text{pellet}}}{V_{\text{apparent}}}}{\rho_{\text{skeletal}}}$$

As shown in the figure 1.16, by combining the micropore and mesopore volumes obtained from N_2 isotherm, the respective micropore porosity and mesopore porosity are calculated according to

$$\varepsilon_{\text{ micro}} = \frac{V_{\text{micro}}}{V_{\text{apparent}}}$$

$$\varepsilon_{\text{ meso}} = \frac{V_{\text{meso}}}{V_{\text{apparent}}}$$

And finally, the macro-pores (extra-granular pores) porosity are calculated according to

$$\varepsilon_{\text{ macro}} = \varepsilon_{\text{total}} - \varepsilon_{\text{micro}} - \varepsilon_{\text{meso}}$$

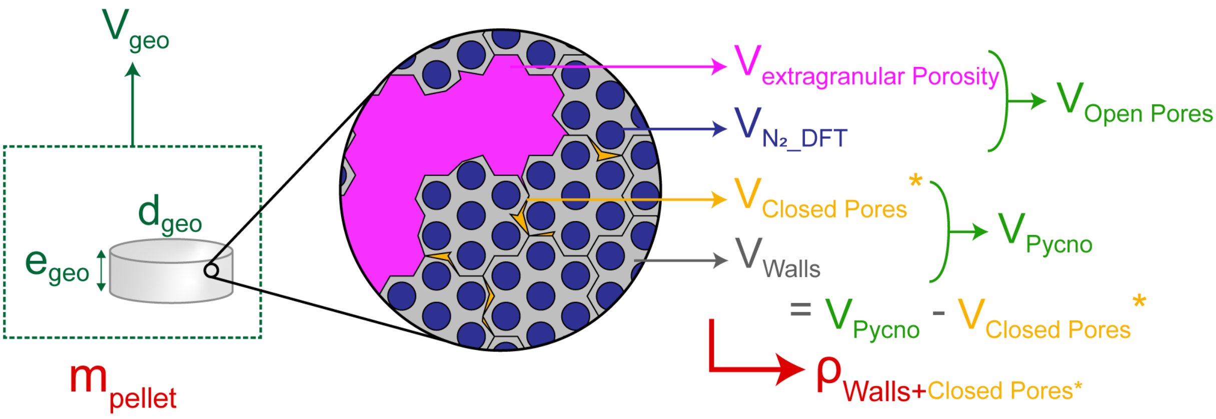

FIGURE 1.16: Calculation of porosities.

1.4.4 Electron microscopy

Use of Scanning Electron Microscope (SEM), Transmission Electron Microscope (TEM) and Scanning Transmission Electron Microscope (STEM) (figure 1.17) for the investigation of porous materials provides a number of advantages. On top of that, they provide high-resolution visual images of the specimen's structure. While the specimen is immediately exposed to the magnified beam, it is also possible to take a snapshot of the changes in structure caused by electron irradiation.

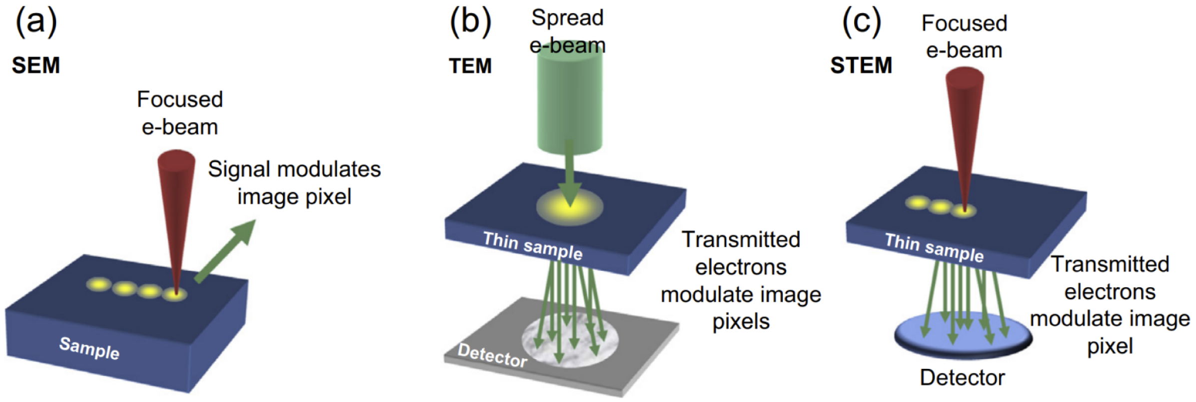

FIGURE 1.17: Schematic of SEM, TEM, and STEM imaging methodology. Figure from reference [77].

1.4.5 Nuclear magnetic resonance (NMR)

Since the publication of the first systematic study of silicates and aluminosilicates using high-resolution solid-state ^{29}Si NMR in 1980 [78], the application of this method has grown rapidly and is quickly becoming a powerful tool in the structural characterization of a wide range of silicates and other silicon-containing materials. Modern solid-state NMR spectrometers can now produce large magnetic field strengths and a wide range of experimental methods. Because ^{29}Si is a spin 1/2 nucleus, magic angle spinning (MAS) produces simple spectra with perfect averaging of the chemical-shift anisotropy, making it the most essential approach for measuring well resolved ^{29}Si NMR spectra of microcrystalline or amorphous materials. Line broadening caused by dipolar ^{29}Si-^{1}H interactions in proton-containing samples may be eliminated by high power proton decoupling, and cross-polarization (CP) can be employed for signal amplification and detection of protons in close proximity to the silicon atom, for example in SiOH groupings. The ranges of ^{29}Si chemical shifts of silicates minerals with different degrees of condensation of SiO^4 tetrahedra are shown in figure 1.18 [79, 80]. (Q^0, nesosilicates; Q^1, sorosilicates; Q^2, inosilicates; Q^3, phyllosilicates; Q^4, SiO_2 polymorphs).

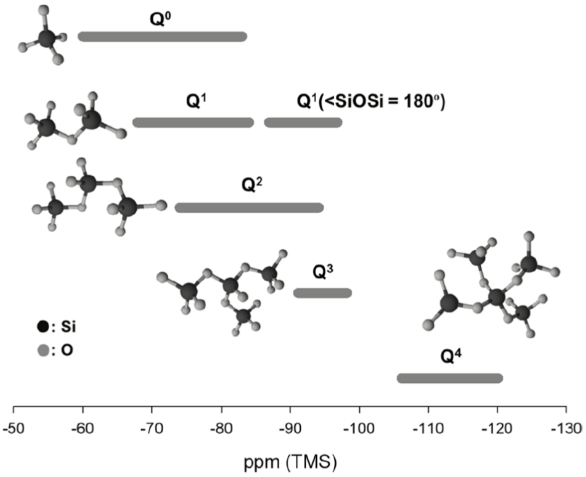

FIGURE 1.18: Classification of silicate minerals according to the degree of polymerization of SiO_4 and their chemical shifts in ^{29}Si NMR. Figure from reference [80]

1.4.6 Infrared (IR)

Infrared spectroscopy provides information on the vibration of chemical bonds. This technique has been applied to provide information on the evolution of the SiO_2 network in the walls. The IR spectra of SiO_2 lattice are characterized by three main absorption bands (figure 1.19) assigned to different vibrational modes of the Si-O-Si bonds [33]: (a) Transverse-optical (TO_1) mode, ρ(Si-O-Si); (b) Transverse-optical (TO_2) mode, ν_s(Si-O-Si); (c) Transverse-optical (TO_3) mode, ν_{as}(Si-O-Si).

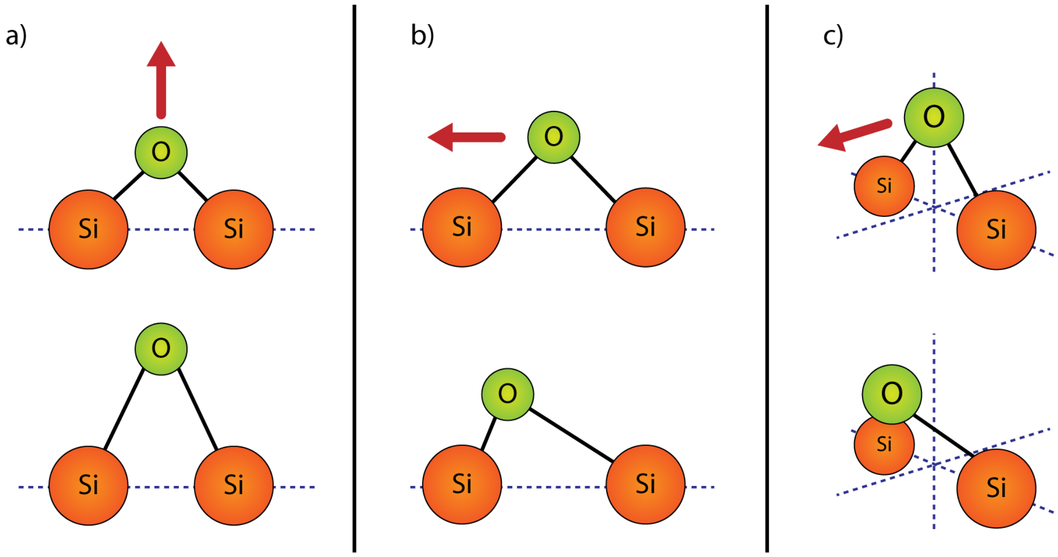

FIGURE 1.19: Schematic representation of the vibrational motions Si-O-Si: (a) symmetric stretching motion along the bisector of the Si-O-Si bridging angle, (b) antisymmetric stretching motion parallel to the Si-Si line between the two bridged cations, (c) rocking motion perpendicular to the Si-O-Si plane. Figure inspired from reference [33].

It is known that the TO_3 (Transverse Optical) vibration band ~ 1080 cm^{-1} measured in infrared is related to the Si-O-Si bond angle by the Lehmann equation [81].

$$\omega_{\text{TO}} = a\sqrt{2\left[(\alpha\sin^2(\frac{\theta}{2}) + \beta\cos^2(\frac{\theta}{2})\right]/m}$$

with α and β - central and non-central force constants
m - mass of oxygen atom
θ - angle of the Si-O-Si bond.
a - This conversion constant = 5.035 x 10^{-12} when α and β are in μm^{-1} and ωTO is in cm^{-1}.

Based on a compilation of a large number of results presented in the literature, Devine [82] proposed an empirical relationship between TO_3 band position and silica density under the effects of temperature and pressure.

$$\omega_{\text{TO}} = 1301.2 - 91\rho$$

In the work of Awazu and Toulemonde *et al.* [83–85], the shift of this band is observed versus irradiation dose, but the amount of displacement is no longer in accordance with the above equation.

In this thesis, the FTIR spectroscopy were acquired between 4000 and 300 cm^{-1} with 4 cm^{-1} resolution.

1.4.7 Cathodoluminescence spectroscopy (CL) and photoluminescence spectroscopy (PL)

The term cathodoluminescence (CL) designates the luminescence induced by energetic electron bombardment. Photoluminescence spectroscopy, often referred to as PL, is when light energy, or photons, stimulate the emission of a photon from any matter. The real structure of silica materials significantly influences their luminescence behavior. Moreover, defect contents and implanted elements dramatically changes the luminescence properties of silicas. Salh *et al.* [86] summarized the main PL and CL emission bands for a-SiO_2 and their proposed associations. Tables extracted from their reference are presented in the Appendix B. Alessi *et al.* [87–89] and Reghioua *et al.* [90] have effectively used these technologies to the monitoring of point defects in silica-based materials.

1.4.8 X-ray reflectivity (XRR)

X-ray reflectivity (XRR) concerns the characterization of thin films. In this case, the incident beam is sent with a low but variable incidence angle between 0 and about 6.5°. The reflected beam is collected by a point detector in a specular way, which means that the angle of reflection is always equal to the angle of incidence (figure 1.20). XRR provides structure information in the (z) direction perpendicular to the layer plane. It is well adapted to the measurement of thin films of thickness varying between 1 and 600 nm. Unlike several techniques such as SEM/TEM give only local information, XRR can provide global and averaged information of the whole analyzed area.

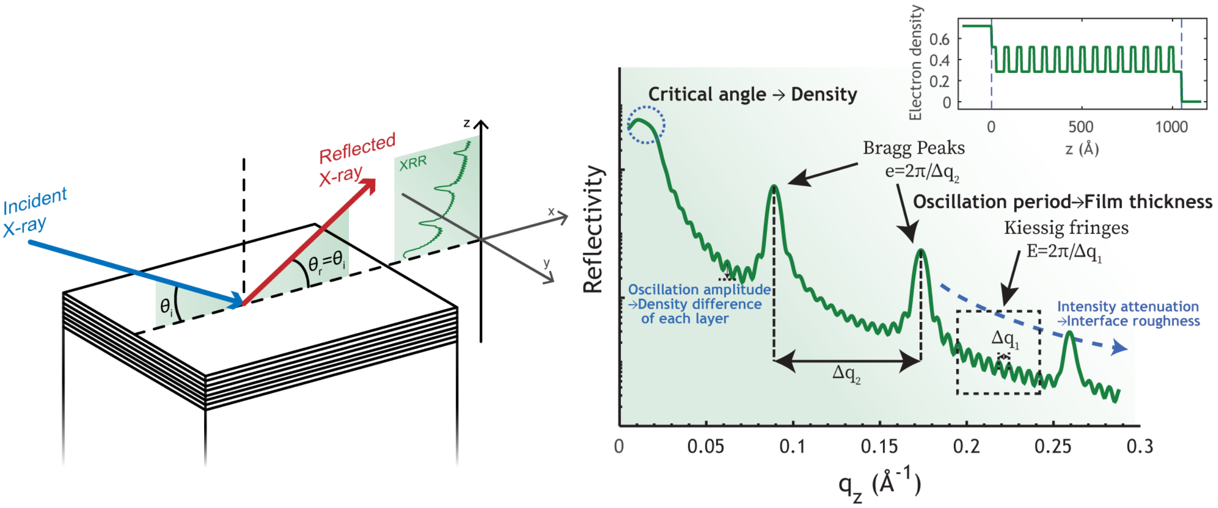

FIGURE 1.20: Schematic of X-ray reflectivity configuration and the information (density, thickness and roughness) extracted from the XRR spectrum.

The reflectivity is defined by the ratio between the reflected intensity and the incident intensity. It is a function of the incidence angle:

$$R(\theta) = \frac{I_r(\theta)}{I_0}$$

As in SAXS, it can be expressed in terms of the transferred vector q

$$q = \frac{4\pi}{\lambda}\mathrm{sin}\theta$$

As shown in fig, analysis of the reflectivity curves can provide several useful information on the structure of thin films:

a) The measurement of the critical angle q_c on the reflectivity curves can give an indication of the electronic density $\rho_e \left(\frac{e^-}{\mathrm{\mathring{A}}^3}\right)$of the material by the relation:

$$\rho_e = \frac{1}{16\pi r_e} q_c^2 = 711 q_c^2$$

This calculated electron density can be converted to a classical density. In the case of non-porous silica with a classical density of 2.2 g/cm^2, the correspond electron density equals to $0.662\ e^-/\mathrm{\mathring{A}}^3$.

b) The periodicity of the Kiessig fringe allows to calculate the total thickness of the layer by the formula:

$$e = \frac{2\pi}{\sqrt{\left(q_z^{n+1}\right)^2 - {q_c}^2} - \sqrt{\left(q_z^{n}\right)^2 - {q_c}^2}}$$

with q^{n+1} and q^n the positions of the adjacent Kiessig fringe.

When the periodicity measurement can be made far enough from the total reflection plateau, the critical angle can be neglected, and the equation above becomes:

$$e = \frac{2\pi}{\Delta q_{z,Kiessig}}$$

c) In the case of periodically repeated multilayers, such as mesoporous layers that consist of pore layers and silica wall layers. Each basic unit "AB" that constitutes the repetition stack layer "ABABAB..." is called a "bilayer" or "sub-layer". In such conditions, the reflectivity is not only modulated by the total thickness but also by the thickness of each "sub-layer". The interference between the periodically reflected beams gives rise to Bragg peaks (called pseudo-Bragg). The position of the Bragg peaks allows to estimate the thickness of the "sub-layer" by the eqation:

$$\varepsilon = \frac{2\pi}{\Delta q_{z,\ Bragg}}$$

Many approximations are adopted when calculating the thickness using the above formulas. In particular, the absorption and roughness of the layers are not taken into account. More accurate information can be obtained by fitting the experimental data with software REFLEX, Firefx, etc.

Chapter 2

The originality of radiation-induced modification: a preliminary study

The synthesis of the classical mesoporous silica powders (SBA-15 and MCM-41) described above will be discussed in this chapter. Furthermore, the behavior of such as-synthesized materials under pressure, temperature, and radiation stress will be investigated and compared. The similarities between each consequence will be evaluated, and the unique characteristics caused by irradiation will be highlighted.

2.1 Synthesis and characterization of mesoporous silica powder

2.1.1 Synthesis

2.1.1.a Synthesis of SBA-15

The SBA-15 silica was prepared by adapting the procedure used by Zhao *et al.*[31]. 10 g of Pluronic P123 triblock copolymer was dissolved in 262 ml of deionized water, and 50 ml of 37% HCl solution was added to the solution. The mixture was left under continuous stirring for 2 h. Then 22.5 ml of TEOS was added drop by drop with stirring at 40 °C during 1 h. The mixture was kept at 40 °C for about 20 h under static conditions, then heated to 100 °C for 48 h. The solid products were filtered off and washed with deionized water and ethanol repeatedly. The resultant powder was then dried at 100 °C for 5 h, then the temperature was gradually raised to 550 °C over a period of 5 h, and finally, the powder was calcined at 550 °C for another 5 h.

2.1.1.b Synthesis of MCM-41

The MCM-41 silica was obtained by a sol-gel process in applying the protocol reported by Kumar *et al.*[39]. 2.4 g of CTAB was dissolved in 120 ml of deionized water at 30 °C and 8 ml of 30% $NH_3{\cdot}H_2O$ solution was added to the solution. The mixture was left under continuous stirring for several minutes, then 10 ml of TEOS was added drop by drop during 20 min at room temperature. Then the system was maintained at room temperature for 20 h without stirring. The precipitation was filtered off and washed with water and ethanol repeatedly. The resultant powder was dried at 80 °C for 1 h and gradually heated to 550 °C over 3 h and calcined for another 3 h.

2.1.2 Characterization

The detailed parameters of the characterization will be presented in the following sections, and the results of the characterization will be summarized in the figure 2.1.

2.1.2.a Nitrogen adsorption/desorption isotherms

The isotherm data were collected at liquid nitrogen temperature (77 K) on Micromeritics Tristar equipment. The powder with known mass was first degassed at 80 °C under vacuum for 48 h. Structural and textural properties were obtained using the adsorption branch of the isotherm through the NLDFT method[69–72].

The shape of MCM-41 and SBA-15 adsorption isotherms (figure 2.1) are characteristic of a type IV curve, and SBA-15 has a noticeable hysteresis loop of type H1 according to IUPAC classification[91].

The pore size distribution calculated from the adsorption and desorption data shows that the as-synthesized SBA-15 powder has two types of pores, mesopores with an average pore size of about 7.3 nm, and a portion of micropores of about 2 nm diameter. As for the as-synthesized MCM-41 powder, only one type of mesopore exists, with a diameter of about 3.7 nm.

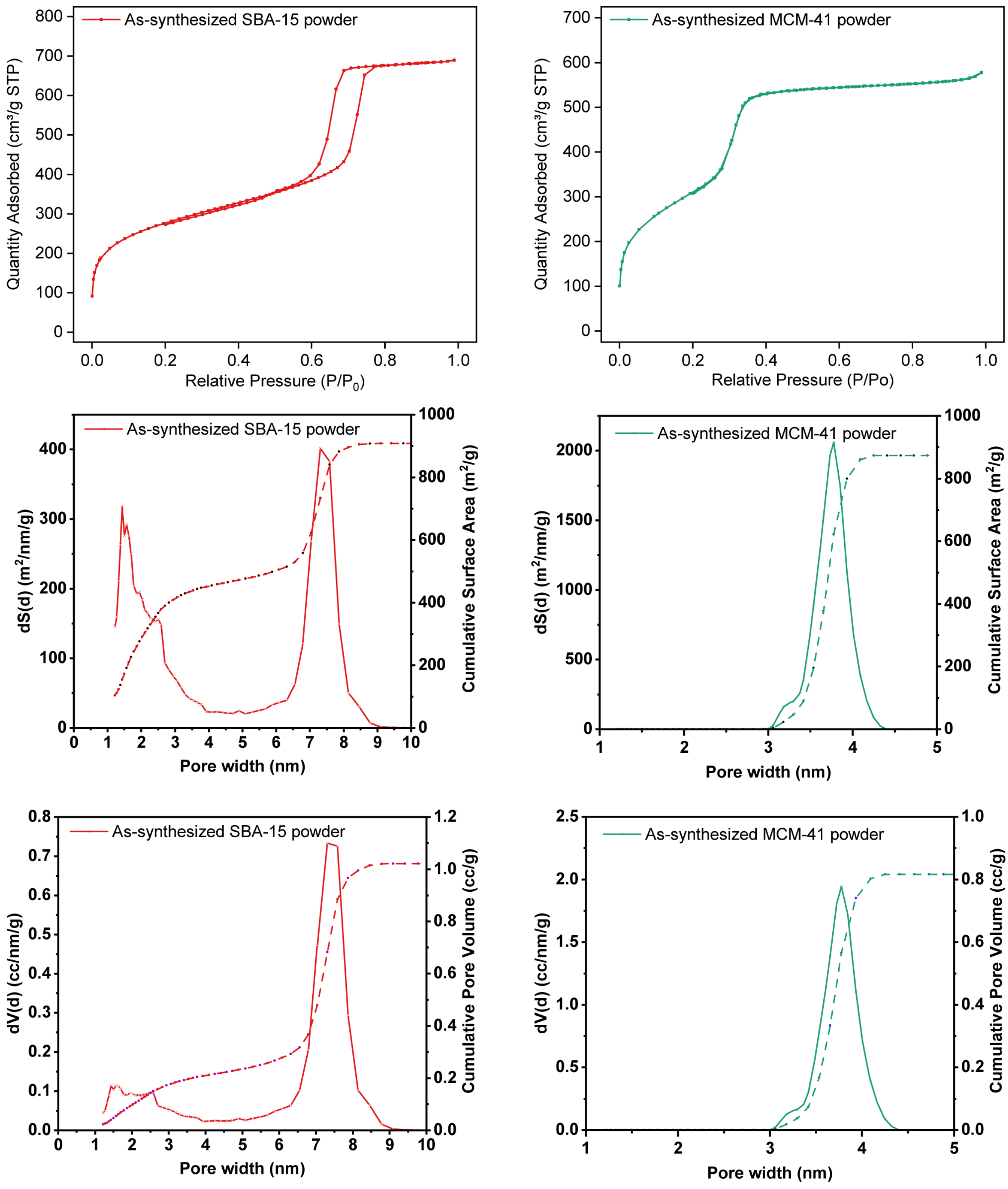

FIGURE 2.1: N_2 adsorption-desorption isotherms and PSD curves for as-synthesized SBA-15 and MCM-41 powder.

2.1.2.b SAXS

The data acquisition time was 1800 s, and silver behenate powder in a sealed Kapton piece was used as the scattering vector calibration standard. The experimental resolution was $\Delta q/q= 0.05$. The image azimuthal average was determined using FIT2D software from ESRF (France), and data corrections (subtractions of empty cell and detector noise) and radial averaging were performed via standard procedures.

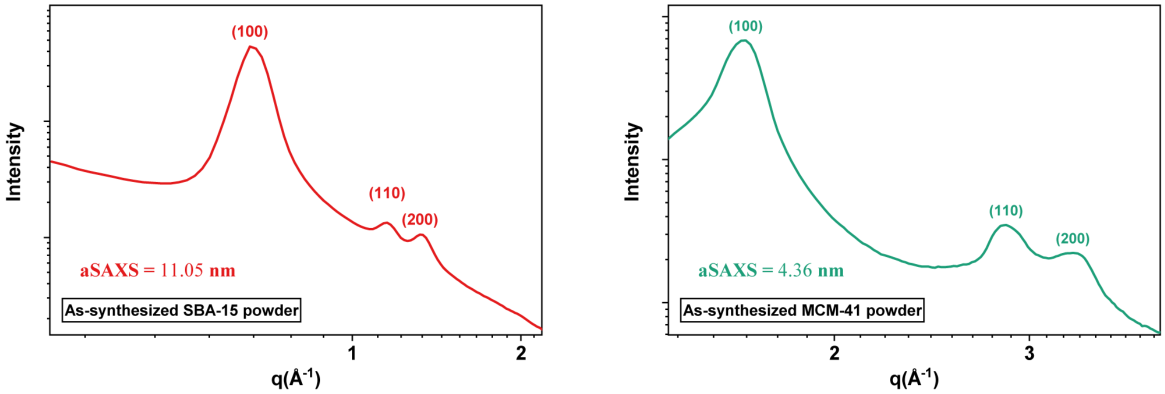

FIGURE 2.2: Small-angle X-ray scattering (SAXS) profiles for as-synthesized SBA-15 and MCM-41 powder

The SAXS pattern of three well-resolved peaks indexed as (100), (110), (200), which can be associated with P6mm hexagonal symmetry. The average distance a_0 between the pores (for 2D hexagonal structure $a_0 = 2d_{100}/\sqrt{3}$, where $d_{100} = 2\pi/q_{100}$) was indicated in the figure 2.2.

Combined SAXS and nitrogen adsorption results show that the silica wall of SBA-15 mesopores is thicker than that of MCM-41 (see table 2.1).

TABLE 2.1: Wall thickness of mesoporous materials obtained by association SAXS-Adsorption / desorption of nitrogen.

Sample	a_0 - SAXS nm	Pore diameter nm	Wall thickness nm
SBA-15	11.05	7.31	3.74
MCM-41	4.36	3.62	0.74

2.1.2.c NMR

Characterization of the framework of silica gels by nuclear magnetic resonance spectroscopy was already reported by Engelhardt *et al.*[92]. In our work, NMR experiments were performed on a BRUKER ADVANCE 400MHz spectrometer equipped with a CP-MAS VTN4 4mm probe. The Larmor frequencies for ^1H and ^{29}Si are 400.1 and 79.5 MHz respectively. The procedure to treat $^1H \rightarrow ^{29}$ Si CP and ^{29}Si hpdec NMR measurements is described as follows: each spectrum was normalized by the integrated intensity and then was deconvoluted to three resonances at ca. -91, -101, -110 ppm, which can be assigned to Q^2, Q^3, Q^4 sites, respectively (figure 2.3).

Basically, the hpdec results tend to be more quantitative than the CP MAS results, as it measures the overall materials while the CP MAS is a more superficial measurement. In subsequent studies, we preferred the hpdec approach, even though it required a much longer characterization time.

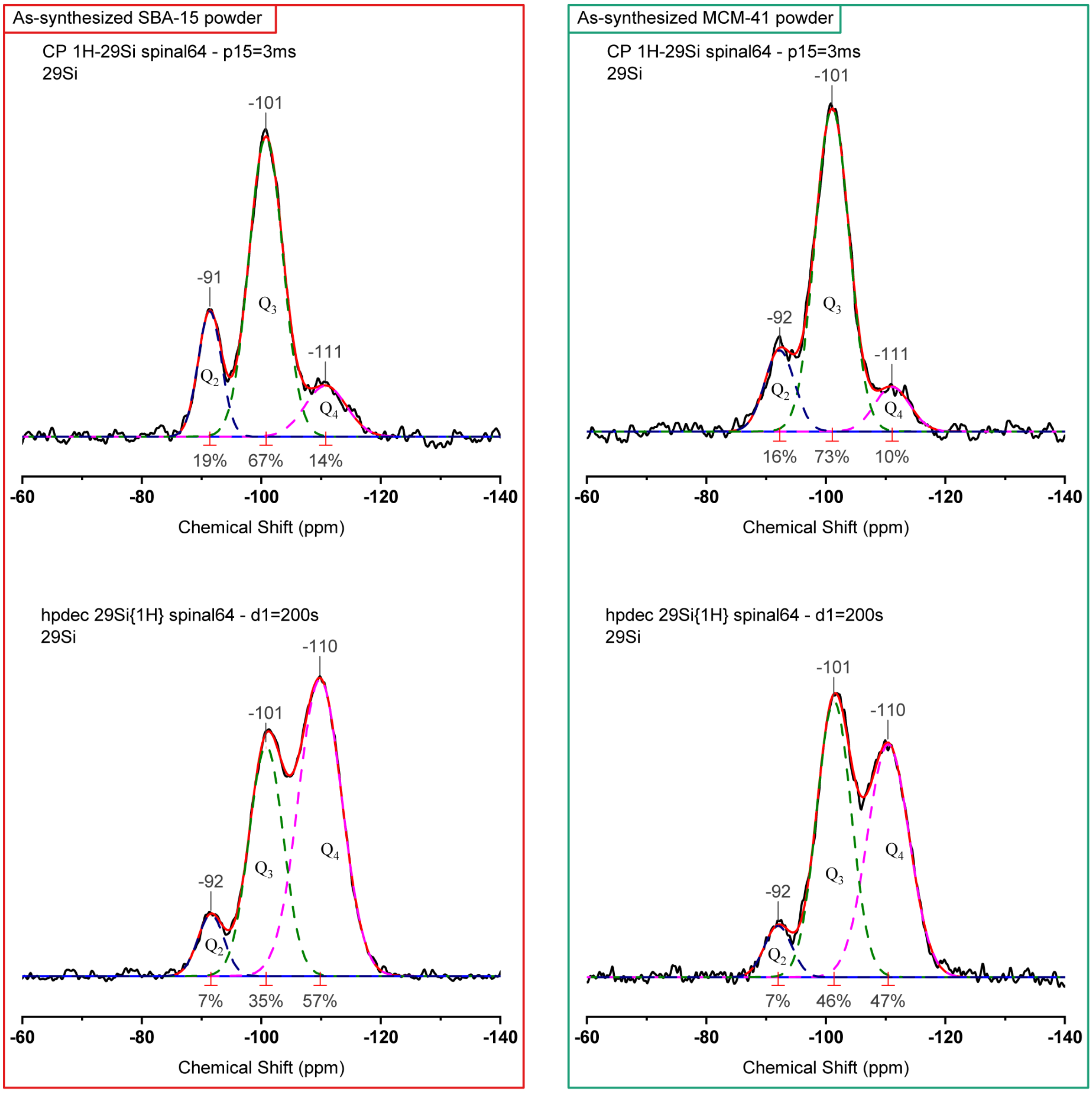

FIGURE 2.3: ^{29}Si CP/MAS and hpdec NMR spectra of as-synthesized SBA-15 and MCM-41 powder.

If we compare the results of hpdec, the degree of polymerization of MCM-41 is a little lower than that of SBA-15, which may be due to the shorter heat treatment time during the synthesis process. This will be discussed in the next section.

2.1.2.d ATR-FTIR measurement

ATR-FTIR spectroscopy was performed in Perkin Elmer Spectrum 100 Fourier Transform Infrared system containing a 45-degree attenuated total mono reflection (ATR) device using a KRS-5 crystal. Spectra (6 acquisitions per sample) were acquired between 4000 and 300 cm^{-1} with 4 cm^{-1} resolution. The IR spectra between 1400 and 750 cm^{-1} were deconvoluted (figure 2.4).

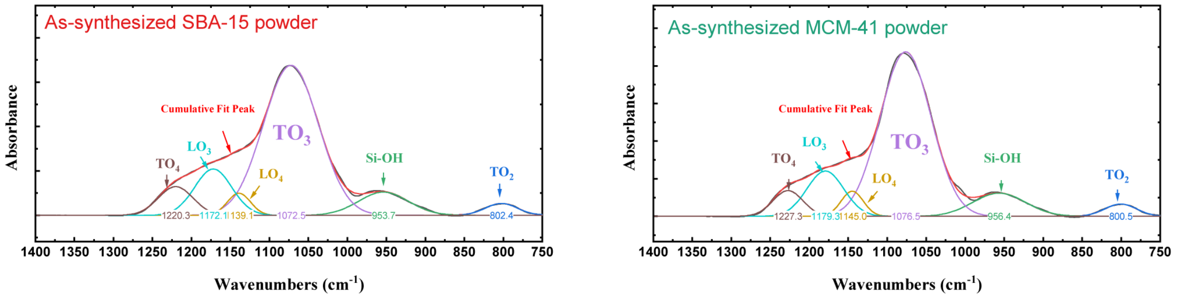

FIGURE 2.4: Deconvolution of FTIR spectra observed on as-synthesized SBA-15 and MCM-41 powder.

A zoom on the 750-1400 cm^{-1} region of the deconvoluted ATR-FTIR spectrum shows the Si-OH, and SiO$_2$ vibration modes. However, LO$_4$, TO$_4$ and TO$_3$ mode vibrations might not represent their real population as the decomposition of the "shoulder region" has been controversial and inconclusive in previous studies. For the discussion afterward, only the TO$_3$ vibrations located around 1074 cm^{-1} will be compared.

2.2 Preliminary study on powder performance under different stress

In the next subsections, the synthesized mesoporous silica powder will be subjected to various stressful conditions, and its corresponding responses will be discussed.

2.2.1 Compression pressure stress

The preliminary study of compression pressure stress was performed on the SBA-15 powder by the pelleting process. The structural behavior under the pressure force will be shown below.

2.2.1.a Pelleting process

Pellets with 8mm diameter were obtained by using laboratory pellet dies (figure 2.5). The as-synthesized powders were first pre-compacted the under the desired pressure, for a period of about 1 min. The pressure is then readjusted until the pressure gauge shows the desired value, which is maintained for another 30 s. For SBA-15 powder, a series of pressures from 125 MPa to 1250 MPa were applied in order to observe the evolution of the mesoporous structure. A suitable pressure is then selected for application to the MCM-41 powder and its pellet will then be characterized to confirm that the mesoporous structure is practically unaffected.

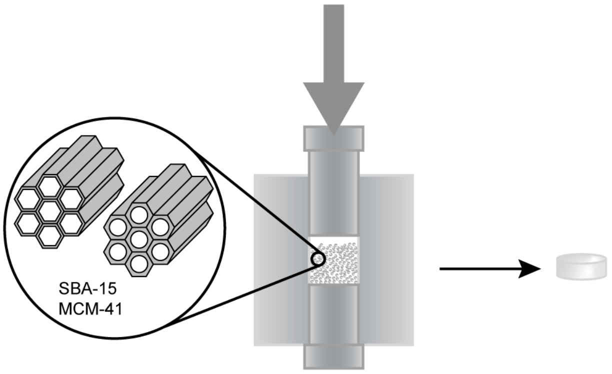

FIGURE 2.5: Pelletization setup

2.2.1.b Pores structural behavior

The figure 2.6 and 2.7 show N_2 adsorption/desorption isotherms and the pore size distributions (PSD) of the compacted SBA-15 pellets under different pressure. We can see that under the pressure of 0 to 250 MPa, the diameter of the original mesopores becomes smaller and the distribution range becomes wider, while the micropores have a small but insignificant increase, which indicates that the mesopores are compressed and deformed under the pressure, but most of the mesopore structure is preserved under the pressure in this range. When the pressure continues to increase, the pore distributions increase sharply and the micropores also increase sharply, which indicates that the mesopores are broken under high pressure and thus compressed to produce micropores. These findings are congruent with those of Hertz *et al.* [93] on porous SiO_2 and SiO_2/TiO_2 monoliths.

However it should be highlighted that the absolute volume and area of the increase in micropores that we see here may not be accurate representations of the real increase. This is due to the fact that when evaluating the pore size distribution from an isotherm, we do it on the assumption that the pores are cylindrical or spherical in shape. Technically speaking, if the mesopore structure is immediately broken by pressure, the micropores generated by the aggregation and extrusion of debris are unlikely to be equivalent to cylindrical or spherical morphologies.

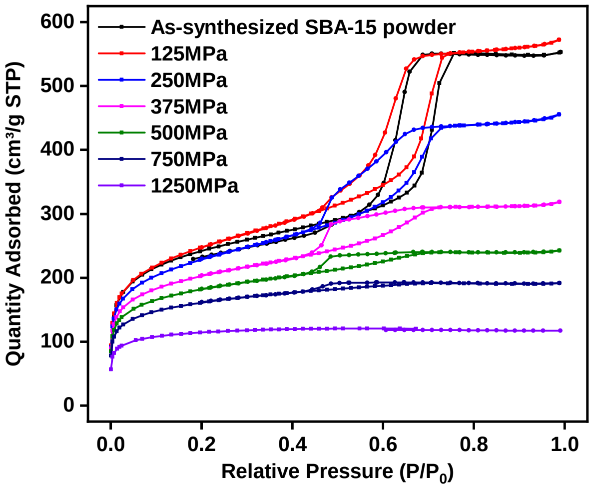

FIGURE 2.6: N_2 adsorption/desorption isotherms associated with SBA-15 pellets compacted at various pressure levels.

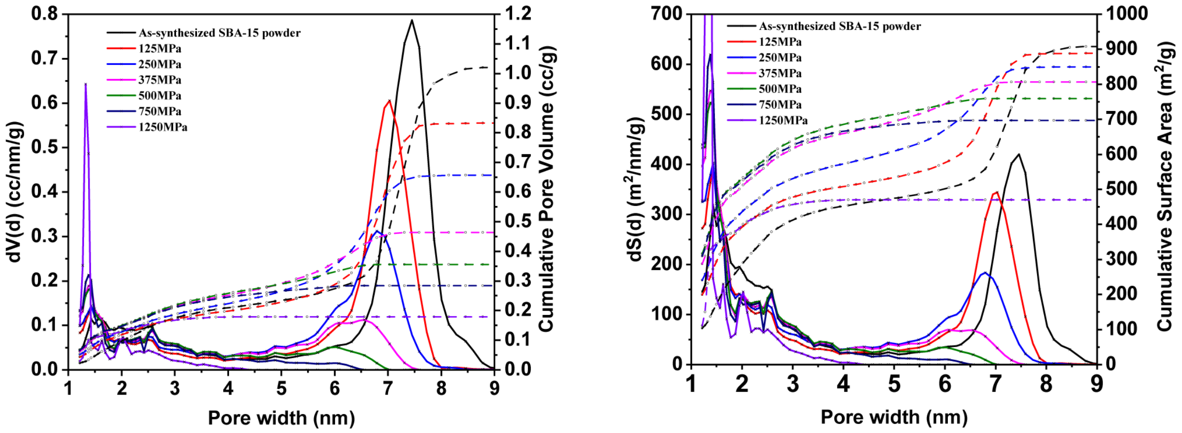

FIGURE 2.7: The pore size distributions obtained from nitrogen adsorption/desorption isotherms of SBA-15 pellets compacted at various pressure levels.

On the one hand, in order to make the pellet compact enough for later experimental operations, and on the other hand, in order to have as much material as possible in a pellet of a certain thickness for later experimental analysis, we choose a pelleting pressure of about 250 MPa, at which we still have enough mesoporous structures.

The MCM-41 pellets were also compacted at this pressure, the PSD of the pellets (figure 2.8) demonstrated that the mesoporous structure of the original MCM-41 powder was also well retained.

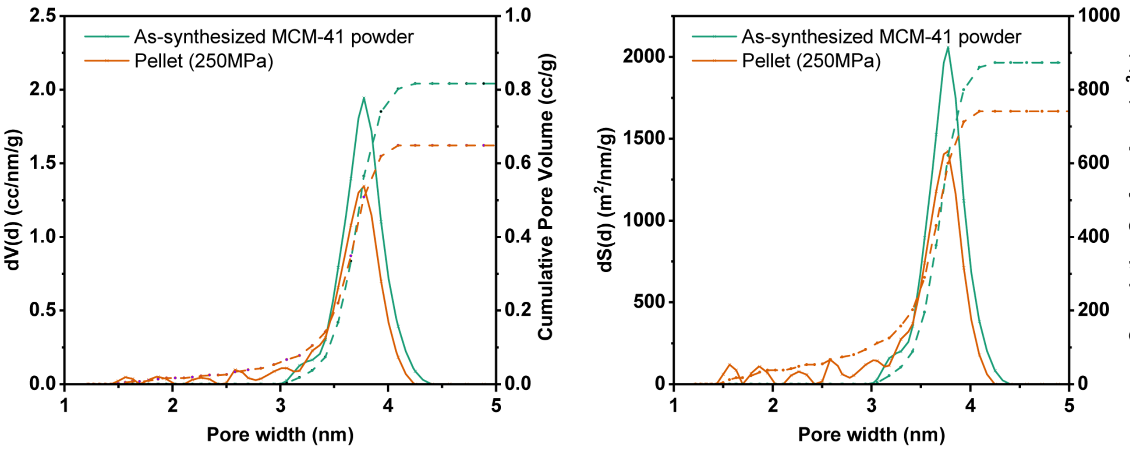

FIGURE 2.8: Comparison of the pore size distributions from as-synthesized MCM-41 powder and from the compacted MCM-41 pellet (250 MPa).

2.2.1.c Silica network modification

NMR analysis has been applied to 125 MPa, 250 MPa, 500 MPa, 1250 MPa SBA-15 pellets and the SBA-15 powder. Figure 2.9 shows the corresponding results, with increasing pelleting pressure, there is a slight decrease in the ratio of Q^4/Q^3, indicating a slight decrease in the degree of polymerization.

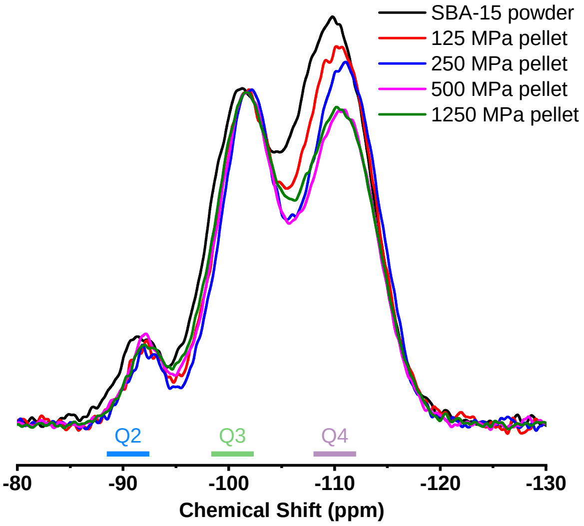

FIGURE 2.9: ^{29}Si hpdec NMR spectra of SBA-15 pellets compacted at 125 MPa, 250 MPa, 500 MPa, 1250 MPa (intensity scaled for comparison).

2.2.2 Thermal stress

The preliminary study of thermal stress was performed on the SBA-15 and MCM-41 pellets compacted under 250 MPa. These pellets were annealed at 400°C, 650°C, 750°C, and 850°C for 4 hours, and then were characterized using the same approach.

2.2.2.a Pores structural behavior

The figure 2.10 shows the pore size distributions obtained from nitrogen adsorption/desorption isotherms of the pellets after annealing at different temperatures. For the mesopores in SBA-15 pellets, we can see that, in the range of annealing temperatures from 400 to 850 °C, the average diameter of the pores shrinks, and the distribution width remains basically unchanged, which can be regarded as a result of homogeneous shrinkage. As for the micropores, the results seem to indicate a direct elimination mechanism. For MCM-41 pellets, the thermal stability of its mesoporous structure appears to be inferior than that of SBA-15 pellets, and as the annealing temperature increases, the mesopores gradually shrink and then disappear.

It should be noted that the micropores in both types of pellets are reduced under annealing, which is the opposite of what is observed under pressure stress. These findings are generally in agreement with the findings of Innocenzi *et al.*[34] Their research looked at porous thin films and discovered that the porosity vanished at temperatures about 800 °C.

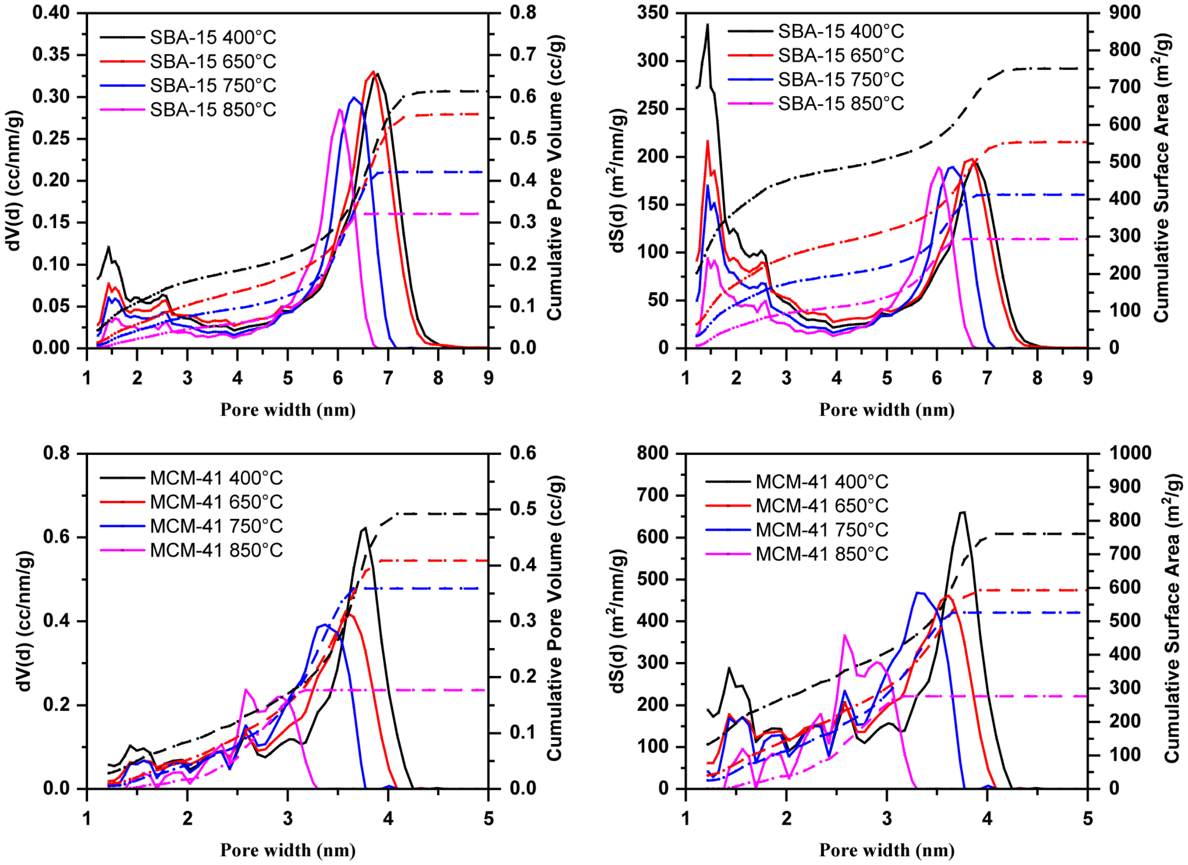

FIGURE 2.10: Effect of annealing temperature on PSD of SBA-15 and MCM-41 pellets.

2.2.2.b Silica network modification

The pellets annealed at 400 °C and 850 °C were analyzed by NMR. Figure 2.11 shows the corresponding results. Once again, its behavior is reversed versus its under-pressure performance, a sharp increase in the Q^4/Q^3 ratio indicating a significant increase in the degree of polymerization.

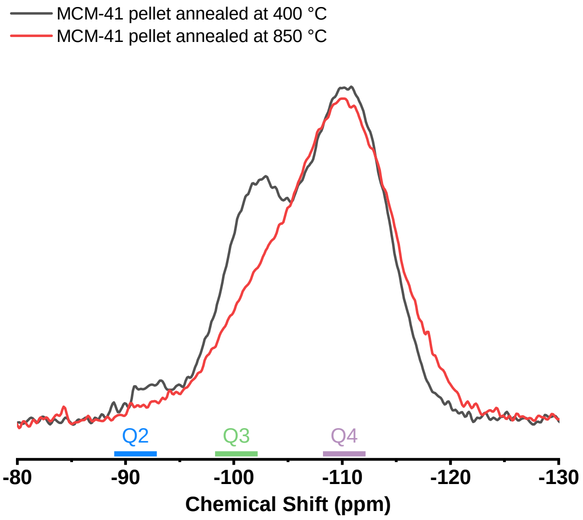

FIGURE 2.11: ^{29}Si hpdec NMR spectra of MCM-41 pellets annealed at 400°C and 850°C (intensity scaled for comparison).

It should be noted that the NMR results of the pellets of SBA-15 and MCM-41 after annealing at 400 °C are identical and both are close to the NMR of SBA-15 powder. The small differences observed in SBA-15 and MCM-41 powder no longer exist, which verifies our previous hypothesis that the differences observed in NMR of the as-synthesized powders should be due to the different heat treatment times during the synthesis process, and that the silica network of MCM-41 has not yet reached a maximum stable state.

2.2.3 Radiation stress

To illustrate radiation effet, SBA-15 and MCM-41 pellets synthesized at 250 MPa and annealed at 400 °C were used for electron irradiation studies, the results of which will be discussed in detail in subsequent sections. Here we will briefly show the results to point out the similarity and the specificity of the irradiation effects compared to pressure or thermal effects.

2.2.3.a Pores structural behavior

The figure 2.12 shows the results of pore size distribution as a function of dose. The detailed parameters of the irradiation experiment will be mentioned later. Here we note that the average diameter of the mesopores decreases and the width of the distribution is almost constant, while the micropores disappear gradually, which is similar to the change in heat treatment and not consistent with the pressure effect.

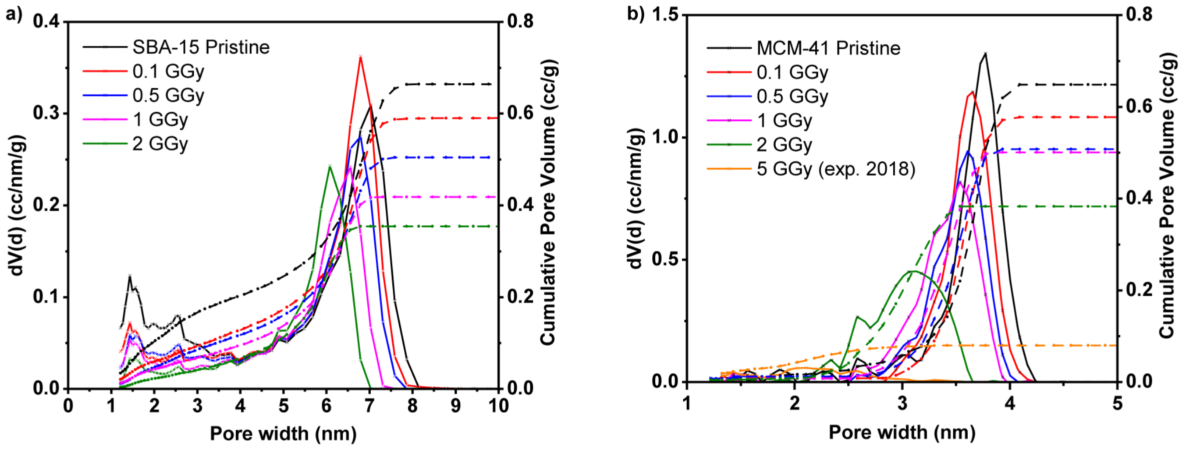

FIGURE 2.12: Pore size distribution of silica samples after 2 MeV electron beam irradiation (a) SBA-15, (b) MCM-41. (Solid line = pore volume, Dash line = cumulative pore volume).

2.2.3.b Silica network modification

As shown in figure 2.13, the Q^n group analysis was employed with direct hpdec NMR acquisition. No significant change was observed in the chemical shift of Q^n peaks. The analysis shows that the Q^4/Q^3 ratio does decreases slightly with increasing dose, which is similar to pressure effect, while the thermal effect is different.

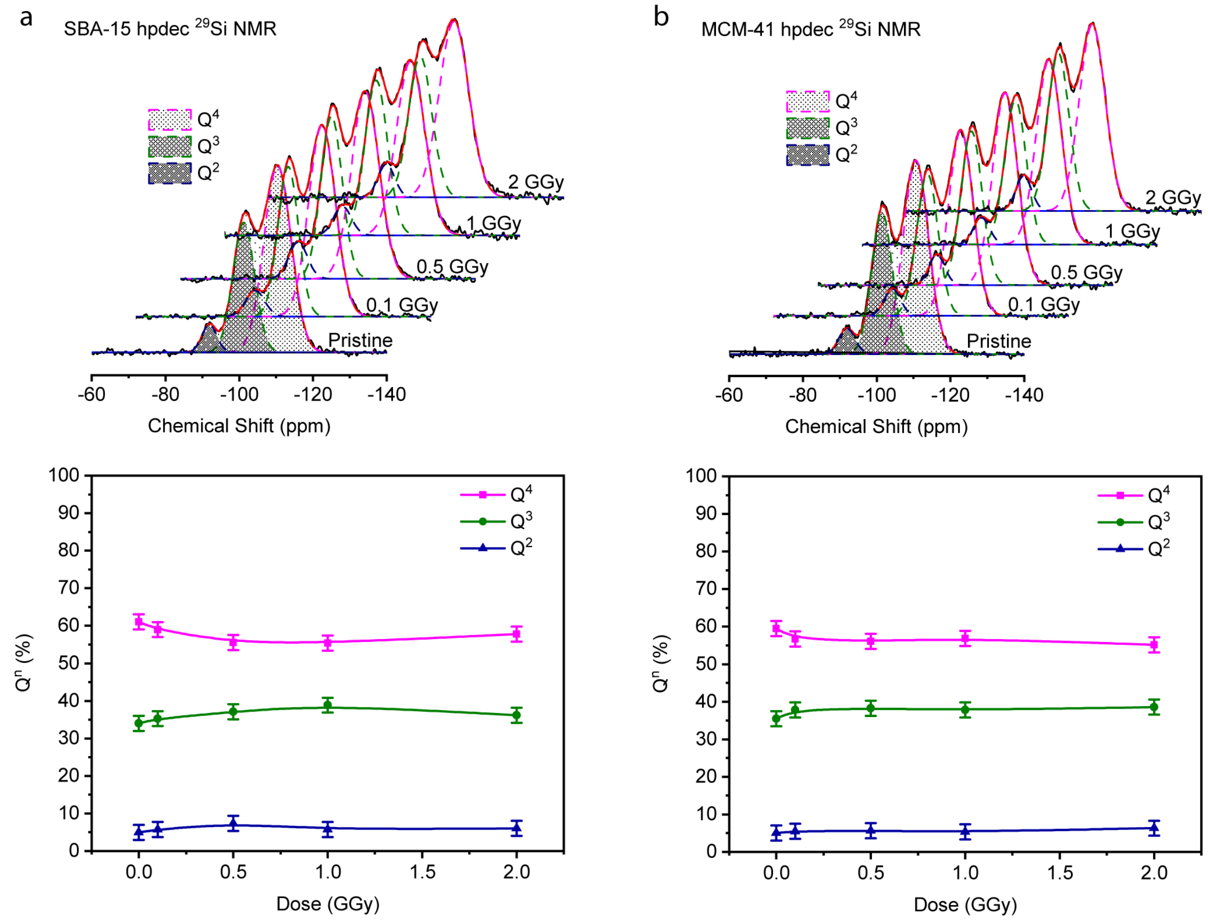

FIGURE 2.13: Deconvolution of hpdec MAS ^{29}Si NMR spectrum and evolution of the Q^n sites of silica samples after 2 MeV electron beam irradiation.

2.2.3.c The particularity of the irradiation effect

The two characterization results above demonstrate that the effect of irradiation on mesoporous silica is specific and it is not caused by a simple combination of pressure and thermal effects. This conclusion is consistent with Devine's findings on the effect of nonporous amorphous silica under irradiation[82]. As mentioned in Chapter I, Devine proposed an empirical relationship between the TO_3 band position in IR and silica density, which is deduced from results obtained on silica under the effects of temperature and pressure.

$$\omega_{\text{TO}} = 1301.2 - 91\rho$$

As for classical silica under irradiation, the determination of the density of silica from the relation leads to an overestimation of the densification of an order of magnitude compared to the results of measurements: 3% experimentally against 30%. Devine concludes that the relation is not usable to account for the results of irradiation, and more generally that the effects of irradiation on the densification of the silica network are not comparable to the effects obtained by the combined action of temperature and pressure.

Part II

Ion Irradiation

Chapter 3

Swift heavy ion irradiation

In this chapter, we will look at the behavior of porous silica when exposed to Swift Heavy Ions (SHI) irradiation. The irradiation experiments were carried out at GANIL facilities, where we investigated four different silica thin films subjected to SHI bombardment. The synthesis of thin silica films will also be presented in this chapter. Two of the thin films are porous silica synthesized by the sol-gel method, one is non-porous silica synthesized by the sol-gel method, and the fourth is a classical thermal synthesized non-porous silica. We will demonstrate the variation of sample thickness with irradiation dose acquired by techniques of XRR and the variation of silica network characteristics with irradiation dose obtained from the results of FTIR. Based on this, it will be possible to determine the damage cross-section under experimental settings. Following that, we will compare the damage cross-section of several materials by comparing the difference of the incident particles with different electron stopping powers and the effect of pores and the synthesis method (sol-gel vs. thermal synthesis) on the radiation tolerance. By following the pore structure with x-ray reflectivity and electron microscopy, we hope to better understand the process of damage induced by the passage of the particle beam through the material.

3.1 Synthesis and stability of as-synthesized mesoporous silica thin films

As previously stated, materials in thin film form should be the most convenient for swift heavy ion irradiation. The detailed synthesis steps will be given here. The stability of the thin film materials during storage and transit will also be discussed to ensure that the changes seen in the following sections are caused by irradiation and not by other sources.

3.1.1 Sample preparation

As stated in Chapter 1, the preparation of mesoporous silica thin films involves the use of dip-coating process, and Evaporation Induced Self Assembly (EISA) was used to create highly structured 2D hexagonal mesoporous silica thin films[94, 95].

3.1.1.a Mesoporous silica thin film synthesized with P123 surfactant (IPc)

In this study, thin films consisting of cylindrical mesopores ϕ ~ 5 nm in 2D hexagonal symmetry are synthesized using the surfactant P123 (same surfactant for SBA-15) and deposited to silicon wafer (SILTRONIX semiconductor quality silicon, thickness of 500–550 µm) by adapting the dip-coating method reported by Dourdain *et al.*[96]:

i). Stock solution preparation: 6.23g of 0.055M HCl/H_2O and 5g of ethanol were combined and stirred together. After that, 8.78g of TEOS was added while stirring for 1 hour;

ii). Dipping solution preparation: Weighed and mixed 25.5g of ethanol and 3.64g of stock solution. Following that, 0.45g of P123 copolymer was injected. The solution was stirred for 2h30. Then 2g of 0.055M HCl/H_2O was added and stirred for 0.5h. The molar ratio of the resultant deposition solution is 1 TEOS : 0.0028 P123 : 15.7 EtOH : 10.8 H_2O : 0.81 HCl;

iii). Dip-coating: The layers were then dip-coated at a constant withdrawal velocity of 15 cm/min onto a silicon wafer that had been precleaned in ethanol. The humidity in the dip-coater chamber was maintained at 50±5%.

The corresponding mixture was known to produce films with the 2D hexagonal P6mm symmetry. This structure and the thickness were examined by XRR.

3.1.1.b Mesoporous silica thin film synthesized with CTAB surfactant (ICc)

A similar synthesis process was used for the synthesis of ICc, but with CTAB as the surfactant, and the humidity and withdrawal velocity were adjusted accordingly:

i). Stock solution preparation: 0.917g of 0.0027M HCl/H_2O and 5.75g of ethanol are weighed into a flask and stirred, then 8.68g of TEOS is added under stirring for 1h;

ii). Dipping solution preparation: 0.911g of CTAB, 19.75 g of ethanol and 1.8 g of 0.055M HCl/H_2O are weighed and stirred until the CTAB is completely dissolved, then the stock solution is added, stirring is maintained for 4.5 days. The resulting deposition solution has a molar ratio of 1 TEOS : 0.06 CTAB : 24 EtOH : 5.3 H_2O : 0.065 HCl;

iii). Dip-coating: to make thin layers of about 80 nm, 21g of ethanol is added to the solution. The layers were then dip-coated at a constant withdrawal velocity of 15 cm/min under a relative humidity of 40%. The resulting layers are dark blue in color, indicating a thickness of ~80-100 nm.

3.1.1.c Non-porous silica thin film synthesized with sol-gel process (NPc)

The non-porous silica thin films are also synthesized without the use of surfactant by the dip-coating method:

i). Preparation of the stock solution: 0.35g of HCl/H_2O at 0.055M and 2.65g of ethanol are weighed in a flask and stirred, then 4g of TEOS is added under stirring for another 1h.

ii). Preparation of the dipper solution: 15.6g of ethanol and 1.44g of HCl/H_2O are weighed and stirred, then all the stock solution (about 7g) is added under stirring for 3h.

iii). Dip-coating: The relative humidity is 50% ± 5 during dip-coating. The withdrawal velocity is adjusted so that the films obtained are dark blue, indicating a thickness of about 80 nm.

3.1.1.d Aging and sintering step of as-prepared thin films

Aging is required to stabilize newly synthesized thin film materials and to form a well-connected sol-gel network. Samples were stocked at room temperature for two months of ageing and then heated at 400 °C for 5 hours. This calcination is necessary because sol-gel materials have a high concentration of uncondensed wet silanol (-Si-OH) groups and these groups can undergo radiolysis condensation during irradiation. Furthermore, as demonstrated in Kucheyev's work[97–

99], the chemicals formed are anticipated to play an essential role in the irradiation-induced mechanical properties (elastic modulus and hardness) evolution of low-density silica nanofoams (aerogels). However, this is not the major focus of our investigation, and we want to minimize the impact of these factors. Thermal treatment is a highly efficient method for removing the most of these silanol groups.

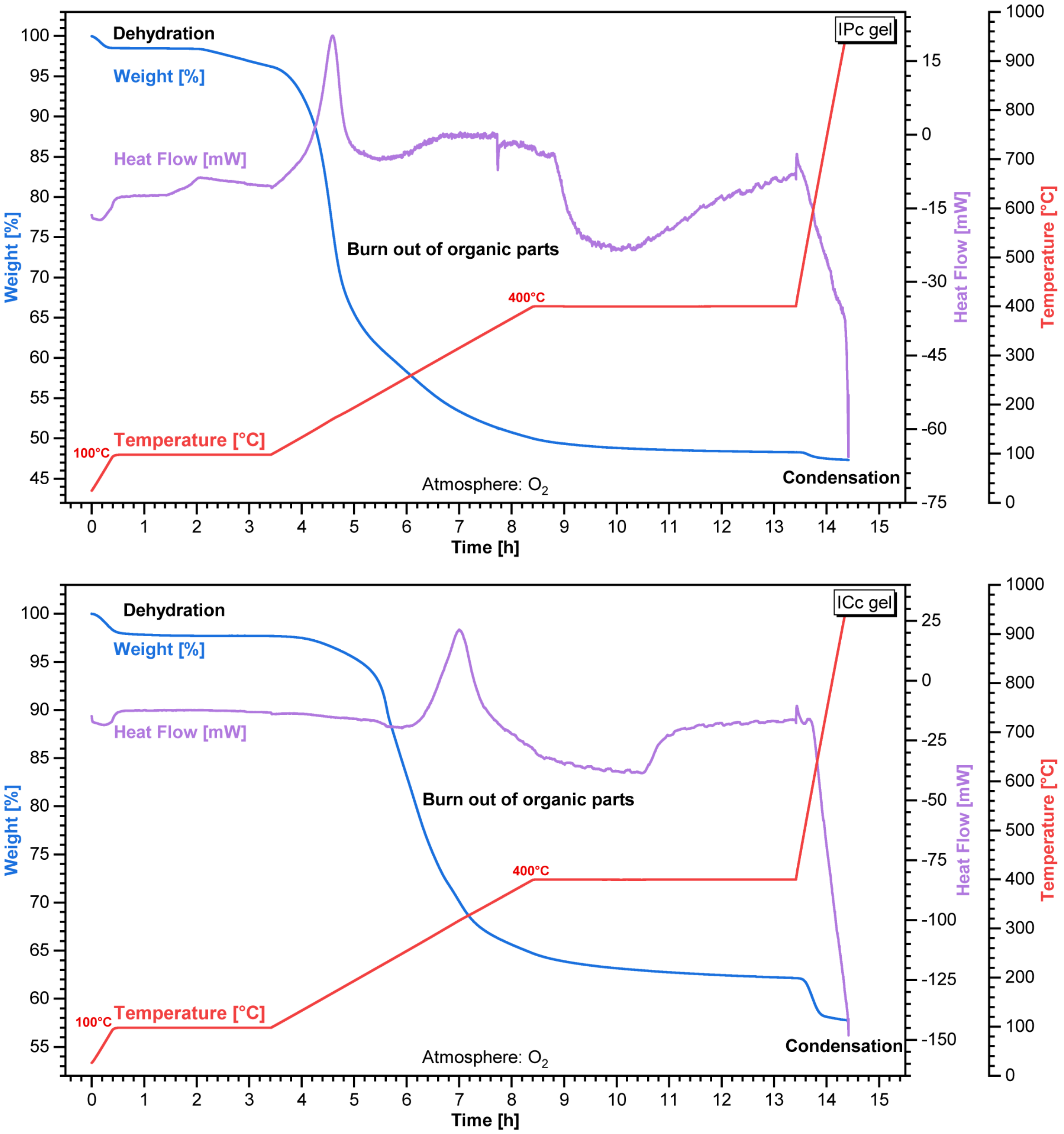

FIGURE 3.1: Decomposition of silica gels in a TGA, purple curve is the heat flow signal, blue curve is the mass loss

To establish the optimal program for thermal treatment, a thermogravimetric study was performed. However, the thin layer formed by dip-coating has insufficient mass to permit such analysis. As a result, we established the optimal procedure for the gel formed by ageing the dipping solution under a relative humidity of 40% at room temperature without depositing it on the silicon wafer, which exhibits striking similarities to the gel deposited into thin films. The obtained result is presented in figure 3.1 and indicates that at temperatures more than 400°C, no further mass loss owing to the removal of organic components occurs. Simultaneously, when the annealing temperature exceeds 550 °C, condensation occurs, converting the porous silica produced by sol gel to thermodynamically created silica, consequently bringing the risk of damaging the pore structure.

Carbon analysis indicates that less than 0.05 % of residual carbon remains in the gel following treatment at 400 °C. These findings are similar with the work of Innocenzi *et al.*[34], who demonstrated by infrared analysis that residual surfactants are completely removed from mesoporous silica thin films after annealing at 350°C. Additionally, we evaluated the samples using infrared (transmission mode), and found no CH_2 band on the thin layers annealed at 400 °C.

These disparate results demonstrate the efficacy of a 400 °C treatment, which prompted us to calcinate all samples at this temperature using the thermal cycle depicted in figure 3.2. The slow heating rate minimizes damage to the pore structure caused by abrupt temperature fluctuations, while a preheating dwell (3h - 100 °C) assures complete removal of adsorbed water and acts as an extra fast aging step that aids in the stabilization of the silica network.

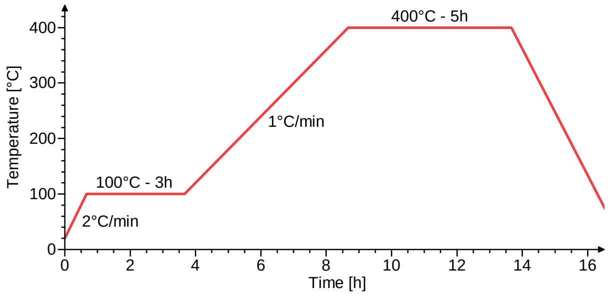

FIGURE 3.2: Temperature program for thermal treatment of thin films prepared by sol-gel dip coating technique

This heating step is used to process all subsequent IPc, ICc, and NPc specimens in this thesis.

3.1.1.e Non-porous silica thin film synthesized with thermal process (SiO_2 therm)

Additionally, thermally grown silica thin films from SIL'TRONIX Silicon Technologies were also applied to compare thermosynthesized silica networks with those synthesized by the sol-gel method. Previous studies related to irradiation of these materials have already been done by Toulemonde *et al.*[100]. It is composed of two 90 nm (± 10%) silica layers on each side of a silicon wafer with a thickness of 525 ± 25 µm. In the future discussion, this will be referred to as SiO_2 therm. The comparison is most noticeable in the infrared's characterization.

3.1.2 Thin film morphology and the structure of ordered pores

Focused Ion Beam/Scanning Transmission Electron Microscopy (FIB/STEM) and X-Ray Reflectivity (XRR) were utilized to investigate the morphology and the porous structure of the as-prepared thin film.

3.1.2.a FIB/STEM

To prepare STEM samples, the so-called "lift-out" method was utilized. A FEI Helios NanoLab 660 Dualbeam FIB-SEM equipped with a gallium ion source was used to prepare the foil. Prior to milling, a trench of the as-synthesized thin film was sputter-coated with 500 nm carbon to provide a protective covering. On top of the carbon layer, a 1-μm-thick platinum coating was subsequently placed to provide further protection. Finally, a 200 nm thick foil specimen was cut from the thin film for morphological observation. The picture 3.3 illustrates a schematic diagram of the cross-section observation.

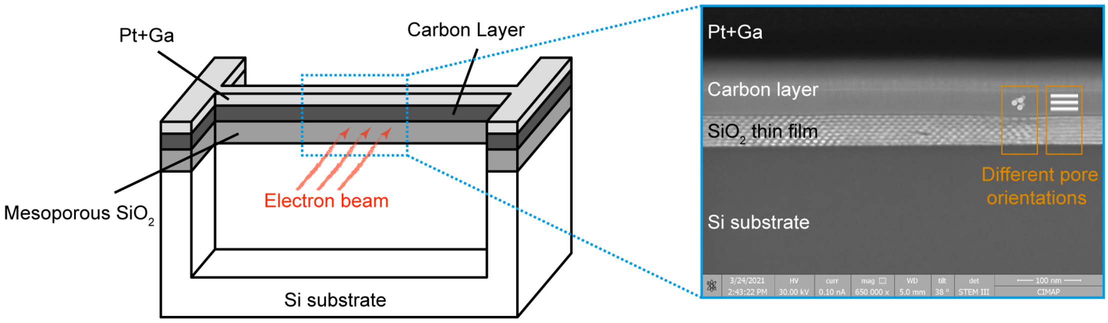

FIGURE 3.3: A schematic diagram of the sample observed by electron microscopy

The cross-sectional view of the two porous thin films mentioned above is shown in figure 3.4.

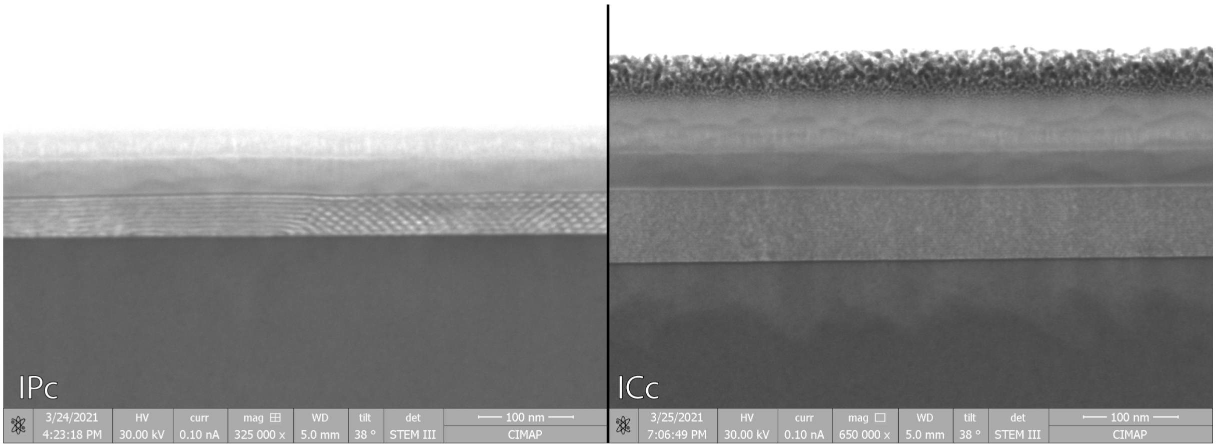

FIGURE 3.4: Examples of cross-sectional view STEM image of the porous silica thin films, on the left is IPc and on the right is ICc

The pores in the two respective thin films (IPc and ICc) are organized in an interlayer pattern. Additionally, it can be seen that the pore in IPc is cylindrical but not singularly orientated. The poor resolution of the ICc images prevents us from delving deeper into the morphology of the pores.

3.1.2.b XRR

XRR measurements were carried out using a Bruker D8 Advance diffractometer equipped with a specimen stage that enables vertical movement. The main optics configuration for XRR analysis included a Cu $K_{\alpha 1,2}(\lambda = 1.54184\ \text{Å})$ source, a Göbel mirror, a motorized divergence slit, a fixed 0.2 mm slit, an automated absorber, another fixed 0.2 mm slit after the absorber, and 2.5° Sollers slits.[101] The data were gathered using a Lynxeye detector operating in the "0D" mode. We gathered standard θ-2θ scans with a step size of 0.005° and a scanning time of 2s. The resolution of this configuration has been assessed to be 0.01°.

According to Salah *et al.* [102], geometric adjustment was made in the area of the plateau of total external reflection. On the raw curve (see figure 3.5 left), we notice that the direct beam at extremely small angles results in a quasi-linear increase in the signal. This rise is due to the increased exposure of the sample at small angles by the fractional beam (see figure 3.5 right). By describing the reflected intensity as a function of the sample size L, the beam width d, and the angle θ , a geometric correction, $I_{\text{corr}} = \frac{I_0 \sin(\theta) L}{d}$, may be performed.

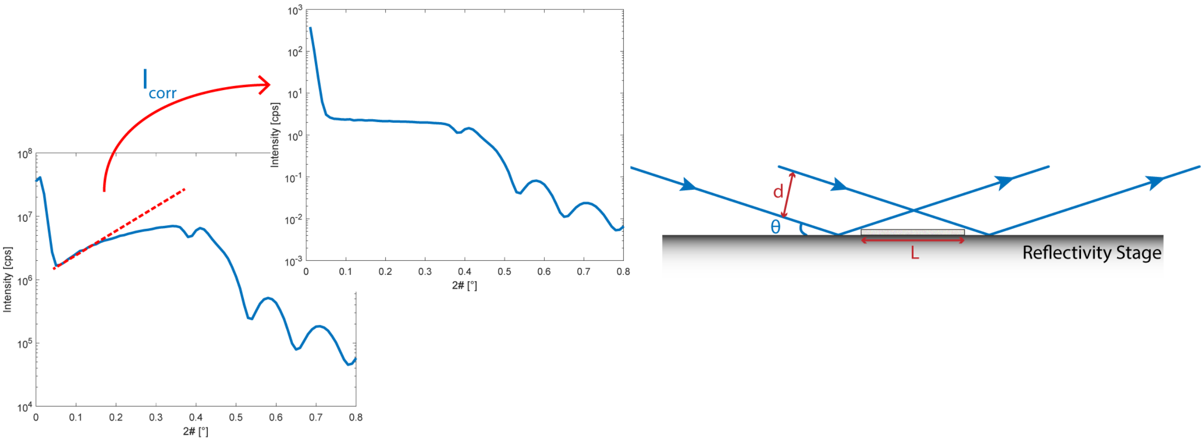

FIGURE 3.5: XRR adjustment on the basis of the span of geometrical factor

Finally, the logarithm of the normalized intensity, $R = I_{\text{corr}}/I_0$, was plotted against the wave vector transfer, $q\ \left(\text{Å}^{-1}\right)$, as mentioned in the chapter 1.

3.1.3 Total thickness and interlayer thickness of the thin films

The most valuable information from XRR measurements for our research is the total thickness of the layer and the thickness of the interlayer. In this paragraph, we will compare the four different approaches for estimating the thickness and provide error estimates.

3.1.3.a Method 1: Analyses of FIB/STEM images

The figure 3.6 illustrates two thin film materials (IPc and ICc) that were measured in cross-sectional scans with a certain range of grayscale deviations profile computed using Fiji (imageJ).

The porous layers and interlayers are visible, and their thicknesses can be deduced from the grayscale profile (see table 3.1). While this approach is more straightforward, it does have the following major drawbacks: To begin, the image is very localized and may be inaccurate due to the specificity of the area selected randomly to produce the foil; Second, the porous structure of the foil might be altered during the foil preparation process due to bombardment by gallium beams or during the STEM observation due to bombardment by electron beams, both of which may result in inaccuracies; Third, while the interlayer of IPc is more noticeable, that of ICc is limited by the resolution of the electron microscopy; Finally, the process of preparing and acquiring such an image is time consuming and laborious.

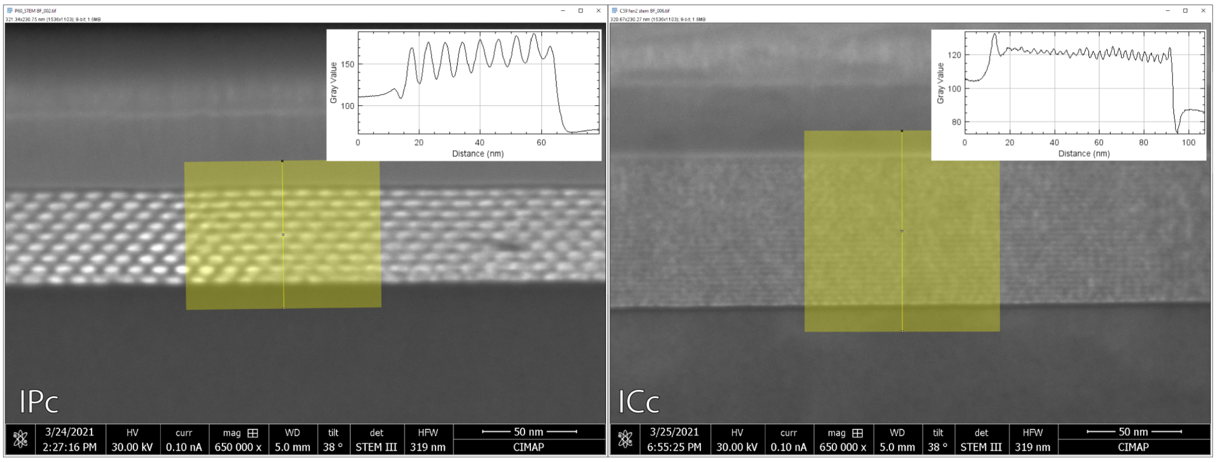

FIGURE 3.6: Measuring thickness of the total layer and interlayers with ImageJ

Additionally, there is a dim layer between the silicon wafer and the porous film material, which might be a spontaneously generated silica layer. However, because the boundary of this "buffer" layer is not fully apparent and as its thickness is only 2~3nm, we will treat it as a measurement error for the following analysis.

3.1.3.b Method 2: Periodic measurement of kiessig fringes and Bragg peaks from XRR

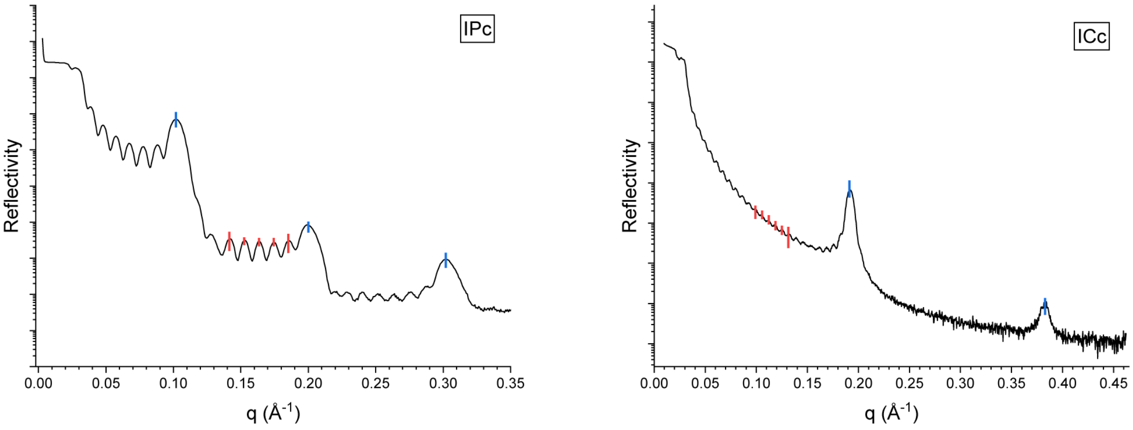

FIGURE 3.7: Illustration showing the measurement of Bragg peaks and kiessig fringes, red markers for kiessig fringes and blue markers for Bragg peaks

As mentioned in the first chapter, the thickness of the thin layer may be estimated by measuring the period of kiessig fringes, and the thickness of the interlayer by measuring the period of bragg peaks. The figure shows the reflectivity curves of the IPc and ICc thin films examined by FIB/STEM in the preceding paragraph. For fringes intensity maxima considerably beyond the critical angle, the distance between two adjacent maxima is approximately equal to $\Delta\theta$. And the layer thickness is determined by: $d \approx \frac{\lambda}{2\Delta\theta} = \frac{2\pi}{2\Delta q}$. As shown in the figure 3.7, a somewhat more accurate estimate may be achived by summing up several fringes and then dividing $\Delta\theta$ by the number of fringes[103]. The corresponding results of thickness calculations with periodic measurement are summarized in table 3.1.

3.1.3.c Method 3: Fringe number analysis in XRR

A. Van der Lee[103] also summarizes a more complicated, but more precise, approach for determining the layer thickness. The interference of waves reflected at the surface and those reflected at the interface between film substrates, similar to Bragg's law for diffraction, can lead to the derivation of an extended Bragg's law:

$$\sin^2\theta = \frac{m^2\lambda^2}{4d^2} + \sin^2\theta_c$$

By plotting the fringe position $\sin^2\theta_m$ versus the squared fringe number m^2, theoretically a straight line will be obtained, with slope equal to $\frac{\lambda^2}{4d^2}$ and y-axis abscissa equal to $\sin^2\theta_c$.[104–106] Therefore, the thickness of the thin film d and the critical angle θ_c, or even $q_c = \frac{4\pi}{\lambda}\sin\theta_c$ can be deduced further.

Assuming no absorption, using the equation below [107], The electron density can be experimentally determined:

$$q_c = 3.75 \times 10^{-2}\sqrt{\rho_e}$$

where ρ_e is in e^-/Å^3. Caution should be exercised in that this is only applicable to a single layer or change in refractive index. The presence of additional layers within a sample might result in the shift of critical angle.

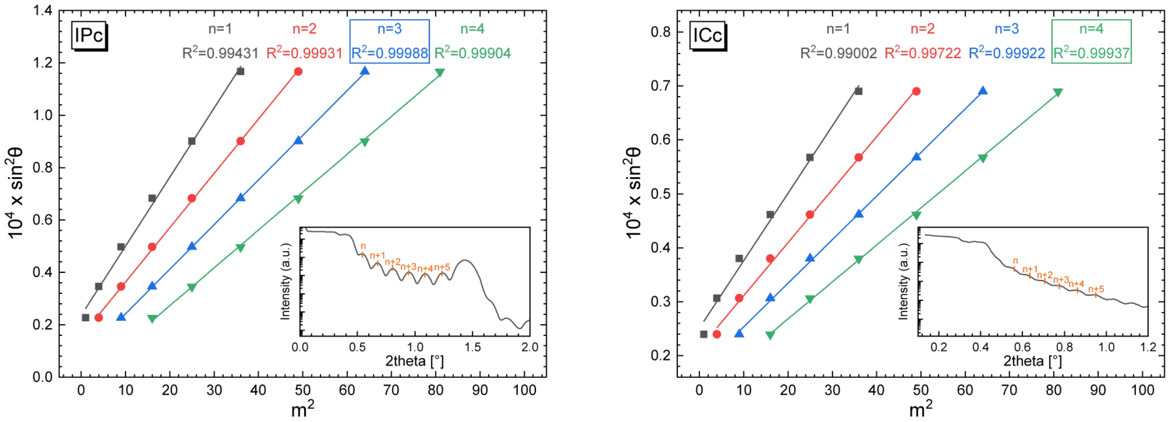

FIGURE 3.8: Examples showing that distinct incremental indexes m are assumed and fitted independently in order to get more precise data

There are also drawbacks to using this approach in practice. Firstly, it can be difficult to assign the correct index m to detected amplitude peaks because the earliest maxima, in particular, are obscured by the extremely quick fall-off just beyond the critical angle. As shown in figure 3.8, this limitation may be accounted for by experimenting with various incremental indexes m and then determining the correct m value using the R^2 of the linear fit. The corresponding results of thickness calculations with the most appropriate fringe number m are summarized in table 3.1. Another limitation of this approach is that there are likely insufficient identifiable Bragg peak maxima to construct a credible line for estimating interlayer thickness.

3.1.3.d Method 4: XRR Data fitting with reflex20 software

The experimental XRR curves can also be calculated using the reflex20 program proposed by Gibaud *et al.* [107]. The figure 3.9 compares the fitted (blue) and experimental (orange) curves for the two thin film IPc and ICc, as well as the calculated average electron density profiles. The corresponding thicknesses are also given in the table 3.1.

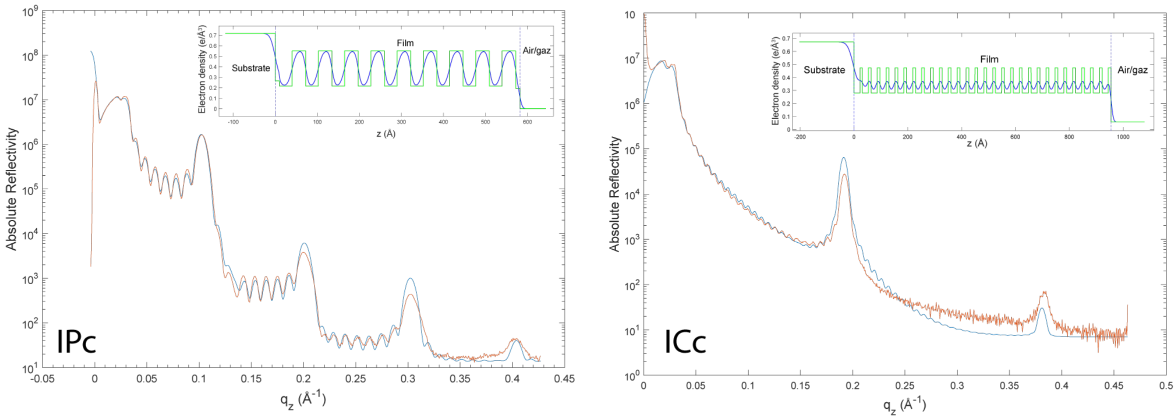

FIGURE 3.9: X-ray reflectivity (XRR) patterns from IPc and ICcand the best fit to XRR data by Reflex20, respectively

Indeed, as many elements other than thickness can impact the fit results, such fits are not always achievable, even under the assumption that all interlayers of the material are perfectly identical.

Conclusion

TABLE 3.1: Summary of thickness determined by different methods

Thickness [nm]		Method 1	Method 2	Method 3	Method 4
IPc	total	52.8±3.2	57.2±2.9	59.0±1.3	58.2±1.6
	interlayer	5.7±0.9	6.3±0.4	6.2±0.3	6.2±0.3
ICc	total	86.5±5.4	96.2±4.9	93.0±2.5	95.5±3.3
	interlayer	2.8±0.5	3.3±0.2	3.3±0.1	3.3±0.1

Nota bene: The 2-3 nm "buffer" layer is omitted here, however this 2-3 nm will eventually be accounted for as an error in following analysis.

Several ways of processing XRR data gave fairly comparable findings, as indicated in the table 3.1, and all were somewhat bigger than those detected directly by the electron microscope. The explanation for this might be that the sample was irradiated with ion or electron beams during the preparation and observation of the electron microscope, which could cause structural alterations, as discussed in a later section. However, with sufficient care, e.g. adding protective layers, shortening the scanning duration, and so on, the morphology observed by electron microscopy remains informative. In the subsequent experiments, we will mainly use XRR to measure the total thickness and the interlayer thickness, and analyze the data using the period measurement method. FIB/STEM will also be used for morphological observations.

3.1.4 Stability of the as-synthesized thin films

As predicted and understood, each synthesis has instabilities, and the thickness and pore structure of each film cannot be identical, it is fair to conduct measurements on the same specimen prior to and after irradiation to determine the changes caused by irradiation. This caution, however, can only rule out the partial dependability of the synthesis, but not the following aspects that may contribute to instability: humidity, temperature, and spontaneous changes in the film over long periods of storage. As a result, pre-experiments were conducted to investigate these variables. The results and related discussion are shown in the appendix C. We can safely infer that the changes in the film material that we saw before and after irradiation are really produced by irradiation and not by any other sources.

3.2 Irradiation experiment

3.2.1 Irradiation set-up

Irradiations by swift heavy ions have been performed on the IRRSUD and SME beamlines of GANIL. The image 3.10 below shows the instrument installation scheme for the IRRSUD beamline irradiation experiment, and the SME beamline operates on the same fundamental concept. The particle beam is blasted perpendicular to the sample in all SHI irradiation studies. Simultaneously, the synthesized thin film sample is connected to a cooling system to ensure that the temperature does not exceed 50 °C during every experiment.

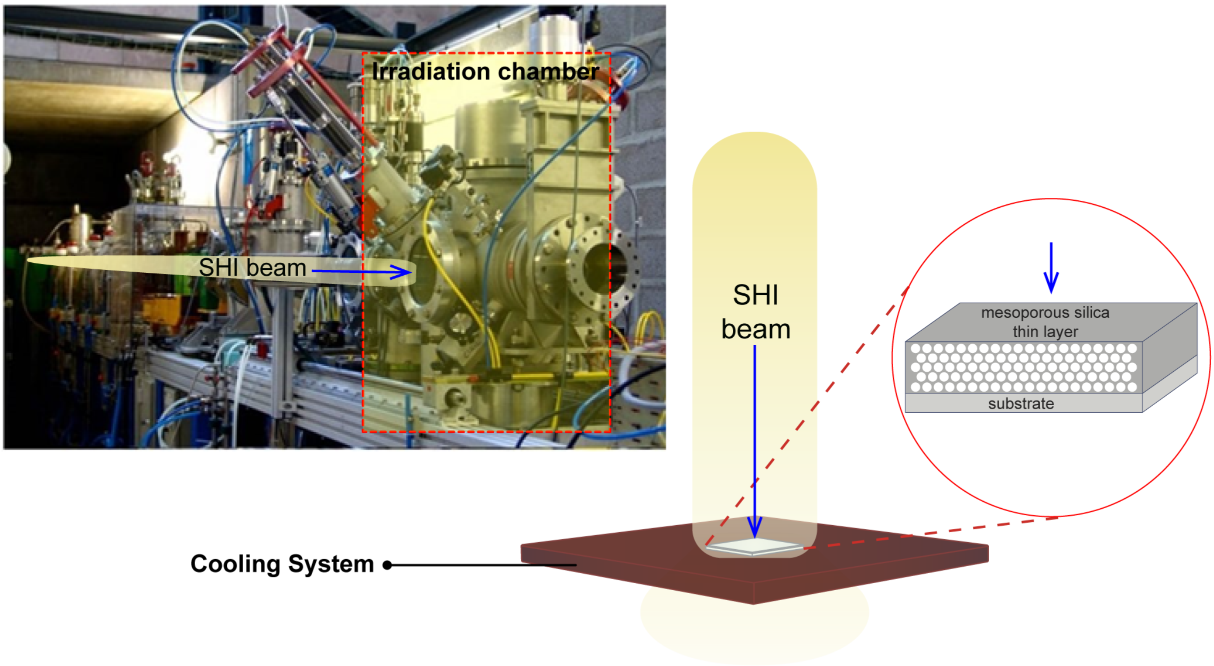

FIGURE 3.10: Photo of the irradiation line and schematic diagram showing the relative orientation of the sample and beamline

3.2.2 Irradiation parameters

The table 3.2 below summarizes the properties of the beams employed. The stopping power dE/dx is computed using a density of 2.2 g/cm^3, which is equivalent to dense silica (TRIM 2013 calculation). It is worth noting that the electronic dE/dx of C is less than the threshold for track production in silica (2-4 keV/nm for 2.2 g/cm^3)[108]. Electronic stopping of Ar is near to this threshold, Ni and Kr's S_e is somewhat over it, and Xe's dE/dx is definitely above it (See figure 3.11). All of these irradiations have a negligible ballistic impact.

TABLE 3.2: Summary of ion beams

Ion	Ion energy MeV/A	S_e keV/nm	S_n keV/nm	Flux ions/(cm^2.s)	Max dose ions/cm^2	Beamline-date
$^{12}C^{4+}$	0.98	1.1	1.10E-03	5~7e9	1.80E+15	IRRSUD-2019
$^{12}C^{4+}$	0.98	1.1	1.10E-03	3~4e9	4.00E+14	IRRSUD-2021
$^{48}Ca^{18+}$	9.17	2.9	1.70E-03	1~2e9	1.10E+14	SME-2019
$^{36}Ar^{10+}$	0.98	4.5	1.00E-02	4~6e9	2.30E+14	IRRSUD-2021
$^{58}Ni^{9+}$	0.57	6.5	3.30E-02	5~6e9	1.50E+14	IRRSUD-2019
$^{86}Kr^{18+}$	0.86	8.7	3.90E-02	4~5e9	2.00E+14	IRRSUD-2021
$^{129}Xe^{23+}$	0.71	11.8	9.20E-02	6~7e9	5.00E+14	IRRSUD-2019
$^{136}Xe^{23+}$	0.71	11.8	9.20E-02	3~4e9	5.00E+13	IRRSUD-2020
$^{136}Xe^{19+}$	0.55	10.7	1.14	3~4e9	8.00E+13	IRRSUD-2021

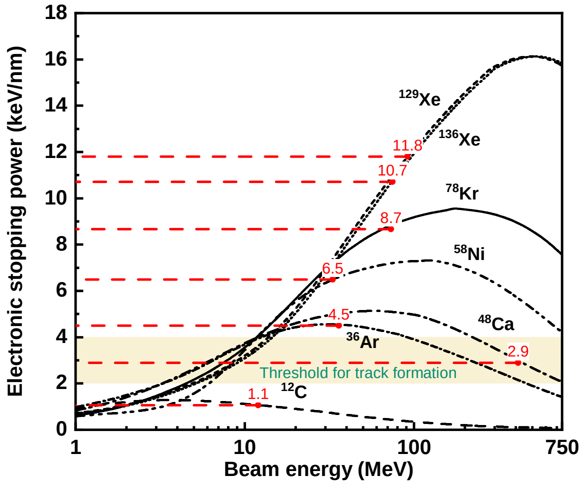

FIGURE 3.11: TRIM 2013 calculation of electronic stopping power in 2.2 g/cm^3 SiO$_2$, the light yellow area represents the threshold for track formation in silica reported by Klaumünzer *et al.*[108]

3.3 Results

The primary technique for determining the thickness of thin film materials is XRR, along with a few samples observed by FIB/STEM to study morphology. Chemical characteristics are determined using FTIR.

3.3.1 XRR measurement

The raw curves of XRR measurements before and after irradiation are shown in Appendix D. It should be noted that under Carbon irradiation, an unidentified layer appears to be deposited on the original material (as observed in the silicon wafer). This could be due to impurities in the irradiation chamber depositing on the sample under the influence of the carbon beam. As it is not a concern for us in this study, this phenomenon will therefore not be discussed in detail.

3.3.1.a Fluctuation of the Bragg peaks

In the very first place, we will not address the overall thickness changes achieved with these findings, the corresponding results will be discussed in detail in the coming discussion sections. We will begin by examining the fluctuation of the Bragg peaks, which is in respect to the structural order of the pores.

The fluences necessary for full elimination of the XRR's Bragg peak under irradiation with various particle conditions are summarized in the following table 3.3. With increasing electronic stopping power, the dose required to totally destroy the interlayer structure reduces, as does the necessary energy deposition.

TABLE 3.3: Summary of fluctuation of Bragg peaks in XRR measurements

Ion	Ion energy	S_e	Minimum fluence		Corresponding energy deposition
			IPc	ICc	
	MeV/A	keV/nm	ions/cm^2	ions/cm^2	keV/cm^3
$^{12}C^{4+}$	0.98	1.1	$\gg$1.8e15	$\gg$1.8e15	$\gg$1.9e22
$^{48}Ca^{18+}$	9.17	2.9	$\gg$1.0e14	$\gg$1.0e14	$\gg$2.9e21
$^{36}Ar^{10+}$	0.98	4.5	2.3e14	2.3e14	1.0e22
$^{58}Ni^{9+}$	0.57	6.5	1.0e14	>1.5e14	$\geq$6.5e21
$^{86}Kr^{18+}$	0.86	8.7	8.0e13	8.0e13	7.0e21
$^{136}Xe^{19+}$	0.55	10.7	4.0e13	4.0e13	4.3e21
$^{129}Xe^{23+}$	0.71	11.8	5.0e13	2.5e13	~3.0e21
$^{136}Xe^{23+}$	0.71	11.8	4.0e13	2.0e13	~2.3e21

Here the energy deposition is calculated using: Energy deposition$_{\text{electronic}}$ = Fluence × S_e.

We provide two particular examples to demonstrate the relationship between the Bragg peak in XRR and the morphology observed using electron microscopy. FIB/STEM observations were performed for IPc under carbon irradiation at a fluence of 3e13 ions/cm^2 and under Xenon irradiation at a fluence of 1e13 ions/cm^2. And their XRR curves are presented in figure 3.12 below, we can observe that the evolution of the amplitude of their bragg peaks is significantly different with the same magnitudes of fluence.

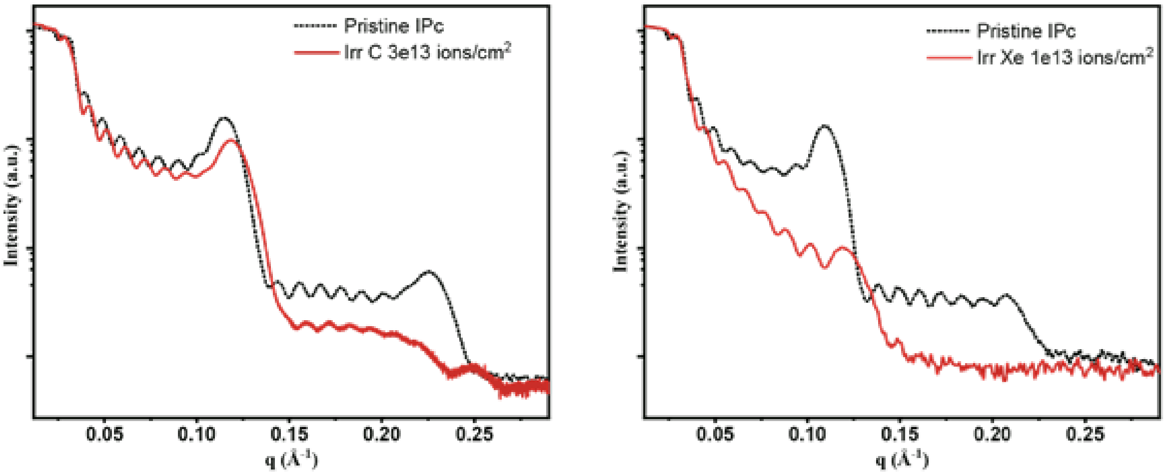

FIGURE 3.12: XRR curves after 3e13 ions/cm^2 of 12 MeV Carbon beam irradaition (left) and 1e13 ions/cm^2 of 92MeV Xenon beam irrdiation (right), there is a significant difference in the variation of Bragg peak.

The morphology revealed by electron microscopy can very well indicate the source of this discrepancy. Two STEM pictures of the specimen's cross section and two SEM images of the specimen's top view are shown here (figure 3.13). After being bombarded with carbon ion beams, we can see that the pores remain visible, albeit their form has changed from cylindrical to elliptical. Additionally, the top view reveals the porous structure's classical fingerprint. Unlike the carbon bombardment, after xenon bombardment, we observe an entirely different type of damage structure. From a cross-sectional perspective, the pore structure is nearly imperceptible and is replaced with a tunnel-like damage structure. The top view of the specimens shows clearly that the bombardment left numerous tunnel-shaped penetration tracks. An illustration is given to show the difference between the two damage patterns.

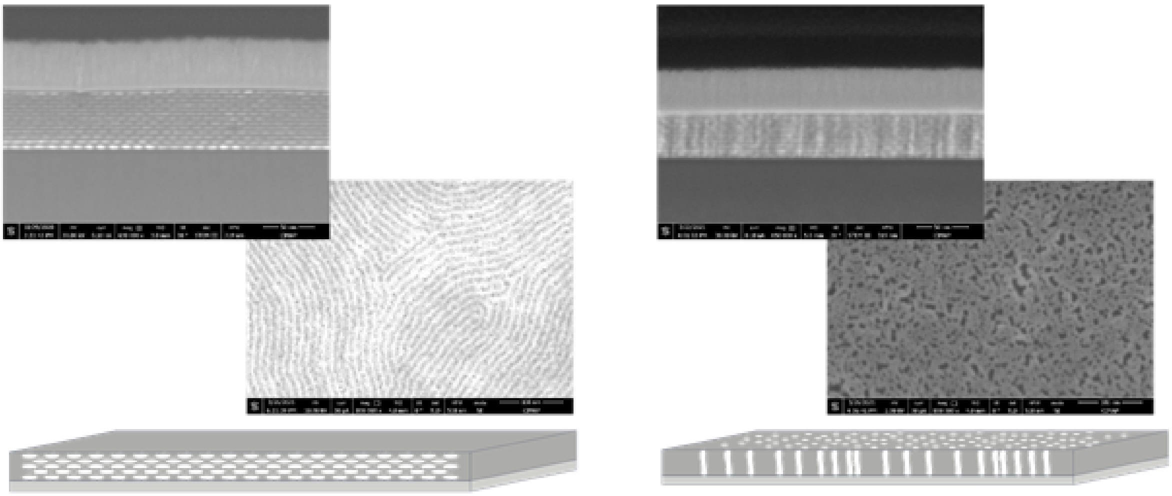

FIGURE 3.13: The morphology of silicon dioxide thin film revealed by electron microscopy after 3e13 ions/cm^2 of 12 MeV Carbon beam irradiation (left) and 1e13 ions/cm^2 of 92MeV Xenon beam irradiation (right)

3.3.1.b Thickness versus fluence

The next subsections will discuss the thickness evolution of IPc and ICc under irradiation. The following graphs provide our first insight into the trend of thickness variation in response to diverse particle irradiations.

Carbon beam irradiation

Carbon irradiation was undertaken twice, the first in 2019 (figure 3.14) and the second in 2021 (figure 3.15). Except for the flux, which was roughly half of what it was in 2019, the parameters for these two irradiations were identical. It can be seen from the results that the change in flux does not result in any statistically significant difference. Both runs reveal the same trend: the reduction in thickness caused by carbon ion irradiation is not considerable, hardly reaching 10%. When the dose is increased to 10^{15} ions/cm^2, at which point a thickness change of ~20% can be noticed.

It should be noticed that the bragg peak is present at all doses, and the variation in thickness of the "interlayer" calculated by the bragg peak is in excellent agreement with the variation in the total thickness calculated by the Kiessig fringes, indicating that the structural order of the pores is not disrupted by irradiation.

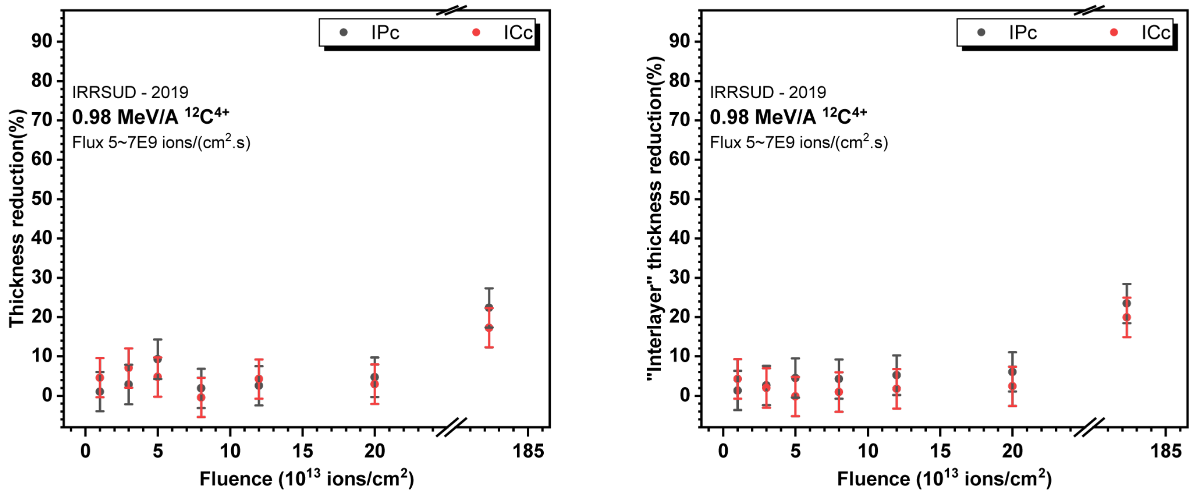

FIGURE 3.14: The reduction of total thickness and interlayer thickness as a function of the fluence

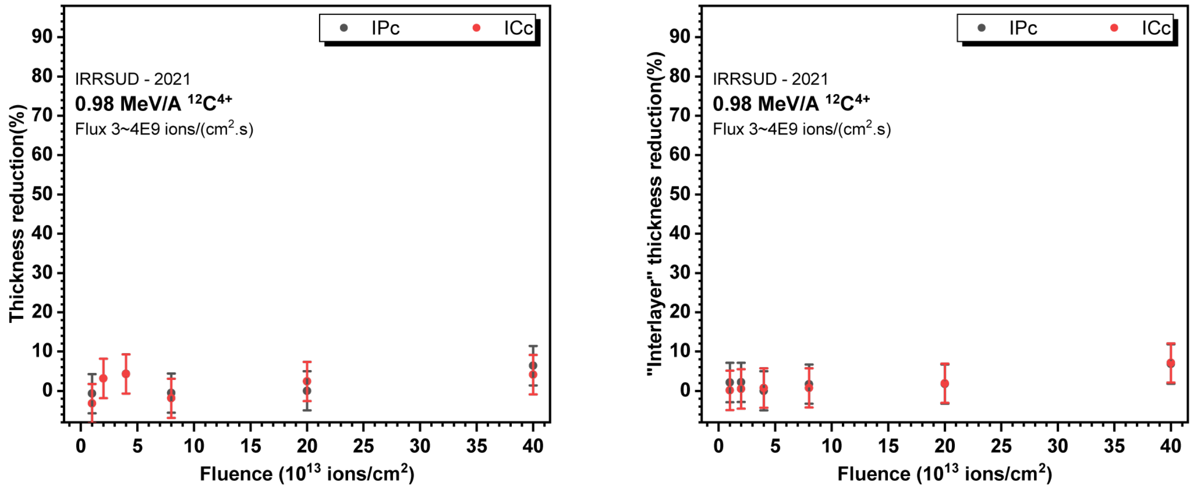

FIGURE 3.15: The reduction of total thickness and interlayer thickness as a function of the fluence

Calcium beam irradiation

Calcium irradiation generated a more substantial thickness change than carbon irradiation, with a thickness reduction rate of more than 10% already occurring at a fluence of 1.1x10^{14} ions/cm^2 (see figure 3.16). Under all experimental conditions, it is still possible to calculate the interlayer by bragg peak, and the change stays in excellent agreement with the overall thickness change, indicating that calcium ions do not cause severe fluctuations in pore structure order.

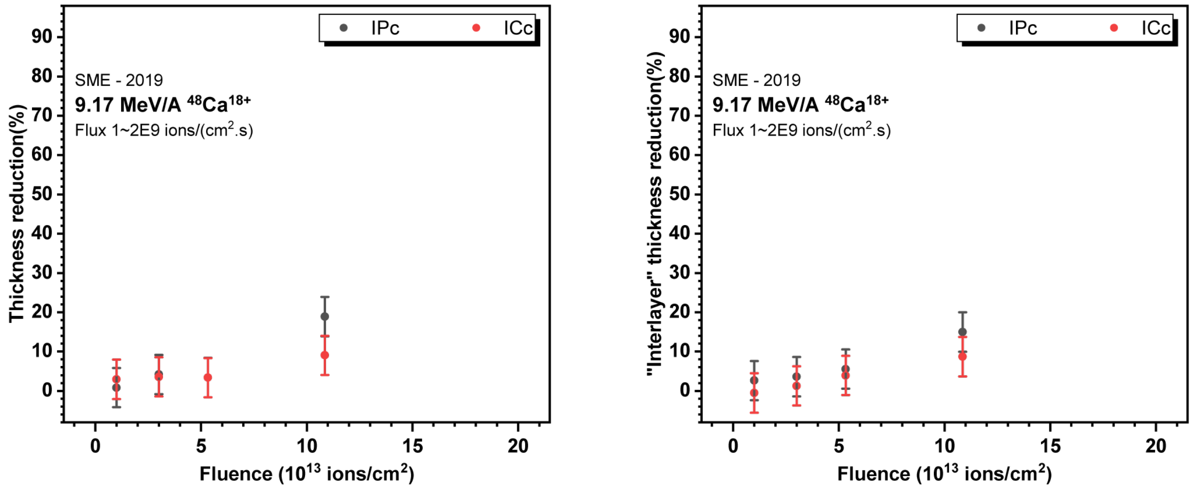

FIGURE 3.16: The reduction of total thickness and interlayer thickness as a function of the fluence

Argon beam irradiation

Compared to carbon and calcium irradiation, the reduction in film thickness is more pronounced in argon irradiation. The Bragg peak is no longer detectable at a dose of approximately

2.3x10^{14} ions/cm^2 (figure 3.17), indicating that the original "interlayer" lamellar structure has already been disrupted. However, when the bragg peak is still visible, the reduction in interlayer thickness is still strongly consistent with the reduction in total thickness, leading us to reasonably conclude that at this time, the reduction in total thickness is still due to radiation-induced shrinkage of pores.

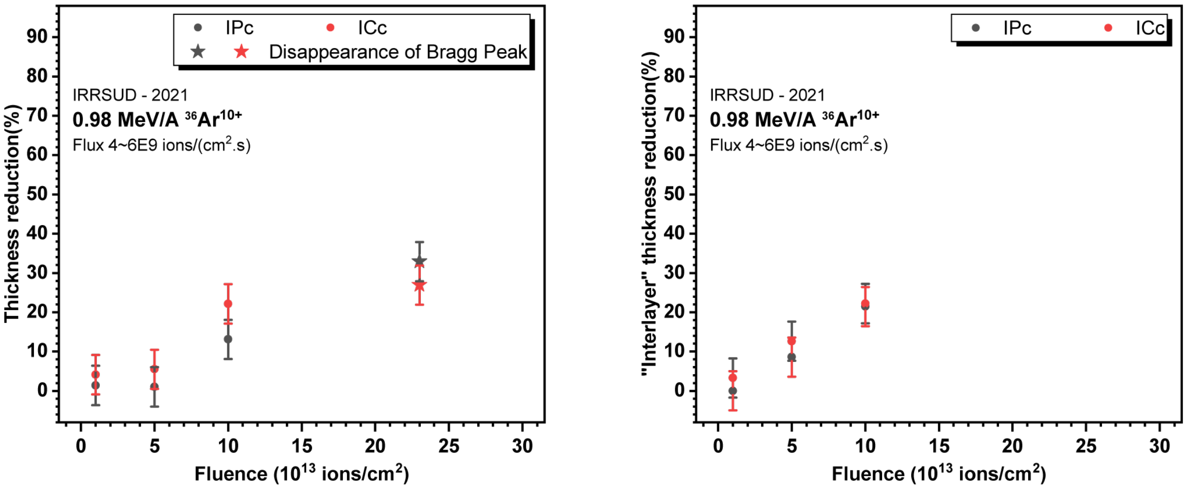

FIGURE 3.17: The reduction of total thickness and interlayer thickness as a function of the fluence

Nickel beam irradiation

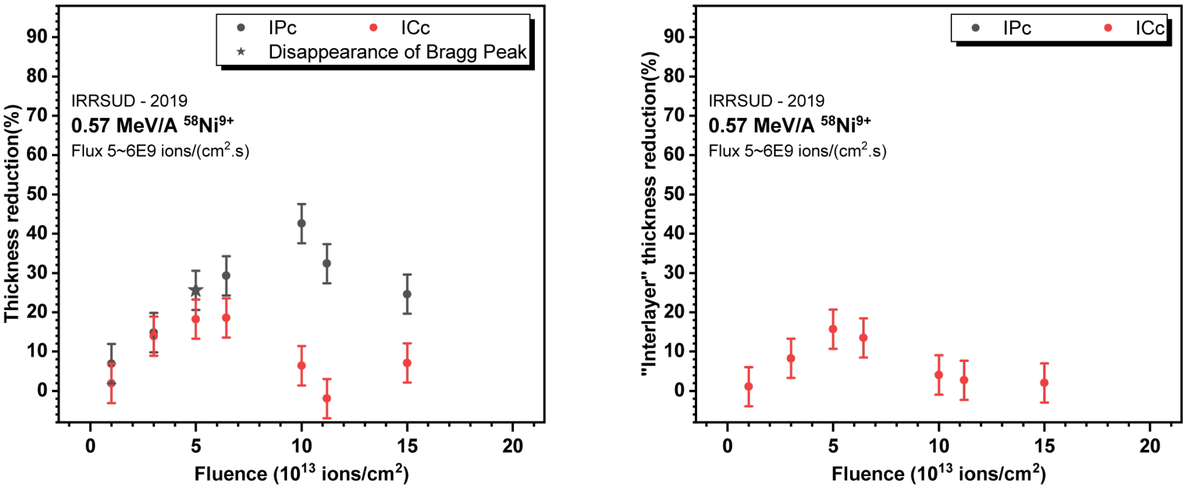

FIGURE 3.18: The reduction of total thickness and interlayer thickness as a function of the fluence

Note: The experimental result of nickel irradiation is rather peculiar; as fluence increases, the thickness alteration of the porous film first increases and then decreases, which has not been observed in other irradiations. We have not found a reasonable explanation for the moment. We have planned to conduct a new experiment, but the planned experiment was cancelled due to the COVID-19 epidemic; thus, this experimental result should be treated with caution.

Krypton beam irradiation

Under Krypton irradiation, the bragg peak disappears at a fluence of 8x10^{13} ions/cm^2, and after the structure of the "interlayer" is disrupted, the total thickness detected by XRR continues to shrink (figure 3.19). This reduction in thickness cannot be considered to be caused by the shrinkage of the pores in the original porous thin films.

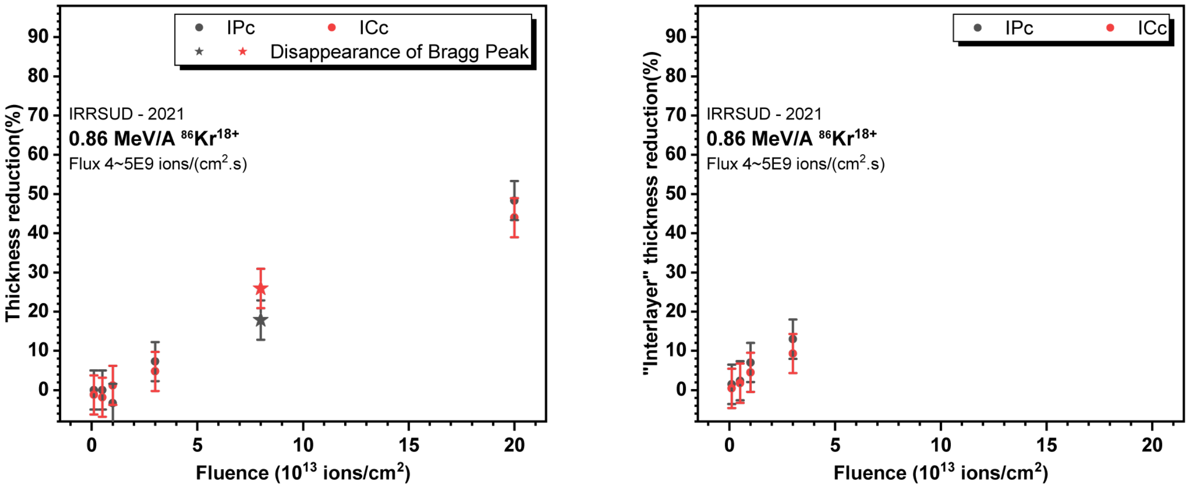

FIGURE 3.19: The reduction of total thickness and interlayer thickness as a function of the fluence

Xenon beam irradiation

The xenon irradiation was performed three times, with the first run in 2019 (figure 3.20) having a wide fluence range, eventually reaching 5x10^{14} ions/cm^2. However, we can see that at less than 5x10^{13} ions/cm^2, the bragg peak had already completely disappeared, and the total thickness measured by XRR was still decreasing sharply after that. The second and third runs were completed in 2020 (figure 3.21) and 2021 (figure 3.22), respectively. Despite the fact that the maximum fluence of these two runs was limited to a relatively low value, we can see that the bragg peak completely disappears at a fluence of approximately 2x10^{13} ions/cm^2. Before this fluence, if we use the previous arguments, we can still argue that the reduction in the total film thickness is directly related to the shrinkage of the original pores in the silica thin films.

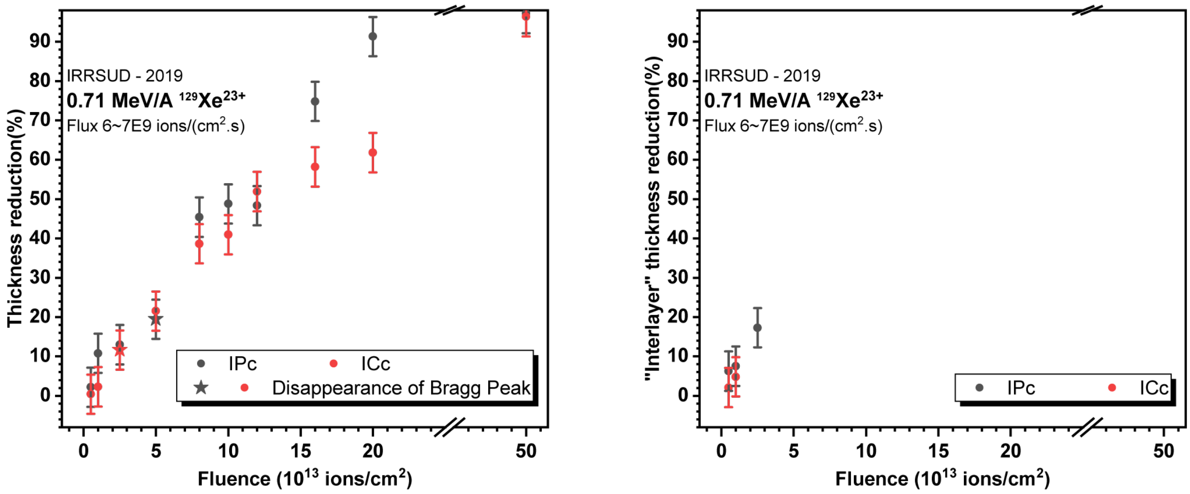

FIGURE 3.20: The reduction of total thickness and interlayer thickness as a function of the fluence

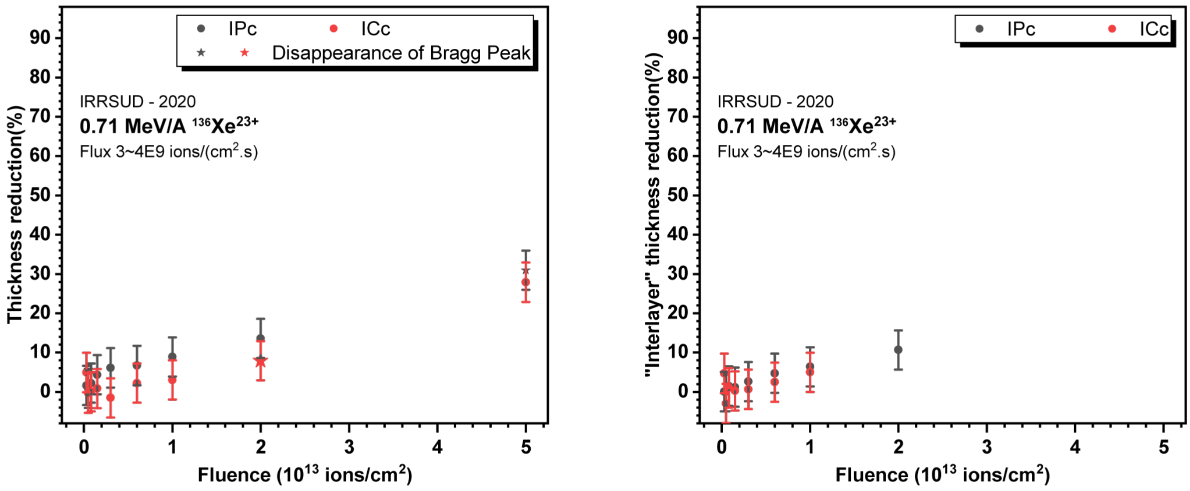

FIGURE 3.21: The reduction of total thickness and interlayer thickness as a function of the fluence

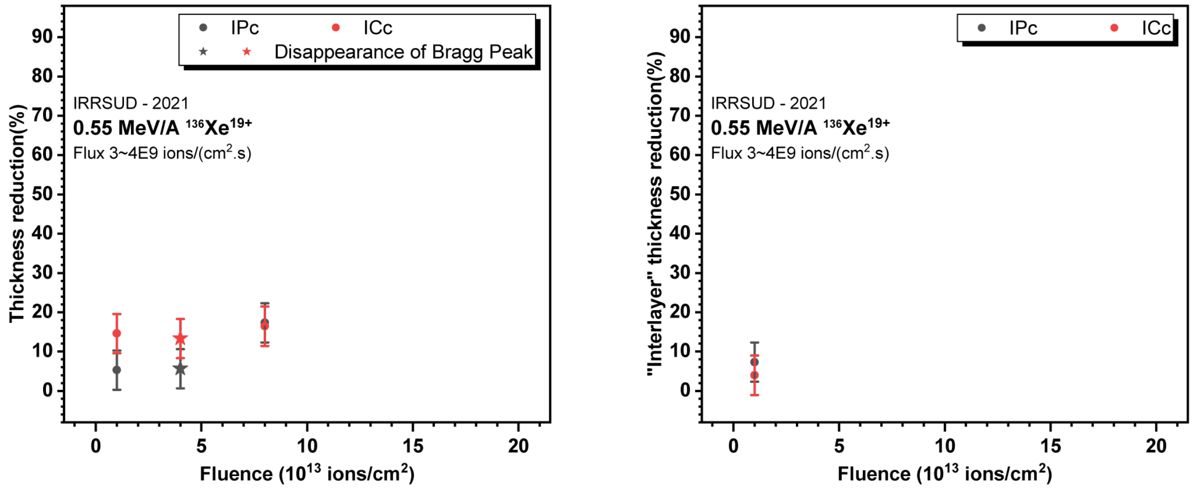

FIGURE 3.22: The reduction of total thickness and interlayer thickness as a function of the fluence

3.3.1.c Calculation of cross-section

Based on the results of thickness variation presented in the previous section, we can conclude that the total thickness variation of the porous silica film material under irradiation is highly consistent with the thickness variation of the interlayer when the interlayer structure has not yet been annihilated. In other words, at low fluences, the thickness change of the interlayer is the main factor impacting the overall thickness change. The thickness of the interlayer measured by XRR, on the other hand, reflects the pore diameter plus the thickness of the pore wall. The drop in the observed thickness of the interlayer structure may be attributed to the change in the pore volume, as previously stated. Therefore, we intend to apply a model to calculate the effective cross-section of the irradiation process in an early stage.

One potential model was proposed by Marples in the 1980s to estimate a cross-section of the irradiation process[109]. This model was first used to explain the swelling of glasses under internal irradiation. and later on external irradiation by other researchers[110–112]. This assertion was based on the assumption that the change in property, swelling or densification, is proportional to the fraction of damaged volume. With this hypothesis, Marples's equation can be written as:

$$\frac{\Delta h}{h} = \left(\frac{\Delta h}{h}\right)_{\text{sat}} (1 - \exp(-\nu R t)) = \left(\frac{\Delta h}{h}\right)_{\text{sat}} (1 - \exp(-\sigma \Phi))$$

Δh is the evolution of macroscopic properties (thickness, pore volume, density, mechanical property, etc.). The index "sat" means the saturation state. In this work, the term υRt can be replaced by $\sigma\Phi$ where σ is the cross-section, and Φ is the fluence.

This model was used to examine the data of interlayer thickness. As previously stated (note of figure 3.18), the results of Ni2019 will not be included in this section. Additionally, the results of Xe2019 and Xe2020 are not included in this section for statistical reasons due to a lack of sufficient points acquired. Furthermore, because no plateau stage can be directly observed in the tendency, we must apply an indirect approach to determine the saturation value.

As previously stated, the drop in interlayer thickness may be interpreted as a reduction in the volume of pores in the porous silica film material; hence, the saturation value can be defined as the point at which initial porosity in the porous silica film material is completely closed.

The method used to determine the initial porosity is described here. In section 1.2.3.3, we employ the XRR data processing approach, which enables us to acquire not only the thickness of the thin film material, but also the global electron density, from which the average density may be derived. By comparing IPc, ICc, and NPc, we can determine the material's initial porosity for IPc and ICc.

For the unirradiated example of IPc, ICc, their corresponding global densities are 1.2 ± 0.1 g/cm^3 and 1.3 ± 0.1 g/cm^3. This value for non-porous silica thin film NPc (sol-gel) is around 2.0 ± 0.1 g/cm^3. Hence, the initial porosity for IPc and ICc is 40% and 35%, respectively.

Using the initial porosity of 40% to 35% as the theoretical saturated state value, the data of interlayer thickness was fitted with Marples' equation. The results of the fit using Marples' equation are shown in the figure 3.23. In the fit, data with the same stopping power were merged (C-2019 and C-2021).

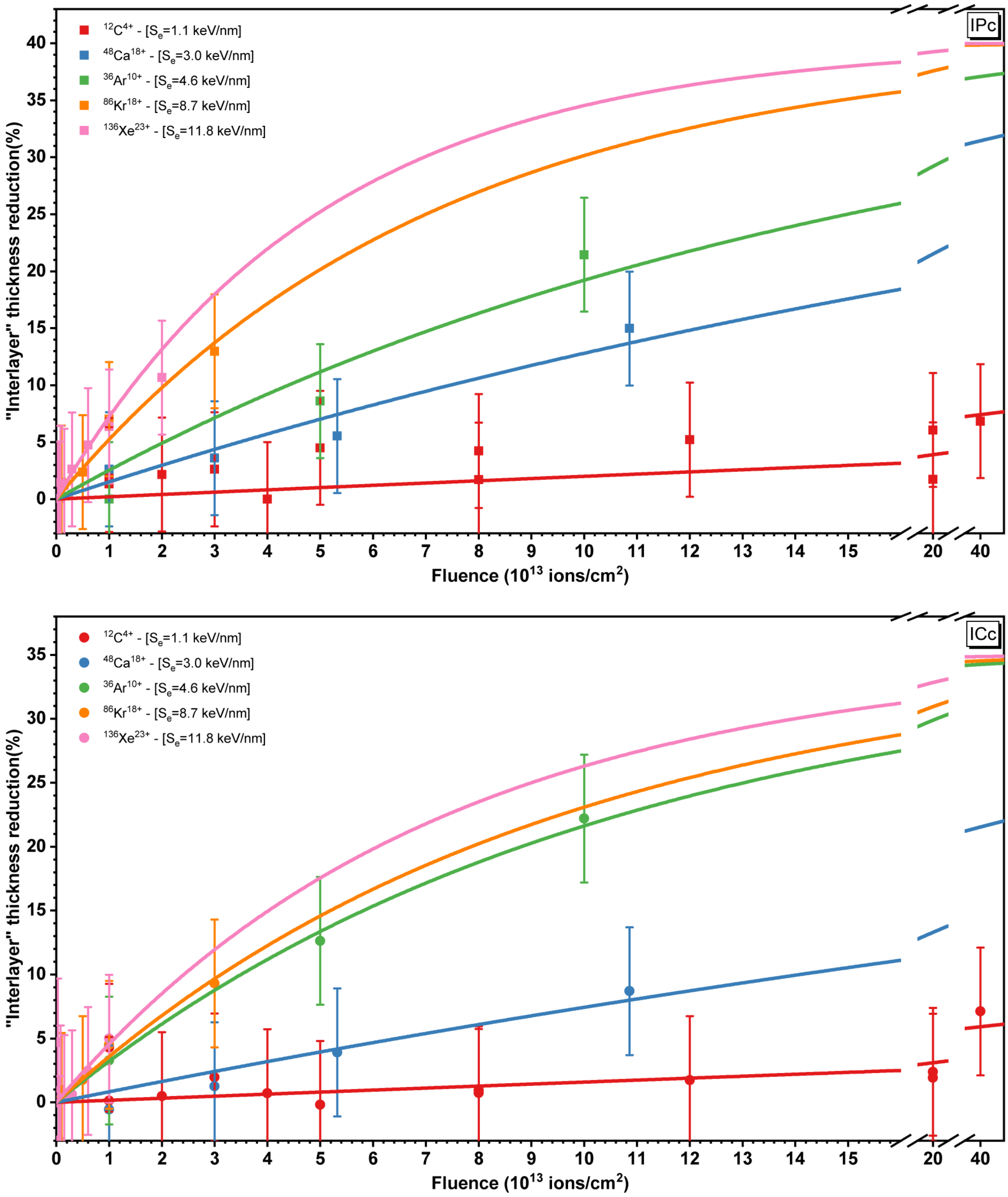

FIGURE 3.23: Fit of Marples' equation to data from XRR interlayer thickness Measurement.

The following figure 3.24 plots the corresponding effective cross-section versus S_e calculated by the model. As observed in the data, cross section is positively associated with S_e and there is no statistically significant difference between IPc and ICc.

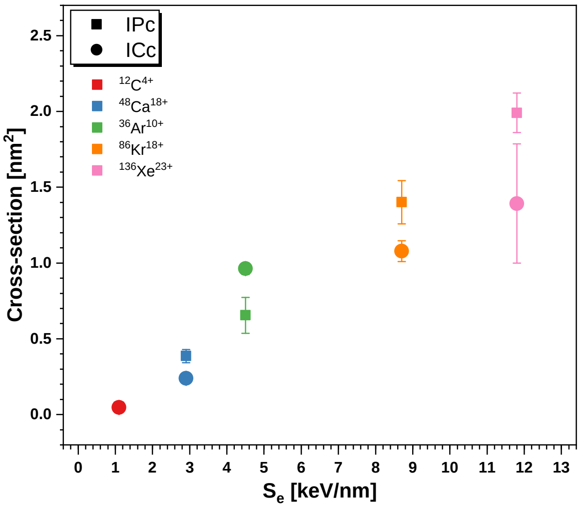

FIGURE 3.24: Effective cross-sections obtained from XRR versus electronic stopping power for IPc and ICc

The damage cross section estimated here is around a few nm^2, indicating that when the fluence utilized in the experiment surpasses 10^{14} ions/cm^2, the damage to the sample is no longer caused by a single particle bombardment. In fact, it is at this order of magnitude of fluence that we observe the complete disappearance of the bragg peak.

Using a cylindrical shape as an assumption for the trajectory influenced by particles, the radii are calculated from the relation below.

$$R = (\sigma/\pi)^{1/2}$$

The results are summarized in tables 3.4 and will be discussed later.

TABLE 3.4: Radius deduced from the damage cross section

Ion	Ion energy MeV/A	S_e keV/nm	Radii$_{IPc}$ nm	Radii$_{ICc}$ nm
$^{12}C^{4+}$	0.98	1.1	0.13 ± 0.02	0.12 ± 0.01
$^{48}Ca^{18+}$	9.17	2.9	0.35 ± 0.04	0.28 ± 0.04
$^{36}Ar^{10+}$	0.98	4.5	0.46 ± 0.08	0.55 ± 0.02
$^{86}Kr^{18+}$	0.86	8.7	0.67 ± 0.07	0.59 ± 0.04
$^{136}Xe^{23+}$	0.71	11.8	0.80 ± 0.05	0.67 ± 0.19

A note of caution is due here since the effective cross-sections presented in this section represent the probability for an incident ion to alter the pore structure in the porous silica at relatively low irradiation doses and are not directly comparable to the published data for non-porous amorphous silica determined by IR, saxs or chemical etching[113], which is ten times larger. Their data represent the effect of irradiation on the silica network in the absence of pores. The effect of irradiation on the pore wall (silica network) and the related discussion will be discussed later.

3.3.1.d Total thickness reduction versus electronic energy deposition

The total thickness reduction of two kinds of porous silica films, IPc and ICc, as a function of electronic energy deposition is represented in the figure 3.25. The theoretical values provided by the SRIM/TRIM computations, as well as the dose received, are used to compute the electronic energy deposition. We can observe that for both types of porous materials, the evolution follows a general tendency: at the same energy, the total thickness reduction grows with increasing electronic stopping power.

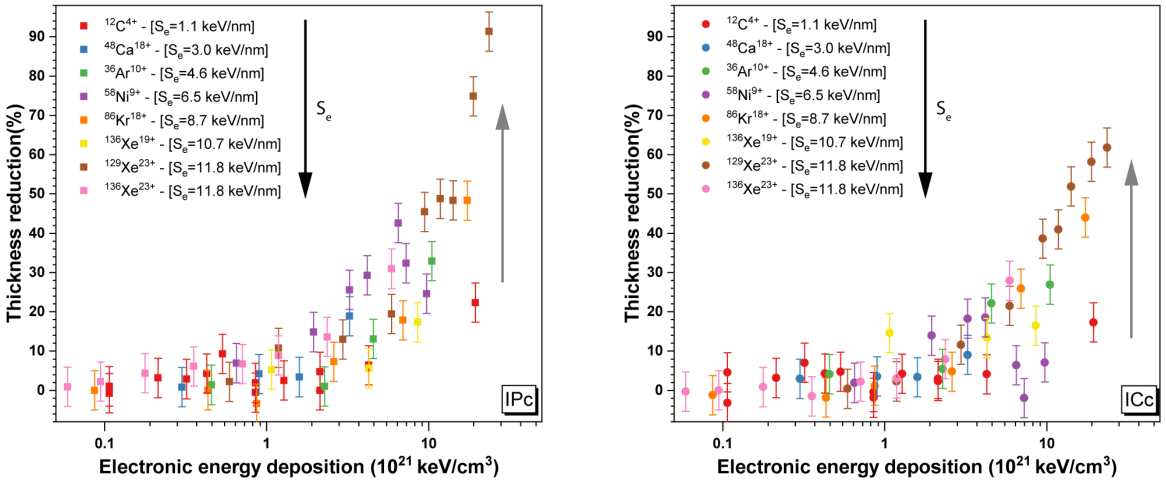

FIGURE 3.25: The total thickness reduction of two kinds of porous silica films, IPc and ICc, as a function of electronic energy deposition

It is crucial to note that this tendency becomes more obvious at higher energy levels, particularly once the percentage reduction in the overall thickness of the film exceeds the "initial porosity", which was previously described. Consequently, it can be concluded that, once the porous film material reaches this state (i.e., after the pores have almost completely disappeared), the effect of an increase in energy deposition on the material is closely related to typical damages on non-porous silica network (e.g., formation of tracks, sputtering...).

3.3.2 FTIR measurement

3.3.2.a Spectrum acquisition

The Perkin Elmer Spectrum 100 Fourier Transform Infrared system was used for FTIR spectroscopy. Spectra (6 acquisitions per sample) were collected between 4000 and 300 cm^{-1} at a resolution of 4 cm^{-1}. Due to the existence of at the SiO2/wafer Si interface, the spectra will contain many oscillations caused by reflections (figure 3.26). As a result, the spectrum obtained cannot be directly utilized. This effect is amplified when the resolution is excellent. We smooth the spectrum using Perkin Elmer™ software, and the outcome is shown in Figure 3.26 (orange line). The increase in absorbance in the region (2500 - 1500 cm^{-1}) due to Mie scattering is not apparent [114]. Therefore, we simply employ the instrument's automated baseline correction function to correct the instrument-induced deviations. The oscillations between 1800 and 1400 cm^{-1} are caused by the presence of CO_2 and water during the measurement, but these signals do not interfere with the information sought for this research.

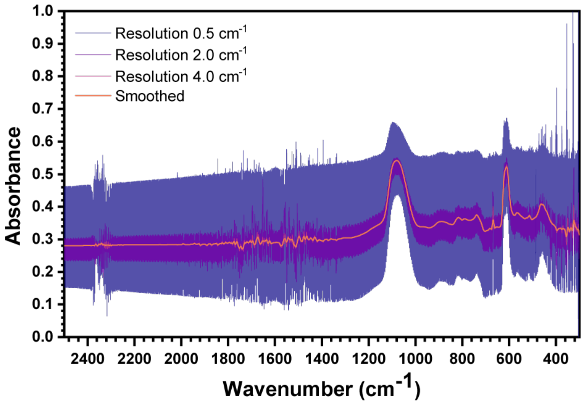

FIGURE 3.26: FTIR spectrum of non-irradiated silica thin film with different resolutions and the smoothed curve

3.3.2.b Spectrum analysis method

The infrared analysis provides a response for the entire sample, as it is completely traversed by the FT-IR Transmission analysis beam. Even at the greatest projected range (412.8 MeV Ca), the TRIM calculation (figure 3.27) indicates that the incident particles will settle in the silicon substrate and will have no effect on the back side of the silica thin film.

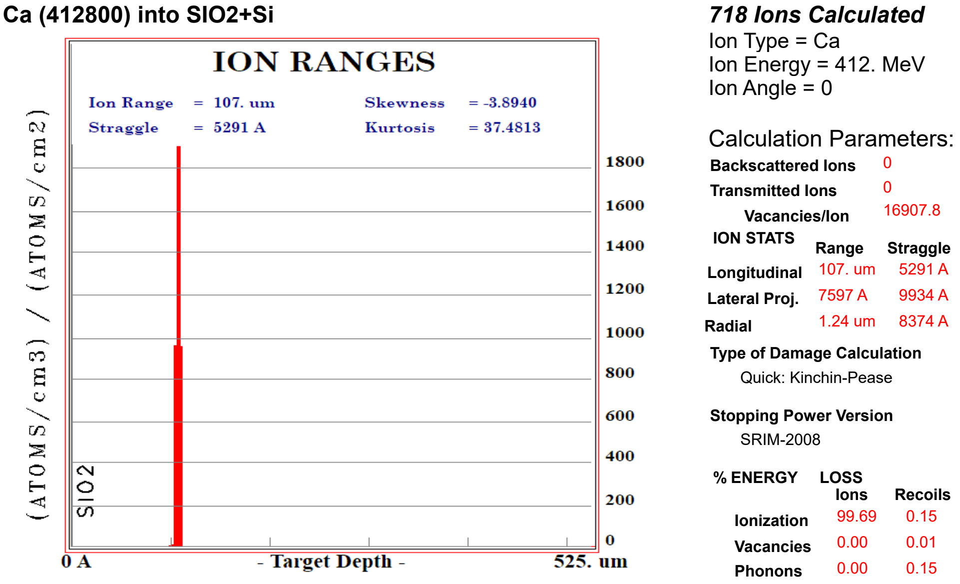

Ion Range = 107. um
Straggle = 5291 A
Skewness = -3.8940
Kurtosis = 37.4813

718 Ions Calculated

Ion Type = Ca
Ion Energy = 412. MeV
Ion Angle = 0

Calculation Parameters:

Backscattered Ions	0
Transmitted Ions	0
Vacancies/Ion	16907.8

ION STATS	**Range**	**Straggle**
Longitudinal	107. um	5291 A
Lateral Proj.	7597 A	9934 A
Radial	1.24 um	8374 A

Type of Damage Calculation
Quick: Kinchin-Pease

Stopping Power Version
SRIM-2008

% ENERGY LOSS	**Ions**	**Recoils**
Ionization	99.69	0.15
Vacancies	0.00	0.01
Phonons	0.00	0.15

FIGURE 3.27: TRIM calculation for 412.8 MeV Ca beam irradaition on SiO_2/Si samples with silicon wafer thickness ~525 µm.

Even if the pure silicon wafer does not absorb the infrared signal theoretically, we always witness an absorption, which is most likely due to the doping of these materials of type P, or potentially due to the irradiation impact on the silicon wafer (figure 3.28).

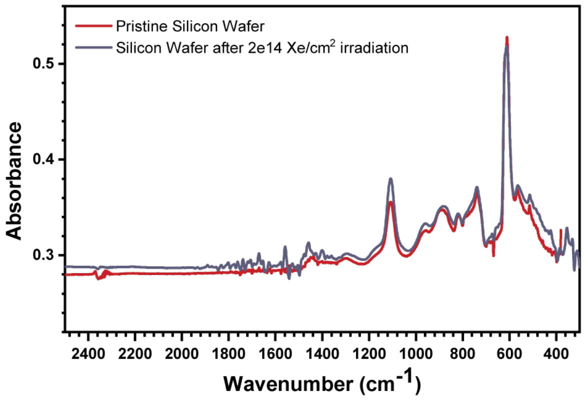

FIGURE 3.28: FTIR spectrum of pure silicon wafer before and after irradiation

The following approach (figure 3.29) was used to keep only the effects caused by irradiation in a-SiO_2 layers:

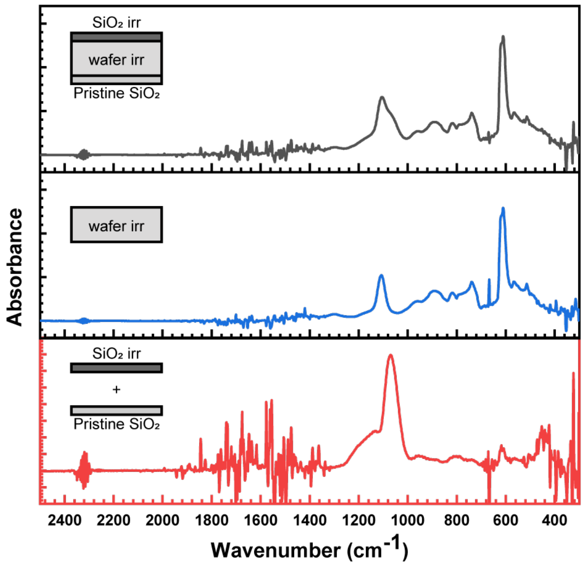

FIGURE 3.29: Subtraction scheme of the silicon wafer FTIR spectrum from the FTIR spectrum of a-SiO_2/Si/a-SiO_2 samples

a) Spectrum of an irradiated sample containing an irradiated a-SiO_2 layer + an irradiated c-Si + a pristine a- SiO_2 layer was collected

b) Spectrum of an irradiated Si wafer was collected

c) The resulting spectrum contains the IR response of an irradiated a-SiO_2 layer and a pristine a-SiO_2 layer was calculated by subtracting b) from a).

The IR spectra that follow have been processed in this manner. Nevertheless, the further treatment (figure 3.30) could theoretically be performed to obtain the response of the pristine a-SiO_2 layer from the unirradiated samples:

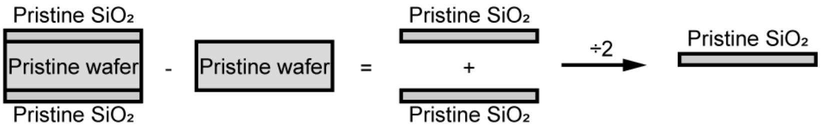

FIGURE 3.30: Scheme for calculating FTIR spectrum of one pristine SiO_2 layer from the FTIR spectrum of pristine a-SiO_2/Si/a-SiO_2 samples

In practice, however, since the synthesized thin films are not perfectly symmetrical on both sides of the silicon wafer. Their thickness, pore arrangement, and other characteristics might vary slightly. A larger error may be introduced in the subsequent processing by following such a processing to obtain the pristine SiO_2 layer. As a result, this step was omitted from future treatment. On this premise, the results to be presented later will be a qualitative comparison and not quantitative due to the presence of the unirradiated SiO_2 layer.

3.3.2.c Evolution of IR spectra with irradiation fluence

The following figures (figure 3.31 - 3.39) contain the raw FTIR spectra obtained before and after irradiation. We are interested in the range between 1150 and 900 cm^{-1}. This area provides information on the TO longitudinal mode of the Si-O bond in the a-SiO_2 lattice (between 1020 and 1100 cm^{-1}).

Following all the irradiations we have done (except Xe2019), in the case of non-porous silica (NPc and SiO_2 therm), the IR spectra reveal a red shift of the TO band's absorption maximum, which is coherent with the documented irradiation-related evolution in the literature[83, 85, 110, 113]. This tendency, however, is not as prominent in porous silica (IPc and ICc). As for Xe-2019 irradiation, we found that the IR spectrum was blueshifted at maximal dose, and the total intensity dropped. In conjunction with our discussion in the preceding section, the observed shift is because the silica layer on the side that was bombarded has been lost due to the extremely high dose of irradiation used in this example. The silicon wafer may have also received a significant impact under bombardment, resulting in an increase in the complexity of the IR signal during the experiment.

Carbon beam irradiation

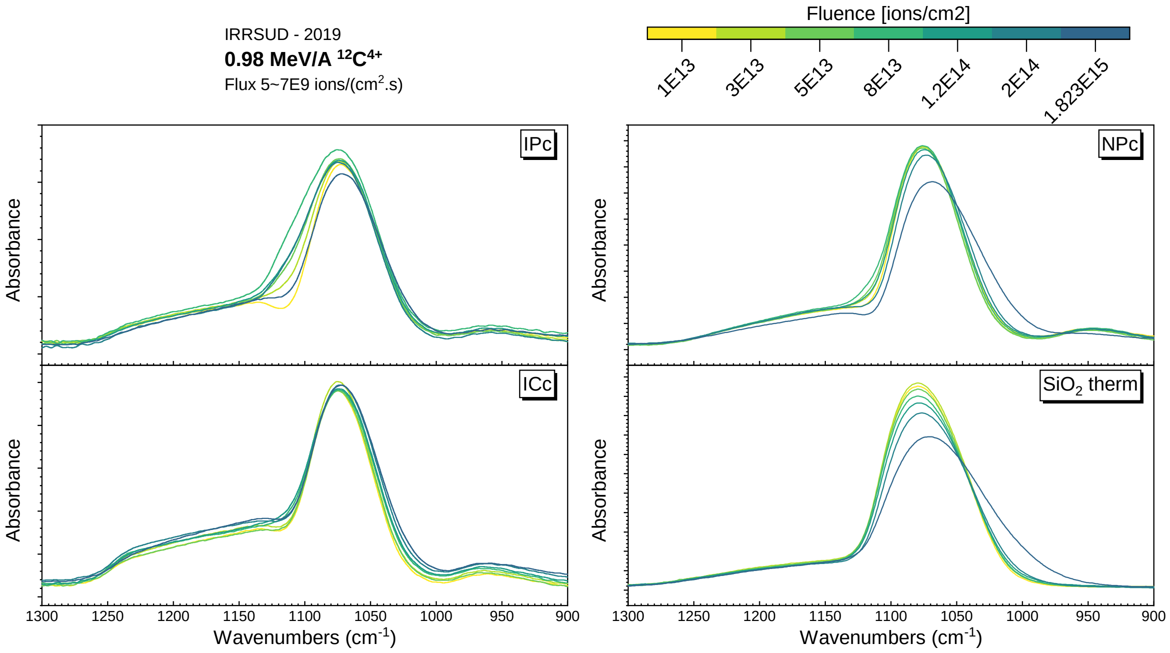

FIGURE 3.31: The IR band related to TO mode from raw infrared spectrum as a function of the fluence

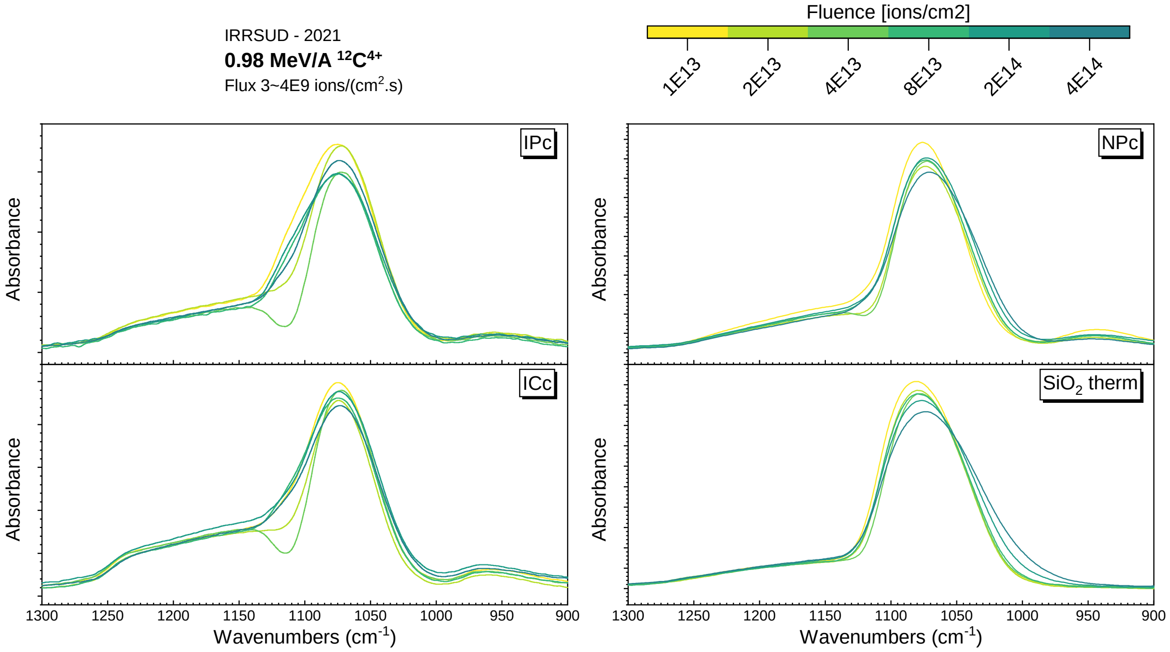

FIGURE 3.32: The IR band related to TO mode from raw infrared spectrum as a function of the fluence

Calcium beam irradiation

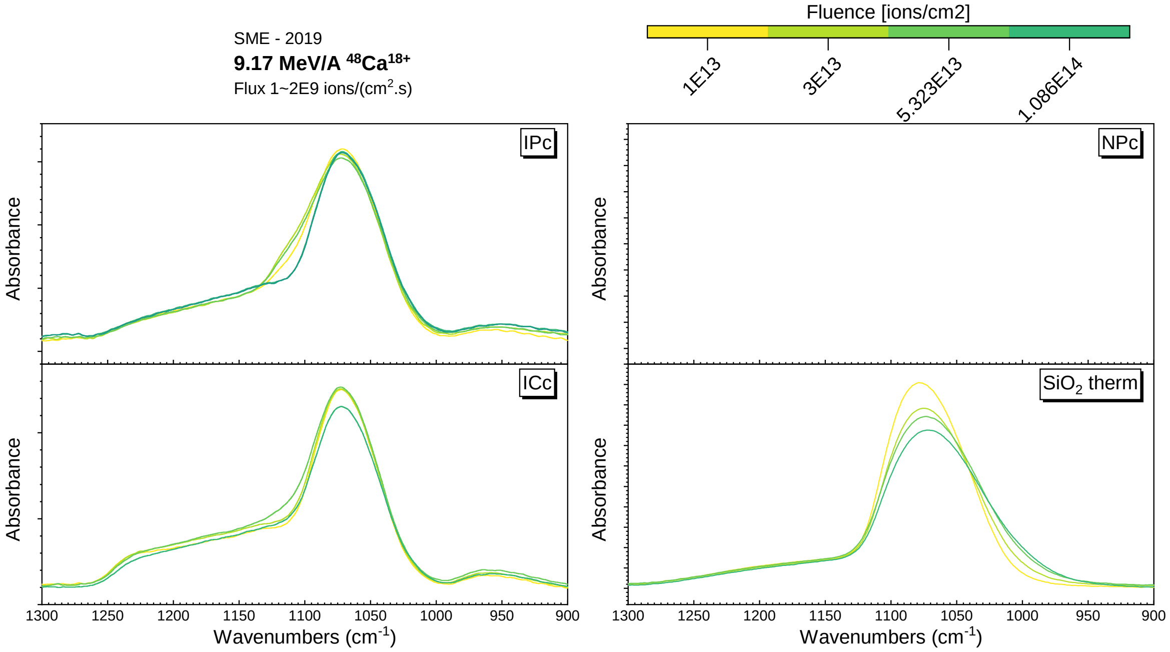

FIGURE 3.33: The IR band related to TO mode from raw infrared spectrum as a function of the fluence

Argon beam irradiation

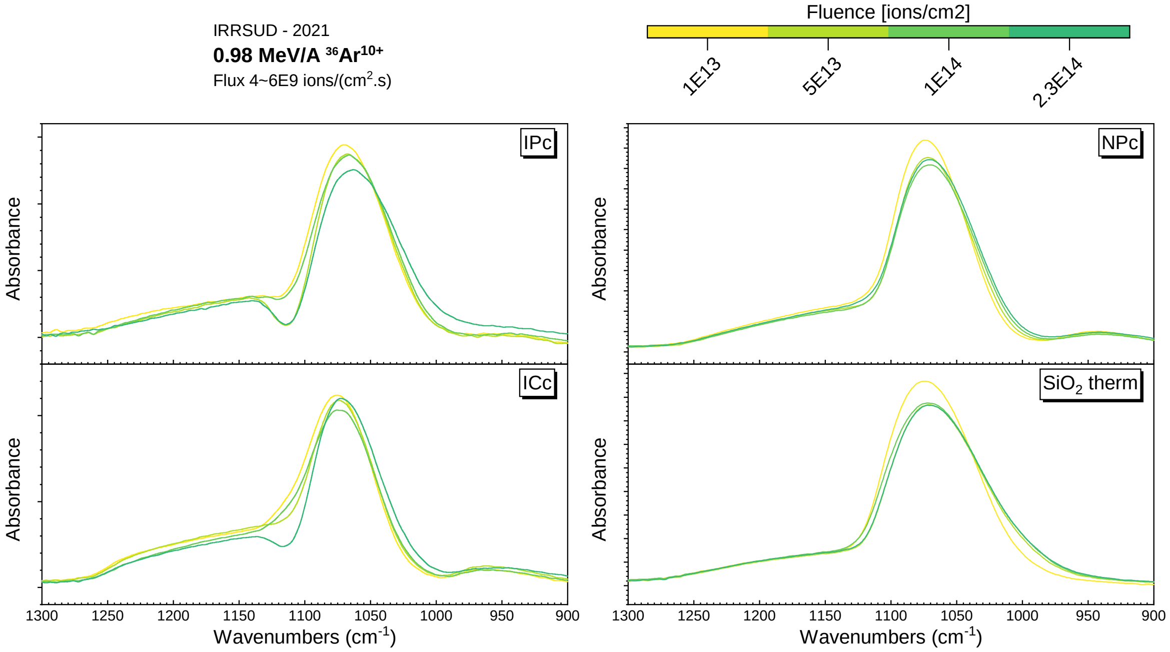

FIGURE 3.34: The IR band related to TO mode from raw infrared spectrum as a function of the fluence

Nickel beam irradiation

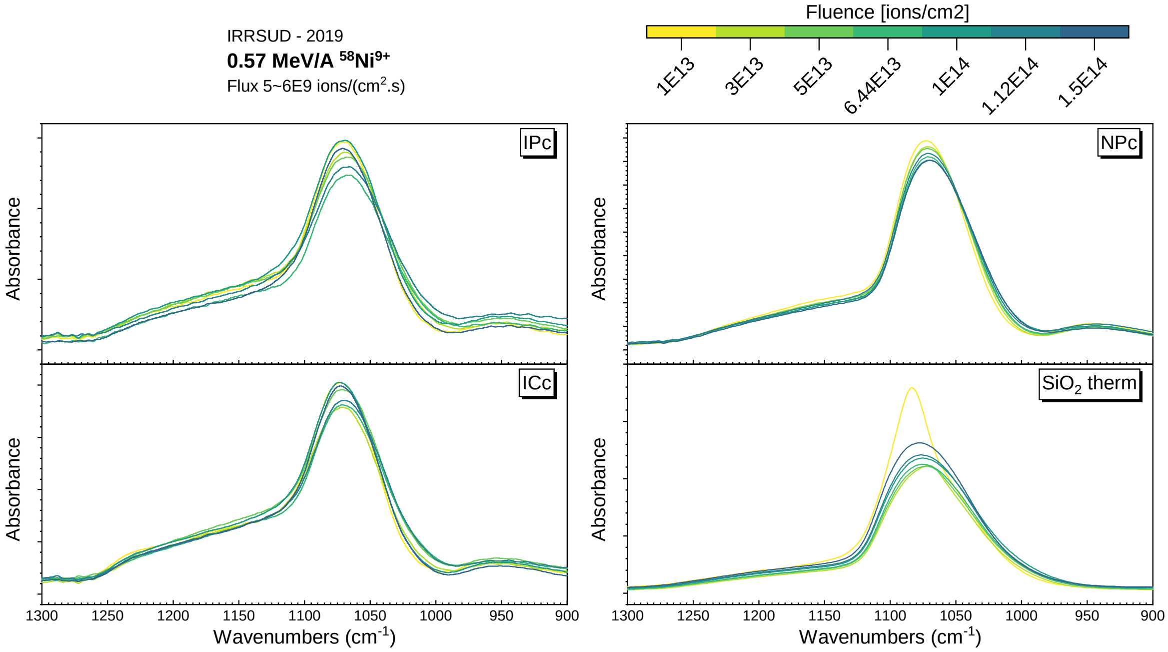

FIGURE 3.35: The IR band related to TO mode from raw infrared spectrum as a function of the fluence

Note: Similar to the experimental XRR results, the results of nickel beam irradiation is rather peculiar. In particular, for SiO_2 therm, the peak in the IR spectrum TO_3 is abnormal. Thus, this experimental result should be treated with caution before any repeated experiments.

Krypton beam irradiation

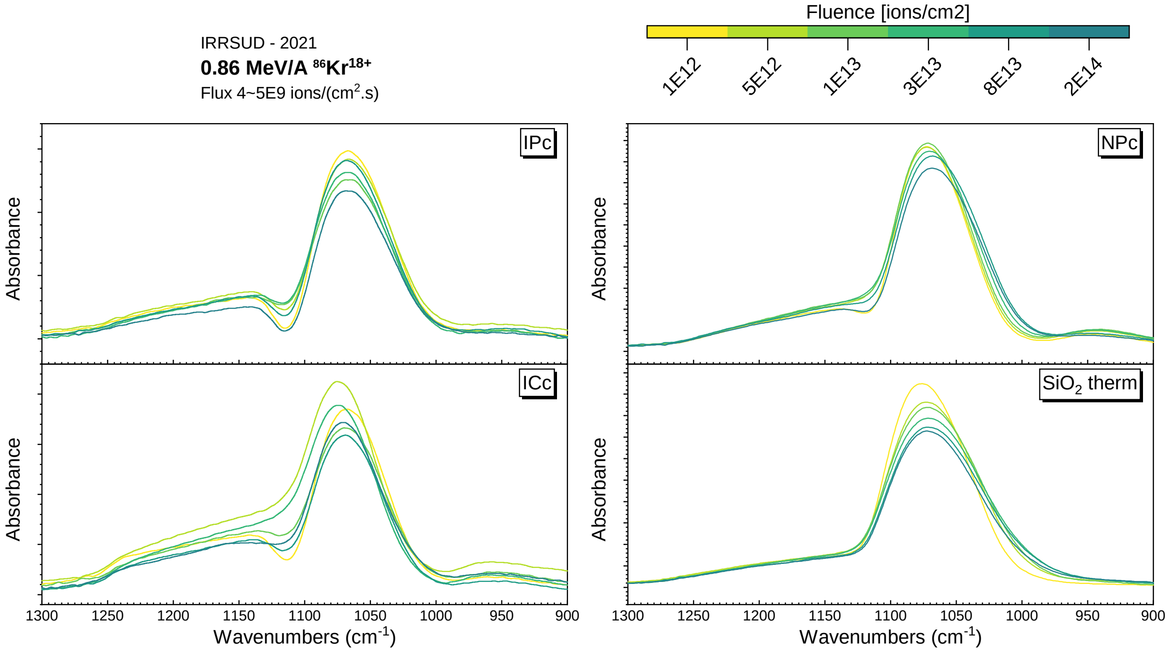

FIGURE 3.36: The IR band related to TO mode from raw infrared spectrum as a function of the fluence

Xenon beam irradiation

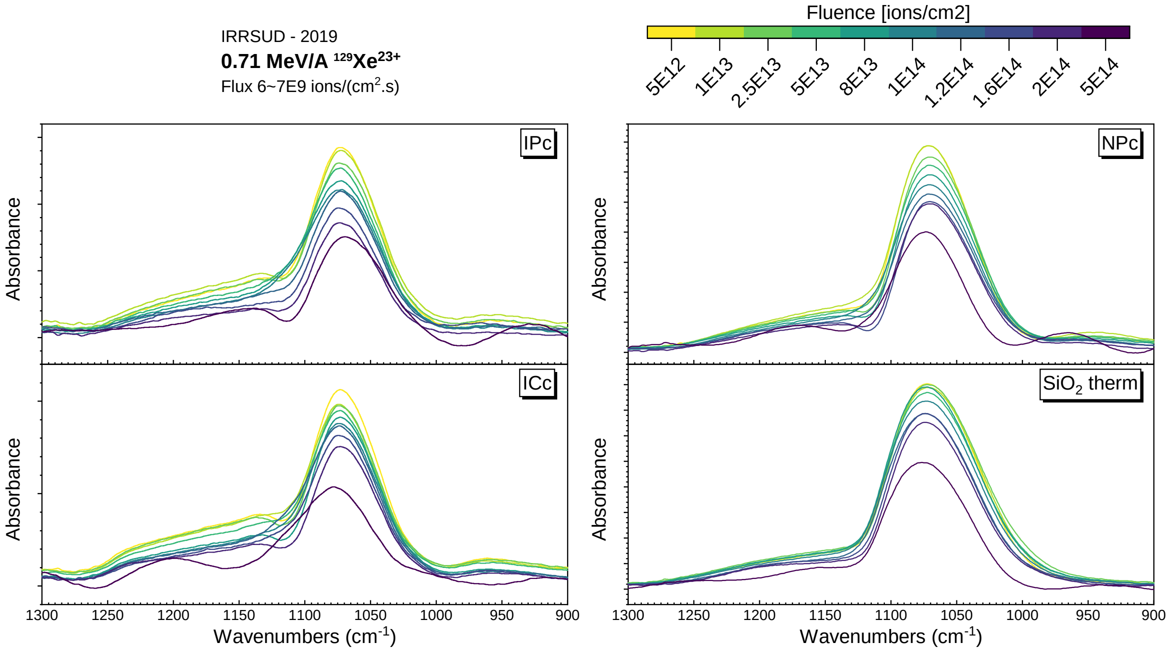

FIGURE 3.37: The IR band related to TO mode from raw infrared spectrum as a function of the fluence

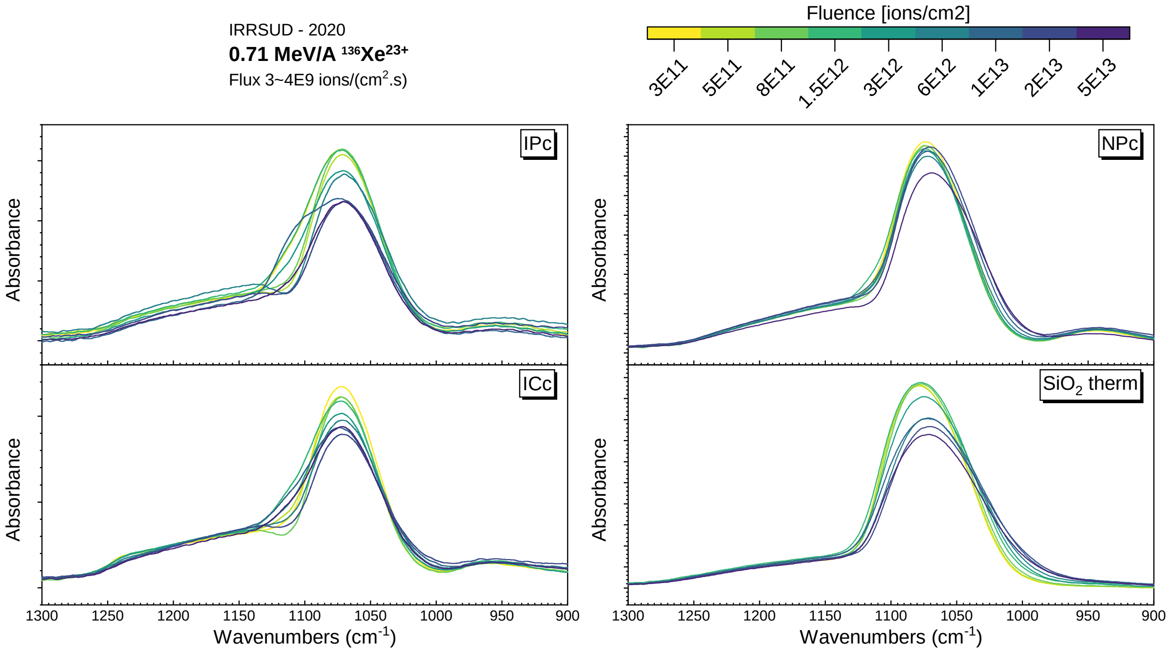

FIGURE 3.38: The IR band related to TO mode from raw infrared spectrum as a function of the fluence

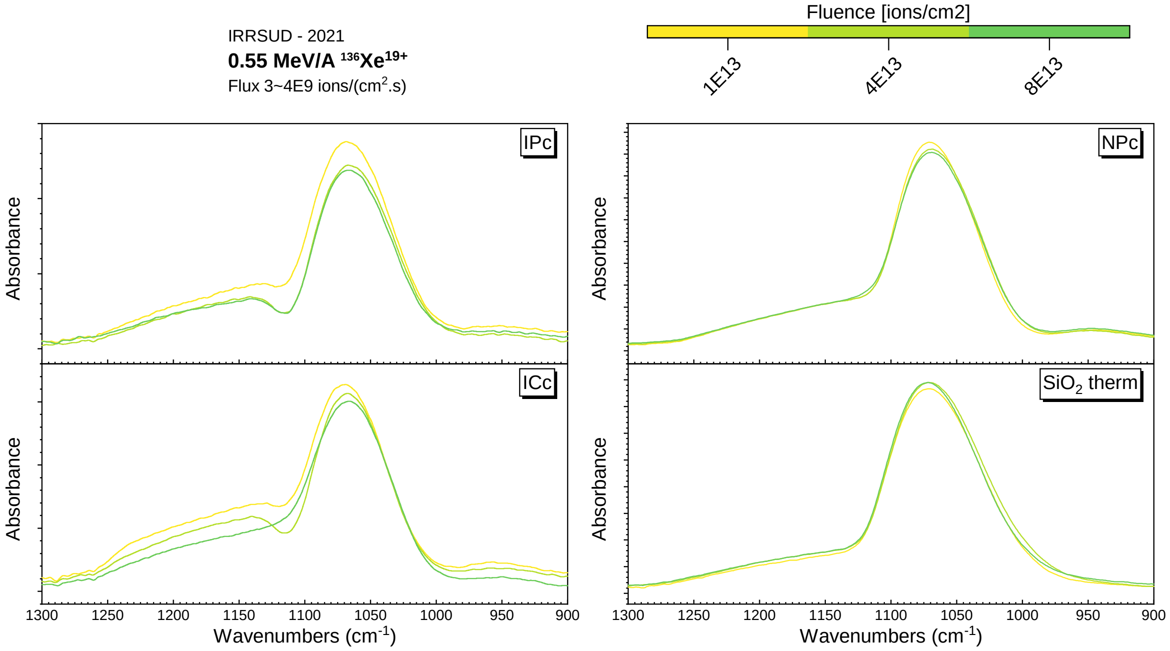

FIGURE 3.39: The IR band related to TO mode from raw infrared spectrum as a function of the fluence

Note: The results from the last three points from IR spectra of Xe 2019 irradiation are not meaningful, since when combined with the XRR data, the irradiated SiO_2 layer has been severely damaged and has ended up losing material, and it is questionable about a substance is residual or not on the irradiated side of silicon wafer.

3.3.2.d Frequency shift: observation and discussion

Awazu[115] (figure 3.40) and Rotaru *et al.*[113] (figure 3.41) previously demonstrated that the evolution of the absorption bands reveals the existence of a displacement limit towards lower wave number values, referred to as saturation. They show that when thermal silica is irradiated, the damage is saturated at a wave number of 1044 cm^{-1}. This position is independent of the incident ion for energies around 1-2 MeV/u.

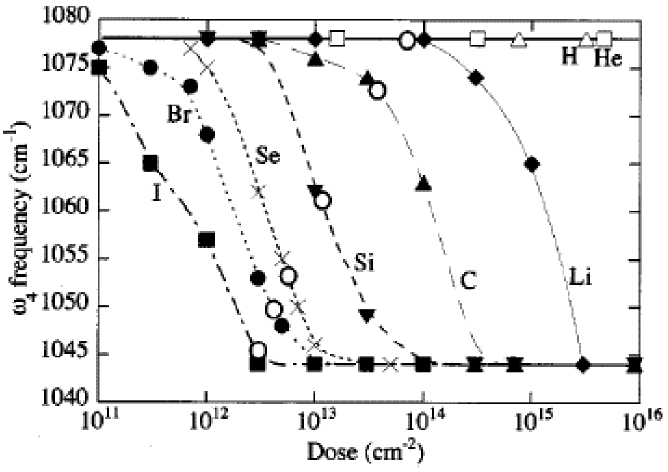

FIGURE 3.40: Frequency at an absorption maximum of the ω_4 band against dose. Figure extracted from ref [115]

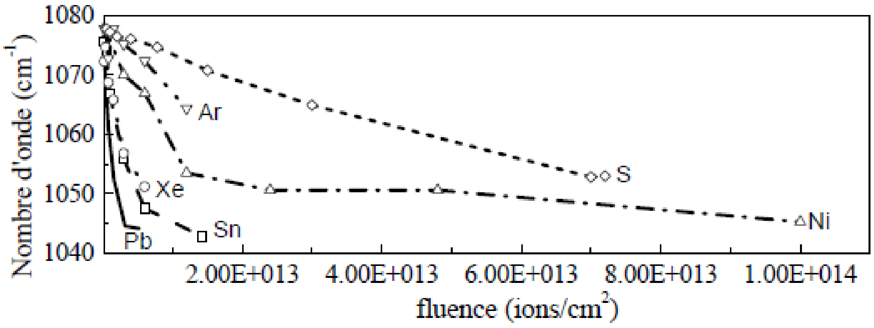

FIGURE 3.41: Frequency at an absorption maximum of the TO band against dose. Figure extracted from ref [113]

This limit was not seen to be attained in our investigation. The frequency displacement, on the other hand, is just about 10 cm^{-1} (figure 3.42). This is explained by the fact that, as previously stated, the IR spectra we examined always contain a contribution from a pristine silica layer, making it impossible to directly obtain this saturation threshold.

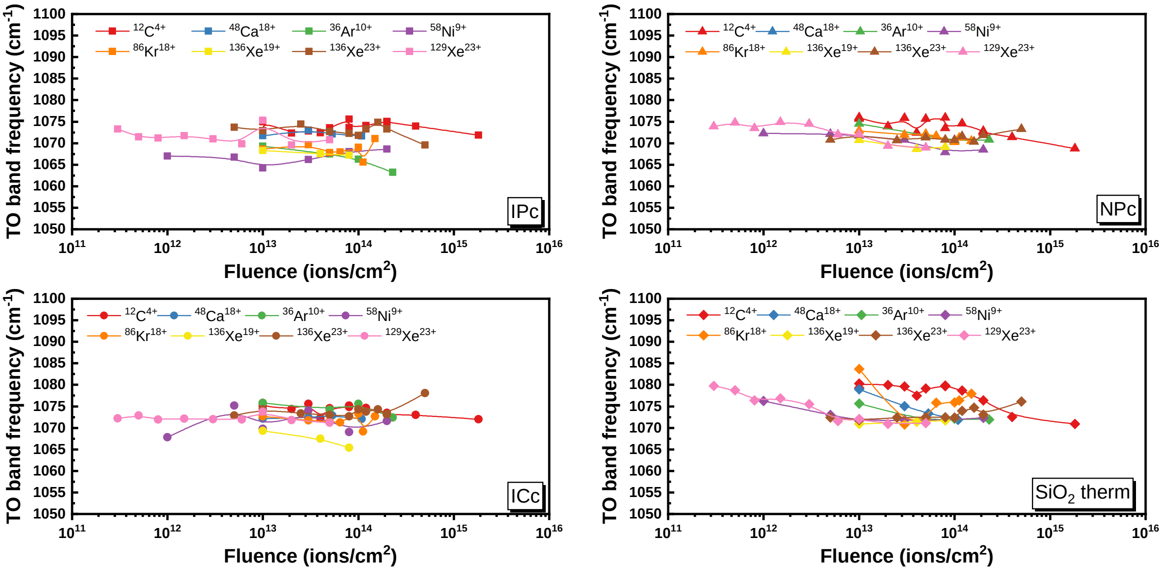

FIGURE 3.42: Frequency at an absorption maximum of the TO band against dose for SHI irradaition in this study.

In fact, according to the theory of Benyagoub *et al.*[116], the passage of an ion in a virgin zone produces a maximum damage. That is to say, "the passage of an ion across a zone that has already been traversed does not result in additional damage." The transformation of the material following the irradiation is done by the passage from the non-irradiated phase to the irradiated phase. This alteration was noticed when neutrons were used for irradiation[117]. We will assign for each of these two "phases" a position for the TO_3 vibration mode (Transverse Optical vibration of Si-O bonds in silica's tetrahedral elementary lattice).

From this point on, the previously measured TO_3 bands can be considered a combination of two peaks, one "pristine" and one "irradiated". This enables us to deconvolute the peaks and hence analyze the effects of irradiation quantitatively. The TO_3 peaks will be processed as indicated in the figure 3.43, a third peak will be added to the "shoulder position" approximately 1170 ± 20 cm^{-1} to represent other vibration modes that we are not interested in (TO_4 and LO vibrations). And eventually a fourth peak will also be added at about 950 ± 20 cm^{-1} to represent other vibration modes due to Si-OH in the case of sol-gel synthesized thin films (IPc, ICc and NPc).

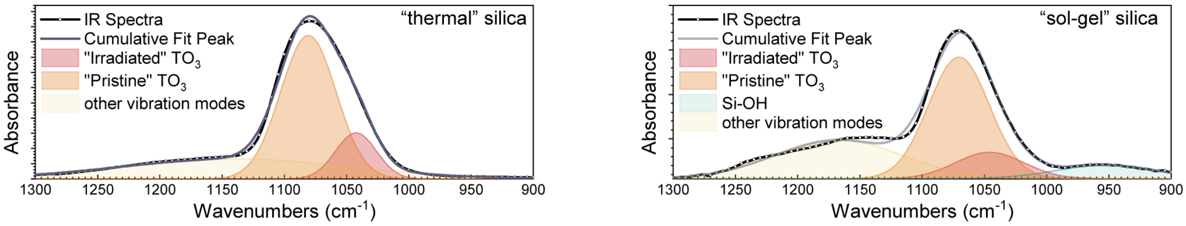

FIGURE 3.43: Schematic representation of the decomposition of the TO peak

The final stage is to determine the locations of the "pristine" and "irradiated" TO_3 peaks of thin film materials independently.

To accomplish the aim of identifying the position of unirradiated peaks, we measured 31 unirradiated samples of each material separately and then calculate the averaged wavenumbers of the TO_3 peaks. The calculation is performed with Origin Pro software. The IR spectra of "pristine" samples, which will not contain the "irradiated" peak, are deconvoluted mathematically with gaussian functions, the results are shown in the table 3.5.

TABLE 3.5: Summary of the properties of pristine TO_3 peaks

	Pristine TO_3 position [cm^{-1}]	Pristine TO_3 FWHM [cm^{-1}]
IPc	1069.5±0.2	66.9±0.7
ICc	1070.6±0.2	58.3±0.8
NPc	1067.2±0.7	68.4±0.7
SiO_2 therm	1075.8±0.3	71.5±0.8

We can note that for the three silica thin films synthesized by the sol gel method, the position of the TO_3 peak has a smaller value of wavenumber than the thermally grown silica thin films, which is reasonable considering the difference of the highest processing temperature encountered during their synthesis. The values obtained for "SiO_2 therm" are quite close to those published in the literature (1076 cm^{-1} [118], 1073 cm^{-1} [113], 1078 cm^{-1} [83]).

The location of the irradiated TO_3 peak, on the other hand, is not immediately apparent. The following methodology will be applied.

First, we will focus on the group that received the highest dose for each irradiation (except for the Xenon-2019 irradiation group for which we will use the 4th maximum dose for the reasons mentioned before). Their IR spectra will be mathematically fitted, with the position and FWHM of the pristine TO_3 peak fixed using the value calculated above (table 3.5) but the peak height permitted to change. The position of the "shoulder position" peak will be allowed to move within the range given above (950 ± 20 cm^{-1} and 1170 ± 20 cm^{-1}). The position and FWHM of the post-irradiation peak will not be fixed, and they will be deduced from the mathematical best-fit of the software.

In the second step, we plot the position of irradiated TO_3 peak versus S_e. If we observe that the position of this TO_3 peak is approximately the same at different maximum doses, as reported by Awazu *et al.* (fiture 3.40), we may estimate the theoretical value of the irradiated TO_3 peak.

Based on this method, we plotted the position of the "irradiated" TO_3 peak at the maximum dose for different ion irradiation (figure 3.44). We can see that this method is feasible for the two non-porous thin film silica materials (NPc and SiO_2 therm). Except for the experimental results of SiO_2 therm under Ni beam bombardment which deviates far from the other experiments. As we have mentioned before in the XRR results, this data will not be taken into account. We can reasonably assume that at the maximum dose of the experiment, the side that was bombarded by the particles reached a saturated state of damage. The fitted "saturated" position of the TO_3 peak after irradiation of NPc and SiO_2 therm is 1023.4 ± 3.1 cm^{-1} and 1037.7 ± 4.0 cm^{-1}. The infrared peak shift (~40 cm^{-1}) is in good agreement with that reported in the literature. [83, 110, 111]

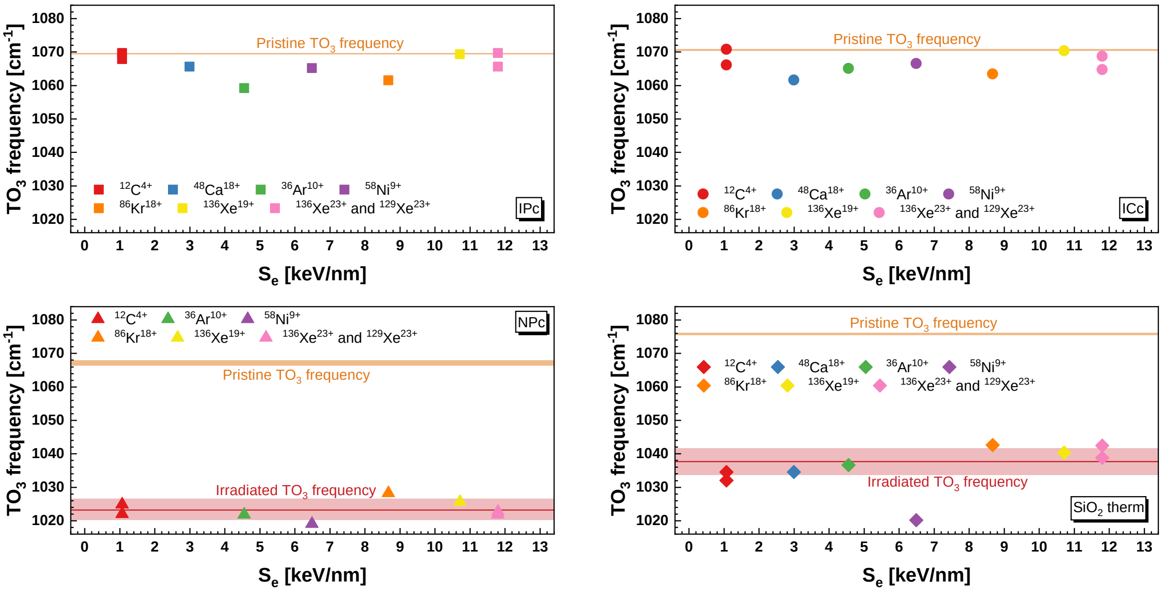

FIGURE 3.44: The final position of the "irradiated" TO$_3$ peak at the maximum dose under different ion irradiations. Data from Ni irradiation for SiO$_2$ therm will be excluded from the subsequent discussion for statistical reasons.

The fitted infrared TO$_3$ peak frequencies for the two porous thin film silica materials (IPc and ICc) are close to the pristine value, which may be interpreted mathematically as a splitting of the Gaussian peak. That is, chemically speaking, the values are meaningless, as there are no discernible distinctions between the pristine and irradiated states. Despite this, we can state qualitatively that porous materials suffer far less damage than non-porous materials under our experimental settings.

3.3.2.e Irradiated TO$_3$ area

Once the position of the irradiated TO$_3$ peak has been found (for NPc and SiO$_2$ therm), we may deconvolve the IR spectra of the samples at each dose and furthermore conduct the calculation of cross-section. This section will provide a rapid explanation of the fundamentals of theory.

In an infrared spectrum, if we define $I_0(\omega)$ and $I(\omega)$ be the intensities recorded respectively without and with sample, in the case where the IR transmission beam is perpendicular to the sample, δ be the optical path traveled by a photon in the sample of thickness L and refractive index n. We can define the absorbance $A(\omega)$ and absorption $\alpha(\omega)$ by:

$$A(\omega) = -\log\left[\frac{I(\omega)}{I_0(\omega)}\right]$$

$$\alpha(\omega) = -\frac{1}{\delta}\ln\left[\frac{I(\omega)}{I_0(\omega)}\right] = \frac{2.3A(\omega)}{\delta}$$

A vibrational transition results in an absorption band on the infrared spectrum. The volume concentration of oscillators N [cm-3], is related to the absorption by the relation [119]:

$$N = \frac{1}{\Gamma} \int\limits_{\omega} \frac{\alpha(\omega)\mathrm{d}\omega}{\omega}$$

where the integral is performed on a domain around the average frequency of the absorption band. Γ is the average absorption strength associated with the vibrational transition. For a symmetric absorption band (as in the case of a Gaussian) the concentration of oscillators is written:

$$N = \frac{1}{\Gamma} \int\limits_{\omega} \frac{\alpha(\omega)\mathrm{d}\omega}{\omega} \approx \frac{1}{\Gamma\omega} \left(\frac{2.3}{\delta}\right) A_I$$

where A_I is the area of the absorption band. This relation, allows to calculate, the concentration of the oscillators, which vibrate around an average frequency, ω. According to this relation, the number of oscillators N is proportional to the area of the absorption band A_I.

The Marples' equation mentioned before can be rewritten as:

$$\frac{N_{\text{Irr}}}{N_0} = \left(\frac{N_{\text{Irr}}}{N_0}\right)_{\text{sat}} (1 - \exp(-\nu R t))$$

where N_{Irr} is the number of oscillators that corresponds to the new band induced by irradiation.

The following equation can be further deduced:

$$A_I = (A_I)_{\text{sat}} (1 - \exp(-\sigma\Phi))$$

where A_I is the area of the absorption band induced by irradiation at such a fluence, $(A_I)_{\text{sat}}$ is the area of the absorption band induced by irradiation in the case of a complete damage of the target.

Due to the fact that our IR tests are not in situ, we cannot use the absolute area of the irradiated TO_3 peak to estimate the damage cross section. Instead, we may use the % of this area, which is similar to a homogenization step to compensate for the differences in between samples.

The increase of the peak area for the irradiated TO_3 peak for NPc and SiO_2 therm is shown in figure 3.45 as a function of ion fluence. A saturation level is reached for SiO_2 therm under high fluence radiation. At high fluences, the saturation level of the peak area remains at a relatively low level (~35% of the overall band area). This is due to the IR absorption in the unirradiated vitreous SiO_2 on the back side of the sample. As for the NPc samples, no saturation level has been detected with the current fluence. It is worth noting that when the S_e of the incident particles rises, the irradiated TO_3 area grows faster with fluence.

By comparing the two non-porous silica, the radiation induced damage (increase of the irradiated TO_3 peak area) to the sol-gel silica occurs at a higher fluence and is also smaller. This indicates that the silica synthesized by this method has a certain degree of irradiation resistance.

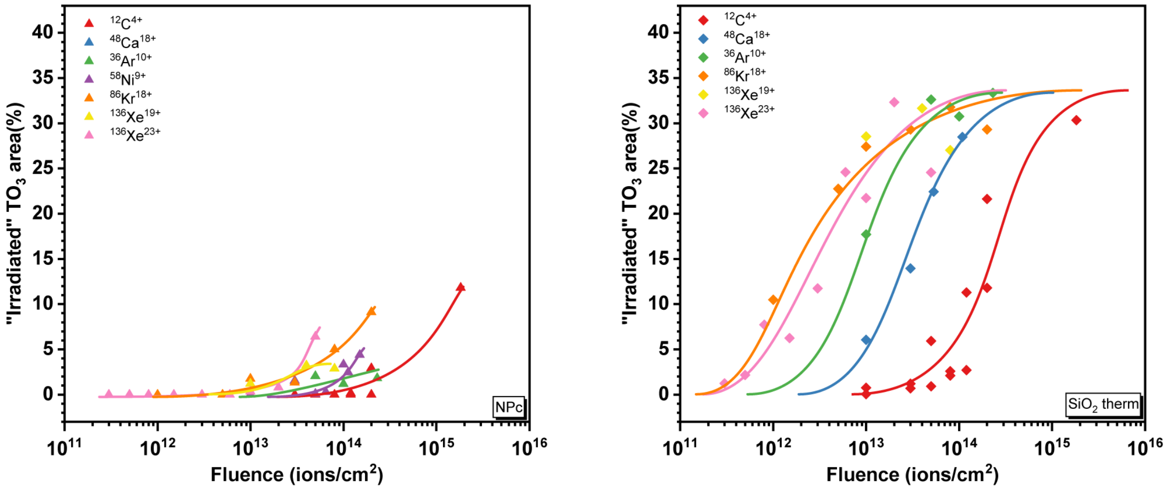

FIGURE 3.45: The area of the irradiated TO_3 absorption band as a function of the fluence. All lines are a guide for the eyes.

3.3.2.f Calculation of cross-section

The evolution of the peak area as a function of fluence ($\sigma\Phi$) in SiO_2 therm, as shown by the data points in figure 3.45(right), is fitted using the marples method. The probability for an incident ion to impact the virgin part of the silica network with a cross section σ is calculated. The fitting results and the resulting cross section are plotted in the figure 3.46 and figure 3.47, respectively.

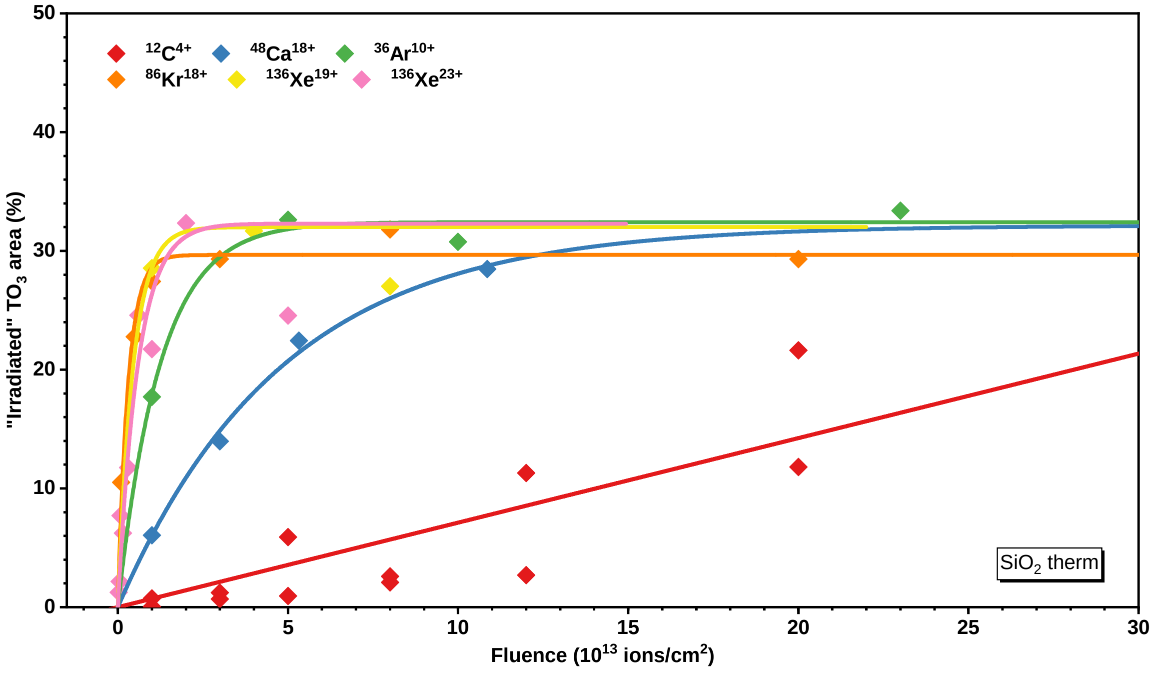

FIGURE 3.46: Fit of Marples' equation to area of irradiated TO_3 bands from FTIR Measurement

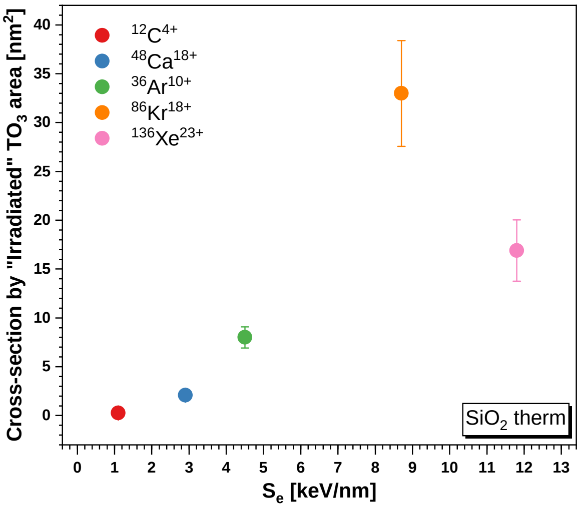

FIGURE 3.47: Cross sections obtained from FT-IR versus electronic stopping power for non-porous thermal silica thin films

The related radii calculated with a cylindrical geometry for the ion track are summarized in table 3.6. Results are in good agreement with the value reported by Rotaru[113] except for the case of Xe irradiation. It is necessary to proceed with caution while studying the results of Xe irradiations in this scenario since the SiO_2 thin film may be destroyed as a consequence of sputtering and other effects caused by the bombardment of Xe particles. Alternatively, if the amount of native silica remaining is insufficient, our above series of operations on data processing, which is an attempt to remove the unaffected silica on the back side, may have an impact on the results, resulting in an underestimation of the value of radii.

TABLE 3.6: Radius deduced from the damage cross section

Ion	Ion energy MeV/A	S_e keV/nm	Radii nm
$^{12}C^{4+}$	0.98	1.1	0.3 ± 0.1
$^{48}Ca^{18+}$	9.17	2.9	0.8 ± 0.1
$^{36}Ar^{10+}$	0.98	4.5	1.6 ± 0.2
$^{86}Kr^{18+}$	0.86	8.7	3.2 ± 0.5
$^{136}Xe^{23+}$	0.71	11.8	2.3 ± 0.4

3.4 Conclusion

In this chapter, we have investigated the influence of swift heavy ion beam irradiation on porous SiO_2 thin films in electronic energy deposition up to $2x10^{22}$ keV/cm^3 under different conditions. Data treatment of pre-/post-irradiation X-ray reflectivity (XRR) characterizations reveals that there has been a marked decrease of film thickness with increasing energy deposition. The trend is stopping power dependent.By monitoring the interlayer thickness of the porous silica thin film during the low irradiation dose stage, we determined that the damage radius of IPc and

ICc grew from 0.1 nm to about 0.8 nm as S_e increased from about 1 keV/nm to 12 keV/nm. According to FT-IR measurements, the damage radius in thermosynthesized nonporous silica rises with increasing S_e from 0.3 nm to around 3 nm under the same irradiation conditions. Globally, the chance of an incident ion altering non-porous silica is less than that of dense silica when the irradiation dose is insufficient to totally destroy the pore structure; in other words, the presence of the pore structure imposes on the silica a certain irradiation tolerance. The infrared observation of the TO_3 peak shifting in the silica network also supports this conclusion. The displacement of the TO_3 peak is more dramatic in thermosynthesized silica than gol-gel synthesized silica. In porous silica, on the other hand, this change is very modest and barely noticeable. In conclusion, we may state that under the same particle bombardment, irradiation-induced damage follows the following rules:

$$SiO_2\, therm > NPc \gg ICc \approx IPc$$

Furthermore, a shift in the TO_3 peak from around 1070 to 1040 cm^{-1} would indicate a decrease in the Si-O-Si bond angle. One explanation for the considerable reduction in bond angle is the transition from six-membered rings to planar three-membered rings[115]. This transition is said to be related to the process that a-SiO_2 is reaching equilibrium at a high temperature and then being swiftly quenched to room temperature[120]. This phenomenon can be explained by the thermal spike model, which predicts that energy is thermalized rapidly and locally, resulting in short but extremely high temperatures along the ion track. We will attempt to apply this model in the next chapter to explain the behavior of silica thin films exposed to irradiation.

In addition to this, we can conclude that the silica of the pore wall does not experience the isotropic shrinkage effect discussed in section 1.2.5.b since we do not witness a significant shift in the TO_3 bands of the infrared spectrum in porous silica, which is proportional to the silica density [110], and even if this effect did occur, we believe that it would result in contraction of the pore wall rather than shrinkage of the pore volume.

We cannot, however, totally rule out the possibility of the hammering effect presented in section 1.2.5.a. In fact, if we look at the cross-section of the sample in FIB/TEM (figure 3.48), we can observe that, when exposed to ionizing radiation, the circular pores transform into elliptical shapes. Although it appears as the whole thin film sample has been hammered, additional investigation into this phenomena is necessary to fully comprehend. As previously stated, the hammering effect has only been seen in non-porous materials, i.e. in the walls of pores, and not in the pores themselves. When the pore wall is in contact with the particle beam, no significant deformation of the pore wall has been seen in either the front or rear of the particle incident direction. Second, the ion hammering is predicted to occur at $S_e > 2$ keV/nm, but we also found that in our Carbon irradiation studies ($S_e = 1$ keV/nm). If we assume that the shape change is not caused by the FIB process of fabricating the foils, then the shrinkage of the pore and transition from a circle to an ellipse can still be explained by the thermal spike model besides ion hammering, and if we look at the Xe example, we can see that the pore has disappeared and tracks have appeared, which cannot be explained by hammering. Finally, while we cannot rule out the possibility of the hammering effect, we believe that it is not the primary element responsible for the shrinkage or distortion of the pores. In the following chapter, we will use the thermal spike model without assuming the ion hammering to explain our observations.

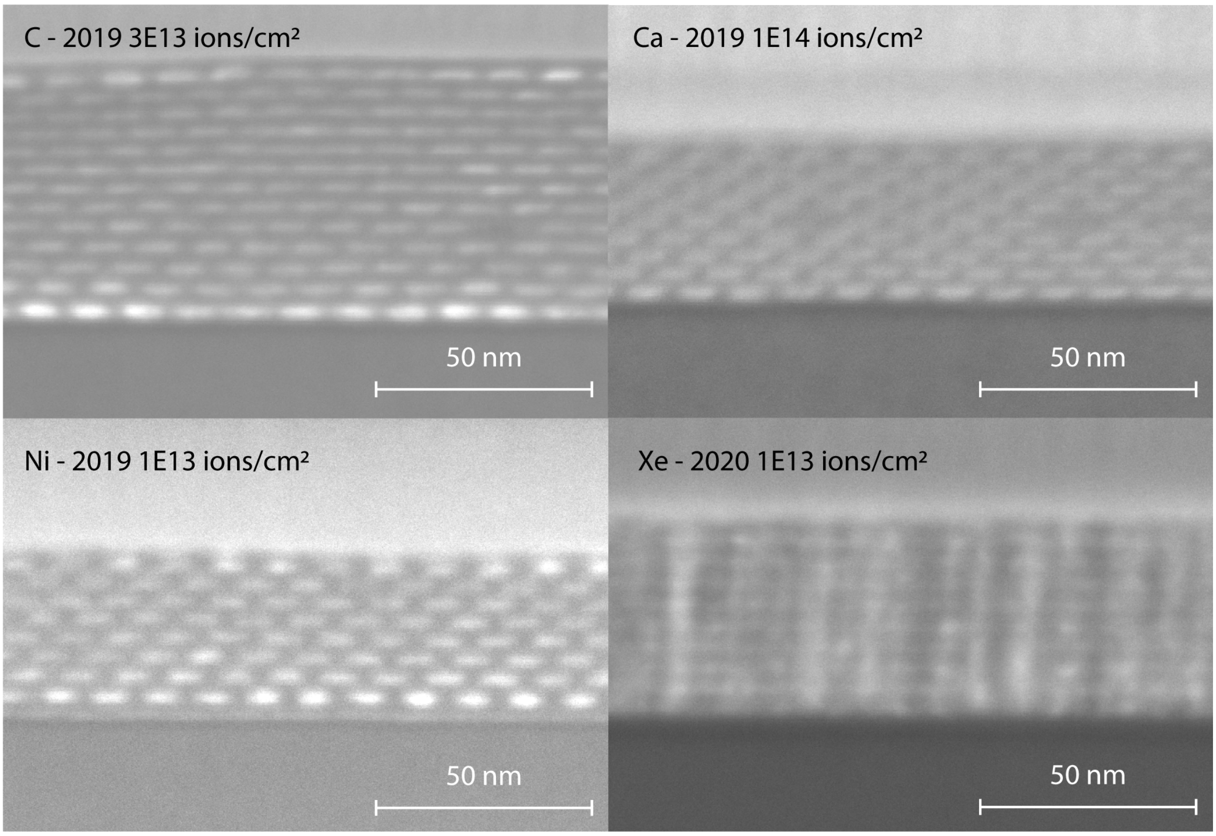

FIGURE 3.48: Cross-sectional view of irradiated samples.

Chapter 4

Application of the inelastic thermal spike model

This chapter will discuss the modeling of mesoporous silicas subjected to irradiation. The purpose of this section is to attempt to explain the phenomena described in this chapter under swift heavy ion (SHI) irradiations.

Regarding electronic effects, to our knowledge there is no study concerning the modeling of mesoporous silica under irradiation. Only several theoretical models have been proposed to explain radiation-induced damage, in particular the appearance of latent tracks in the material caused by the incident ions in the electronic stopping power regime since the early 1950s. Two of the most often referenced models include the coulomb explosion model for insulators proposed by Fleischer *et al.*[121–123] and the thermal spike model, which was first proposed by Dessauer [124] and has since been widely developed and adopted [125–131].

4.1 Coulomb explosion model vs. thermal spike model

This section will provide a brief description of the two models stated above, as well as the reason for choosing the more suitable models for our given system.

The coulomb explosion concept was based on the assumption that an energetic incident ion would form a cylindrical zone of highly ionized matter along its trajectory. A massive explosion occurs within 10^{-15} to 10^{-13} seconds due to the highly repulsive electrostatic forces that exist before electrical neutrality is restored. This process results in the production of a significant disruption of a certain portion of the lattice. However, there is no development of this model that can be used to describe the impact in quantitative terms.

The thermal spike model consists in assuming that the energy of the incident particle is shared between electrons by the electron-electron interaction during the slowing down process. And then it is converted into thermal energy in the subatomic system by electron-phonon coupling. When high electronic excitations and strong electron-phonon coupling occur, it is expected that a high-temperature cylinder will develop along the incident ion trajectory, with a temperature greater than the melting and vaporization temperatures. Chronologically, electronic excitation and ionization are two processes that occur in less than 10^{-16} s after irradiation with energetic ions. The thermalization of energy on electrons takes place in a time of 10^{-15} to 10^{-14} s. The transfer of energy from the electrons to the atoms becomes substantial between 10^{-14} to 10^{-12} s, depending on the coupling between the two systems. After 100 ps, this region cools and returns to room temperature in a phase distinct from the original, resulting in the production of a latent track. [124, 128, 132].

This approach has been backed by a growing number of research throughout the years. Sigrist and Balzer [133] have shown that, for insulators, the electronic stopping power threshold as inferred from chemical etching of numerous insulators has a strong association with the thermal conductivity of the insulators. Furthermore, velocity measurements of ejected atoms from an insulator [134] confirmed the possibility of the thermal evaporation process.

Furthermore, numerous researchers [84, 108, 116, 135] have demonstrated that the thermal spike model is appropriate for amorphous silica. Current research achievements, particularly the advancement of mathematical description by our colleagues Dufour *et al.* [136] at the CIMAP in CAEN, also facilitate our application. Their work discusses the essential refining of the computation owing to the nature of the materials under consideration, eventually composite films constituted of nanocylinders or nanospheres embedded in an insulating matrix. In our study, we will try to further extend its application in our porous silica system.

4.2 Mathematical description

Mathematically, the inelastic thermal spike model may be formulated by two coupled equations governing the energy diffusion on the electron and lattice subsystem, respectively [130, 137, 138]. The time-dependent thermal transient process is initially expressed in cylindrical geometry as:

Energy diffusion on the electrons:

$$C_e\left(T_e\right)\frac{\partial T_e}{\partial t}=\nabla\left(K_e\nabla T_e\right)-g\left(T_e-T_a\right)+A_e(r,t)$$

Energy diffusion on the atoms:

$$C_a\left(T_a\right)\frac{\partial T_a}{\partial t}=\nabla\left(K_a\nabla T_a\right)+g\left(T_e-T_a\right)+A_a(r,t)$$

where T_e, T_a are the temperature for the electronic and atomic systems respectively; K_e and K_a are the thermal conductivity for the electronic and atomic systems respectively; C_e and C_a are the specific heat for the electronic and atomic systems respectively; g the electron-phonon coupling constant; and $A_{e,a}(r,t)$ the energy density deposited by the incident ion at time t and at radius r. Here, $A_a(r,t)$ can be ignored since $\frac{S_n}{S_e}<10^{-2}$ in our experimental condition.

The form of the first spatial energy deposition, $D(r)$, is determined by the distribution proposed by Waligorski *et al.*[139] and is dependent on the beam energy. As previously proposed by Meftah *et al.*[140], $A_e(r,t)$ can be calculated as

$$A_e(r,t)=C\cdot D(r)\alpha e^{-\alpha t}$$

where $\alpha=1/\pi$ and C is a normalizing constant, so that:

$$\int_{t=0}^{\infty}\int_{r=0}^{r=r_m}A_e(r,t)2\pi r\,drdt=(\mathrm{dE/dx})_e$$

with r_m the maximum projected range for electrons perpendicularly to the ion path.

Later, in the study of Dufour *et al.* [136], a first real 3D version of the model is proposed, in which every physical parameter depends on the position $\overrightarrow{r}(x, y, z)$ in space. Heat transfer processes are redescribed on a three-dimensional scale. An energy variation dQ of an elementary volume dV characterized by a specific heat C is defined as $dQ = C\ dT$, where dT is the temperature variation. The energy brought by the incident ion on the electrons is written as $A_e\left(\overrightarrow{r}, t\right)$ and the thermal conductivities K_e and K_a are written as a 3×3 matrix. The Fick's thermal diffusion law defines the heat flux in a 3D space as $\overrightarrow{j} = \overline{\overline{K}} \cdot \nabla T$. The electron-phonon coupling constant is also rewritten as $g\left(\overrightarrow{r}, t\right)$.

Therefore, the two coupled equations describe the inelastic thermal spike model become:

$$C_e\left(T_e\right)\frac{\partial T_e}{\partial t} = \nabla\left(\overline{\overline{K_e}}\nabla T_e\right) - g\left(\overrightarrow{r}, t\right)\left(T_e - T_a\right) + A_e\left(\overrightarrow{r}, t\right)$$

$$C_a\left(T_a\right)\frac{\partial T_a}{\partial t} = \nabla\left(\overline{\overline{K_a}}\nabla T_a\right) + g\left(\overrightarrow{r}, t\right)\left(T_e - T_a\right) + A_a\left(\overrightarrow{r}, t\right)$$

The energy disposition of the incident particles in some complex systems (nanocylinders or nanospheres embedded in an insulating matrix) is no longer a simple cylindrical shape. Dufour *et al.*, [136] refined the Waligorski's equations and successfully described the incident ions energy deposition in three-dimensional space. The detailed approach will be shown in the appendix E.

4.3 Application of the model to silica thin films

4.3.1 Physical parameters used for the simulation

As shown in the equation, K_e, C_e and g are essential parameters, however, in the case of amorphous silica, which is an insulator, those parameters are unknown. Consequently, the following drastic approximations are made based on the theory of Baranov *et al.*[141]. They suggested that hot electrons in the conduction band of an insulator will behave like hot electrons in a metal, leading to an electronic diffusivity of $D_e \sim 2\, cm^2.s^{-1}$ and $C_e \sim 1\ J.cm^{-3}.K^{-1}$ [142–144]. The electronic thermal conductivity K_e is then deduced from the product of the thermal diffusivity and the specific heat $(K_e = D_e \cdot C_e)$.

The electron-phonon coupling constant g is also likewise unknown for semiconductors and insulators; thus, it must be derived or estimated. Physically, g is linked to the electron-phonon interaction mean time τ_a by the relation $g = C_e/\tau_a$ and to mean energy diffusion length λ of the deposited energy by the relation $\lambda^2 = D_e\tau_a$. Therefore, we can obtain the following equation:

$$g = \frac{K_e}{\lambda^2}$$

These values have been considered independent of temperature in the simulations of Awazu *et al.*[145]. However, in the three-dimensional model presented by Dufour, they contended that such an approach is viable only when the temperature surpasses the bandgap $E_g = k_B T_g$. For thermally grown amorphous SiO_2 films, a bandgap of 9.3 eV was measured by Weinberg *et al.*[146], leading to $T_g \approx 10^5$ K. At $T_e < T_g$ It is necessary to take into consideration the fact that only a fraction of atoms get ionized. A linear law for both $C_e\left(T_e\right)$ and $K_e\left(T_e\right)$ at $T_e < T_g$ (See figures 4.1) has been adopted.

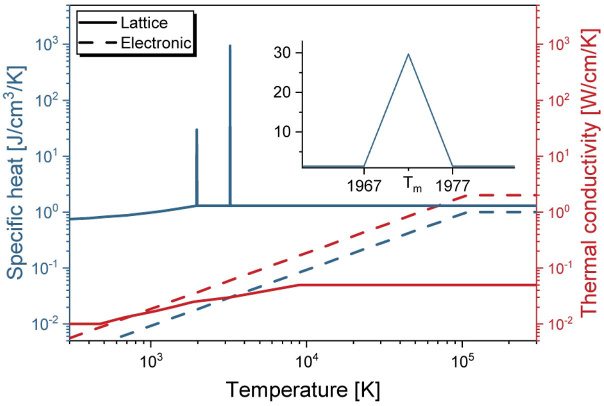

FIGURE 4.1: Electronic (in dotted lines) and atomic (in solid lines) specific heats (blue) and thermal conductivities (red) of SiO_2 as a function of temperature

Therefore, the mean energy diffusion length λ will be the only free parameter in the present calculation. And for amorphous silica, this value can be fitted from experimental results of the track radius. The mean energy diffusion length λ for a-SiO_2 is around 2.5 nm[100]. It was obtained from the results of Busch *et al.* [147] and Benyagoub *et al.*[116].

The two-coupled equations are numerically solved by taking into consideration the temperature dependency of the lattice thermodynamical parameters as well as the solid-liquid phase change. The lattice specific heat C_a and thermal conductivity K_a values are a compilation of data from references [148–151]. The temperature dependence of C_a and K_a are plotted in figure 4.1.

In the event of phase transition, the following procedure is used to account for the latent heat Q_m. For solid-liquid phase transitions occurring at T_a, and for temperatures in the range between $T_m - \Delta T$ and $T_m + \Delta T$, the temperature dependency $C_a\left(T_a\right)$ is adjusted by adding a peak-like function $C_m\left(T_a\right)$ which ensures that $\int_{T_m-\Delta T}^{T_m+\Delta T} C_m(T)dT = Q_m$. (figure 4.1, here $\Delta T = 5\ K$ for melting point). This approach keeps the lattice temperature almost constant during melting as the value of C_a increases towards the melting point. For temperature around the boiling point, $C_a\left(T_a\right)$ is also modified in a similar manner with $\Delta T = 15\ K$.

4.3.2 Geometrical parameters used for the simulation

The FIB/STEM images of the porous silica thin film (See Chapter 3) reveal a cylindrical pore structure for IPc. We then create a simplified representation of the computational box based on this. As seen in the figure, the box is cubic in shape and has a side length of 200 Å. It is composed of seven cylindrical pores that are parallel to the XY-plane. The pores have a diameter of 50 Å, a wall thickness of 10 Å, and a p2mm structure, as specified previously. For the purpose of simplicity, we calculate these pores as though they are filled with air rather than with vacuum. However, we specify here that the incident particles can only interact with silica and cannot be slowed down or lose energy as a result of the presence of air. The Appendix F contains information about the physical properties of air (we used the parameters that come with the program). The basic unit of computation is $dx = dy = dz = 2\mathring{A}$. The incident ion is assumed to reach the target parallel to the z-axis at (x_0, y_0) in the XY-plane (figure 4.2).

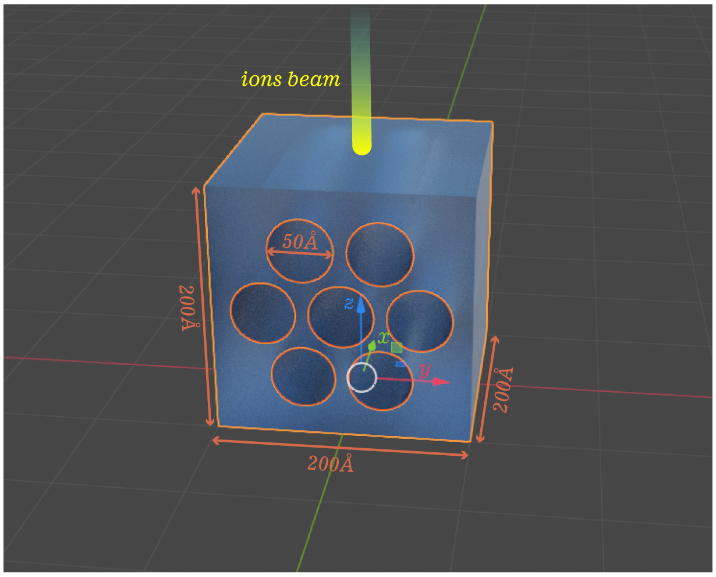

FIGURE 4.2: Schematic diagram of the geometric parameters of the simulated box

4.3.3 Simulation setup

The following table 4.1 summarizes the incident particle parameters and positions used for our simulations. Incident beam coordinates of (0,0) indicate that the incident beam is focused with the pore in the middle of the calculation box; and incident beam coordinates of (0,-15) indicate that the incident beam does not pass through the pore center.

TABLE 4.1: Simulated irradiation conditions

Ion	Ion energy MeV/A	S_e keV / nm	Incident beam coordinates (x_0, y_0)	Thin film structure
$^{12}C^{4+}$	0.98	1.1	(0,0)	Porous
$^{48}Ca^{18+}$	9.17	2.9	(0,0)	Porous
$^{58}Ni^{9+}$	0.57	6.5	(0,0)	Porous
$^{136}Xe^{23+}$	0.71	11.8	(0,0)	Porous
$^{136}Xe^{23+}$	0.71	11.8	(0,-15)	Porous
$^{136}Xe^{23+}$	0.71	11.8	(0,0)	Non-porous

4.4 Results and discussions

According to the 3DTS (3-Dimensional Thermal Spike model), particle bombardment leads to a change in the electronic and lattice temperature. The temperature of the lattice is shown against time in the graphs below. The program's original output is a three-dimensional temperature matrix, but for the sake of clarity, we've displayed a slice of the YZ-plane at x = 0. In addition, we do not display the temperature at all recorded times, but rather merely a subset of those that were recorded (1×10^{-16} s, 2×10^{-15} s, 5×10^{-15} s, 1×10^{-14} s, 2×10^{-14} s, 5×10^{-14} s, 1×10^{-13} s, 2×10^{-13} s, 3×10^{-13} s, 4×10^{-13} s, 5×10^{-13} s, ...).

4.4.1 Temperature profile over time

Figures 4.3 - 4.8 show temperature change over time. When the incident particles come into touch with the material, the temperature of the silica on the trajectory begins to rise gradually over time, followed by a steady rise in temperature of the pore wall close to the trajectory. It is observed that at a given instant, silica temperatures on paths close to the pore are somewhat lower than those far from the pore. As the S_e of the incident particles rises, the temperature of the silica increases more rapidly (see figure 4.3 - 4.6). Furthermore, when we compare the two cases with and without pores (figure 4.6 and 4.8), we can see that the existence of pores increases slightly the range of temperature fluctuations induced by particle bombardment , but the maximum temperature that may be attained within the same range has been lowered.

We may compare the effects of particle beam contact site in figures 4.6 and 4.7. There is minimal difference between the two situations of different incident beam coordinates at the cases of Xe. In fact, the main difference is not caused by a difference in the relative positions of the incident particle trajectory and the pore center; the temperature change is approximately the same when the incident particle trajectory and the pore center are at the same distance. In the real situation, the porous silica thin films feature considerably more than seven pores and several porous sub-layers, therefore the relative position of the incident beam and one pore has negligible impact.

12 MeV Carbon - Centered bombardment

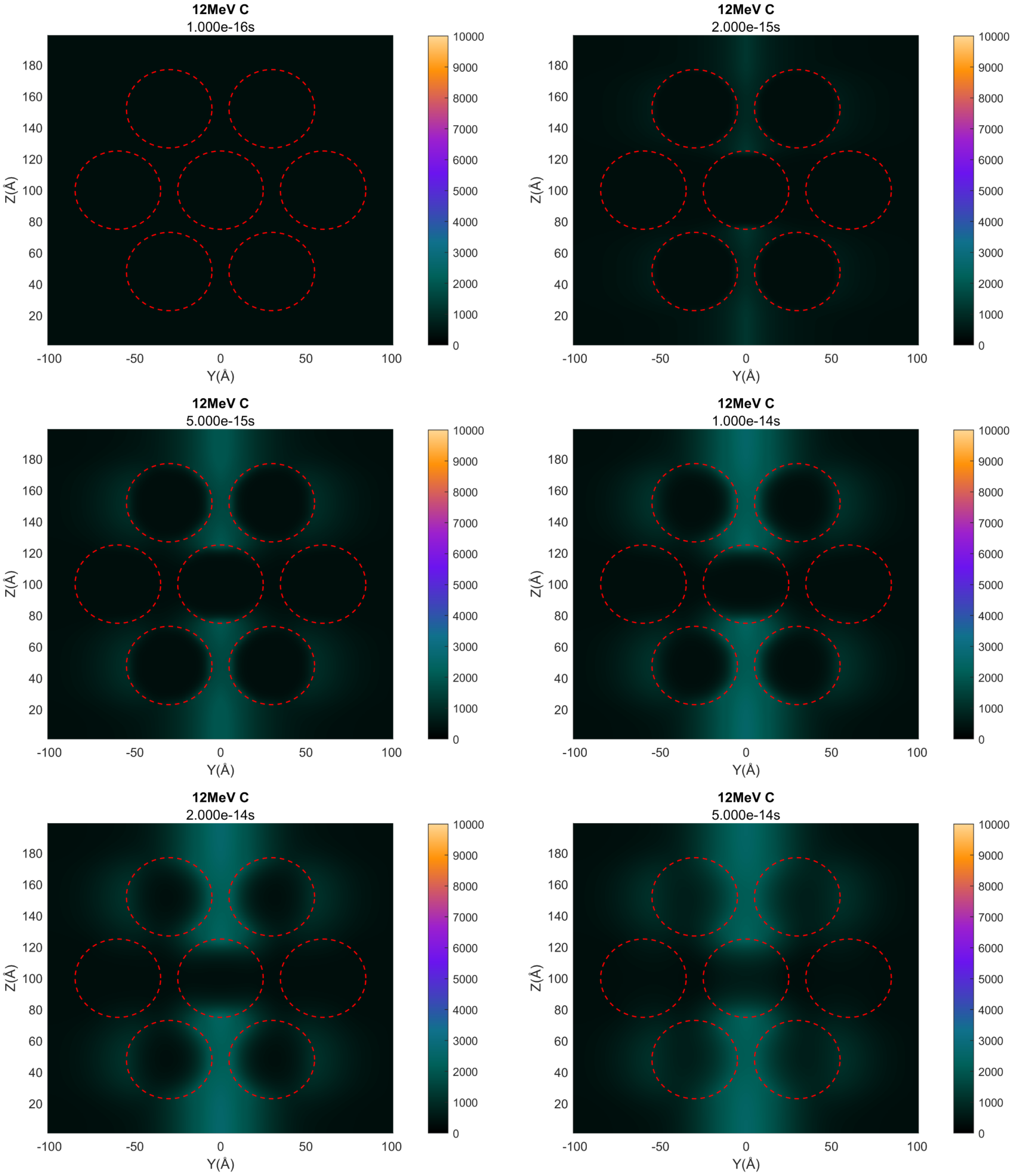

FIGURE 4.3: Slices illustrate the YZ-plane's temperature(K) variation over time at X=0

412.8 MeV Calcium - Centered bombardment

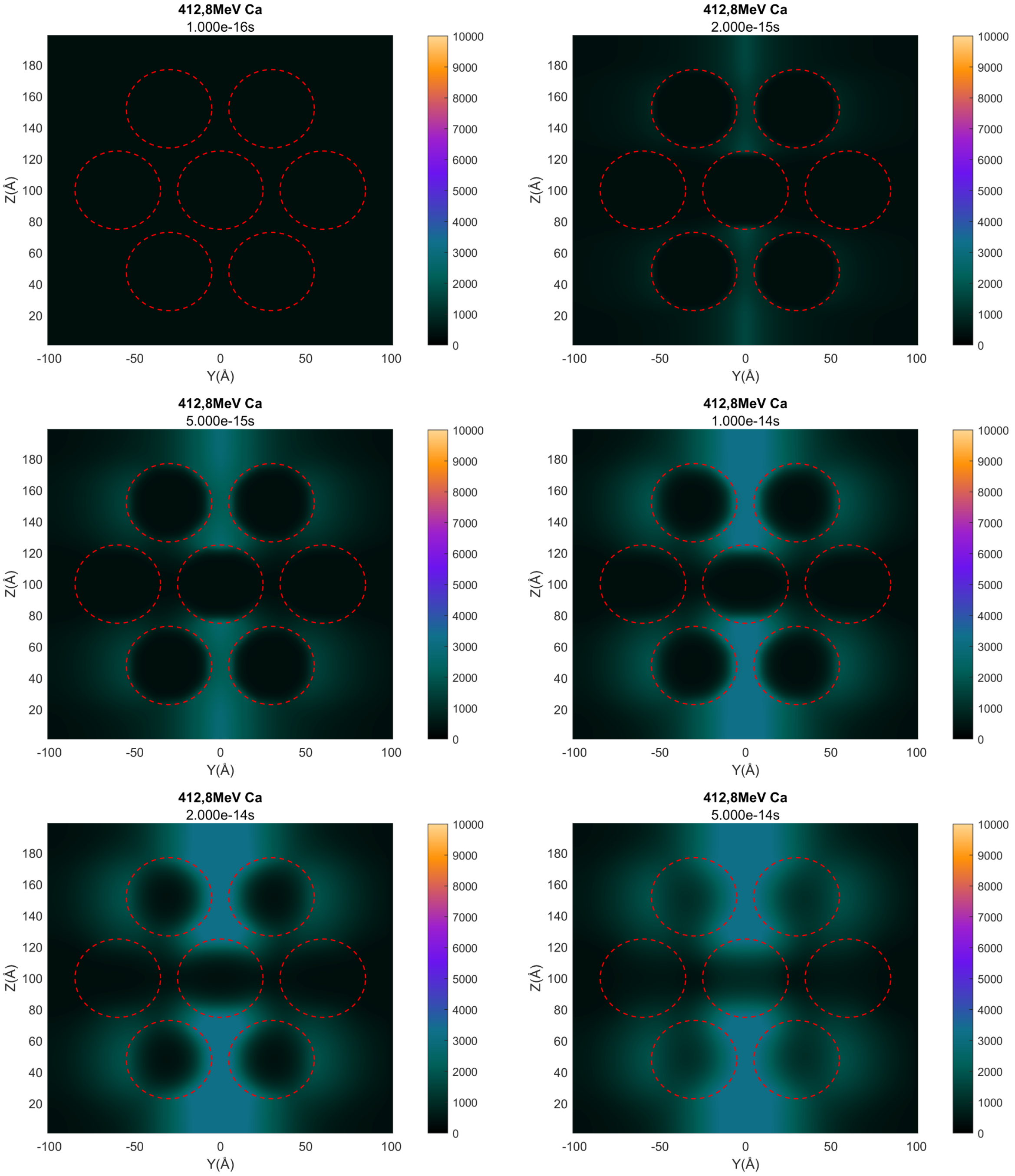

FIGURE 4.4: Slices illustrate the YZ-plane's temperature(K) variation over time at X=0

33 MeV Nickel - Centered bombardment

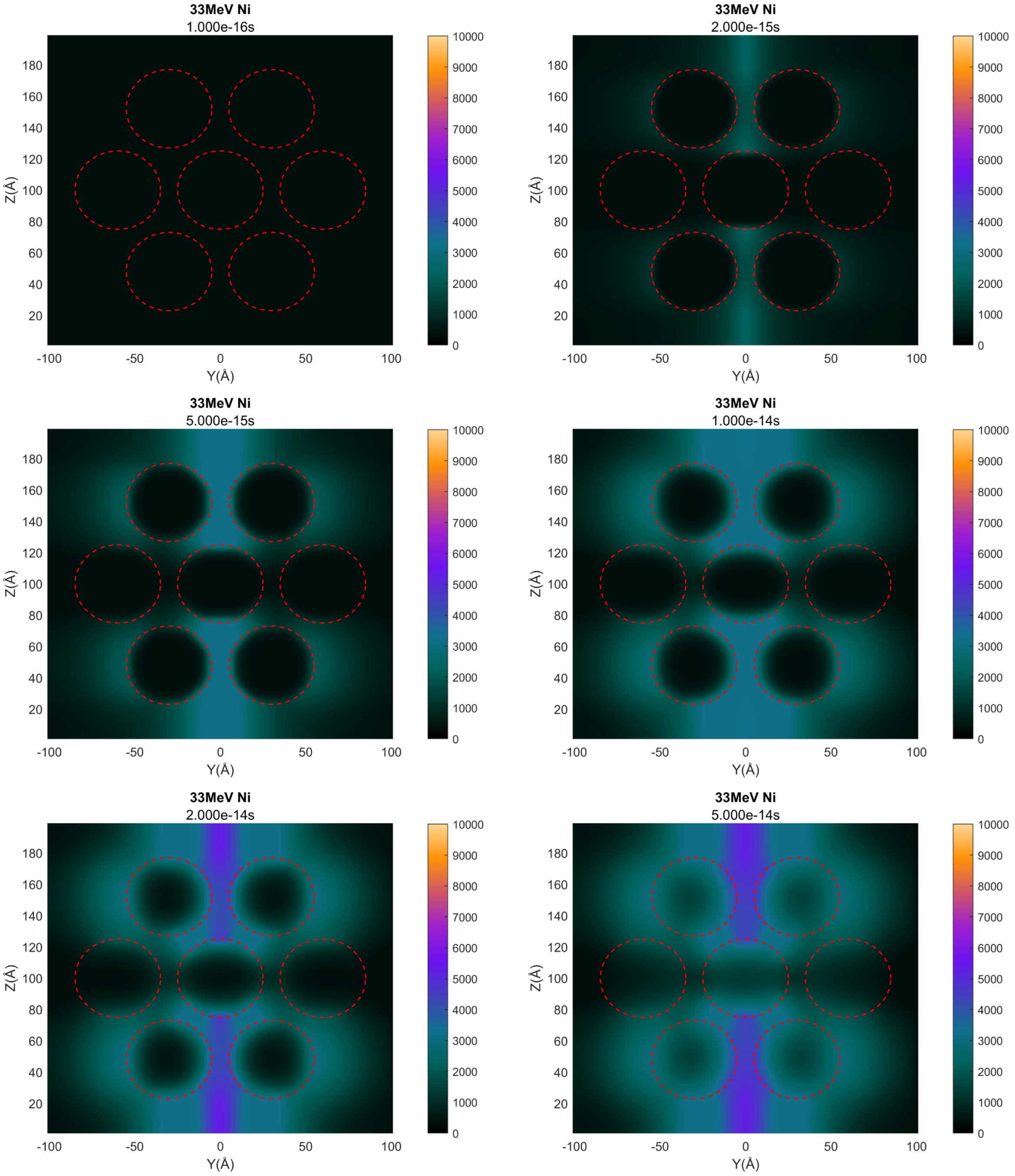

FIGURE 4.5: Slices illustrate the YZ-plane's temperature(K) variation over time at X=0

92 MeV Xenon - Centered bombardment

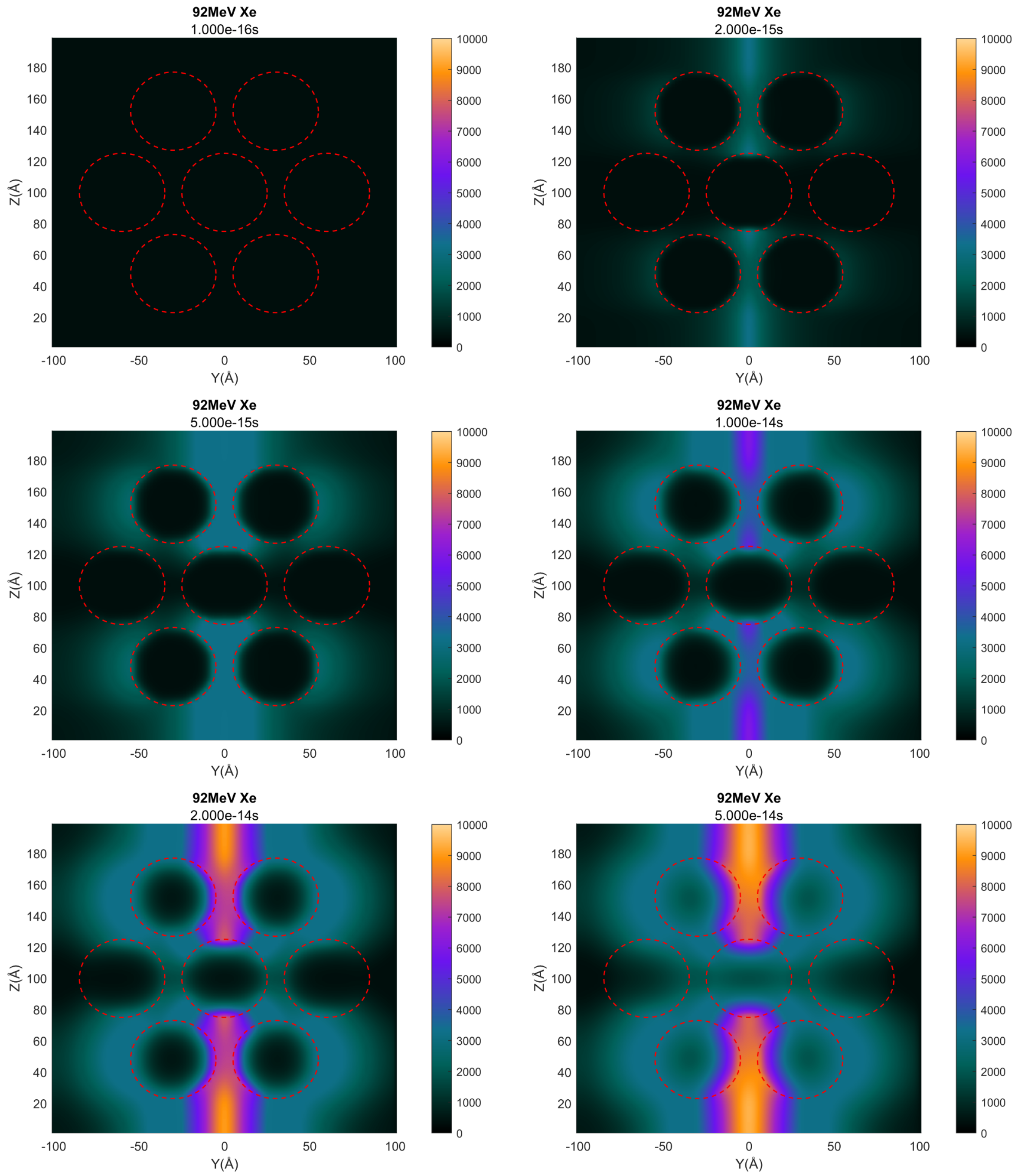

FIGURE 4.6: Slices illustrate the YZ-plane's temperature(K) variation over time at X=0

92 MeV Xenon – Non-Centered bombardment

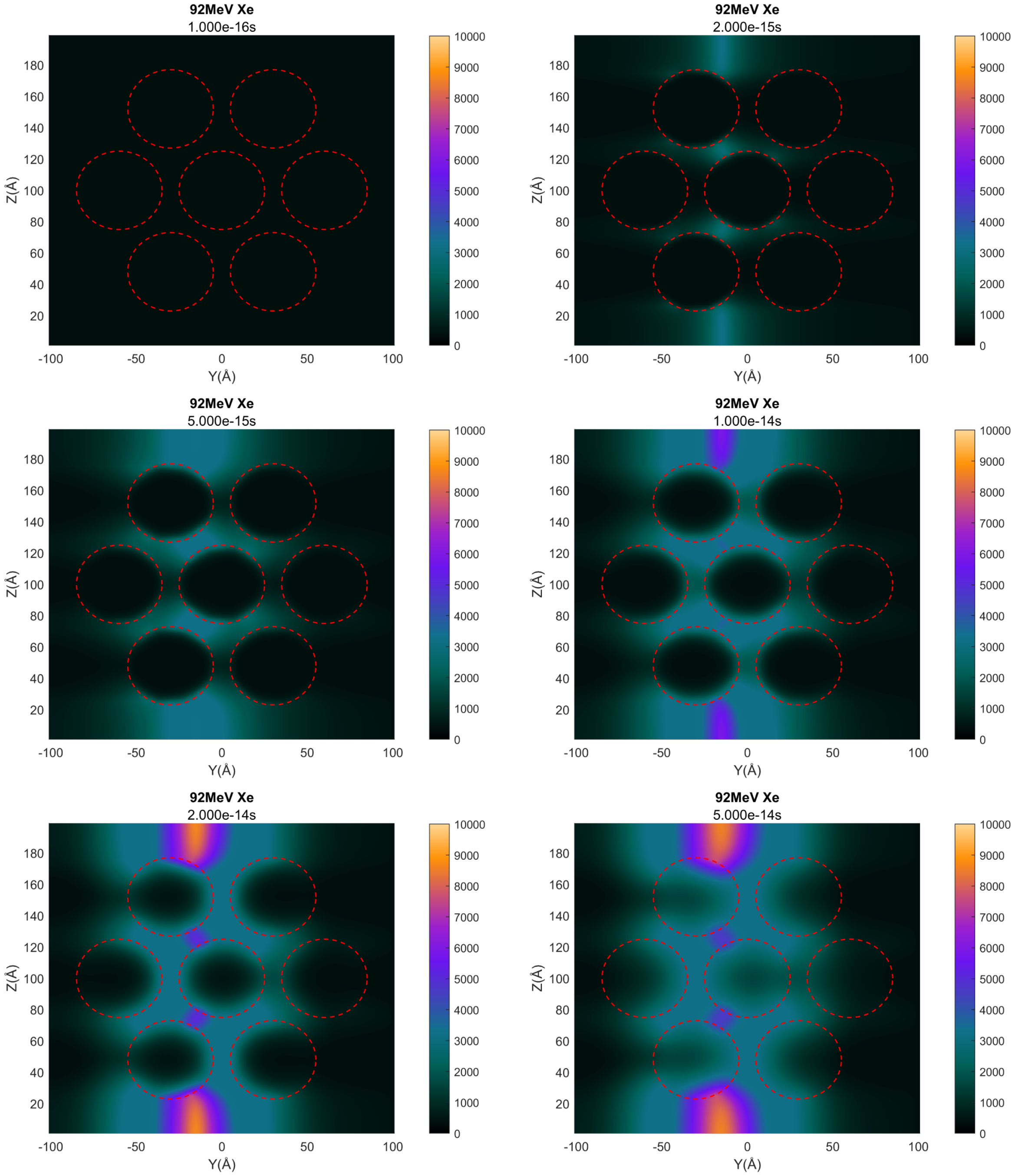

FIGURE 4.7: Slices illustrate the YZ-plane's temperature(K) variation over time at X=0

92 MeV Xenon – Non-porous

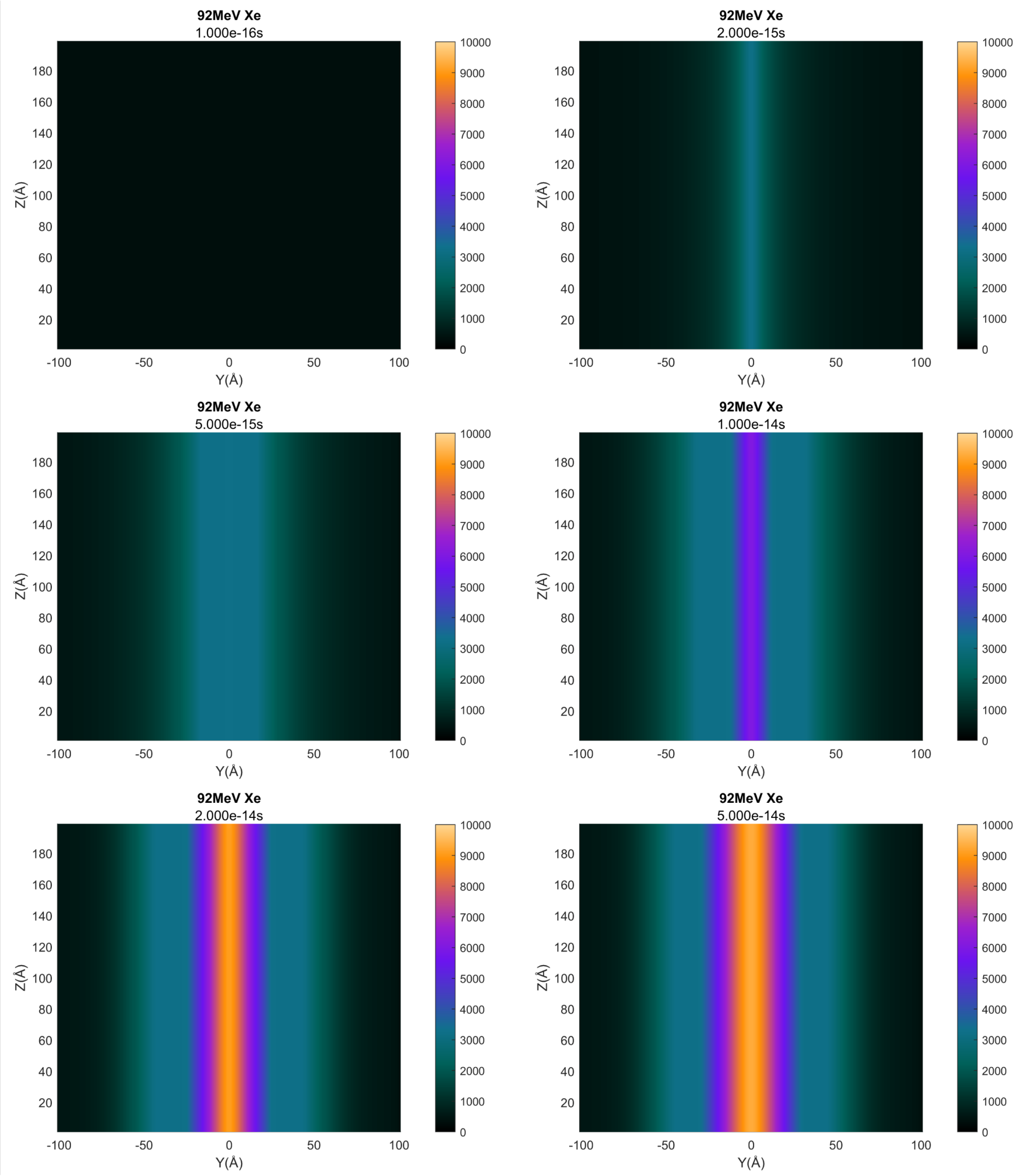

FIGURE 4.8: Slices illustrate the YZ-plane's temperature(K) variation over time at X=0

4.4.2 Electron and atom temperatures versus time

There are several pieces of information worth to be discussed from the temperature evolution, the first of which is the time scale during which the temperature of the assaulted matter changes. In this part, we will only concentrate on the five cases with incident beam coordinates of (0, 0).

Here, we pick a single location from the calculation boxes to monitor the silica wall temperature near the pores. Using the point at coordinates (0,0,130) in the path of the incident particle as indicated in the figure 4.9 on the right, we were able to draw a graph of the electron temperature and atomic temperature recorded at this position as a function of time, which helped to comprehend the situation.

Although we do not simulate many pores, since the region around the ion's trajectory is more or less in touch with pores, the presence of pores greatly lowers the maximum temperature to which the material is subjected compared to non-porous materials.

Furthermore, we can see that, when it comes to the temperature of the pore wall, the higher the S_e value, the higher the temperature that may be obtained.

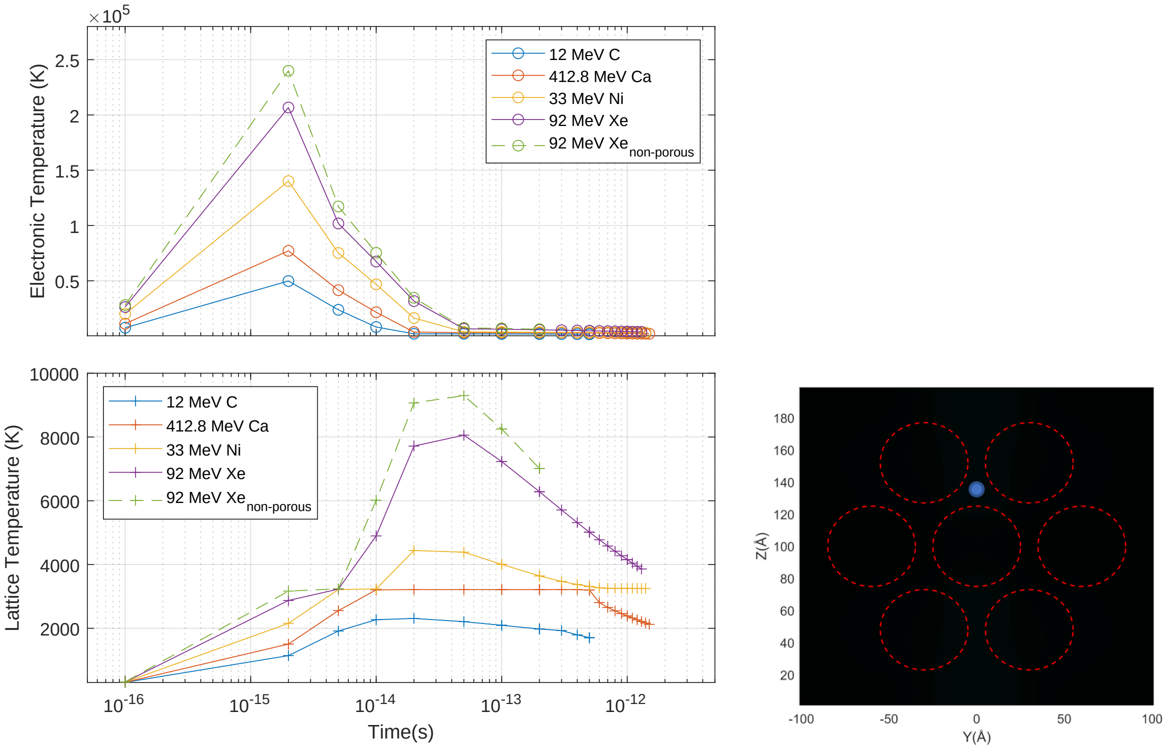

FIGURE 4.9: Electronic temperature (K) and lattice temperature (K) recorded as a function of time (s) in coordinate (0,0,130) (blue point in the figure on the right).

As stated before, thermalization of energy on electrons takes place in a time of 10^{-15} to 10^{-14}s, and the atomic temperature reaches a maximum between 10^{-14} and 10^{-12} s, followed by a somewhat sluggish cooling phase. Indeed, this time period is dependent on the value of mean energy diffusion length λ we selected. Notably, we employed the λ value of thermosynthetic silica owing to the constraints of the available data. We should not be surprised if this value varies between sol gel- and thermo-synthesized silica. Nonetheless, we may do a qualitative analysis of the outcomes based on these findings.

It's vital to remember that these simulations are based on a single particle bombardment. At 10^{-12} s, we can observe that, while the lattice has begun to cool, it is still a long way from returning to its starting temperature (300K). We recall that the particle flow in the real experimental setup is on the order of 10^9 ions/(cm^2.s), and given that the damage cross-section is a few to several tens of nm^2, if we assume that the entire cooling process cannot be completed within the order of 10^4 s. Then, most likely, the same location in the silica will be attacked again. Unfortunately, due to limited arithmetic capacity, we were unable to simulate the system over 10^4 s, but it's reasonable to ignore the possible influence of this factor for the moment.

4.4.3 The maximum temperature recorded for an individual bombardment

To aid in the investigation of the damage process, we plot the highest temperatures measured at each area in the bombarded material (figure 4.10, YZ-plane at x = 0). While these maximum temperatures are not attained simultaneously, they might reflect the strongest influence done by incident particles.

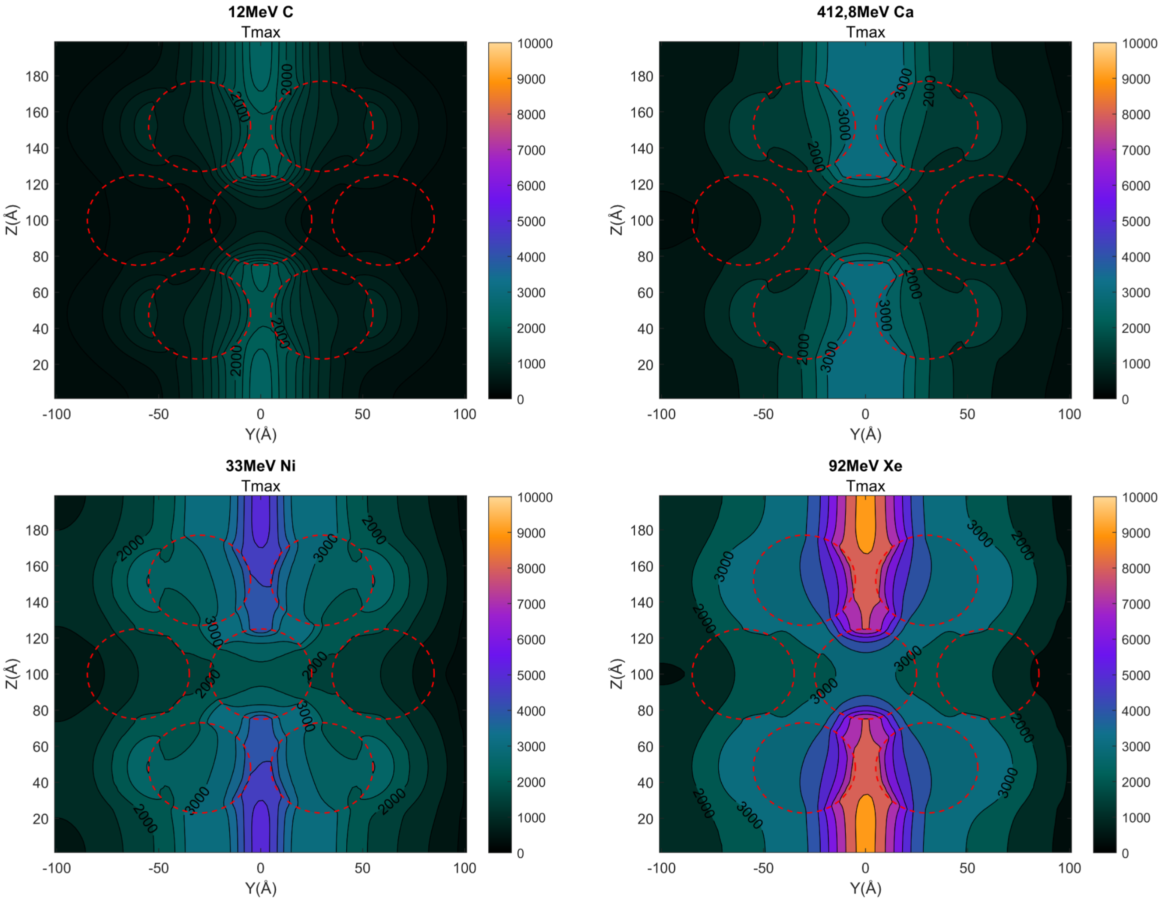

FIGURE 4.10: Highest temperatures recorded of the YZ-plane at X=0

We can observe from the four cases of simulated porous silica that the maximum temperature that the silica atomic subsystem may achieve progressively increases as the electronic stopping power of the incident ions increase. As shown in the figure 4.11, the simulated system may attain a maximum temperature of 2573.5 K when bombarded with 12 MeV C (S_e=1.1 keV/nm), which increases to 3219.4 K, 5326.2 K, and 9405.3 K when bombarded with 412.8 MeV Ca (S_e=2.9 keV/nm), 33 MeV Ni (S_e=6.5 keV/nm), and 92 MeV Xe (S_e=11.8 keV/nm).

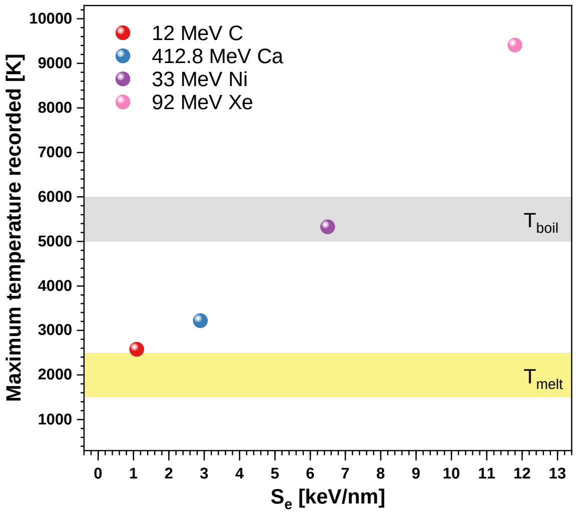

FIGURE 4.11: Maximum temperature (K) recorded in the calculation box as a function of S_e (keV/nm).

This distinction will be explored later in the mechanism discussion and will aid in our comprehension of the empirically observed phenomena described in the earlier sections. Notably, the strong difference between the damage patterns induced by carbon ions and xenon ions.

4.4.4 Insights on the understanding of pore deformation mechanism

In discussing the mechanism of structural changes in porous materials under the effect of irradiation, we would like to highlight Klaumünzer's very illuminating study. Their research focuses on the compaction of nanoporous Vycor glasses when exposed to high-energy ions [17, 18]. Vycor glass is a mesoporous material made mostly of SiO_2 (>96% by mass) and B_2O_3 (3-5%) [149]. Because the B_2O_3 content is so low, it can be called pure amorphous silica.

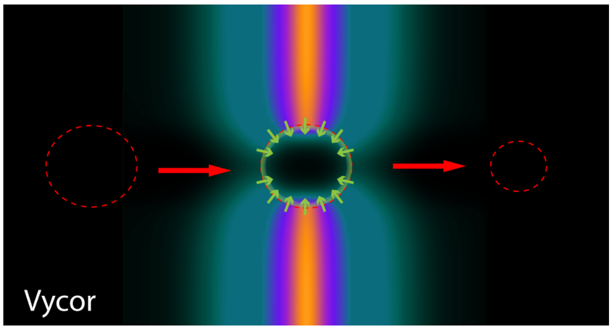

FIGURE 4.12: A simple illustration of Klaumünzer's mechanism regarding pore contraction. The pore in the vycor (SiO_2) is represented by a red dashed line in the figure. Being subjected to high-energy particles, the Vycor can flow into the pore and subsequently freeze (green circle in the figure), causing the pore to gradually shrink.

Klaumünzer's research is predicated on the premise that the fluidic substance in the tracks fills the pores. (See figure 4.12) More precisely, he assumes that the material modified in a track can flow and then freeze due to the transient character of the disruption generated by the ion's passage (a few picoseconds). This process gradually results in the shrinkage of the pores and, eventually, the complete densification of the structure.

We may suggest a potential mechanism of pore shrinking based on his hypothesis and the simulation outcomes. Prior to that, we must establish the track creation criterion. Due to the atoms' rapid heating rate ("superheating scenario"), the equilibrium melting temperature T_m may not be the best parameter to use for determining the energy required to melt the material. This was demonstrated experimentally using femtosecond laser experiments[152], where the temperature rise recorded as a function of the input laser power does not reach a plateau at T_m but continues to climb above T_m. This was also computed by Rethfeld *et al.* [153]: when the heating rate is in the order of 10^{15} K s^{-1}, the temperature permitting the formation of a molten phase is 1.3 times greater than T_m. Luo *et al.*[154] also noted this impact.

In the discussion that follows, we take a rough definition of what we consider to be a case where we can have track formation when the temperature range is between $1.3 \times T_m$ and boiling temperature T_b with $T_m = (2000 \pm 500)$ K and $T_b = (5500 \pm 500)$ K. Furthermore, as proven in research by Meftah *et al.*[148] and Toulemonde *et al.*[155], when $T > T_b$ we believe the sputtering effect to be dominant.

As previously stated in the section 3.3.1.a and illustrated in the figure 4.13 below, the difference in damage pattern between irradiation with a carbon beam and irradiation with a xenon beam is quite noticeable. It is now conceivable to propose a mechanism that might qualitatively account for the difference observed. In the case of carbon irradiation, since the temperature around the trajectory of the incident particles can reach the criteria for track formation and is far from the lower limit temperature for sputtering, we can assume that pores gradually fill with fluidic substance as a result of irradiation, leading to a reduction in the diameter of the pores. This is consistent with Klaumunzer's mechanism. When compared to the sputtering effect, this filling is rather mild, which means that the pore's structural integrity can be retained to a great extent. Due to the innate nature of the film composition (built on a silicon wafer), transverse shrinkage is more difficult to achieve than longitudinal shrinkage. The release of shear force in this process will be skewed in favor of thickness compression, which explains the damage pattern of the "squashed" pores that have been seen.

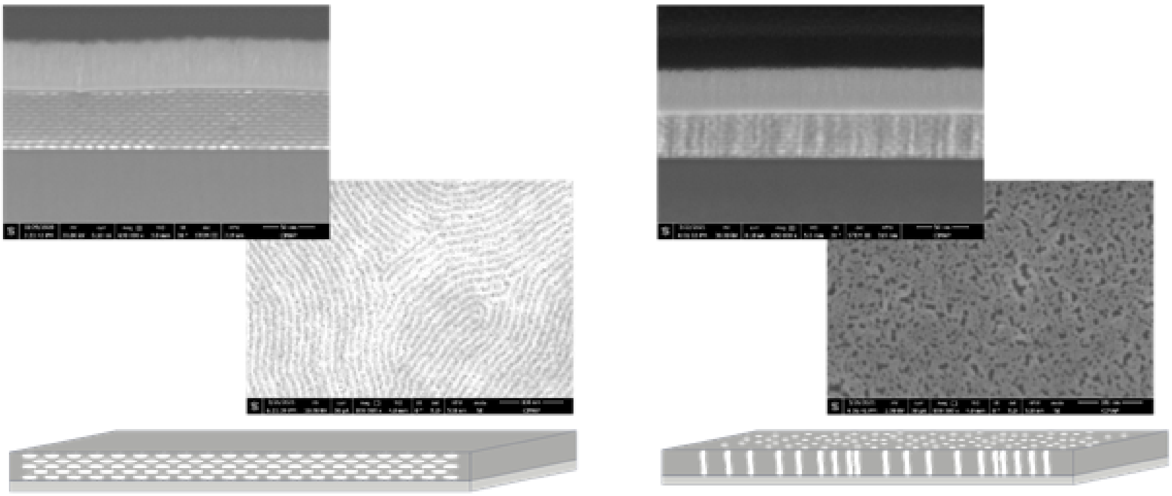

FIGURE 4.13: The morphology of silicon dioxide thin film revealed by electron microscopy after left). 3e13 ions/cm^2 of 12 MeV Carbon beam irradaition and right). 1e13 ions/cm^2 of 92MeV Xenon beam irrdiation

With regard to the situation of xenon beam irradiation, the simulation results reveal that the passage of xenon ions can cause the temperature to rise significantly over the boiling point, allowing a possible sputtering process. Given that sputtering is a type of knockdown and re-deposition process, the original pore structure will have a high possibility of being entirely obliterated, which is also consistent with the damage pattern we saw under the electron microscope.

4.5 Conclusion

A computational box with several cylindrical mesoporous silica is constructed in this chapter, and we use the 3DTS model to simulate what occurs when particles with varying electronic stopping powers bombard the system. The simulation findings show that the interaction of the incident particles with the matter causes the silica near the particle trajectory, to achieve a very high temperature, and that this temperature increases as the S_e increases.

The simulations also provide a mechanistic explanation for the experimental results that were previously reported in our studies. It is feasible to describe the process of pore closure under irradiation by combining the temperature prediction of silica near the pore structure with the mechanism given by Klaumünzer *et al.*[17, 18] We were able to explain the difference in the irradiation-induced damage pattern of mesoporous silica films by comparing the estimated temperature profiles with the criteria for track formation and sputtering.

Finally, the observed transition from circular to elliptical pores may be explained by the extremely tiny thickness to width ratio of the sample, since the sample's length is significantly greater than its thickness, consequently masking the horizontal deformation. The horizontal distortion of the silicon wafer is also limited by the strong bonding of the silicon wafer.

Chapter 5

Light ion irradiation: 16MeV H^+ in CEMHTI

We investigated the irradiation behavior of porous silica under the influence of a variety of swift ions beams with electronic stopping powers ranging from around 1 keV/nm to 12 keV/nm. When considering that beta rays have stopping powers of around 10^{-4} keV/nm (according to ESTAR estimations), we want to have a better knowledge of the effects of radiation in this range. In this part, we will present our study performed in the CEMHTI laboratory using a Van de Graaff accelerator to investigate the irradiation behavior of porous silica, on which we applied 16 MeV H^+.

5.1 Material and methods

5.1.1 Sample preparation

According to the SRIM calculations (see table 5.1), protons have the capacity to penetrate 1.59 mm in non-porous silica with a density of 2.2 g/cm^3, which provides us the possibility to employ pellets as the form of the experimental material. The pellets are prepared with a diameter of 5 mm and a thickness of around 1 mm in order to match the size of the beam.

TABLE 5.1: Ion stopping and penetration range of 16 MeV H^+ obtained from the calculation using SRIM

Ion Energy [MeV]	dE/dx Elec. [keV/nm]	dE/dx Nuclear [keV/nm]	Projected Range [mm]	Longitudinal Straggling [µm]	Lateral Straggling [µm]
16	5.70E-03	2.70E-06	1.59	63.64	58.6

In the same manner as in chapter 2, the porous silica powder (type SBA-15) was synthesized by applying the same method. The pelleting procedure was carried out using 5 mm laboratory pellet dies, with a pressure of 250 MPa being applied. It is essential to notice that this pressure is delivered to the pelleting mold and not to the silica network itself.

The analysis of the nitrogen adsorption/desorption isotherms of the as-prepared pellets verified the presence of mesoporous structures in the pellets. The figure 5.1 presents the calculated pore size distribution. For these 5mm pellets, we get similar results as for the 8mm pellets in chapter 2.

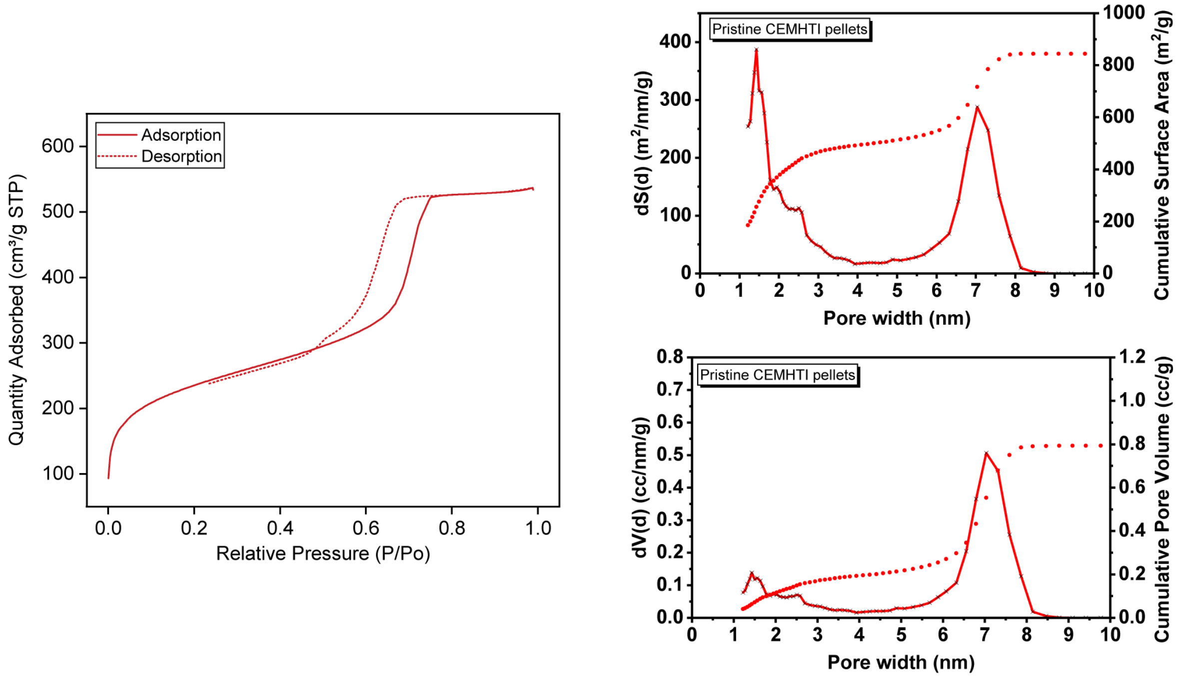

FIGURE 5.1: Nitrogen adsorption isotherm and NLDFT pore size distributions for pristine CEMHTI pellets.

5.1.2 Irradiation parameters

Several key parameters (e.g., fluence, flux, etc.) of irradiation are summarized in the following table 5.2. Here, the conversion between current and flux is

$$\text{Flux} = \frac{\text{Measured current}}{e \times \text{Collimator surface}}$$

with a collimator surface area equal to 0.41 cm^2.

TABLE 5.2: CEMHTI irradiation conditions

Irradiation run	Fluence [H/cm^2]	Average current [µA]	Average flux [H/cm^2/s]
1	3.00E+16	1.04	1.60E+13
2	3.00E+17	1.10	1.70E+13
3	3.00E+16	0.46	7.00E+12
4	2.00E+17	0.54	8.30E+12
5	1.00E+16	0.48	7.30E+12
6	5.00E+17	0.51	7.80E+12

The ion beam is perpendicular to the upper surface of the pellet. Since the pellet is made of pressed mesoporous silica powder, the pores in the pellet are not oriented in a specific order. The perpendicular angle of incidence is chosen only to ensure that the entire pellet receives uniform irradiation. To keep the sample temperature at room temperature, the pellet is placed in a customized sample container that includes a cooling system (figure 5.2).

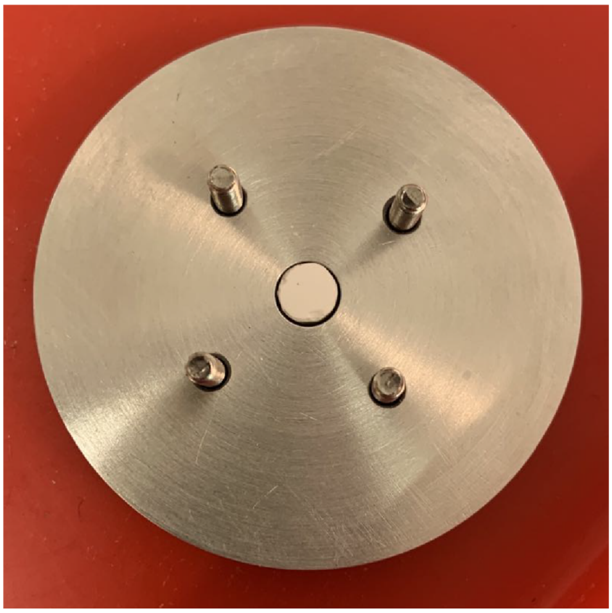

FIGURE 5.2: Photographs of sample containers for irradiation.

Pre-testing is performed before each irradiation to ensure that the beam's bombardment region covers the pellet uniformly. We use a piece of paper for the pre-experiment as a "target" for the particle beam bombardment, and after quick irradiation, we can see that the section of the pellet to be inserted is within the range of the uniform beam bombardment (within a circle with a diameter of 5 mm) (figure 5.3).

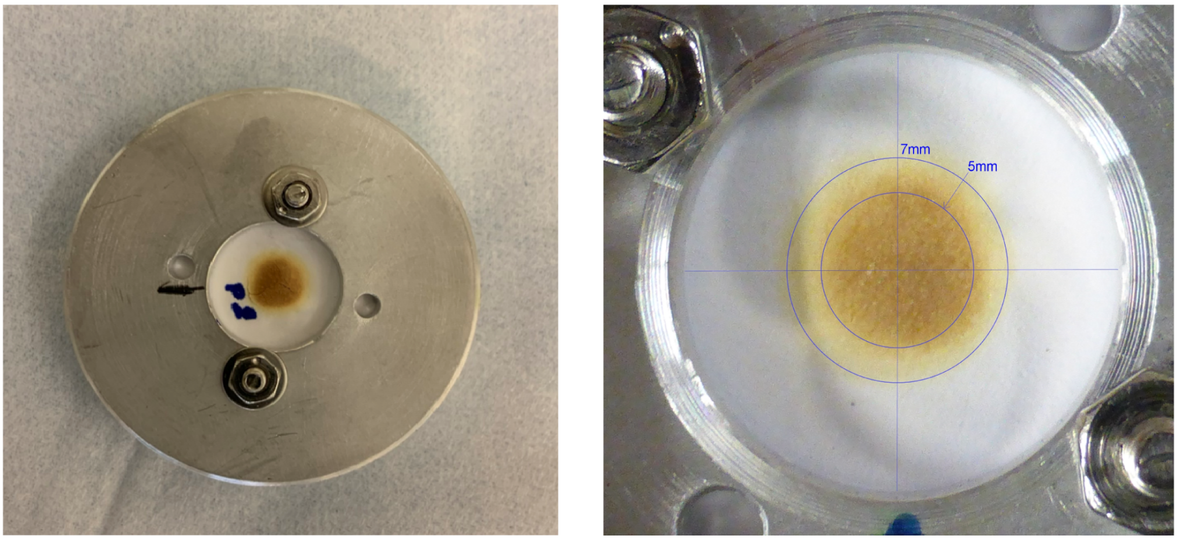

FIGURE 5.3: Images of pre-test irradiation showing the bombarded area.

5.2 Post-irradiation characterizations and results

5.2.1 Direct observation

All of the irradiated pellets kept their original appearance, with the exception of the silica pellet in run 2 (fluence 3.0E+17 H/cm^2, flux 1.7E+13 H/cm^2/s). It has vitrified and has been changed into an opaque sphere-shaped structure (figure 5.4).

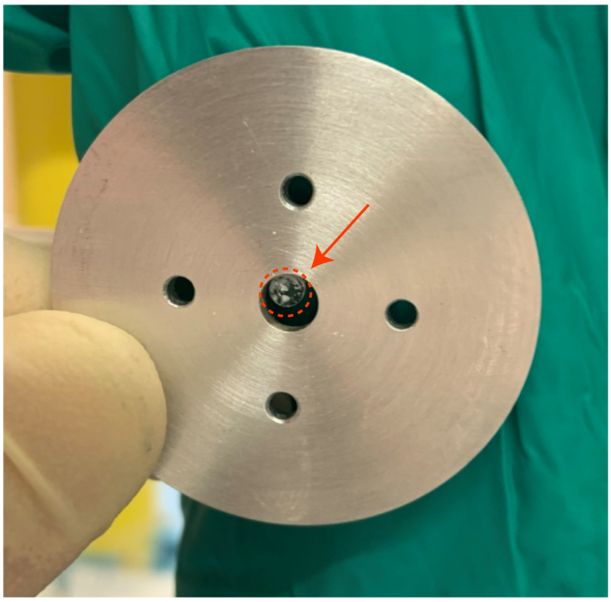

FIGURE 5.4: Opaque sphere-shaped pellet after irradiation.

5.2.2 Nitrogen adsorption/desorption isotherms and PSD

After the samples were exposed to radiation, we conducted post-irradiation nitrogen adsorption/desorption isotherms analysis. The results of these measurements are shown in figure 5.5. With the exception of the sample that was irradiated with a high flux and finally "vitrified" (run n°2), the corresponding pore size distribution (PSD) for the other samples was computed using NLDFT method. The pore size distributions implies that the influence of flux on pore size shrinking is significantly greater than the effect of fluence. When using flux at 1.6×10^{13} H/cm^2/s, where the sample is irradiated at the fluence of just 3.0×10^{16} H/cm^2, the mesopores have already shrunk considerably and the pore size distribution has grown somewhat broader. This is obviously distinct from the mesopore alterations observed in the samples irradiated with a flux around 7.0×10^{12} to 8.3×10^{12} H/cm^2/s. In the latter case, the width of the mesopores reduced with increasing dosage under irradiation, but the width of distribution remained reasonably steady with no notable modifications.

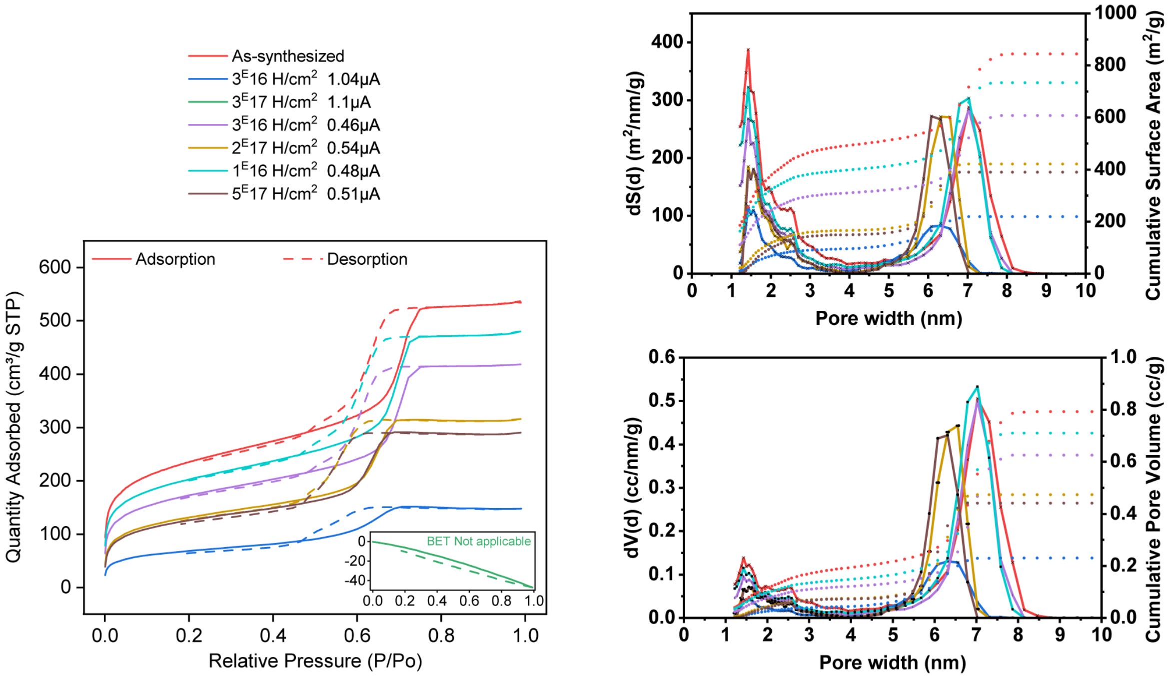

FIGURE 5.5: Nitrogen adsorption isotherm and NLDFT pore size distributions for irradiated CEMHTI pellets.

5.2.3 SAXS

Similar results are revealed by the SAXS measurements. A complete extinction of the peaks is observed in figure 5.6 of run n°2 (table 5.2), which suggests a total loss of pore structure. Moreover, the pellet that was irradiated with a high flux at a small fluence also suffered a significant degradation of the mesopore order. Other samples exposed to low flux radiation, on the other hand, did not show any change in the intensity of the peaks, implying that the overall mesopore structure remained the same, despite the fact that the distance between the pore centers decreased as the fluence increased.

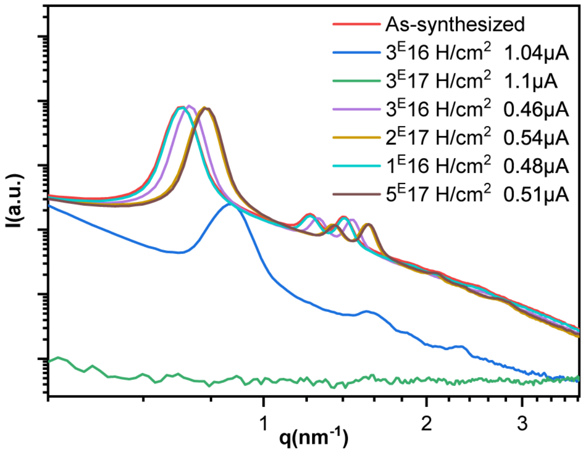

FIGURE 5.6: SAXS analysis of irradiated CEMHTI pellets.

5.3 Discussions

5.3.1 The vitrified pellet - characterization and simulation

According to the appearance observation, as well as the nitrogen adsorption and SAXS data, it appears that the mesoporous silica pellet used in the second run melted during the irradiation, leading to the formation of a glassy material and to the complete elimination of the pores. X-ray diffraction (XRD) data shown in figure 5.7, indicates that Cristobalite may have formed, demonstrating that it was generated as a result of a high-temperature phase transition reaction.

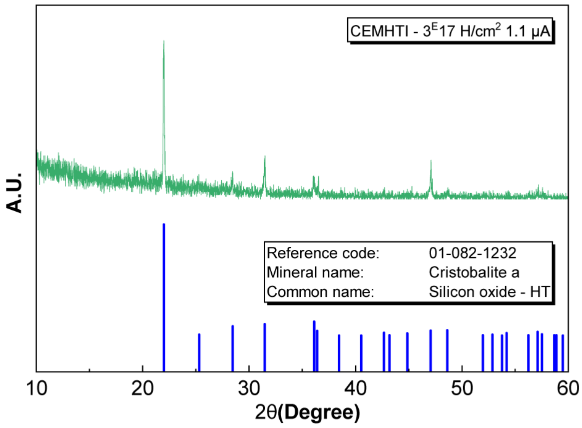

FIGURE 5.7: The XRD patterns of the n°2 CEMHTI pellet and the reference pattern of pure Cristobalite.

A single bombardment of this proton was simulated using a model similar to that described in the preceding chapter, and the results are depicted in figure 5.8. Using a single bombardment, we discovered that the greatest temperature that the system could attain was well below the temperature required to reach the melting point of silica.

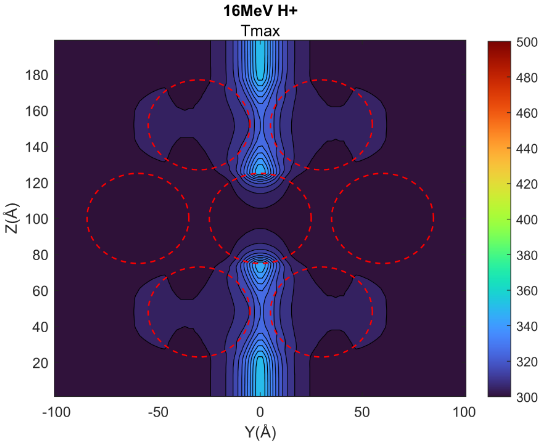

FIGURE 5.8: Simulation maximum temperature maps of 16 H^+ MeV irradiation in CEMHTI.

Figure 5.9 illustrates the variation in electronic temperature and lattice temperature with time in the simulation box. It is shown that the temperature begins to fall back and approaches the ambient temperature after 10^{-12} seconds. The damage cross-section of proton irradiation is likewise in the order of nm^2. Despite the fact that the irradiation run n°2 was carried out under conditions with a flux of 1.7e13 $H/cm^2/s$, the current results reveal that the accumulation of heat from multiple bombardments is impossible. Furthermore, it is unlikely that temperature of the system reaches the melting point of silica.

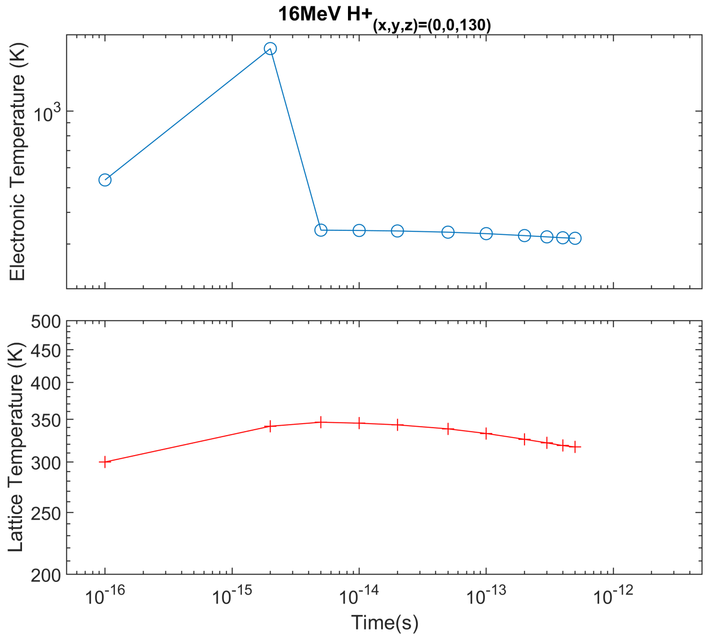

FIGURE 5.9: Electronic temperature (K) and lattice temperature (K) recorded as a function of time (s).

However, a significant flaw in this simulation was that the temperatures of the four sides of the box were all set to the same temperature as the beginning temperature. This setting may have minimal impact on thin film simulations since the small size of thin films and the fact that thin films are attached directly to the sample holder equipped with the cooling device. Nonetheless, when it comes to the proton irradiation of the pellets, it's possible that the cooling efficiency of the experimental cooling system is not be adequate to mantain this hypothesis, that is said thet the initial bounds temperature is not maintained in acceptable limits. We can only offer this probable answer at this stage; further tests must be designed in order to examine this explanation.

5.3.2 Pellets irradiated with a current of around 0.5 μA

For pellets irradiated at a current of 0.5 μA, the structural changes induced by proton irradiation were very different when compared to run n°1 and n°2, where the flux is two times higher. Despite the fact that the flux only fell by half, the findings of nitrogen adsorption/desorption and the results of SAXS demonstrate that the shrinking of the mesopores is considerably more moderate. In contrast to irradiation-induced sintering, which occurred in the case of run n°1 at higher flux, the uniformity of mesopores does not show any significant change as the mesopores shrink. Furthermore, no peak was detected by XRD analysis, which reveals that there are no structure relate to crystalline silica (Cristobalite).

Combining these observations, it is fair to conclude that, in the event of relatively low flux, irradiation-induced sintering is not the cause generating pore shrinkage, or that it is not the primary cause. The possibility of other mechanisms needs to be explored.

Ojovan *et al.*[156] have conducted several quite enlightening studies. They discovered that in many cases, the structural behaviors of micro- and nano-scale samples observed during TEM irradiation of glassy materials could not be explained by overheating of the materials studied. With the use of an electron microscope, they saw the fluidization of amorphous materials, and they pointed out that traditional melting of these glasses would otherwise need temperatures higher than 1200 °C, temperatures that are unlikely to be reached with an electron microscope. Numerous investigations on crystalline phases that were not melted by the electron beam support this result.

Ojovan *et al.*[156] concluded that the fluidization or quasi-melting of the glassy material in high radiation fields (figure 5.10) is not due to thermal melting, but rather to intense radiation-induced bond breakage that occurs as a result of the radiation.

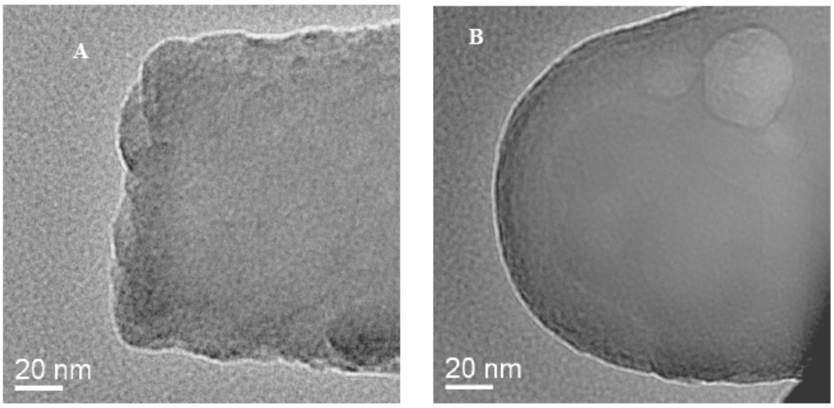

FIGURE 5.10: Transformation of rugged glass fibre end (A) into hemisphere (B) under the 4 nA TEM e-beam continuous irradiation over 30 min. Figure extracted from the ref [156].

A similar mechanism can explain the phenomena observed in our work; fluidization of the silica material under the influence of a proton beam is induced by the breakdown of bonds caused by the passage of the proton which can occur with minimal thermal effects. Afterwards, the stress caused by surface tension forces following the viscous flow process surrounding the trajectory of the impact proton causes the mesopore structure to contract, which causes the proton to hit the wall.

5.4 Conclusion

We demonstrate through studies with 16 MeV H^+ irradiation that shrinkage of the mesoporous silica pore structure may still occur at lower electronic stopping power. Although the mechanism of pore shrinkage under proton beam irradiation may be different from that under swift heavy ion irradiation, the fact that the proton beam successfully changes the pore structure, indicates that beta ray has the same potential to modify the pores, as we will demonstrate in the following section. However, it should be noted that in the case of irradiation with 16 MeV protons at the highest flux (1.70E+13 H/cm^2/s), problems related to insufficient cooling may lead to the fusion of the sample. Similar effects may occur for samples irradiated with a lower flux.

Part III

Electron Irradiation

Chapter 6

Mesoporous silica under 2 MeV electron beam irradiation

In the previous section, we observed the behavior of porous silica under the ion-beam irradiation. Similarly, damage radiation induced by electron beam in scanning or transmission electron microscopes has also been widely reported [112, 157]. Blanford demonstrated that the relative stability of different varieties of MCM-41 silica under electron beam (at an acceleration voltage of 100 to 200 kV) depends on the synthesis conditions and particularly on the presence of residual surfactants in their structure [112]. No work has, however, explicitly examined the structural evolution (e.g., pore size distribution, wall thickness) of ordered mesoporous silicas in regards to the dose, especially at irradiation conditions representative of the energy corresponding to fission products decays (~2 MeV).

To evaluate the dimensional change of ordered mesoporous silica in a regime which is representative of the damage done by beta, gamma disintegrations of fission products, we irradiated pellets obtained by compaction of SBA-15 and MCM-41 powders at low stopping power (~ 10^{-3} keV/nm) with a 2 MeV electron beam. The evolution of the mesoporous structure under irradiation has been addressed to investigate the factors influencing such evolution.

6.1 Material and methods

6.1.1 Preparation of pellets

The as-synthesized SBA-15 and MCM-41 powders (Chapter 2) were compacted into pellets (thickness ~ 1 mm, diameter ~ 8 mm) under a pressure of 250 MPa. Then, the pellets were annealed at 400 °C for 4 h. Following these treatments, the retention of 2D-hexagonal symmetry of the porous structure within the compacted silica pellets is proven by N_2 sorption isotherms at 77 K, Small-angle X-ray scattering (SAXS) patterns and transmission electron microscopy (TEM) images. Our subsequent irradiation experiment results will be compared with pristine pellets as a reference. As a result, the alteration of pores caused by the pelleting process will not affect the conclusion of this study. The scanning electron microscopy (SEM) image (figure 6.1) of samples has shown the presence of extra-granular pores (macro-pores) due to the pelleting procedure. From the helium pycnometry analysis we can distinguish the volume of these large pores from the small pores (micro and meso-pores) inherently present in the silica powders. More details on this point will be discussed further.

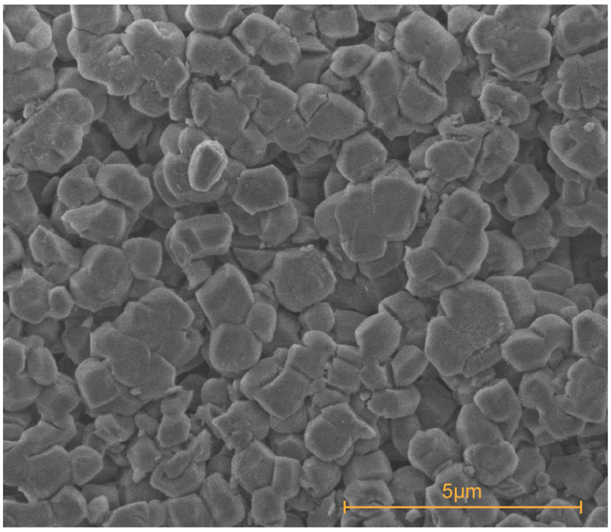

FIGURE 6.1: An SEM image showing the extra-granular pores (macro-pores), caused by the pelleting procedure.

6.1.2 Electron beam irradiation

The apparatus used for irradiation was a NEC Pelletron at the SIRIUS irradiation facility (Laboratoire des Solides Irradiés, Ecole Polytechnique, France). The energy of electron beam was calculated and adjusted to achieve the energy of 2 MeV at the sample surface after attenuation by the necessary fixing devices. Doses of 0.1, 0.5, 1 and 2 GGy were applied on SBA-15 samples, and irradiations were performed at a flux of 8.5 µA/cm^2, which is equivalent to 5.28×10^{13} electrons·cm^{-2}·s^{-1} at room temperature (< 45 °C). MCM-41 were irradiated at 0.1, 0.5, 1, 2 and 5 GGy, with the same experimental conditions. Under these experimental conditions, ESTAR calculations[158] of the stopping power in the specimen thickness (figure 6.2) show that electrons dose deposition can be considered homogeneous on the entire pellet.

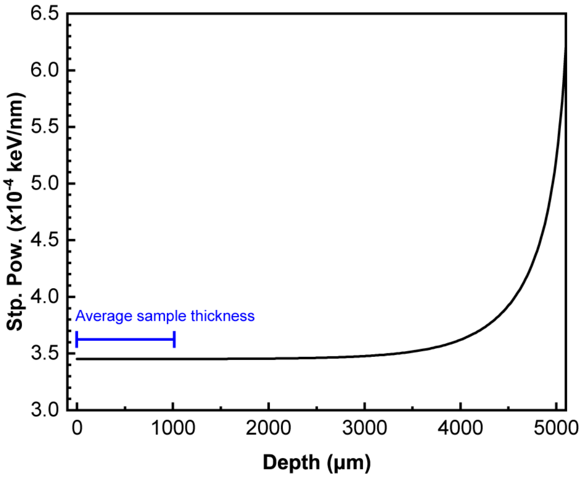

FIGURE 6.2: Stopping power of 2 MeV electrons in mesoporous silicas of density of 2.2 g.cm^{-3}.

6.2 Results and discussions

6.2.1 Evolution of the porous characteristics of the samples versus irradiation

6.2.1.a Helium pycnometry and apparent density of the pellets

We may acquire statistics on the pores in the pellets using the data processing approach described in Chapter 1 section 1.4.3. The porous characteristics of the samples are shown in table 6.1. It is critical to highlight that because to the unique properties of mesoporous silica (highly hydrophilic and intricate porous structure), density measurements may contain some inaccuracy. The average skeletal density of the samples is equal to 2.3 ± 0.1 g.cm^{-3}. This value is consistent with the theoretical density of amorphous silica (*i.e.*, 2.3 g.cm^{-3}). As stated previously, the porosity closure of the samples is very low. The shrinkage of the pellets increases with the radiation dose. This effect is more significant for SBA-15 samples than MCM-41. Unfortunately, the apparent density of the sample MCM-41 irradiated at 5 GGy could not be measured because the sample was broken after irradiation.

TABLE 6.1: Densities, porosities and shrinkage of the samples versus irradiation dose (2 MeV electron beam)

		Before irradiation	After irradiation									
	Dose (GGy)	$\rho_{apparent}$ (g.cm^{-3})	$\rho'_{apparent}$ (g.cm^{-3})	$\rho_{skeleton}$ (g.cm^{-3})	$\varepsilon_{tot.}$ (%)	$\varepsilon_{micro.}$ (%)	$\varepsilon_{meso.}$ (%)	$\varepsilon_{macro.}$ (%)	D (%)	W (nm)	a_0 (nm)	D (nm)
MCM-41	0	0.74	0.74	2.12	65	1	48	16	–	0.5	4.3	3.8
	0.1	0.72	0.76	2.15	65	1	44	20	3.9	0.6	4.3	3.7
	0.5	0.72	0.82	2.38	66	1	41	23	3.5	0.6	4.2	3.6
	1	0.74	0.77	2.28	66	1	39	27	2.1	0.7	4.2	3.5
	2	0.70	0.76	2.23	66	1	29	37	6.7	0.9	4.0	3.1
	5	–	–	–	–	–	–	–	–	1.5	3.6	2.1
SBA-15	0	0.76	0.76	2.23	66	8	44	15	–	3.4	10.4	7.0
	0.1	0.71	0.76	2.21	66	4	41	20	7.0	3.5	10.3	6.8
	0.5	0.73	0.79	2.27	65	4	37	25	4.0	3.5	10.2	6.7
	1	0.77	0.85	2.28	63	3	33	27	8.2	3.5	9.9	6.4
	2	0.77	0.88	2.45	64	2	30	32	13.7	3.5	9.6	6.1

6.2.1.b Nitrogen adsorption/desorption isotherms

The shape of MCM-41 and SBA-15 adsorption isotherms (figure 6.3) are characteristic of a type IV curve, indicating the presence of micro- and meso-pores. Comparably, a decrease in the adsorbed volumes at saturation is observed as a function of the irradiation dose for the two mesoporous silicas. A change in the shape of the isotherm is observed for 5 GGy (type I isotherm), which indicates a total disappearance of the mesoporosity for this sample.

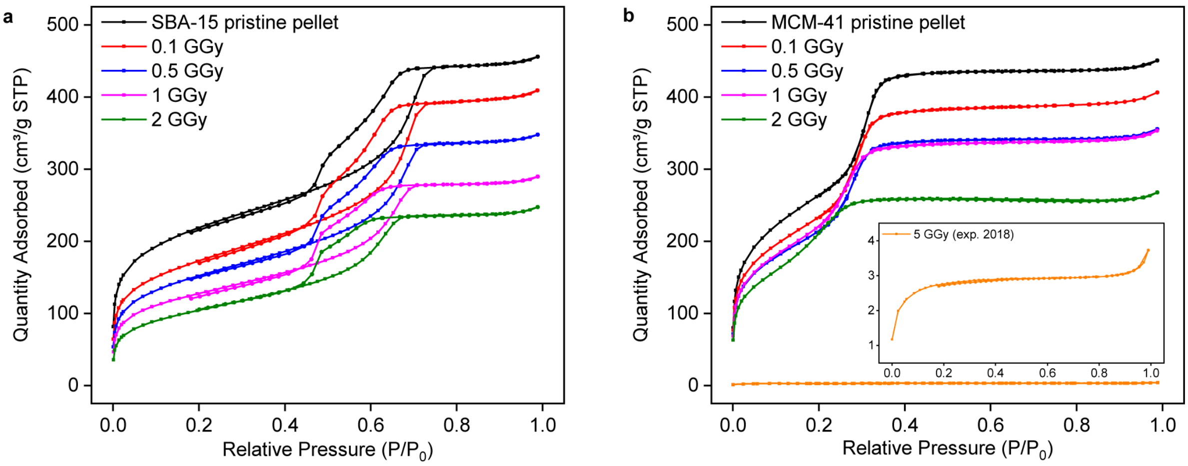

FIGURE 6.3: Nitrogen adsorption / desorption isotherms at 77K of silica pellets, SBA-15 (a) and MCM-41 (b) under 2 MeV electron irradiation.

Figure 6.4 shows the pore size distribution calculated from the nitrogen adsorption isotherm with the density functional theory (DFT) method. This distribution allows calculating the different volumes (V_{micro}, V_{meso}) precisely and, finally, the contribution of each class of porosity (micro, meso, macro) from equations presented in section 1.4.3. These parameters are presented in figure 6.5 and figure 6.6 and detailed in the discussion section that follows.

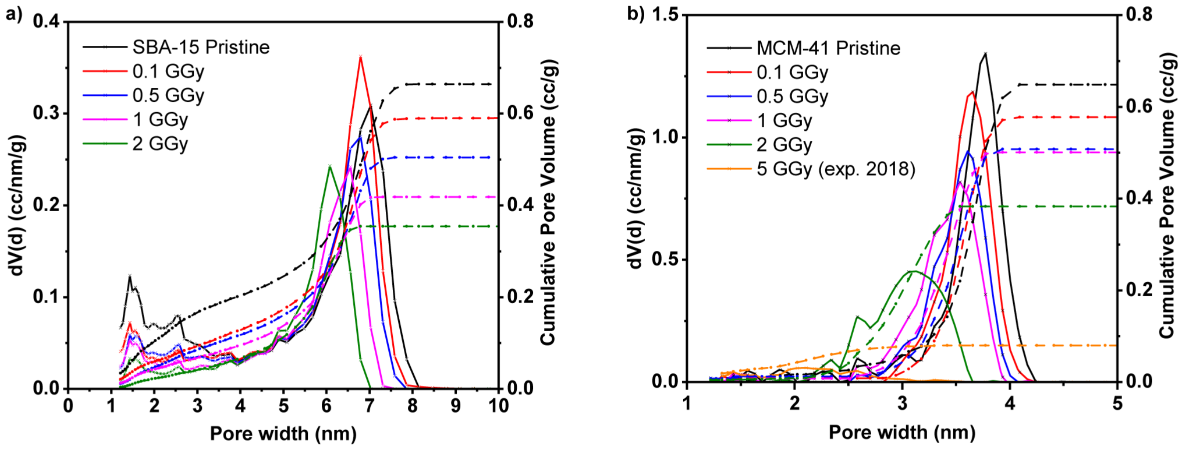

FIGURE 6.4: Pore size distribution of silica samples (a) SBA-15, (b) MCM-41. (Solid line = pore volume, Dash line = cumulative pore volume).

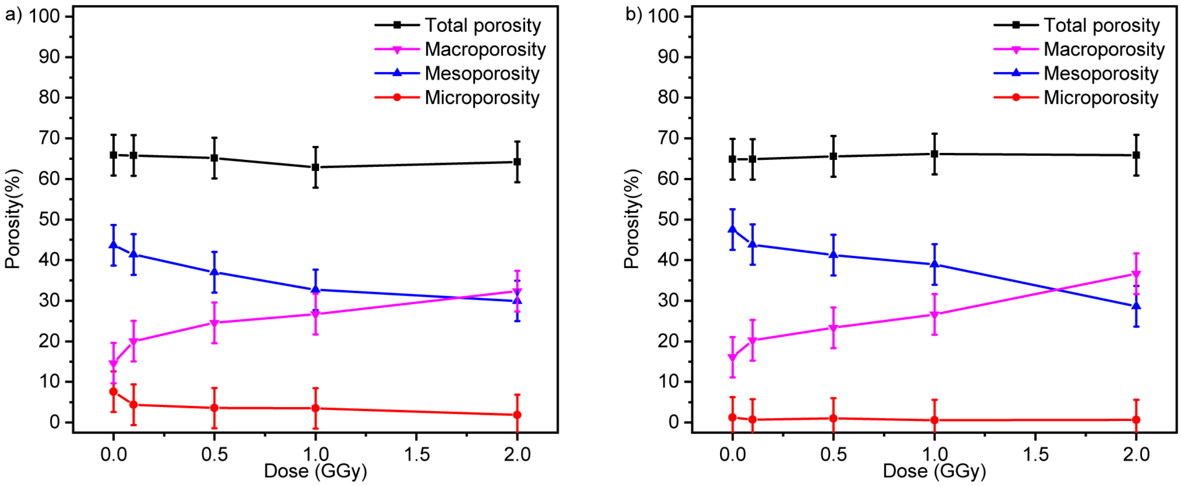

FIGURE 6.5: Evolution of the porosities of the samples with the radiation dose, (a) SBA-15, (b) MCM-41.

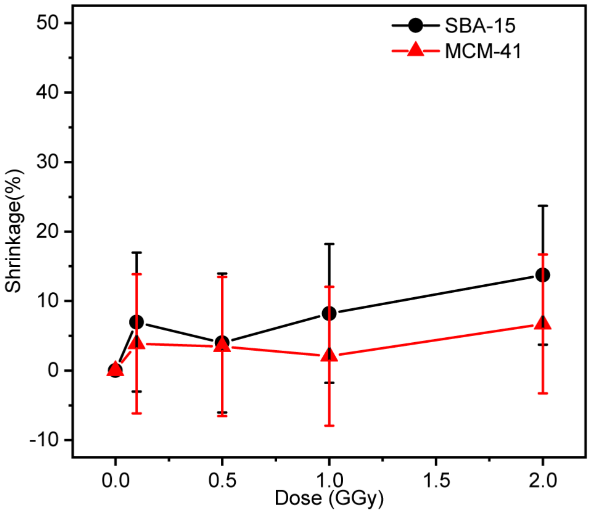

FIGURE 6.6: Evolution of the shrinkage of the samples versus radiation dose.

6.2.1.c Small-angle X-ray scattering (SAXS)

SAXS measurements performed on pellets after electron beam irradiation are shown in figure 6.7. The scattered intensity displays three well-resolved peaks indexed as (100), (110), (200), associated with P6mm hexagonal symmetry. Remarkably, no significant change was observed in SBA-15 structure up to 2 GGy, while MCM-41, a decrease in the intensities of the peaks occurs at 2 GGy with a complete extinction at 5 GGy. For both samples, the structural peaks are shifted to high q values under irradiation, which indicates a decrease of the lattice parameter a_0. The parameter a_0 is equal to the average distance between the pores (for 2D hexagonal structure $a_0 = 2d_{100}/\sqrt{3}$, where $d_{100} = 2\pi/q_{100}$), this decrease of a_0 may result from a decrease of the silica wall or of the pore diameter, or both. Through correlating the various characterization data, this impact will be clearly understood in the following.

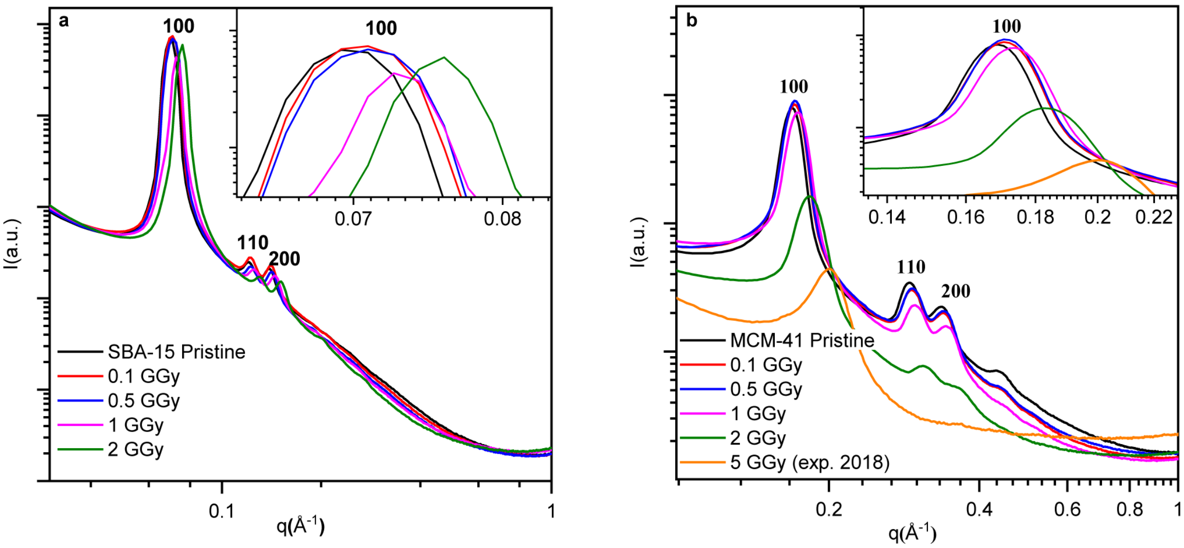

FIGURE 6.7: Small angle X-ray scattering spectra of silica pellets, SBA-15 (a) and MCM-41 (b) under 2 MeV electron irradiation.

6.2.2 Structural characterization of silica

6.2.2.a Nuclear magnetic resonance spectroscopy

Nuclear magnetic resonance spectroscopy was used to evaluate the modification of the silica network. The results obtained from the ^1H and $^1H \rightarrow^{29}$ Si CP analysis are summarized in Appendix G. However, these results are not representative of the bulk volume for the following reasons: Firstly, CP-MAS is quite dependent on the hydration state of the sample, which is independent of irradiation, which means that the spectra are more challenging to compare. Secondly, surface protons can induce faster relaxation of nearby silicon atoms. Therefore, we favored high-power decoupling with magic angle spinning (HPDEC – MAS) NMR direct ^{29}Si acquisition. As shown in figure 6.8, the Q^n group analysis was employed with direct ^{29}Si MAS NMR acquisition. No significant change was observed in the chemical shift of Q^n peaks. It must be noted that the chemical shifts observed are different from those known for α-quartz [159]. This could give a hint that there is no radiation-induced crystallization. A slight increase of the Q^3/Q^4 ratio is observed when going from the as-synthesized material to the irradiated one. The most likely reason for this increase is the breaking of some $Si-(OSi)_4$ structural units into the $Si-(OSi)_3O^-H^+$ structures during the electron beam radiation. However, with a small sample size, caution must be applied, as the variation is ridiculously small compared to the change observed in porosities. Extensively, SiO_2 networks tend to remain at a steady-state, with no significant accumulation of defects.

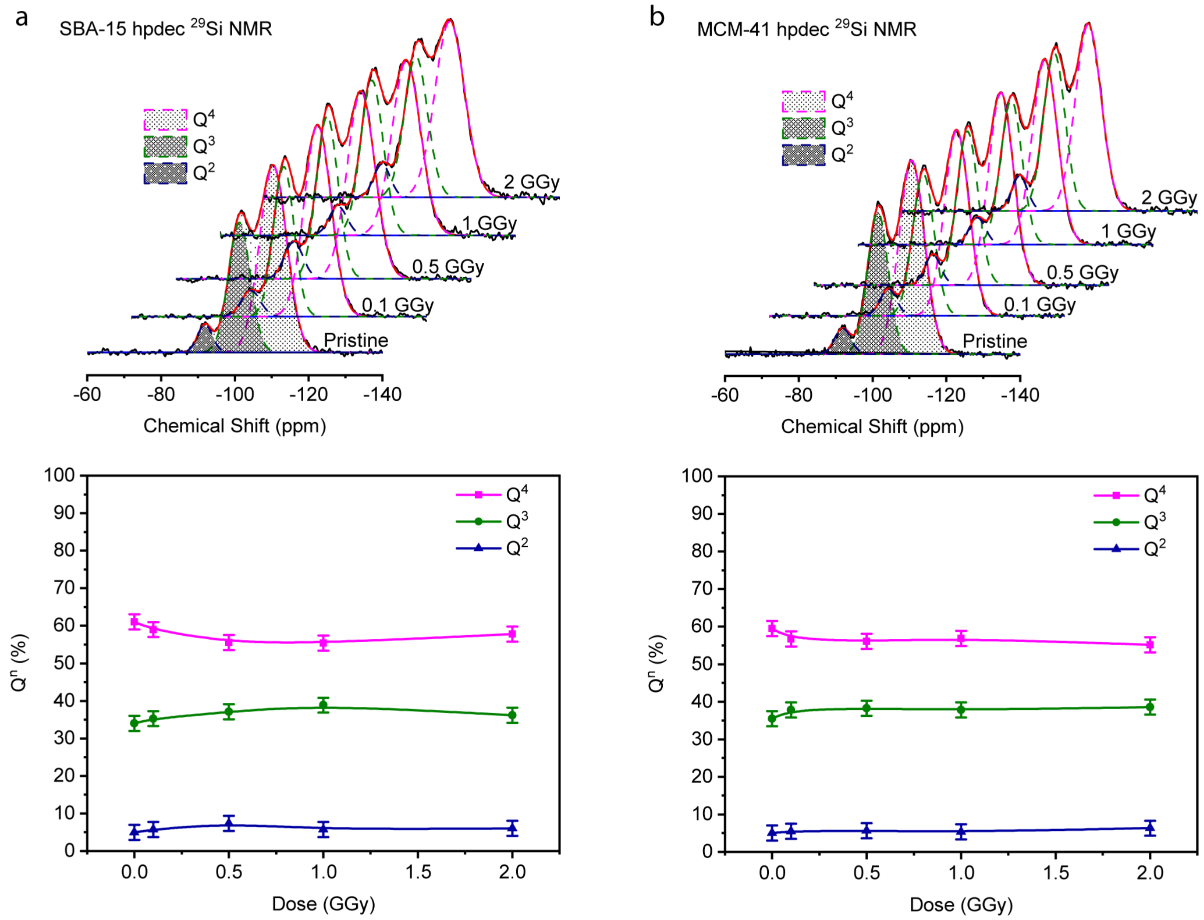

FIGURE 6.8: Deconvolution of hpdec MAS ^{29}Si NMR spectrum and evolution of the Q^n sites.

6.2.2.b ATR-FTIR measurement

A zoom on the 750-1400 cm^{-1} region of the deconvoluted ATR-FTIR spectrum shows the Si-OH, and SiO_2 vibration modes. However, LO_4, TO_4 and TO_3 mode vibrations might not represent their real population as the decomposition of the "shoulder region" has been controversial and inconclusive in previous studies. For the discussion afterward, only the TO_3 vibrations located around 1074 cm^{-1} will be compared after irradiation. Many scholars hold the view that the position of the TO_3 peak is linked to the density of the SiO_2 network, and its shift to lower wavenumber (redshift) is assigned to a reduction in density. As can be seen from figure 6.9, the position of the TO_3 peak did not change within the analytical error, implying that the densification of the SiO_2 network is almost absent or negligible, which is in agreement with the results of NMR.

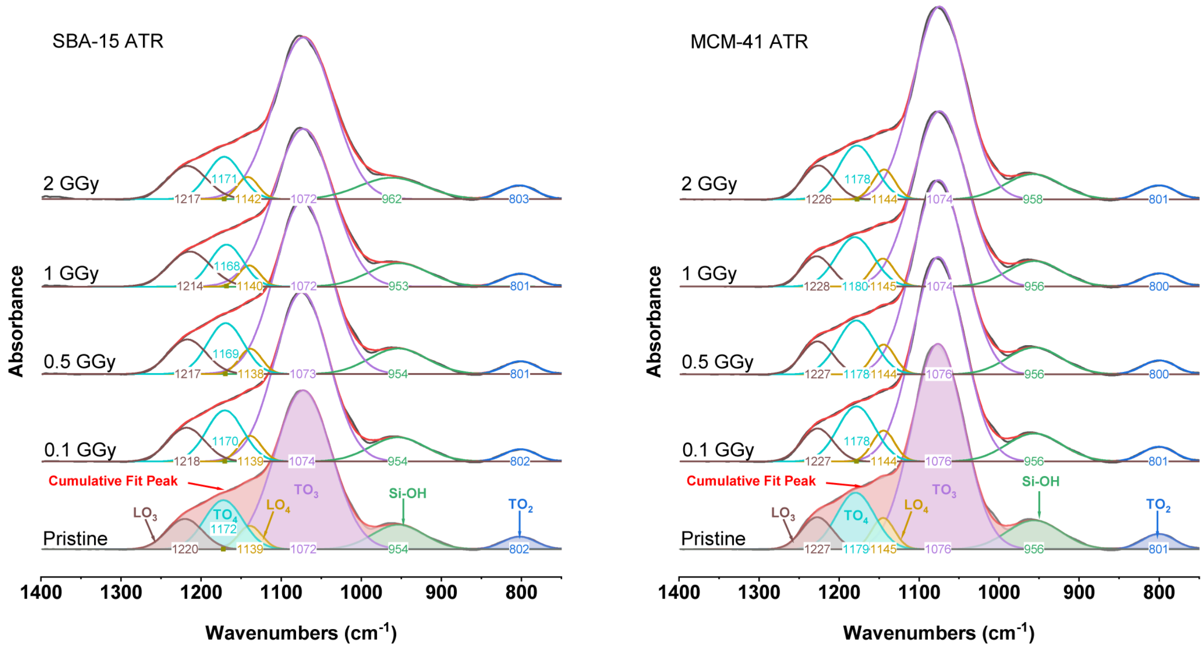

FIGURE 6.9: Deconvoluted ATR-FTIR spectra between 1400 and 750 cm^{-1} and reconstituted spectra after curve fitting.

6.2.2.c Cathodoluminescence

Since ATR-FTIR and NMR methods have not been able to reveal changes in silica networks under a dose range of 0 - 2 GGy. Here we try to use cathodoluminescence to track the point defects under irradiation. One MCM-41 sample was irradiated up to 0.5 GGy, fluence 1.9x10^{18} e$^-$/cm^2, with a flux of 1.4x10^{13} e$^-$/cm^2/s using a current of 5 μA. The results are displayed in the figure 6.10. Here, we detect a signal for NBOHC (band peaking at 650 nm (1.9 eV)) but with no kinetics, which is consistent with our observation of ATR-FTIR and NMR presented previously.

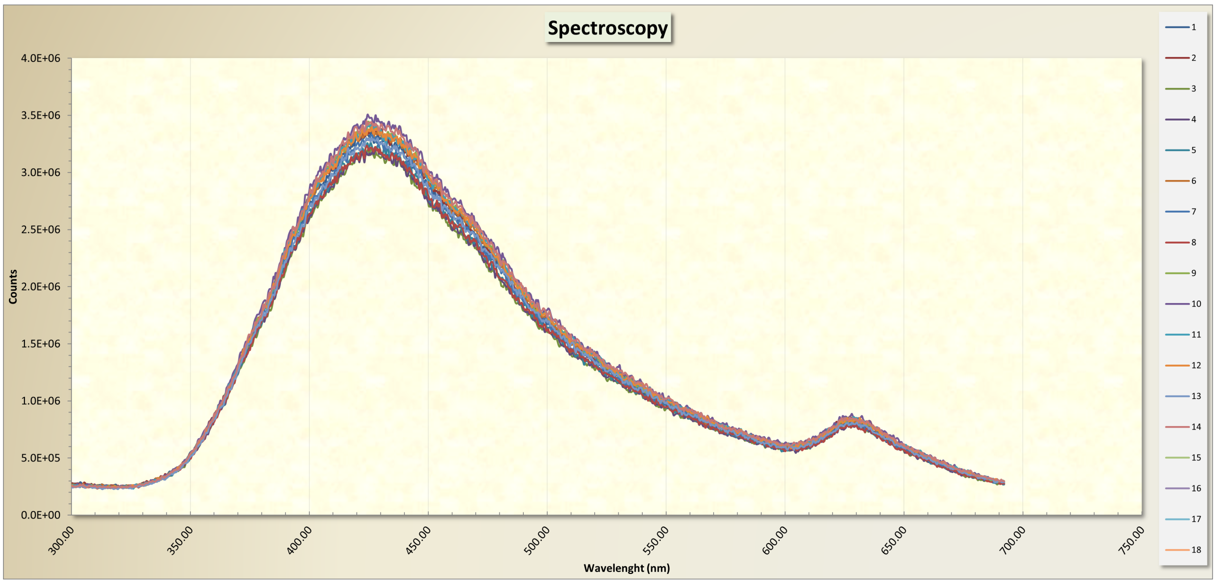

FIGURE 6.10: Cathodoluminescence spectra of MCM-41 under irradiation.

6.2.3 Transmission electron microscopy (TEM)

Though nitrogen gas sorption related techniques, helium pycnometry, and X-ray scattering reveal averaged structures, TEM imaging is much more accurate for determining local structures and default accumulations. Under the experimental irradiation conditions, even though the previous results indicated that most of the mesoporous structures were not damaged, TEM images in figure 6.11 show significant structural collapse when higher doses are applied.

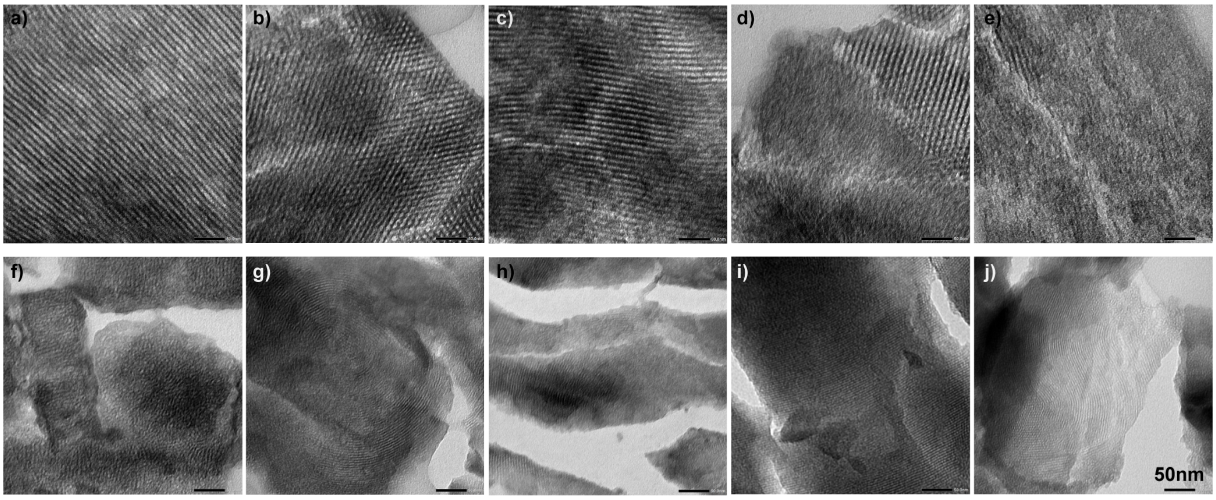

FIGURE 6.11: TEM images of SBA-15 samples: a)-e) sequentially represent pristine - 0.1 - 0.5 - 1.0 - 2.0 GGy and MCM-41 samples: f)-j) sequentially represent pristine - 0.1 - 0.5 - 1.0 - 2.0 GGy.

6.3 Discussion

6.3.1 Evolution of porosity

The first conclusion is that the innate porosities (micro and mesoporosity) decrease with the increase of the radiation dose. Concomitantly, an increase in the shrinkage of the samples and an increase in the macroporosity volume are observed. It can be assumed that the mesoporous silica grains observed in figure 6.1 have densified, generating an increase in intergranular porosity, i.e., macroporosity. These volume changes lead to internal stresses within the pellets, inducing few micro-cracks as observed by SEM (figure 6.12). However, these observations do not highlight an important density of microcracking. It seems that the mesoporous silicas obtained by the sol-gel route exhibit some plasticity, allowing relaxing these constraints partially. This increase in macroporosity could be problematic for the intended application as regards to the leaching of these materials. However, we must keep in mind that the surface area of macropores is ridiculously small compared to the specific surface area of micro and mesopores, and that those macropores are relatively easy to reseal with the help of other means.

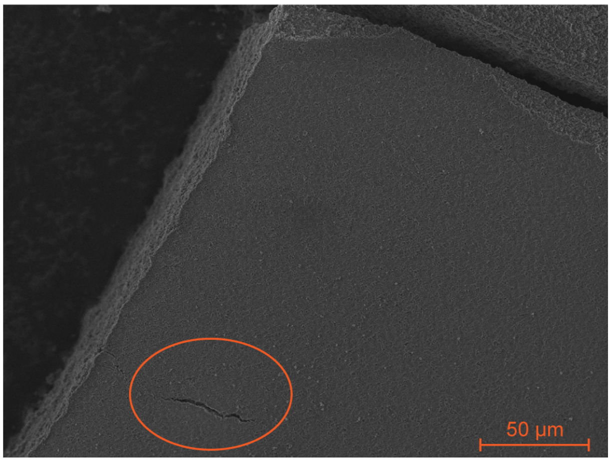

FIGURE 6.12: Micro-cracks observed by SEM in the silica sample.

The second important result obtained from this analysis is the apparent trend of decreasing mesopore diameter. This change occurs from the lowest doses (0.1 GGy) but does not impact the global structure, even at 2 GGy dose, as shown by the shape of N_2 adsorption isotherm curves (figure 6.3). Figure 6.4 also indicates that SBA-15 keeps a narrow pore-size distribution, though it becomes larger for MCM-41. It suggests that SBA-15 still possesses an ordered structure, while the mesoporous structure of MCM-41 is slightly disrupted. This result is supported by SAXS measurements (figure 6.7) and TEM observations (figure 6.11) which show a loss of the organization of the MCM-41 pore network for the highest dose.

The third result concerns silica ligands. The evolution of the lattice parameter a_0 presents the same trends as the one of the pore size (table 6.1), which on a first look confirms the dose-dependent collapse of the mesoporous structure. However, the radiation effect on pore size and silica wall thickness can be decorrelated due to the relation of the different characterization results. The apparent wall thickness W can be calculated from the lattice parameter a_0 and the pore radius r determined via SAXS and nitrogen sorption using the equation:

$$W = a_0 - 2r$$

As presented in table 6.1, the wall thickness W increases with the radiation dose for MCM-41 while it does not significantly evolve for SBA-15. This result shows that the collapse of the structure is mainly due to a pore size decrease for both structures, and confirms the more significant structural disruption of the MCM-41 compared to SBA-15.

The structure of the silica walls was further characterized by NMR and FTIR for the two mesoporous silicas. No significant modification was observed with the irradiation dose, which is consistent with the theoretical density value obtained from pycometric density measurements. Bibliographic results indicate that the amorphous silica densification under irradiation saturates to a value close to 3% [82]. This saturation effect depends on the nature of the projectile, *i.e.*, electrons, ions, neutrons, and more precisely on the interactions (ballistic or electronic) [160]. For electronic interaction, the dose necessary for the evolution of density is greater than 10 GGy and the value of 3% swelling is obtained at approximately 30 GGy. The maximum dose at which the samples were irradiated in this study is much lower, which explains why no significant change was detected.

6.3.2 Collapse mechanism

In recent years, the potential applications of mesoporous materials in the nuclear field have been booming [161], but only a few works have focused on the evolution of nanoporosity under electronic or ionic irradiation. The idea that mesoporosity might be favorable for recombination of irradiation defects due to proximity to surfaces has not been conclusively demonstrated. A few studies on the irradiation of metallic foams show tolerance of some nanoporous metals to irradiation due to the recombination of the defects. This tolerance was dependent on the size of the pores [10, 162].

Studies carried out on all mesoporous oxides show a collapse of the mesoporous structure under irradiation with ions. These works concern damage of ballistic type [13, 14, 163, 164] or under very strong electronic excitations (tracks formation regime) [15, 17, 18] which do not correspond to the irradiation conditions described in this study. The only work related to the damage of mesoporous silicas MCM-41 by electrons was proposed by Blanford *et al.* [112]. However, the irradiation conditions are quite different from those investigated in this study since the samples were irradiated in a TEM, i.e., at a lower energy (100-200 kV) and higher flow rates. Under these conditions, Blanford *et al.* proposed a predominantly radiolytic damage mechanism, with an important contribution from the heating of the samples by the electron beam. Despite the different irradiation conditions, we attempted to compare with the mechanisms proposed by Blanford *et al.*.

First, the sample-heating process does not appear to be operative in our case since the samples are cooled during irradiation, ensuring a maximum specimen temperature of 45 °C. In addition, experimental results performed in our laboratory have shown complete densification and loss of organization of the mesoporous network (SAXS measurement) of SBA-15 heated to 1000 °C, while MCM-41 retains both a fraction of pore volume and its pore network under the same conditions. This result is actually the opposite of what was observed when the samples were irradiated with 2 MeV electrons.

Second, we use the model proposed by Marples in the 1980s to estimate a cross-section of the process and compare it with the results of Blanford *et al.*. Here we assumed that the change in property, swelling or densification, is proportional to the fraction of damaged volume. With this second hypothesis, Marples's equation can be written as:

$$\frac{\Delta\rho}{\rho} = (\frac{\Delta\rho}{\rho})_{\text{sat}}\,(1 - \exp{(-\nu \text{Rt})})$$

$\Delta\rho$ is the evolution of macroscopic properties (pore volume, thickness, density, mechanical property, etc.). The index "sat" means the saturation state. In this work, the term νRt can be replaced by $\sigma\phi$ where σ is the cross-section, and Φ is the fluence.

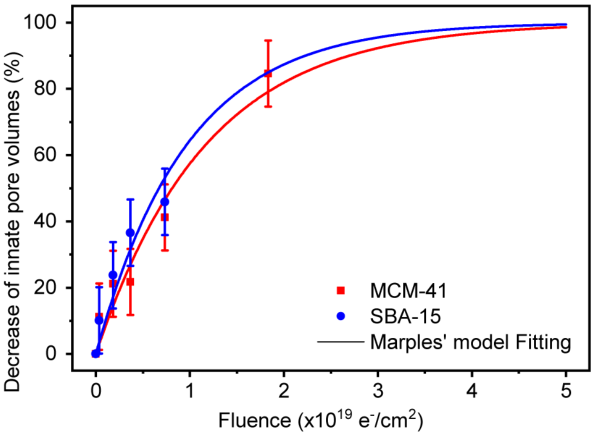

FIGURE 6.13: Pore volumes decrease as a function of fluence for SBA-15 and MCM-41.

In figure 6.13, the evolution of the innate porosities (micro and mesoporosity) (PV) of the mesoporous sample with the fluence is fitted using this model considering a non-porous material (100% compacted) as the final state. The damage cross-sections obtained from the fit are $(9 \pm 2) \times 10^{-20}\text{cm}^2$ for MCM-41 and $(1.4 \pm 0.6) \times 10^{-19}\text{cm}^2$ for SBA-15.

The present study estimated a damage cross-section in the order of $10^{-20} \sim 10^{-19}\text{cm}^2$. Since this study was limited to only one electron energy, it could not include an in-depth comparison of radiolytic and knock-on damage mechanisms. It is necessary to compare the experimental evolution with different electron energy to the corresponding evolutions of the electronic stopping power ("collision" in ESTAR), and of the nuclear stopping power (NIEL) (figure 6.14). Moreover, other authors [27] have observed that the dominant mechanism during the crystalline to amorphous transition of single crystal quartz induced by electron irradiation, depends on the energy of the electrons, i.e. radiolytic process at low energy (100 keV) then knock-on process at higher energy (2.5 MeV). A natural progression of this work is to investigate the material behavior under different ratios of electronic and nuclear stopping powers. Future work would be interesting to repeat the experiments described here using 0.6 - 2.4 MeV electrons.

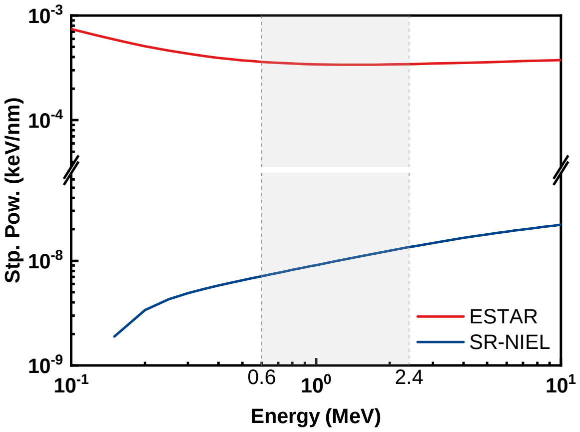

FIGURE 6.14: Electronic (calculated by ESTAR) and non-ionizing energy loss (calculated by SR-NIEL) in silicon dioxide.

6.4 Conclusion

SBA-15 and MCM-41 mesoporous silicas are both susceptible to radiation damage from 2 MeV electron irradiation. Up to a dose of 5 GGy, this damage affects the porous network (change in volume, collapse) and does not affect the density of the silica walls. This irradiation has a greater impact on the porous structure, exhibiting a smaller pore size leading to complete amorphization of the MCM-41 sample, while the SBA-15 is less affected. At a macroscopic scale, this phenomenon results in a withdrawal of the pellets and jointly in an increase of their macroporosity leading to the appearance of certain microcracks. The overall nanoporous volume (mesoporous + microporous) of samples SBA-15 and MCM-41 was affected comparably up to a dose of 2 GGy, respectively $\Delta V/V$: ~ 41% against ~ 45%. Differences were observed in terms of meso and microporosity. The microporosity of the SBA-15 pellets almost completely disappeared and a sharp decrease in the volume of mesoporosity was observed, while the hexagonal structure is well preserved. A greater reduction in the mean diameter of the MCM-41 mesopore was observed, leading to a disappearance of their hexagonal structure.

Chapter 7

Mesoporous silica exposed to various energy electron beams

In the previous chapter, the behavior of mesoporous silica under 2 MeV electron beam irradiation was discussed. We have demonstrated the shrinkage and collapse of pores in mesoporous silica materials due to 2 MeV electron irradiation, as well as the relative stability of chemical properties of the pore walls. The origin of this collapse is not fully understood, but the ballistic effects cannot be completely ruled out in this process. Based on this concept, in order to have a better understanding of the mechanism underlying the collapse of the silicas mesoporous structure by electron (E <2 MeV), we conducted a series of tests on SBA-15 with varying incident electron energy to better understand underlying mechanism: Experiments with incidence electron energies fixed on 0.6-1.2-2.4 and 0.6-0.8-1 MeV were carried out using the LSI platform, while experiments with incident electron energies fixed on 10-30-200 keV were carried out using microscopes on the CIMAP/GANIL platform.

In this chapter, the degree of damage will be reflected by the degree of volume change of pores at 2GGy dose and compared to the trend of effective cross section in experiments with incoming electron energy of 0.6-2.4 MeV. As for experiments with incoming electron energy ranging from 10-200 keV, we will calculate and compare the effective cross section using STEM images.

7.1 Material and methods

7.1.1 Sample preparation

7.1.1.a Pellet for LSI platform

l With the same methods as mentioned in chapter 2, the porous silica powder (type SBA-15 and MCM-41) were synthesized and then pressed into 8 mm diameter pellets at 250 MPa. After pressing into pellets, the pellets of SBA-15 and MCM-41 were annealed at 400 °C for 4 hours, an extra batch of SBA-15 pellets were annealed at 850 °C in order to have a represented the thermal synthesized silica and to substantially reduce microporosity in the pellets.

7.1.1.b Thin film for CIMAP/GANIL platform

200 nm thick foil specimens were prepared from porous thin silica films (type IPc) using the methods presented in the chapter 3.

7.1.2 Electron beam irradiation

7.1.2.a LSI

At the SIRIUS irradiation facility (Laboratoire des Solides Irradiés, Ecole Polytechnique, France), a NEC Pelletron was utilized for irradiation. The energy of the electron beam was estimated and modified to reach energy of 0.6-0.8-1-1.2-2.4 MeV at the sample surface after attenuation by the appropriate fixing devices. The experiment was carried out in two runs, the first (0.6 - 1.2 - 2.4 MeV) in 2020 and the second (0.6 - 0.8 - 1.0 MeV) in 2021.

These irradiations were undertaken to vary the electronic and nuclear stopping powers in order to see the influence of this parameter on the damage of the material. The values reported in the table 7.1 show that the nuclear stopping power evolves significantly (+119%) while the electronic stopping power is little modified (–6%).

TABLE 7.1: Stopping powers calculated by ESTAR and NIRL for 2.2g/cm^2 silica

Electron energy [MeV]	Electronic Stopping Power (ESTAR) [MeV cm^2/g]	[keV/nm]	Nuclear Stopping Power (NIEL) [MeV cm^2/g]	[keV/nm]
0.6	1.64	3.61E-04	3.23E-05	7.12E-09
0.8	1.58	3.47E-04	3.72E-05	8.18E-09
1.0	1.55	3.41E-04	4.13E-05	9.09E-09
1.2	1.54	3.39E-04	4.50E-05	9.90E-09
2.0 (chapter 6)	1.55	3.41E-04	5.67E-05	1.25E-08
2.4	1.56	3.44E-04	6.13E-05	1.35E-08

The irradiation conditions for both experiments are the same, as described below. A 2 GGy dosage was given on mesoporous silica materials, and irradiations were carried out at a current of around 25 µA, which is equivalent to around 5E13 $e^{-}.cm^{-2}.s^{-1}$ at ambient temperature (<45 °C). ESTAR calculations [158] of the stopping power in the specimen thickness demonstrate that electron dose deposition may be deemed homogenous for the whole pellet under these experimental circumstances. However, it should be noted that the pellets from the two tests may differ somewhat owing to the various synthesis batches, and we examine the differences of each pellet itself before and after irradiation to minimize unnecessary uncertainty. To monitor the evolution of the pores, nitrogen adsorption, SAXS, and helium pycnometry were used.

7.1.2.b GANIL/CIMAP

Electron beam irradiation was performed in the FEI Helios system with a beam energy of 10 keV and 30 keV, and in the JEOL JEM F200 system with a beam energy of 200 keV. To achieve the irradiation by electronic microscopie, a lift-out of the IPc specimen was realized using the method mentioned before in chapter 3. An area of the 200 nm thick foil was selected for the necessary focusing processes and other optimization of the electron microscope parameters. Once the electron beam was focused and stable, the electron beam was temporarily blocked and then the foil sample was moved slightly to an area that had not been bombarded by the electron beam. A series of micrographs of increasing dose was then recorded using the irradiation parameters are shown in table 7.2 and 7.3.

TABLE 7.2: Stopping powers of electron microscopy irradaition

Beam voltage [kV]	Electronic Stopping Power (ESTAR) [MeV cm^2/g]	[keV/nm]	Nuclear Stopping Power (NIEL) [MeV cm^2/g]	[keV/nm]
10	17.8	3.92E-03	0	0
30	7.80	1.72E-03	0	0
200	2.32	5.10E-04	1.54E-05	3.39E-09

TABLE 7.3: Electron microscopy irradiation parameters

Beam voltage (kV)	Current (pA)	Dwell time (µs)	Final Dose (e$^-$.cm^{-2})
10	100	10	2.12E+20
30	100	10	2.12E+20
200	176*	10	9.05E+20

*The current value reported here for the 200 kV experiment is an approximation; owing to the experimental conditions, we are unable to confirm the precise current values acquired by the samples.

The geometric parameters of irradiation are shown in the schematic diagram 7.1. We examine the thickness fluctuation of the mesoporous silica layer as well as the pore variation in real-time images.

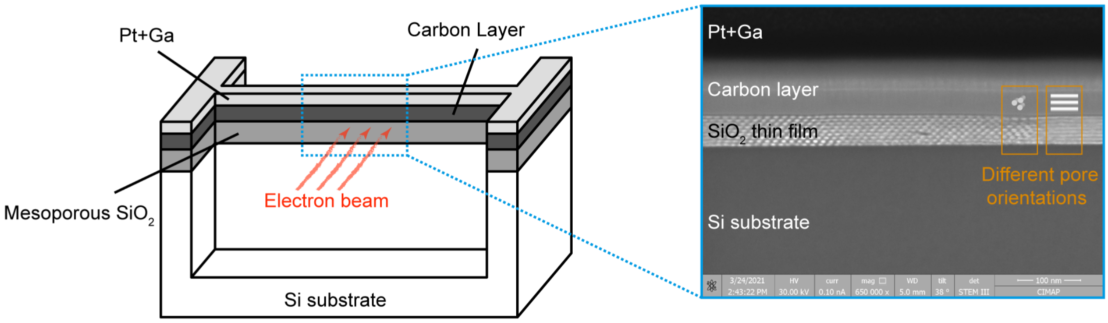

FIGURE 7.1: A schematic diagram of the electron microscopy irradiation set-up.

7.2 Results

7.2.1 Experiments with incident electron energies fixed on 0.6 - 2.4 MeV

7.2.1.a Isotherm curve and PSD

After irradiation, all examined mesoporous silicas exhibit a decrease in adsorbed gas volumes at saturation (figure 7.2). The degree of decrease is classified as follows:

MCM-41 > SBA-15 annealed at 400 °C > SBA-15 annealed at 850 °C

All adsorption isotherms of MCM-41 and SBA-15 pellets are characteristic of a type IV curve, indicating the presence of meso-pores before and after irradiation.

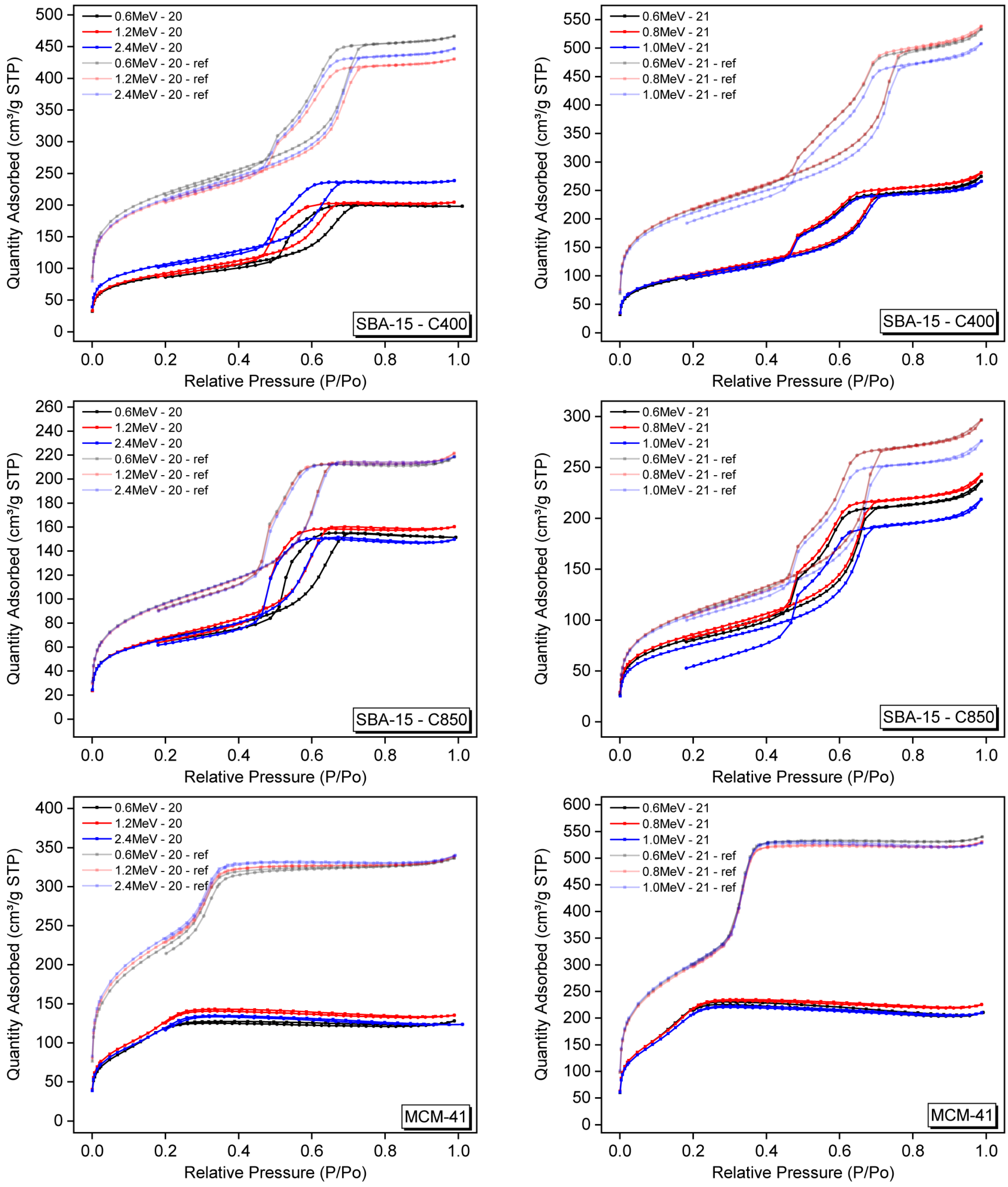

FIGURE 7.2: Nitrogen adsorption / desorption isotherms at 77K of silica pellets under electron beam irradiation.

The pore size distribution estimated from the nitrogen adsorption isotherm using the density functional theory (NLDFT) technique is shown in figure 7.3. The pore volumes in each sample decreased after electron beam irradiation. Furthermore, for the 400°C annealing temperature treatment, the decrease of mesopores is less than the reduction of micropores. These findings were in good accord with the findings presented in Chapter 6. As for the pellets suffered 850°C treatment, as mentioned before in chapter 2, it does not significantly affect the mesopore structure, but it can be seen from the pore size distributions that the volume of the micropores is greatly reduced. At the same time, a higher degree of polymerization of the pore walls should also occur. The mesopores of SBA-15 appear to be less impacted by electron beam irradiation in pellets that have experienced a relatively high annealing temperature (850 °C compared to 400 °C).

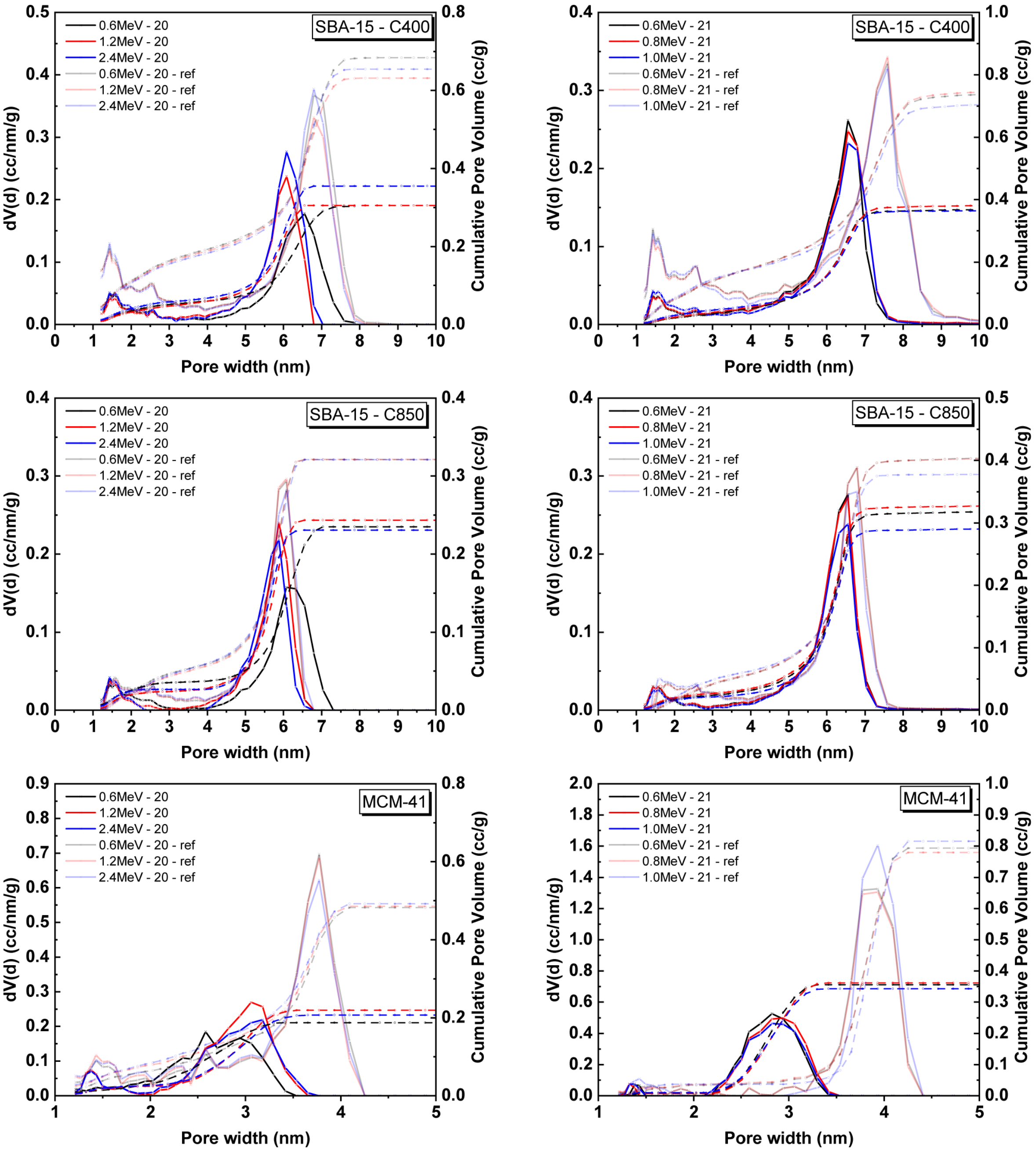

FIGURE 7.3: Pore size distribution of silica samples under electron beam irradiation.

7.2.1.b SAXS

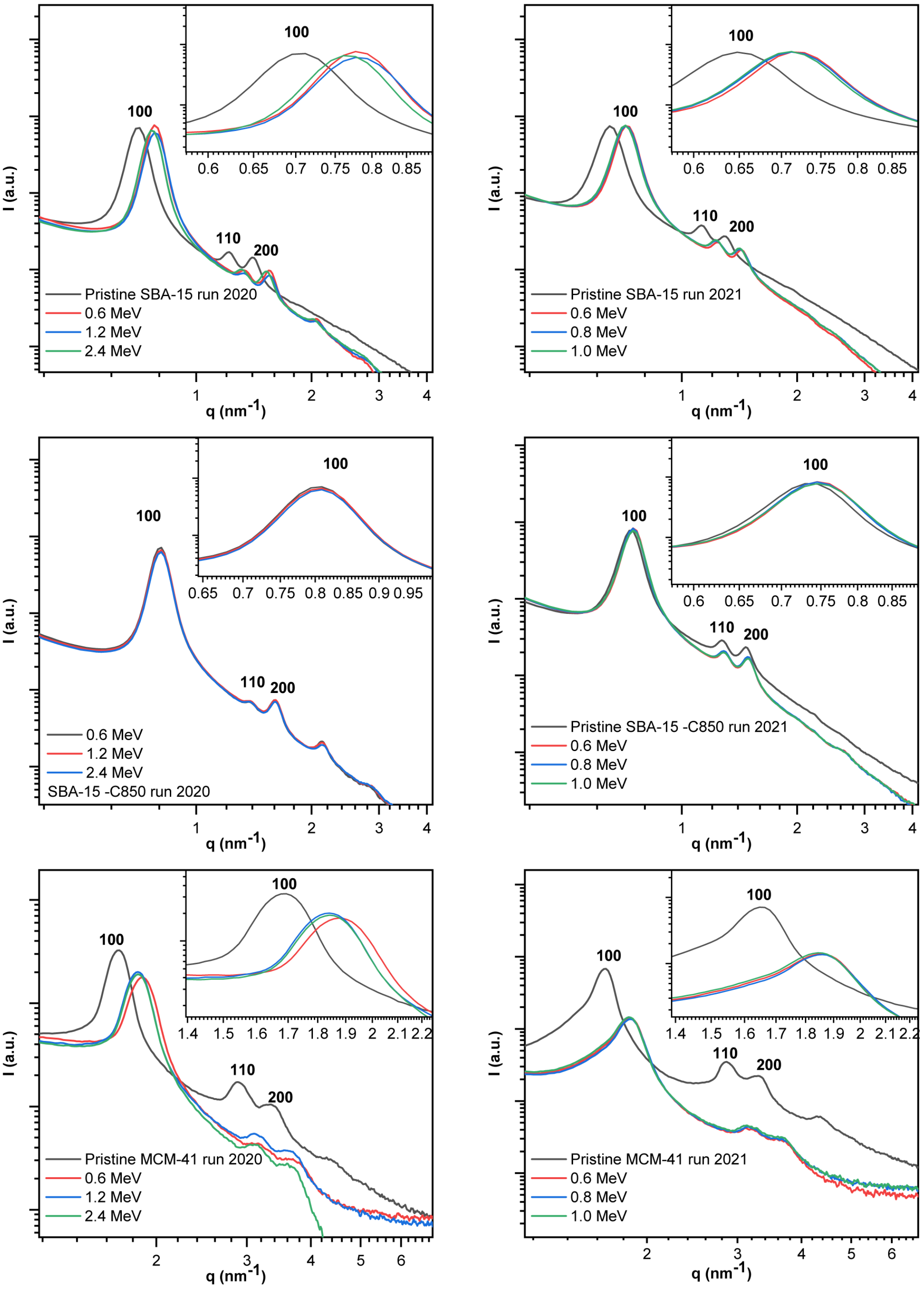

FIGURE 7.4: SAXS pattern of silica samples under electron beam irradiation.

Figure 7.4 shows SAXS data taken on pellets following electron beam irradiation. The scattering intensity shows three well-resolved peaks labeled (100), (110), and (200), which are linked with p6mm hexagonal symmetry. Under irradiation, the structural peaks for each sample shift to high q values, indicating a reduction in the lattice parameter a_0. (for 2D hexagonal structure $a_0 = 2d_{100}/\sqrt{3}$, where $d_{100} = 2\pi/q_{100}$). The intensity of SBA-15 is relatively constant before and after irradiation, indicating that the orderliness of its mesoporous structure has not been significantly affected; on the contrary, the intensity of the three peaks in MCM-41 is significantly reduced, indicating that the orderliness of the pores in MCM-41 has been significantly disrupted.

7.2.1.c Helium pycnometry measurements

Density analysis by helium pycnometry is used to obtain information on the skeletal density of porous silica pellets under electron irradiation. The statistics are shown in the table 7.4.

Due to the tiny mass of each pellet (less than 50 mg), this pycnometry measurement is extremely prone to measurement error. A variation of just 0.5 mg in the mass measurement can result in around 1 percent change in the final computed percentage value. Despite our best attempts to take precautions and remove as much of the adsorbed water vapor as possible, due to the hydrophilicity of porous silica, the final results should really be interpreted with caution.

Previous studies based on non-porous silica [66, 67, 110] have demonstrated that particle or ionizing radiation could induces a densification in a-SiO_2 which attains a constant value ~ 3% with respect to the relaxed network. In fact, the results shown here is not in conflict with their findings. First, we are far from reaching the desired dose necessary for the evolution of density, as mentioned in chapter 5, which is greater than 10 GGy and the value of 3% swelling is obtained at approximately 30 GGy. Second, our study is on porous silica, and our findings have shown that the pores in this type of silica shrink or close under the effect of irradiation. Our Skeletal density measured by helium pycnometry actually includes the possible existence of closed pores in the silica pore walls. Therefore, it is possible that the reduction in skeletal density shown here is the result of an overall reduction in skeletal density due to the closure of the originally open pores in the pore walls by irradiation.

As a matter of fact, the data presented here are not at odds with their findings. First, as previously stated in Chapter 6, we are still far from achieving the ideal dose necessary for the evolution of density, which is larger than 10 GGy, and the value of 3 % swelling is attained at roughly 30 GGy. Second, our research is focused on porous silica, and our studies have revealed that the pores in porous silica can shrink or close when exposed to electron beam. When we use helium pycnometry to assess our skeletal density, we take into account the density of closed pores in the silica skeletal if it exists. As a result, the observed decrease in skeletal density is most likely the result of an overall decrease in skeletal density induced by the closure of previously open pores induced by radiation.

TABLE 7.4: Summary of the skeletal density of silica samples under electron beam irradiation.

Skeletal density (g/cm^3)			Pristine	Irradiated	%
SBA-15 C400	Run 2020	0.6 MeV	2.19	2.21	0.9%
		1.2 MeV	2.19	2.21	1.1%
		2.4 MeV	2.19	2.23	1.8%
	Run 2021	0.6 MeV	2.18	2.17	-0.3%
		0.8 MeV	2.18	2.17	-0.4%
		1.0 MeV	2.19	2.16	-1.7%
SBA-15 C850	Run 2020	0.6 MeV	2.27	2.21	-2.5%
		1.2 MeV	2.27	2.23	-1.6%
		2.4 MeV	2.27	2.23	-2.0%
	Run 2021	0.6 MeV	2.33	2.26	-3.0%
		0.8 MeV	2.34	2.26	-3.7%
		1.0 MeV	2.31	2.27	-1.4%
MCM-41	Run 2020	0.6 MeV	2.19	2.21	0.9%
		1.2 MeV	2.19	2.21	1.1%
		2.4 MeV	2.19	2.23	1.8%
	Run 2021	0.6 MeV	2.27	2.21	-3.0%
		0.8 MeV	2.31	2.23	-3.3%
		1.0 MeV	2.29	2.25	-1.9%

7.2.2 Experiments with incident electron energies fixed on 10 - 30 - 200 keV

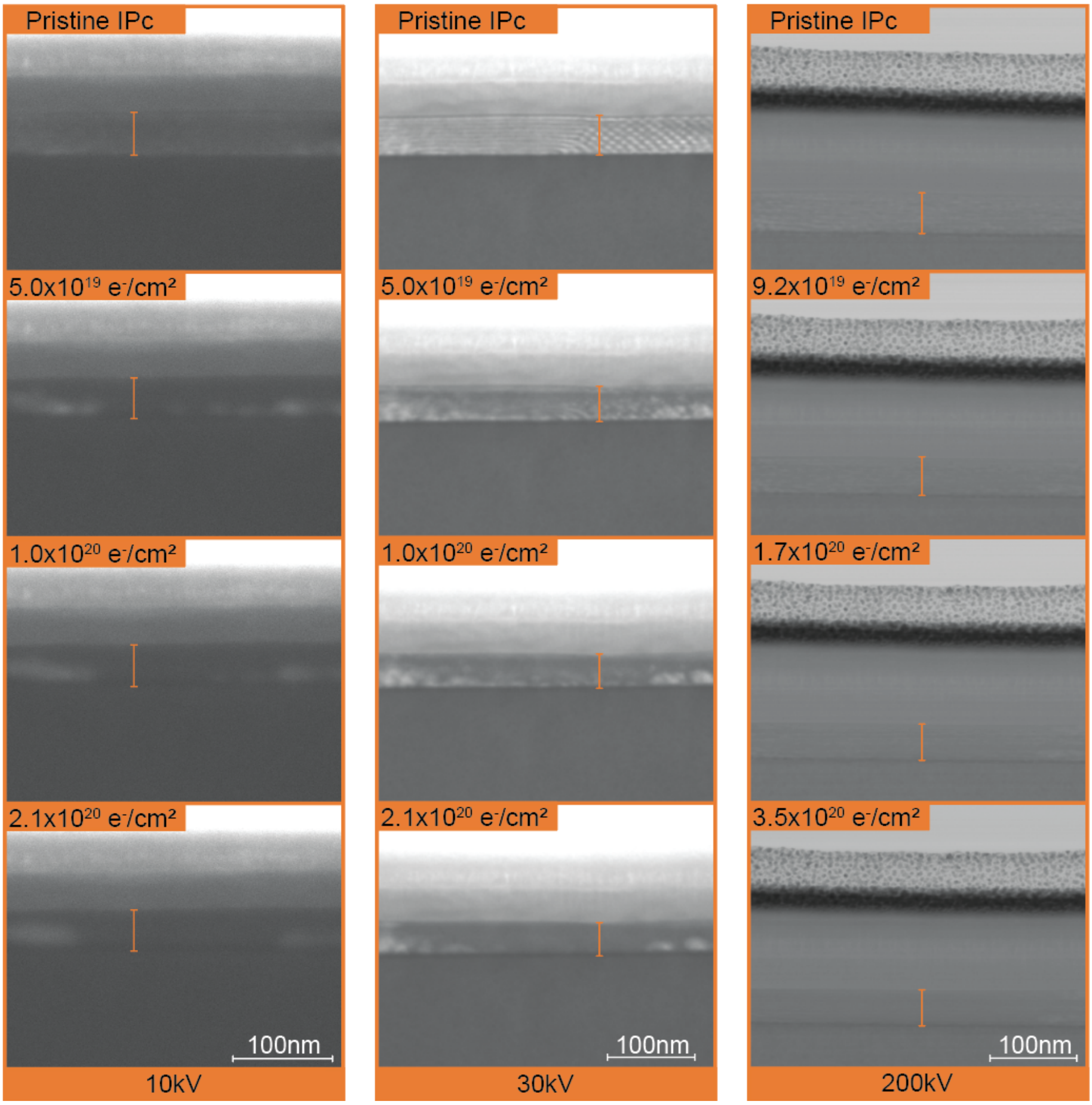

FIGURE 7.5: Select frames from STEM movies of IPc foil that was modified by the electron beam upon increasing the dose.

Figure 7.5 shows four representative in situ thickness measurements of IPc foil taken from the bright-field micrograph STEM movie of cross-section FIB specimen of each experiment. In all cases, we can observe a reduction in the thickness of the mesoporous silica layer and a gradual collapse of the pores. The dose required for the last observable pore to disappear increases with increasing incident electron energy.

The evolution of the thickness of the porous silica film with dose is shown in figure 7.6.

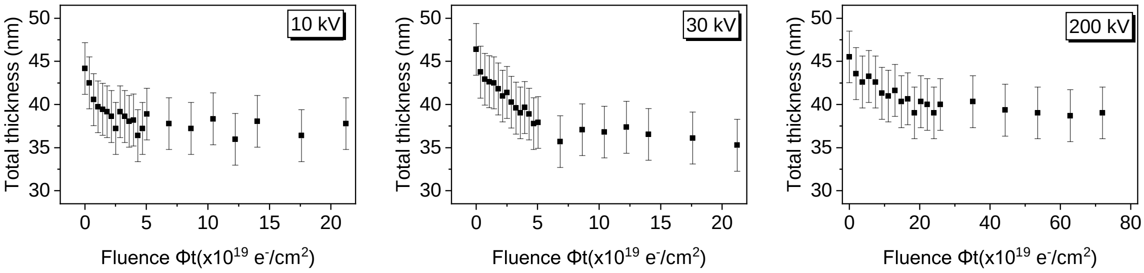

FIGURE 7.6: Absolute thickness of IPc foils vs. electron beam exposure dose.

Under this experimental condition, the sample is exposed to an irradiation flux several orders of magnitude greater than that used in the LSI electron irradiation experiments, and we must account for the possibility of an increase in sample temperature caused by the electron beam bombardment, as well as the possibility of further changes in the pore structure. Although we were unable to directly measure the temperature in this experiment, we can infer from the change in the Gallium (Ga) layer in the image that the electron beam bombardment did not considerably increase the temperature of the silica film. Since Ga is an element with a relatively low melting point (302.9146 K), if the temperature of the silica film increases greatly, it is unlikely that the Ga layer will be in a strikingly uniform position in successive scans. Consequently, it is reasonable to disregard any temperature-related modifications in the porous silica thin films.

7.3 Discussion

7.3.1 Experiments with incident electron energies fixed on 0.6 - 2.4 MeV

The results of two experiments at LSI (the first (0.6 - 1.2 - 2.4 MeV) in 2020 and the second (0.6 - 0.8 - 1.0 MeV) in 2021) demonstrated that the behavior of the three mesoporous silica (SBA-15-C400, SBA-15-C800 and MCM-41) after being irradiated with a dosage of 2 GGy did not depending significantly on the incident electron energy (in the range of 0.6 - 2.4 MeV). The pore structure changes deduced from the results of nitrogen adsorption and SAXS are constant and uniform across this range of incoming electron energy. In the meanwhile, the results of ESTAR and NIEL calculations show (figure 7.7) that the nuclear stopping power evolves significantly while the electronic stopping power is little modified within the range of 0.6 - 2.4 MeV. As a result, we may deduce that the "radiolytic" process dominates the pore structure evolution in this range of incident electron energy.

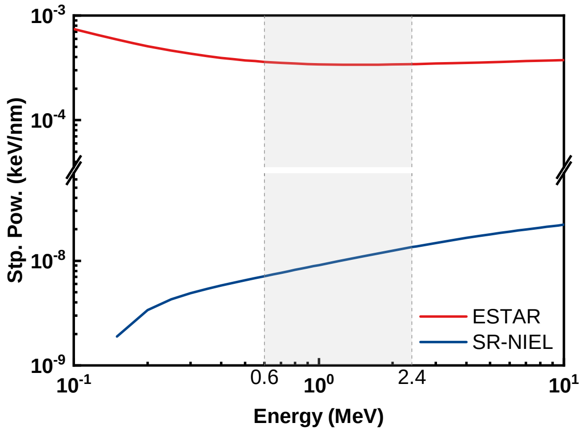

FIGURE 7.7: Ionizing (calculated by ESTAR) and non-ionizing energy loss (calculated by SR-NIEL) in silicon dioxide.

Meanwhile, if we focus on the two types of silica annealed at 400 °C, we can see the effect of pore size. The micropores in SBA-15 are the most affected, as these pores tend to close immediately; followed by the mesopores in MCM-41, where the volume is significantly reduced, the overall structure (as determined by the SAXS results) is affected but still maintains a certain degree of orderliness. The most stable pores are those mesopores in SBA-15 (which have a bigger diameter than those in MCM-41), and although their volume is decreased, the SAXS findings indicate that their orderliness remains stable. We may deduce that the pore structure becomes more stable as the pore diameter grows in the region of 1 nm to 8 nm.

The annealing temperature is another factor that contributes to the stability of the pore structure. The mesopore performance of SBA-15 at various annealing temperatures reveals that at the present experimental dosage (2 GGy), the pellets subjected to a higher annealing temperature exhibit less mesopore alteration. This is consistent with the finding obtained by Blanford *et al.* [112] after electron microscopic irradiation of MCM-41.

7.3.2 Experiments with incident electron energies fixed on 10 - 30 - 200 keV

After measuring the thickness of the mesoporous silica layer in each image (figure 7.6), apparent cross-section σ can be roughly estimated by assuming that the reduction of thickness (τ) follows a simple Poisson law as $\tau = \tau_{\max}(1 - \exp(-\sigma \bullet \Phi t))$.

Following the same arguments as in chapter 3, 40% is taken here as "saturation" value τ_{max}, even if this value is not reached in our observation time. The fabrication of FIB samples, in fact, leaves a layer of carbon on the thin film material, and this layer is also a potential factor that causes the reduction rate of the film thickness to decrease significantly and almost stagnate once reach approximately 15 - 20 %. The saturation value of 40 % was set could also reduce the effect of the carbon layer on the final statistical results to a certain level. The figure 7.8 shows the results of the fit with the corresponding apparent cross-section σ, table 7.5 summarizes the radius deduced from the damage cross section.

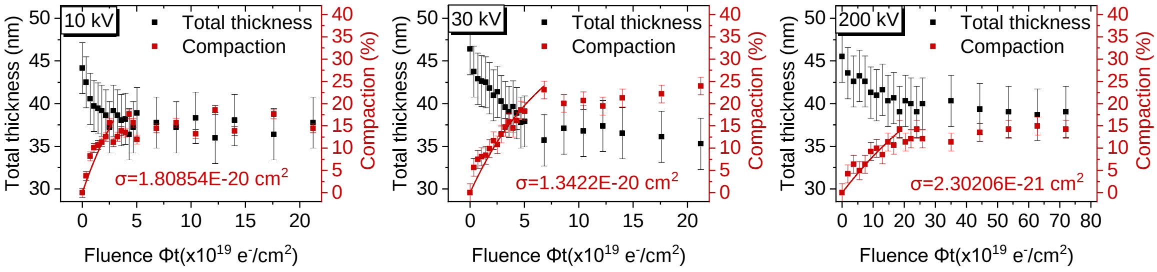

FIGURE 7.8: Fitted results and the corresponding apparent cross-sections.

TABLE 7.5: Radius deduced from the damage cross section

Beam voltage (kV)	Total stopping power ($\times 10^{-3}$ keV/nm)	Cross-section ($\times 10^{-6}$ nm^2)	Radius ($\times 10^{-4}$ nm)
10	3.92	1.81±0.18	7.6±0.8
30	1.72	1.34±0.06	6.5±0.3
200	0.43	0.99±0.07	5.6±0.4

The calculation results of effective cross-section values σ also show that σ(10kV) >σ(30kV) >σ(200kV), which follows the same trend of radiolytic cross-section as calculated theoretically (figure 7.9). These results suggest that the radiolytic mechanism dominates under experimental conditions within the electron beam energy of 10kV-200kV.

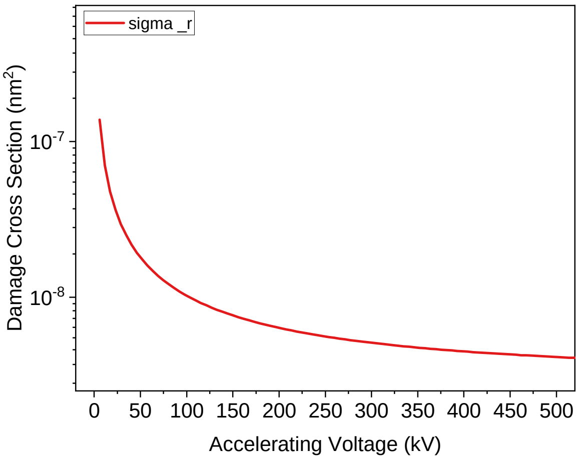

FIGURE 7.9: Theoretical radiolytic cross-sections of non-porous silica obtained based on the method described by Blanford *et al.* [112].

7.4 Conclusion

We can see from the experimental data presented in this chapter that, electron irradiation at various energy levels between 10keV to 2.4MeV induced pore shrinkage. The change of dominant damage mechanism reported in nonporous monocrystalline silicon was not observed under the present experimental conditions with porous silica, and the radiolytic mechanism is always the dominant damage mechanism.

However, we cannot rule out alternative processes, such as the one reported by Ojovan *et al.* [156] for the irradiation-induced modification of viscosity.

General conclusion and future work

The behavior of ordered mesoporous silica materials under irradiation in the electronic regime has been explored in this PhD thesis. Two different morphologies of ordered mesoporous silica were synthesized: thin film silica on a wafer substrate and mesoporous silica pellet compacted from conventional SBA-15 and MCM-41 powders. The successful synthesis of such ordered mesoporous silica has made it feasible to appropriately apply several irradiation facilities (GANIL, CEMHTI, LSI,...) for external irradiation studies and the subsequent characterizations.

The diverse experimental conditions were carefully designed to encompass as much as possible the range of electronic stopping power from 10^{-4} keV/nm to 12 keV/nm on the one hand, and to match the capabilities of the different irradiation facilities on the other hand. The irradiation experiments can be classified into two primary categories: ion beam irradiation and electron beam irradiation. In the ion beam irradiation studies, swift heavy ions with a range of energies (0.98 MeV/A carbon, 9.17 MeV/A calcium, 0.98 MeV/A argon, 0.57 MeV/A nickel, 0.86 MeV/A krypton, and 0.55 - 0.71 MeV/A xenon) were used in order to keep ballistic effects to a bare minimum. In the electron beam irradiation experiments, irradiation with incident electron energies ranging 10 kV - 30 kV - 200 kV was achieved using the electron microscope in CIMAP, whereas irradiation with incident electron energies ranging from 0.6 MeV to 2.4 MeV was achieved using the accelerator of LSI. In addition, a series of 16 MeV H^+ ion irradiation studies carried out at CEMHTI partially closed the stopping power gap that existed between SHI and electron irradiation.

The following are the major outcomes from this thesis:

- SHI irradiation: The total thickness of both types of porous silica thin films (IPc and ICc) decreased under irradiation. More precisely, at low doses, the total thickness reduction was positively correlated with the interlayer thickness reduction. Damage radius was found to be positively correlated with the S_e of the incident particles. At high dosages, distinct patterns of damage were observed, which were S_e dependent. When compared to the non-porous material, the IR data reveal that the existence of pores mitigates the irradiation-induced changes in the silica network. The mechanism is satisfactorily explained by a simulation based on the 3DTS model.

- H^+ irradiation: Monitoring the structure of the SBA-15 pellet demonstrates that bombardment with 16 MeV H^+ can promote mesopore contraction. The possible mechanism is briefly discussed.

- Electron irradiation: Under electron irradiation at 2 MeV, mesopores in SBA-15 and MCM-41 pellets were shrunk progressively, but no significant changes in the chemical characteristics of the silica network were found (NMR, IR, etc.). The follow-up irradiation experiments using varied incident electron energy (0.6 - 2.4 MeV) suggest a radiolytic damage process. Parallelly, electron microscopy irradaition investigations indicate that the shrinkage of the pores observed in a different incident electron energy range (10 - 200 kV) is dominated by a radiolytic process.

Under all irradiation conditions, the pore structure as well as the characteristics of the pore wall silica network were monitored. All of the experimental results demonstrated that the ordered pore structures were subjected to certain level of irradiation-induced alteration. The volume of the pores shrank, or even collapsed to different degrees. We have made several attempts to determine the damage radius under different irradiation circumstances by following the fluctuation of the pores with influence. These damage radius are depicted in the figure I as a function of total stopping power, together with damage radius obtained for non-porous silica that have been explored in this work or published by Toulemonde *et al.* [84, 85] and Rotaru *et al.* [113], as well as damage radius obtained for mesoporous silica irradiated in the ballistic regime that have been obtained in earlier research of Lou *et al.* [16]

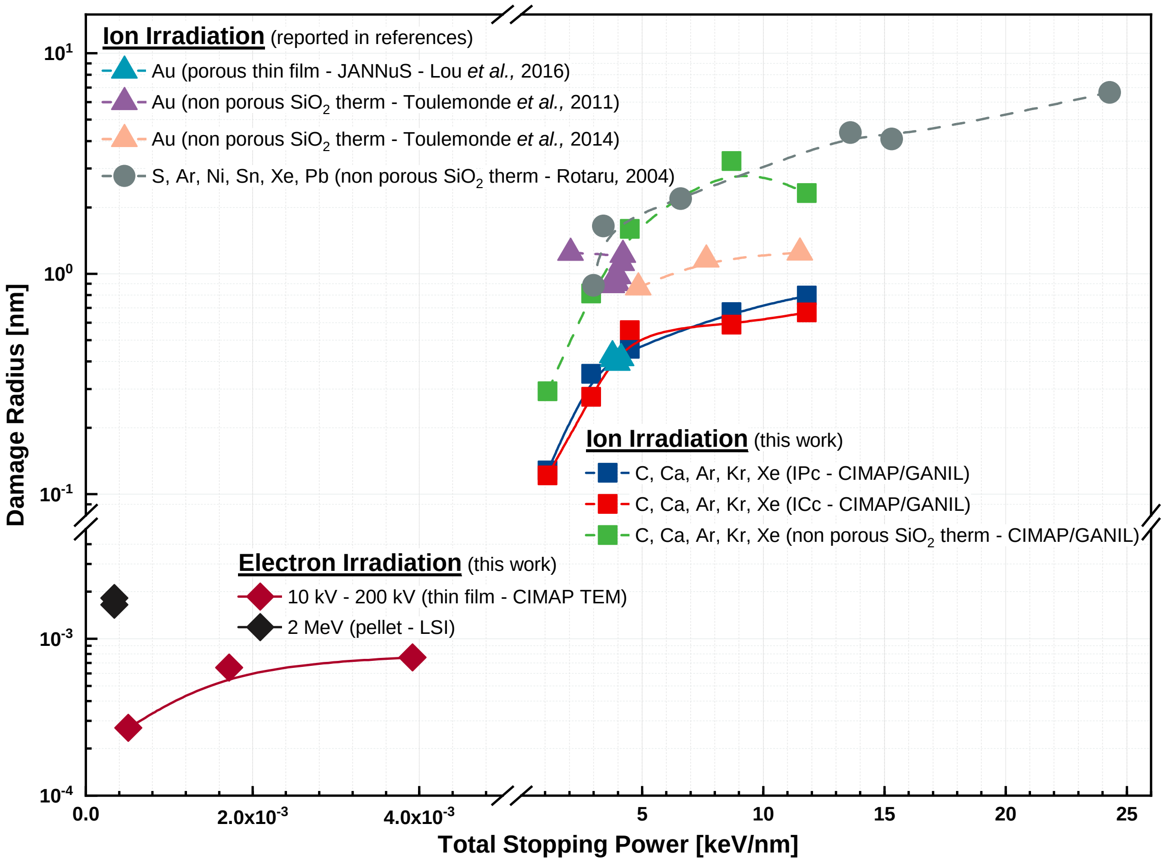

Figure I. Summary of damage radius as a function of total stopping power. Solid lines indicate results obtained from porous silica and dashed lines indicate results obtained from nonporous silica. Triangles indicate damage radius obtained from the Au ion beam irradiation[16, 84, 85], in which S_n cannot be ignored or even dominated over S_e.

The first thing that stands out in the data is the difference between porous and non-porous silica, with non-porous silica having a greater damage radius at the same total stopping power. Although the total stopping power includes S_n and S_e and the mechanisms of SHI and Au beam irradiation are not identical, we can focus on the two sets of results: those of Lou *et al.* [16] on porous silica and Toulemonde *et al.* [84, 85] on nonporous silica under Au irradiation; and the findings of this thesis on porous and nonporous silica under SHI irradiation in conjunction with the findings for nonporous reported by Rotaru *et al.* [113]. The comparison of damage radius demonstrates that the presence of pores significantly decreases the chance of radiation-induced material alteration. This result indicates that the presence of pores slows the accumulation of irradiation-induced damage. This conclusion is supported by the results in Chapter 3 on IR, which demonstrate that the IR changes caused by irradiation of the silica network in the porous silica material are less than nonporous silica at the same dosage.

When this is combined with the fact that pore shrinkage occurs under all irradiation settings, we may infer that irradiation causes a smooth shrinking of the mesopores in the mesoporous material while having a relatively mild impact on the silica in the pore walls. As demonstrated in the pre-experiments (Chapter 2) and the section on electron irradiation (Chapter 6 and 7), irradiation causes a more mild shrinkage of the pores than pressure does, and the mesopores shrink gradually rather than collapsing completely.

Additionally, as seen in Figure I, the damage radius rises with increasing stopping power for ion irradiation. When we compare the results of Lou *et al.*[16] from Au beam irradiation to the results from SHI of the current work, we notice that when a porous structure is present, the total stopping power has a dominant effect on the damage radius, and appears to have nothing to do with their regime (ballistic or electronic). Indeed, this finding is corroborated by the synergy of nuclear and electronic energy losses during ion-irradiation processes on nonporous vitreous silicon dioxide reported by Toulemonde *et al.*[85]

Concerning the experimental results discussed in Chapter 4 (different damage pattern dependent on S_e), they are more likely to be similar to the classical damage (track formation and sputtering) in nonporous materials caused by ion beam bombardment. In fact, when S_e is large enough, the pore structure is completely closed (or destroyed) at low dose, as can be seen from the disappearance of the bragg peak in XRR. This implies that the possibility of pore closure by irradiation is determined by the total stopping power but the final damage pattern presented in the material at higher doses will be determined by the different radiation mechanisms (elastic collision in the nuclear regime, inelastic thermal process in the electronic regime (track creation or sputtering).

With regard to electron beam irradiation, the damage cross section caused by a 2 MeV electron beam is one order of magnitude greater than that caused by 10 kV - 200 kV electron beams. This may be due to the difference in damage mechanism or the material form (bulk vs. foil), which is more likely to be the latter as the damage mechanism is shown to be the same (radiolytic mechanism) based on the analytical discussion of the results in Chapters 6 and 7.

In general, the mesoporous materials we investigated demonstrated differing levels of pore structural shrinkage over the particle irradiation range of 10^{-4} keV/nm to greater than 12 keV/nm of electronic stopping power. Indeed, it is inferred that porous materials such as mesoporous silica, but maybe also MOF and other materials, are suitable matrices for packaging nuclear waste. As demonstrated in the ANR Automact project [165], an all-in-one separation/conditioning technology for the collection and treatment of actinide elements and their fission products (I, Cs...) based on porous material with auto-irradiation-induced pore closing appears promising.

Additionally, this work may serve as an inspiration for deep geological disposal of vitrified waste packages from nuclear fuel reprocessing. On the surface of nuclear glasses, alteration gels are formed. A porous gel layer is created, and this study implies that this porous material layer may self-heal as a result of radiation exposure.

Despite these promising outcomes, there are still certain problems that need to be answered and further investigation is necessary:

- Except for the Ca case (9.17 MeV/A), the majority of incident particles in ion irradiations have kinetic energies between 0.5 and 1 MeV/A. In other words, in this scenario, we do not take into account the velocity effect. Whereas existing works [166–169] assert that the velocity effect is essential in the radiation-induced damage process, the damage is higher at low velocity than at high velocity for the same value of dE/dx.

- In a previous study on nonporous SiO_2 quartz, Meftah *et al.* [148] discovered that the latent track is not always continuous and cylindrical around the track formation thresholds (~2 keV/nm). The possibility that a comparable effect may occur in the porous material was not discussed in this thesis.

- We noticed that when SBA-15 is irradiated with electrons, the micropores tend to close abruptly, but the mesopores progressively shrink. However, no significant difference in irradiation behavior due to pore size was seen in other irradiation studies (IPc vs. ICc, SBA-15 vs. MCM-41). It is necessary to explore materials with a broader variety of pore diameters to determine whether there is a radius threshold of pore contraction and closure behavior. If this potential threshold has ever existed, it would be interesting to know if it can be taken as a comparison with the window of radiation resistance reported by Bringa *et al.*[10]

Bibliography

[1] W. J. Weber, R. C. Ewing, C. A. Angell, *et al.*, “Radiation Effects in Glasses Used for Immobilization of High-level Waste and Plutonium Disposition”, *Journal of Materials Research*, vol. 12, no. 8, pp. 1948–1978, 2011 (cit. on p. 1).

[2] R. C. Ewing, W. J. Weber, and F. W. Clinard, “Radiation effects in nuclear waste forms for high-level radioactive waste”, *Progress in Nuclear Energy*, vol. 29, no. 2, pp. 63–127, 1995 (cit. on p. 1).

[3] G. H. Kinchin and R. S. Pease, “The Displacement of Atoms in Solids by Radiation”, *Reports on Progress in Physics*, vol. 18, no. 1, pp. 1–51, 1955 (cit. on p. 1).

[4] G. Ackland, “Controlling radiation damage”, *Science*, vol. 327, no. 5973, pp. 1587–1588, 2010 (cit. on p. 1).

[5] Y.-Q. Chang, Q. Guo, J. Zhang, *et al.*, “Irradiation effects on nanocrystalline materials”, *Frontiers of Materials Science*, vol. 7, no. 2, pp. 143–155, 2013 (cit. on p. 1).

[6] A. Misra, M. J. Demkowicz, X. Zhang, *et al.*, “The radiation damage tolerance of ultra-high strength nanolayered composites”, *Jom*, vol. 59, no. 9, pp. 62–65, 2007 (cit. on p. 1).

[7] M. Samaras, W. Hoffelner, and M. Victoria, “Irradiation of pre-existing voids in nanocrystalline iron”, *Journal of nuclear materials*, vol. 352, no. 1-3, pp. 50–56, 2006 (cit. on p. 1).

[8] N. Nita, R. Schaeublin, M. Victoria, *et al.*, “Effects of irradiation on the microstructure and mechanical properties of nanostructured materials”, *Philosophical Magazine*, vol. 85, no. 4-7, pp. 723–735, 2005 (cit. on p. 1).

[9] S. Wurster and R. Pippan, “Nanostructured metals under irradiation”, *Scripta Materialia*, vol. 60, no. 12, pp. 1083–1087, 2009 (cit. on p. 1).

[10] E. M. Bringa, J. D. Monk, A. Caro, *et al.*, “Are nanoporous materials radiation resistant?”, *Nano Letters*, vol. 12, no. 7, pp. 3351–5, 2012 (cit. on pp. 1, 131, 152).

[11] V. Luca, W. K. Bertram, J. Widjaja, *et al.*, “Synthesis of mesoporous zirconium titanates using alkycarboxylate surfactants and their transformation to dense ceramics”, *Microporous and Mesoporous Materials*, vol. 103, no. 1, pp. 123–133, 2007 (cit. on p. 1).

[12] J. H. Simmons, P. B. Macedo, A. Barkatt, *et al.*, “Fixation of radioactive waste in high silica glasses”, *Nature*, vol. 278, no. 5706, pp. 729–731, 1979 (cit. on p. 2).

[13] Y. Lou, S. Dourdain, C. Rey, *et al.*, “Structure evolution of mesoporous silica under heavy ion irradiations of intermediate energies”, *Microporous and Mesoporous Materials*, vol. 251, pp. 146–154, 2017 (cit. on pp. 2, 6, 131).

[14] Y. Lou, B. Siboulet, S. Dourdain, *et al.*, “Molecular dynamics simulation of ballistic effects in mesoporous silica”, *Journal of Non-Crystalline Solids*, vol. 549, p. 120 346, 2020 (cit. on pp. 2, 131).

[15] Y. Lou, G. Toquer, S. Dourdain, *et al.*, “Structure evolution of mesoporous silica SBA-15 and MCM-41 under swift heavy ion irradiation”, *Nuclear Instruments and Methods in Physics Research Section B: Beam Interactions with Materials and Atoms*, vol. 365, pp. 336–341, 2015 (cit. on pp. 2, 131).

[16] Y. Lou, “Behavior of mesoporous silica under ionic irradiation”, Thesis, 2016 (cit. on pp. 2, 6, 19, 150, 151).

[17] S. Klaumünzer, “Radiation compaction of porous Vycor glass”, *Nuclear Instruments and Methods in Physics Research Section B: Beam Interactions with Materials and Atoms*, vol. 166-167, pp. 459–464, 2000 (cit. on pp. 2, 19, 105, 107, 131).

[18] S. Klaumünzer, “Radiation compaction of nanoporous Vycor glass”, *Nuclear Instruments and Methods in Physics Research Section B: Beam Interactions with Materials and Atoms*, vol. 191, no. 1-4, pp. 356–361, 2002 (cit. on pp. 2, 19, 105, 107, 131).

[19] J. F. Ziegler, J. P. Biersack, and U. Littmark, *The stopping and range of ions in solids*. New York, N.Y.: Pergamon, 1985 (cit. on pp. 6, 7).

[20] J. Ziegler, J. Biersack, and M. Ziegler, *SRIM, the Stopping and Range of Ions in Matter*. SRIM Company, 2013 (cit. on pp. 6, 169).

[21] J. Keinonen, “Atomic Collisions in Matter”, in *Electrostatic Accelerators: Fundamentals and Applications*, R. Hellborg, Ed. Berlin, Heidelberg: Springer Berlin Heidelberg, 2005, pp. 486–505 (cit. on p. 7).

[22] M. L. Forcada, A. Gras-Martí, N. R. Arista, *et al.*, “Interaction of a Charged Particle With a Semi Infinite Non Polar Dielectric Liquid”, in *Interaction of Charged Particles with Solids and Surfaces*, A. Gras-Marti, H. M. Urbassek, N. R. Arista, *et al.*, Eds. Boston, MA: Springer US, 1991, pp. 639–645 (cit. on p. 7).

[23] S. Powers, “Ranges for Protons and Alpha Particles”, *ICRU report*, vol. 49, p. 116, 1993 (cit. on p. 7).

[24] G. Moliere, “Theorie der streuung schneller geladener teilchen i. einzelstreuung am abgeschirmten coulomb-feld”, *Zeitschrift für Naturforschung A*, vol. 2, no. 3, pp. 133–145, 1947 (cit. on p. 7).

[25] M. J. Berger, M. Inokuti, H. H. Anderson, *et al.*, “Report 37”, *Journal of the International Commission on Radiation Units and Measurements*, no. 2, NP–NP, 1984 (cit. on p. 8).

[26] P. R. M.J. Boschini and M. Tacconi, *SR-NIEL Calculator: Screened Relativistic (SR) Treatment for Calculating the Displacement Damage and Nuclear Stopping Powers for Electrons, Protons, Light- and Heavy- Ions in Materials (version 7.7.1); [Online] available at INFN sez. Milano-Bicocca, Italy [2021, December]: http://www.sr-niel.org/*. Online Database, 2014 (cit. on p. 8).

[27] H. Inui, H. Mori, T. Sakata, *et al.*, “Electron irradiation induced crystalline-to-amorphous transition in quartz single crystals”, *Journal of Non-Crystalline Solids*, vol. 116, no. 1, pp. 1–15, 1990 (cit. on pp. 8, 17, 132).

[28] T. Yanagisawa, T. Shimizu, K. Kuroda, *et al.*, “The preparation of alkyltrimethylammoniumkanemite complexes and their conversion to microporous materials”, *Bulletin of the Chemical Society of Japan*, vol. 63, no. 4, pp. 988–992, 1990 (cit. on p. 10).

[29] J. S. Beck, J. C. Vartuli, W. J. Roth, *et al.*, “A new family of mesoporous molecular sieves prepared with liquid crystal templates”, *Journal of the American Chemical Society*, vol. 114, no. 27, pp. 10 834–10 843, 1992 (cit. on p. 10).

[30] A. J. Schwanke, R. Balzer, and S. Pergher, “Microporous and Mesoporous Materials from Natural and Inexpensive Sources”, in *Handbook of Ecomaterials*, L. M. T. Martínez, O. V. Kharissova, and B. I. Kharisov, Eds. Cham: Springer International Publishing, 2019, pp. 3379–3399 (cit. on p. 11).

[31] D. Zhao, J. Feng, Q. Huo, *et al.*, “Triblock Copolymer Syntheses of Mesoporous Silica with Periodic 50 to 300 Angstrom Pores”, *Science*, vol. 279, no. 5350, pp. 548–552, 1998 (cit. on pp. 11, 13, 31).

[32] C. J. Brinker and G. W. Sherer, *Sol-Gel Science*. San Diego: Academic Press, 1990 (cit. on p. 12).

[33] P. Innocenzi, “Infrared spectroscopy of sol-gel derived silica-based films: a spectra-microstructure overview”, *Journal of Non-Crystalline Solids*, vol. 316, no. 2, pp. 309–319, 2003 (cit. on pp. 12, 26, 27).

[34] P. Innocenzi, P. Falcaro, D. Grosso, *et al.*, “Order-Disorder Transitions and Evolution of Silica Structure in Self-Assembled Mesostructured Silica Films Studied through FTIR Spectroscopy”, *Journal of Physical Chemistry B*, vol. 107, no. 20, pp. 4711–4717, 2003 (cit. on pp. 12, 40, 50).

[35] C. Sanchez, C. Boissière, D. Grosso, *et al.*, “Design, Synthesis, and Properties of Inorganic and Hybrid Thin Films Having Periodically Organized Nanoporosity”, *Chemistry of Materials*, vol. 20, no. 3, pp. 682–737, 2008 (cit. on p. 12).

[36] S. Girard, A. Alessi, N. Richard, *et al.*, “Overview of radiation induced point defects in silica-based optical fibers”, *Reviews in Physics*, vol. 4, p. 100 032, 2019 (cit. on p. 12).

[37] Y. Lu, R. Ganguli, C. A. Drewien, *et al.*, “Continuous formation of supported cubic and hexagonal mesoporous films by sol-gel dip-coating”, *Nature*, vol. 389, no. 6649, pp. 364–368, 1997 (cit. on p. 13).

[38] T.-H. Tran-Thi, R. Dagnelie, S. Crunaire, *et al.*, “Optical chemical sensors based on hybrid organic-inorganic sol-gel nanoreactors”, *Chemical Society Reviews*, vol. 40, no. 2, pp. 621–639, 2011 (cit. on p. 13).

[39] D. Kumar, K. Schumacher, C. du Fresne von Hohenesche, *et al.*, “MCM-41, MCM-48 and related mesoporous adsorbents: their synthesis and characterisation”, *Colloids and Surfaces, A: Physicochemical and Engineering Aspects*, vol. 187-188, pp. 109–116, 2001 (cit. on pp. 13, 31).

[40] R. L. Mozzi and B. E. Warren, “The structure of vitreous silica”, *Journal of Applied Crystallography*, vol. 2, no. 4, pp. 164–172, 1969 (cit. on p. 14).

[41] R. J. Bell and P. Dean, “The structure of vitreous silica: Validity of the random network theory”, *Philosophical Magazine*, vol. 25, no. 6, pp. 1381–1398, 1972 (cit. on p. 14).

[42] T. Gerber and B. Himmel, “The structure of silica glass”, *Journal of non-crystalline solids*, vol. 83, no. 3, pp. 324–334, 1986 (cit. on p. 14).

[43] M. A. Stevens-Kalceff, “Electron-irradiation-induced radiolytic oxygen generation and microsegregation in silicon dioxide polymorphs”, *Physical Review Letters*, vol. 84, no. 14, p. 3137, 2000 (cit. on p. 15).

[44] J. Song, L. R. Corrales, G. Kresse, *et al.*, “Migration of O vacancies in α-quartz: The effect of excitons and electron holes”, *Physical Review B*, vol. 64, no. 13, p. 134 102, 2001 (cit. on p. 15).

[45] Z.-Y. Lu, C. J. Nicklaw, D. M. Fleetwood, *et al.*, “Structure, Properties, and Dynamics of Oxygen Vacancies in Amorphous SiO_2”, *Physical review letters*, vol. 89, no. 28, p. 285 505, 2002 (cit. on p. 15).

[46] G. Gobsch, H. Haberlandt, H.-J. Weckner, *et al.*, “Calculation of the g-tensor and ^{29}Si hyperfine tensors of the E’ centre in silicon dioxide”, *Physica Status Solidi B: Basic Solid State Physics*, vol. 90, no. 1, pp. 309–317, 1978 (cit. on p. 16).

[47] D. L. Griscom, E. J. Friebele, and G. H. Sigel Jr, “Observation and analysis of the primary ^{29}Si hyperfine structure of the E’ center in non-crystalline SiO_2”, *Solid State Communications*, vol. 15, no. 3, pp. 479–483, 1974 (cit. on p. 16).

[48] R. A. Weeks, “Paramagnetic resonance of lattice defects in irradiated quartz”, *Journal of Applied Physics*, vol. 27, no. 11, pp. 1376–1381, 1956 (cit. on p. 16).

[49] R. A. Weeks and C. M. Nelson, “Trapped electrons in irradiated quartz and silica: II, electron spin resonance”, *Journal of the American Ceramic Society*, vol. 43, no. 8, pp. 399–404, 1960 (cit. on p. 16).

[50] D. L. Griscom, “E’ center in glassy SiO_2: Microwave saturation properties and confirmation of the primary Si 29 hyperfine structure”, *Physical Review B*, vol. 20, no. 5, p. 1823, 1979 (cit. on p. 16).

[51] J. Isoya, J. A. Weil, and L. E. Halliburton, “EPR and abinitio SCF-MO studies of the Si·H-Si system in the E’ 4 center of α-quartz”, *Journal of Chemical Physics*, vol. 74, no. 10, pp. 5436–5448, 1981 (cit. on p. 16).

[52] M. Stapelbroek, D. L. Griscom, E. J. Friebele, *et al.*, “Oxygen-associated trapped-hole centers in high-purity fused silicas”, *Journal of Non-Crystalline Solids*, vol. 32, no. 1-3, pp. 313–326, 1979 (cit. on p. 16).

[53] E. J. Friebele, D. L. Griscom, M. Stapelbroek, *et al.*, “Fundamental Defect Centers in Glass: The Peroxy Radical in Irradiated, High-Purity, Fused Silica”, *Physical Review Letters*, vol. 42, no. 20, pp. 1346–1349, 1979 (cit. on p. 17).

[54] A. A. Bobyshev and V. A. Radtsig, “Optical absorption spectra of paramagnetic defects in glassy SiO_2”, *The Soviet Journal of Glass Physics and Chemistry*, vol. 14, no. 4, pp. 274–279, 1989 (cit. on p. 17).

[55] R. A. B. Devine and A. Golanski, “Creation and annealing kinetics of magnetic oxygen vacancy centers in SiO_2”, *Journal of Applied Physics*, vol. 54, no. 7, pp. 3833–3838, 1983 (cit. on p. 17).

[56] G. W. Arnold and W. D. Compton, “Radiation Effects in Silica at Low Temperatures”, *Physical Review*, vol. 116, no. 4, pp. 802–811, 1959 (cit. on p. 17).

[57] R. L. Pfeffer, “Damage center formation in SiO_2 thin films by fast electron irradiation”, *Journal of Applied Physics*, vol. 57, no. 12, pp. 5176–5180, 1985 (cit. on p. 17).

[58] E. Dooryhee, Y. Langevin, J. Borg, *et al.*, “Characterization of defects formed in amorphous SiO_2 by high energy ions using electron spin resonance and optical spectroscopy”, *Nuclear Instruments and Methods in Physics Research Section B: Beam Interactions with Materials and Atoms*, vol. 32, no. 1, pp. 264–267, 1988 (cit. on p. 17).

[59] H. M. Naguib and R. Kelly, “Criteria for bombardment-induced structural changes in non-metallic solids”, *Radiation Effects*, vol. 25, no. 1, pp. 1–12, 1975 (cit. on pp. 17, 18).

[60] S. S. Batsanov, “The concept of electronegativity. Conclusions and prospects”, *Russian Chemical Reviews*, vol. 37, no. 5, p. 332, 1968 (cit. on p. 18).

[61] A. Benyagoub, S. Löffler, M. Rammensee, *et al.*, “Ion-beam-induced plastic deformation in vitreous silica”, *Radiation Effects and Defects in Solids*, vol. 110, no. 1–2, pp. 217–219, 1989 (cit. on p. 18).

[62] S. Klaumünzer, C. Li, S. Löffler, *et al.*, “Ion-Beam-Induced plastic deformation: A universal behavior of amorphous solids”, *Radiation Effects and Defects in Solids*, vol. 108, no. 1, pp. 131–135, 1989 (cit. on p. 18).

[63] A. Hedler, S. L. Klaumünzer, and W. Wesch, “Amorphous silicon exhibits a glass transition”, *Nature Materials*, vol. 3, no. 11, pp. 804–809, 2004 (cit. on p. 18).

[64] T. van Dillen, M. J. A. de Dood, J. J. Penninkhof, *et al.*, “Ion beam-induced anisotropic plastic deformation of silicon microstructures”, *Applied Physics Letters*, vol. 84, no. 18, pp. 3591–3593, 2004 (cit. on p. 18).

[65] V. Lotito, M. Karlusic, M. Jaksic, *et al.*, “Shape Deformation in Ion Beam Irradiated Colloidal Monolayers: An AFM Investigation”, *Nanomaterials (Basel)*, vol. 10, no. 3, 2020 (cit. on p. 18).

[66] W. Primak, “Fast-Neutron-Induced Changes in Quartz and Vitreous Silica”, *Physical Review*, vol. 110, no. 6, pp. 1240–1254, 1958 (cit. on pp. 19, 141).

[67] E. P. EerNisse and C. B. Norris, “Introduction rates and annealing of defects in ion-implanted SiO_2 layers on Si”, *Journal of Applied Physics*, vol. 45, no. 12, pp. 5196–5205, 1974 (cit. on pp. 19, 141).

[68] E. Lamour, “Transport of Fast Ions through Solid and Clusters under Intense Laser Pulses: Interaction dynamics probed by X-ray spectroscopy”, Thesis, 2012 (cit. on p. 20).

[69] C. Lastoskie, K. E. Gubbins, and N. Quirke, “Pore size distribution analysis of microporous carbons: a density functional theory approach”, *Journal of Physical Chemistry*, vol. 97, no. 18, pp. 4786–4796, 1993 (cit. on pp. 22, 32).

[70] P. I. Ravikovitch and A. V. Neimark, “Characterization of Micro- and Mesoporosity in SBA-15 Materials from Adsorption Data by the NLDFT Method”, *Journal of Physical Chemistry B*, vol. 105, no. 29, pp. 6817–6823, 2001 (cit. on pp. 22, 32).

[71] N. A. Seaton, J. P. R. B. Walton, and N. quirke, “A new analysis method for the determination of the pore size distribution of porous carbons from nitrogen adsorption measurements”, *Carbon*, vol. 27, no. 6, pp. 853–861, 1989 (cit. on pp. 22, 32).

[72] Z. Zhang and Z. Yang, “Theoretical and practical discussion of measurement accuracy for physisorption with micro- and mesoporous materials”, *Chinese Journal of Catalysis*, vol. 34, no. 10, pp. 1797–1810, 2013 (cit. on pp. 22, 32).

[73] E. P. Barrett, L. G. Joyner, and P. P. Halenda, “The determination of pore volume and area distributions in porous substances. I. Computations from nitrogen isotherms”, *Journal of the American Chemical society*, vol. 73, no. 1, pp. 373–380, 1951 (cit. on p. 22).

[74] L. G. Joyner, E. P. Barrett, and R. Skold, “The determination of pore volume and area distributions in porous substances. II. Comparison between nitrogen isotherm and mercury porosimeter methods”, *Journal of the American Chemical Society*, vol. 73, no. 7, pp. 3155–3158, 1951 (cit. on p. 22).

[75] G. Horváth and K. Kawazoe, “Method for the calculation of effective pore size distribution in molecular sieve carbon”, *Journal of Chemical Engineering of Japan*, vol. 16, no. 6, pp. 470–475, 1983 (cit. on p. 22).

[76] J. R. Françoise ROUQUEROL, R. Isabelle BEURROIES Philip LLEWELLYN, and DENOYEL, “Texture des materiaux divises - Taille de pores des materiaux nanoporeux par adsorption d’azote”, *Techniques de l’Ingénieur*, 2017 (cit. on p. 22).

[77] B. J. Inkson, “Scanning electron microscopy (SEM) and transmission electron microscopy (TEM) for materials characterization”, in *Materials Characterization Using Nondestructive Evaluation (NDE) Methods*, G. Hübschen, I. Altpeter, R. Tschuncky, *et al.*, Eds. Woodhead Publishing, 2016, pp. 17–43 (cit. on p. 25).

[78] E. Lippmaa, M. Maegi, A. Samoson, *et al.*, “Structural studies of silicates by solid-state high-resolution silicon-29 NMR”, *Journal of the American Chemical Society*, vol. 102, no. 15, pp. 4889–4893, 1980 (cit. on p. 25).

[79] M. Magi, E. Lippmaa, A. Samoson, *et al.*, “Solid-state high-resolution silicon-29 chemical shifts in silicates”, *Journal of Physical Chemistry*, vol. 88, no. 8, pp. 1518–1522, 1984 (cit. on p. 26).

[80] G. Rim, A. K. Marchese, P. Stallworth, *et al.*, “^{29}Si solid state MAS NMR study on leaching behaviors and chemical stability of different Mg-silicate structures for CO_2 sequestration”, *Chemical Engineering Journal*, vol. 396, p. 125 204, 2020 (cit. on p. 26).

[81] A. Lehmann, L. Schumann, and K. Hübner, “Optical Phonons in Amorphous Silicon Oxides. I. Calculation of the Density of States and Interpretation of LO-TO Splittings of Amorphous SiO_2”, *Physica Status Solidi B: Basic Solid State Physics*, vol. 117, no. 2, pp. 689–698, 1983 (cit. on p. 27).

[82] R. A. B. Devine, “Macroscopic and microscopic effects of radiation in amorphous SiO_2”, *Nuclear Instruments and Methods in Physics Research Section B: Beam Interactions with Materials and Atoms*, vol. 91, no. 1, pp. 378–390, 1994 (cit. on pp. 27, 43, 131).

[83] K. Awazu, S. Ishii, K. Shima, *et al.*, “Structure of latent tracks created by swift heavy-ion bombardment of amorphous SiO_2”, *Physical Review B*, vol. 62, no. 6, pp. 3689–3698, 2000 (cit. on pp. 27, 73, 83).

[84] M. Toulemonde, W. Assmann, Y. Zhang, *et al.*, “Material Transformation: Interaction between Nuclear and Electronic Energy Losses”, *Procedia Materials Science*, vol. 7, pp. 272–277, 2014 (cit. on pp. 27, 92, 150, 151).

[85] M. Toulemonde, W. J. Weber, G. Li, *et al.*, “Synergy of nuclear and electronic energy losses in ion-irradiation processes: The case of vitreous silicon dioxide”, *Physical Review B*, vol. 83, no. 5, p. 054 106, 2011 (cit. on pp. 27, 73, 150, 151).

[86] R. Salh, “Defect Related Luminescence in Silicon Dioxide Network: A Review”, in *Crystalline Silicon - Properties and Uses*. InTech, 2011, ch. Chapter 8 (cit. on pp. 28, 171, 172).

[87] A. Alessi, J. Kuhnhenn, G. Buscarino, *et al.*, “The Relevance of Point Defects in Studying Silica-Based Materials from Bulk to Nanosystems”, *Electronics*, vol. 8, no. 12, 2019 (cit. on p. 28).

[88] A. Alessi, A. Guttilla, S. Girard, *et al.*, “Radiation Effects on Aluminosilicate Optical Fibers: Spectral Investigations From the Ultraviolet to Near-Infrared Domains”, *Physica Status Solidi A: Applications and Materials Science*, vol. 216, no. 3, p. 1 800 485, 2018 (cit. on p. 28).

[89] A. Alessi, D. Di Francesca, S. Agnello, *et al.*, “Evidence of different red emissions in irradiated germanosilicate materials”, *Journal of Luminescence*, vol. 177, pp. 127–132, 2016 (cit. on p. 28).

[90] I. Reghioua, S. Girard, M. Raine, *et al.*, “Cathodoluminescence Characterization of Point Defects in Optical Fibers”, *IEEE Transactions on Nuclear Science*, vol. 64, no. 8, pp. 2318–2324, 2017 (cit. on p. 28).

[91] M. Thommes, K. Kaneko, A. V. Neimark, *et al.*, “Physisorption of gases, with special reference to the evaluation of surface area and pore size distribution (IUPAC Technical Report)”, *Pure and Applied Chemistry*, vol. 87, no. 9-10, pp. 1051–1069, 2015 (cit. on p. 32).

[92] G. Engelhardt and D. Michel, *High-resolution solid-state NMR of silicates and zeolites*. United States: John Wiley and Sons,New York, NY, 1987 (cit. on p. 34).

[93] A. Hertz, V. FitzGerald, E. Pignotti, *et al.*, “Preparation and characterisation of porous silica and silica/titania monoliths for potential use in bone replacement”, *Microporous and Mesoporous Materials*, vol. 156, pp. 51–61, 2012 (cit. on p. 37).

[94] S. Dourdain, A. Mehdi, J. F. Bardeau, *et al.*, “Determination of porosity of mesoporous silica thin films by quantitative X-ray reflectivity analysis and GISAXS”, *Thin Solid Films*, vol. 495, no. 1, pp. 205–209, 2006 (cit. on p. 47).

[95] M. Yan, M. J. Henderson, and A. Gibaud, “Grating induced micelle alignment of mesostructured silica films”, *Applied Physics Letters*, vol. 91, no. 2, p. 023 104, 2007 (cit. on p. 47).

[96] S. Dourdain, J.-F. Bardeau, M. Colas, *et al.*, “Determination by x-ray reflectivity and small angle x-ray scattering of the porous properties of mesoporous silica thin films”, *Applied Physics Letters*, vol. 86, no. 11, p. 113 108, 2005 (cit. on p. 47).

[97] S. O. Kucheyev, A. V. Hamza, and M. A. Worsley, “Ion-beam-induced stiffening of nanoporous silica”, *Journal of Physics D: Applied Physics*, vol. 42, no. 18, p. 182 003, 2009 (cit. on p. 48).

[98] S. O. Kucheyev, Y. M. Wang, A. V. Hamza, *et al.*, “Light-ion-irradiation-induced thermal spikes in nanoporous silica”, *Journal of Physics D: Applied Physics*, vol. 44, no. 8, p. 085 406, 2011 (cit. on p. 48).

[99] E. Van Cleve, S. Charnvanichborikarn, and S. O. Kucheyev, “Controlling surface hydroxylation of nanoporous silica by ion bombardment”, *Journal of Physics D: Applied Physics*, vol. 45, no. 44, p. 445 307, 2012 (cit. on p. 48).

[100] M. Toulemonde, C. Dufour, E. Paumier, *et al.*, “Does the Latent Track Occurrence in Amorphous Materials Result from a Transient Thermal Process?”, *MRS Proceedings*, vol. 504, p. 99, 1997 (cit. on pp. 50, 94).

[101] S. Szenknect, S. Finkeldei, F. Brandt, *et al.*, “Monitoring the microstructural evolution of $Nd_2Zr_2O_7$ pyrochlore during dissolution at 90 °C in 4 M HCl: Implications regarding the evaluation of the chemical durability”, *Journal of Nuclear Materials*, vol. 496, pp. 97–108, 2017 (cit. on p. 52).

[102] F. Salah, B. Harzallah, and A. van der Lee, “Data reduction practice in X-ray reflectometry”, *Journal of Applied Crystallography*, vol. 40, no. 5, pp. 813–819, 2007 (cit. on p. 52).

[103] A. van der Lee, “Grazing incidence specular reflectivity: theory, experiment, and applications”, *Solid State Sciences*, vol. 2, no. 2, pp. 257–278, 2000 (cit. on p. 54).

[104] A. Segmüller, “Observation of X-ray interferences on thin films of amorphous silicon”, *Thin Solid Films*, vol. 18, no. 2, pp. 287–294, 1973 (cit. on p. 54).

[105] W. Hink and W. Petzold, *Z. Angew. Phys.* 1958, vol. 10, p. 553 (cit. on p. 54).

[106] T. C. Huang, R. Gilles, and G. Will, “Thin-film thickness and density determination from x-ray reflectivity data using a conventional power diffractometer”, *Thin Solid Films*, vol. 230, no. 2, pp. 99–101, 1993 (cit. on p. 54).

[107] A. Gibaud and G. Vignaud, “Specular Reflectivity from Smooth and Rough Surfaces”, in *X-ray and Neutron Reflectivity: Principles and Applications*, J. Daillant and A. Gibaud, Eds. Berlin, Heidelberg: Springer Berlin Heidelberg, 2009, pp. 85–131 (cit. on pp. 54, 55).

[108] S. Klaumünzer, “Ion tracks in quartz and vitreous silica”, *Nuclear Instruments and Methods in Physics Research Section B: Beam Interactions with Materials and Atoms*, vol. 225, no. 1-2, pp. 136–153, 2004 (cit. on pp. 57, 58, 92).

[109] J. A. C. Marples, “Dose rate effects in radiation damage to vitrified radioactive waste”, *Nuclear Instruments and Methods in Physics Research Section B: Beam Interactions with Materials and Atoms*, vol. 32, no. 1-4, pp. 480–486, 1988 (cit. on p. 66).

[110] R. A. B. Devine, “Ion implantation- and radiation-induced structural modifications in amorphous SiO_2”, *Journal of Non-Crystalline Solids*, vol. 152, no. 1, pp. 50–58, 1993 (cit. on pp. 66, 73, 83, 88, 141).

[111] M. Toulemonde, S. M. M. Ramos, H. Bernas, *et al.*, “MeV gold irradiation induced damage in α-quartz: Competition between nuclear and electronic stopping”, *Nuclear Instruments and Methods in Physics Research Section B: Beam Interactions with Materials and Atoms*, vol. 178, no. 1-4, pp. 331–336, 2001 (cit. on pp. 66, 83).

[112] C. F. Blanford and C. B. Carter, “Electron radiation damage of MCM-41 and related materials”, *Microscopy and Microanalysis*, vol. 9, no. 3, pp. 245–63, 2003 (cit. on pp. 66, 121, 131, 145, 146).

[113] C. ROTARU, “SiO_2 on silicon : behavior under heavy ion irradiation”, Thesis, 2004 (cit. on pp. 69, 73, 80, 81, 83, 87, 150, 151).

[114] G. Mie, “Beiträge zur Optik trüber Medien, speziell kolloidaler Metallösungen”, *Annalen der Physik*, vol. 330, no. 3, pp. 377–445, 1908 (cit. on p. 70).

[115] K. Awazu and H. Kawazoe, “Strained Si-O-Si bonds in amorphous SiO_2 materials: A family member of active centers in radio, photo, and chemical responses”, *Journal of Applied Physics*, vol. 94, no. 10, pp. 6243–6262, 2003 (cit. on pp. 80, 81, 88).

[116] A. Benyagoub, S. Löffler, M. Rammensee, *et al.*, “Plastic deformation in SiO_2 induced by heavy-ion irradiation”, *Nuclear Instruments and Methods in Physics Research Section B: Beam Interactions with Materials and Atoms*, vol. 65, no. 1, pp. 228–231, 1992 (cit. on pp. 82, 92, 94).

[117] W. Primak, L. H. Fuchs, and P. Day, “Radiation damage in insulators”, *Physical Review*, vol. 92, no. 4, p. 1064, 1953 (cit. on p. 82).

[118] C. T. Kirk, “Quantitative analysis of the effect of disorder-induced mode coupling on infrared absorption in silica”, *Physical Review B*, vol. 38, no. 2, pp. 1255–1273, 1988 (cit. on p. 83).

[119] M. H. Brodsky, M. Cardona, and J. J. Cuomo, “Infrared and Raman spectra of the silicon-hydrogen bonds in amorphous silicon prepared by glow discharge and sputtering”, *Physical Review B*, vol. 16, no. 8, pp. 3556–3571, 1977 (cit. on p. 84).

[120] A. E. Geissberger and F. L. Galeener, “Raman studies of vitreous SiO_2 versus fictive temperature”, *Physical Review B*, vol. 28, no. 6, p. 3266, 1983 (cit. on p. 88).

[121] R. L. Fleischer, P. B. Price, R. M. Walker, *et al.*, “Criterion for Registration in Dielectric Track Detectors”, *Physical Review*, vol. 156, no. 2, pp. 353–355, 1967 (cit. on p. 91).

[122] R. L. Fleischer, P. B. Price, R. M. Walker, *et al.*, *Nuclear tracks in solids: principles and applications*. Univ of California Press, 1975 (cit. on p. 91).

[123] R. L. Fleischer, *Tracks to Innovation: Nuclear Tracks in Science and Technology*. Springer New York, 1998 (cit. on p. 91).

[124] F. Dessauer, “ber einige Wirkungen von Strahlen. I”, *Zeitschrift fr Physik*, vol. 12, no. 1, pp. 38–47, 1923 (cit. on p. 91).

[125] L. T. Chadderton and I. M. C. Torrens, *Fission Damage in Crystals* (Methuen’s monographs on physical subjects). Methuen, 1969 (cit. on p. 91).

[126] P. Jordan, “Methods and results of radiobiology”, *Radiologica*, vol. 3, p. 157, 1938 (cit. on p. 91).

[127] F. Seitz, “On the disordering of solids by action of fast massive particles”, *Discussions of the Faraday Society*, vol. 5, pp. 271–282, 1949 (cit. on p. 91).

[128] F. Seitz, “Displacement of atoms during irradiation”, *Solid State Physics.*, vol. 2, pp. 307–442, 1956 (cit. on p. 91).

[129] G. J. Dienes and G. H. Vineyard, *Radiation effects in solids*. Interscience Publishers, 1957, vol. 2 (cit. on p. 91).

[130] I. M. Lifshits, M. I. Kaganov, and L. V. Tanatarov, “On the theory of radiation-induced changes in metals”, *Journal of Nuclear Energy. Part A. Reactor Science*, vol. 12, no. 1-2, pp. 69–78, 1960 (cit. on pp. 91, 92).

[131] S. Klaumünzer, M.-d. Hou, and G. Schumacher, “Coulomb Explosions in a Metallic Glass Due to the Passage of Fast Heavy Ions?”, *Physical Review Letters*, vol. 57, no. 7, pp. 850–853, 1986 (cit. on p. 91).

[132] M. Toulemonde, C. Dufour, and E. Paumier, “Transient Thermal-Process after a High-Energy Heavy-Ion Irradiation of Amorphous Metals and Semiconductors”, *Physical Review B*, vol. 46, no. 22, pp. 14 362–14 369, 1992 (cit. on p. 91).

[133] A. Sigrist and R. Balzer, “Investigations on the formation of tracks in crystals”, *Radiation Effects*, vol. 34, no. 1-3, pp. 75–76, 1977 (cit. on p. 92).

[134] L. E. Seiberling, J. E. Griffith, and T. A. Tombrello, “A thermalized ion explosion model for high energy sputtering and track registration”, *Radiation effects*, vol. 52, no. 3-4, pp. 201–209, 1980 (cit. on p. 92).

[135] C. Rotaru, F. Pawlak, N. Khalfaoui, *et al.*, “Track formation in two amorphous insulators, vitreous silica and diamond like carbon: Experimental observations and description by the inelastic thermal spike model”, *Nuclear Instruments and Methods in Physics Research Section B: Beam Interactions with Materials and Atoms*, vol. 272, pp. 9–14, 2012 (cit. on p. 92).

[136] C. Dufour, V. Khomenkov, G. Rizza, *et al.*, “Ion-matter interaction: the three-dimensional version of the thermal spike model. Application to nanoparticle irradiation with swift heavy ions”, *Journal of Physics D: Applied Physics*, vol. 45, no. 6, p. 065 302, 2012 (cit. on pp. 92, 93, 185).

[137] M. Toulemonde, E. Paumier, and C. Dufour, “Thermal spike model in the electronic stopping power regime”, *Radiation Effects and Defects in Solids*, vol. 126, no. 1-4, pp. 201–206, 1993 (cit. on p. 92).

[138] M. Toulemonde, C. Dufour, A. Meftah, *et al.*, “Transient thermal processes in heavy ion irradiation of crystalline inorganic insulators”, *Nuclear Instruments and Methods in Physics Research Section B: Beam Interactions with Materials and Atoms*, vol. 166, pp. 903–912, 2000 (cit. on p. 92).

[139] M. P. R. Waligórski, R. N. Hamm, and R. Katz, “The radial distribution of dose around the path of a heavy ion in liquid water”, *International Journal of Radiation Applications and Instrumentation. Part D. Nuclear Tracks and Radiation Measurements*, vol. 11, no. 6, pp. 309–319, 1986 (cit. on pp. 92, 185).

[140] A. Meftah, J. M. Costantini, N. Khalfaoui, *et al.*, “Experimental determination of track cross-section in $Gd_3Ga_5O_{12}$ and comparison to the inelastic thermal spike model applied to several materials”, *Nuclear Instruments and Methods in Physics Research Section B: Beam Interactions with Materials and Atoms*, vol. 237, no. 3, pp. 563–574, 2005 (cit. on p. 92).

[141] I. Baranov, Y. V. Martynenko, S. O. Tsepelevich, *et al.*, “Inelastic sputtering of solids by ions”, *Soviet Physics Uspekhi*, vol. 31, no. 11, p. 1015, 1988 (cit. on p. 93).

[142] M. Toulemonde, J. M. Costantini, C. Dufour, *et al.*, “Track creation in SiO_2 and $BaFe_{12}O_{19}$ by swift heavy ions: a thermal spike description”, *Nuclear Instruments and Methods in Physics Research Section B: Beam Interactions with Materials and Atoms*, vol. 116, no. 1-4, pp. 37–42, 1996 (cit. on p. 93).

[143] Y. V. Martynenko and Y. N. Yavlinskii, “Cooling of the electron gas of a metal at high temperatures”, in *Soviet Physics Doklady*, vol. 28, p. 391 (cit. on p. 93).

[144] N. W. Ashcroft and N. D. Mermin, *Solid state physics*, Generic, 1976 (cit. on p. 93).

[145] K. Awazu, X. Wang, M. Fujimaki, *et al.*, “Elongation of gold nanoparticles in silica glass by irradiation with swift heavy ions”, *Physical Review B*, vol. 78, no. 5, p. 054 102, 2008 (cit. on p. 93).

[146] Z. A. Weinberg, G. W. Rubloff, and E. Bassous, “Transmission, photoconductivity, and the experimental band gap of thermally grown SiO_2 films”, *Physical Review B*, vol. 19, no. 6, pp. 3107–3117, 1979 (cit. on p. 93).

[147] M. C. Busch, A. Slaoui, P. Siffert, *et al.*, “Structural and electrical damage induced by high-energy heavy ions in SiO_2/Si structures”, *Journal of Applied Physics*, vol. 71, no. 6, pp. 2596–2601, 1992 (cit. on p. 94).

[148] A. Meftah, F. Brisard, J. M. Costantini, *et al.*, “Track formation in SiO_2 quartz and the thermal-spike mechanism”, *Phys Rev B Condens Matter*, vol. 49, no. 18, pp. 12 457–12 463, 1994 (cit. on pp. 94, 106, 152).

[149] D. R. Lide, *CRC handbook of chemistry and physics: a ready-reference book of chemical and physical data*. CRC press, 1995 (cit. on pp. 94, 105).

[150] R. H. Perry, D. W. Green, and J. O. Maloney, *Perry’s Chemical Engineers’ Handbook*. McGraw-Hill, 1984 (cit. on p. 94).

[151] Y. S. Touloukian, R. W. Powell, C. Y. Ho, *et al.*, “Thermophysical Properties of Matter-The TPRC Data Series. Volume 10. Thermal Diffusivity”, Thermophysical and Electronic Properties Information Analysis Center . . ., Report, 1974 (cit. on p. 94).

[152] P. Hermes, B. Danielzik, N. Fabricius, *et al.*, “Evaporation of atoms from femtosecond laser-heated gallium arsenide”, *Applied Physics A: Solids and Surfaces*, vol. 39, no. 1, pp. 9–11, 1986 (cit. on p. 106).

[153] B. Rethfeld, A. Kaiser, M. Vicanek, *et al.*, “Ultrafast dynamics of nonequilibrium electrons in metals under femtosecond laser irradiation”, *Physical Review B*, vol. 65, no. 21, p. 214 303, 2002 (cit. on p. 106).

[154] S.-N. Luo, T. J. Ahrens, T. Çağın, *et al.*, “Maximum superheating and undercooling: Systematics, molecular dynamics simulations, and dynamic experiments”, *Physical Review B*, vol. 68, no. 13, p. 134 206, 2003 (cit. on p. 106).

[155] M. Toulemonde, W. Assmann, C. Trautmann, *et al.*, “Jetlike Component in Sputtering of LiF Induced by Swift Heavy Ions”, *Physical Review Letters*, vol. 88, no. 5, p. 057 602, 2002 (cit. on p. 106).

[156] M. Ojovan and G. Mobus, “On radiation-induced fluidization (quasi-melting) of silicate glasses”, *MRS Proceedings*, vol. 1193, p. 275, 2009 (cit. on pp. 116, 147).

[157] N. Jiang, “Electron beam damage in oxides: a review”, *Reports On Progress in Physics*, vol. 79, no. 1, p. 016 501, 2016 (cit. on p. 121).

[158] *NIST Estar, Stopping Power and Range Tables for Electrons*, Online Database (cit. on pp. 122, 136).

[159] G. Kowalczyk and J. E. Roberts, “Solid State ^{29}Si NMR determination of crystalline silica in natural iron oxide pigments”, *Analytica Chimica Acta*, vol. 286, no. 1, pp. 25–35, 1994 (cit. on p. 126).

[160] T. A. Dellin, D. A. Tichenor, and E. H. Barsis, “Volume, index-of-refraction, and stress changes in electron-irradiated vitreous silica”, *Journal of Applied Physics*, vol. 48, no. 3, pp. 1131–1138, 1977 (cit. on p. 131).

[161] P. Makowski, X. Deschanels, A. Grandjean, *et al.*, “Mesoporous materials in the field of nuclear industry: applications and perspectives”, *New Journal of Chemistry*, vol. 36, no. 3, pp. 531–541, 2012 (cit. on p. 131).

[162] J. Li, C. Fan, Q. Li, *et al.*, “In situ studies on irradiation resistance of nanoporous Au through temperature-jump tests”, *Acta Materialia*, vol. 143, pp. 30–42, 2018 (cit. on p. 131).

[163] A. M. Manzini, M. A. Alurralde, G. Giménez, *et al.*, “The radiation response of mesoporous nanocrystalline zirconia thin films”, *Journal of Nuclear Materials*, vol. 482, pp. 175–186, 2016 (cit. on p. 131).

[164] A. Manzini, M. Alurralde, and V. Luca, “Radiation response of cubic mesoporous silicate and borosilicate thin films”, *Nuclear Instruments and Methods in Physics Research Section B: Beam Interactions with Materials and Atoms*, vol. 415, pp. 54–63, 2018 (cit. on p. 131).

[165] Project-ANR-18-CE05-0016-2018, *Solid Fixation and Auto-Conditioning of Actinide Elements coming from Contaminated Liquid Outflows. (Séparation sur solide et* ***AUTO****-conditionne****M****ent d’****ACT****inides provenant d’effluents contamines)*, Grant, 2018 (cit. on p. 151).

[166] M. Toulemonde, S. Bouffard, and F. Studer, “Swift heavy ions in insulating and conducting oxides: tracks and physical properties”, *Nuclear Instruments and Methods in Physics Research Section B: Beam Interactions with Materials and Atoms*, vol. 91, no. 1, pp. 108–123, 1994 (cit. on p. 152).

[167] A. Meftah, F. Brisard, J. M. Costantini, *et al.*, “Swift heavy ions in magnetic insulators: A damage-cross-section velocity effect”, *Physical Review B*, vol. 48, no. 2, pp. 920–925, 1993 (cit. on p. 152).

[168] J. Jensen, A. Dunlop, S. Della-Negra, *et al.*, "A comparison between tracks created by high energy mono-atomic and cluster ions in Y3Fe5O12", *Nuclear Instruments and Methods in Physics Research Section B: Beam Interactions with Materials and Atoms*, vol. 146, no. 1, pp. 412–419, 1998 (cit. on p. 152).

[169] P. I. Gaiduk, A. N. Larsen, J. L. Hansen, *et al.*, "Discontinuous tracks in relaxed Si0.5Ge0.5 alloy layers: A velocity effect", *Applied Physics Letters*, vol. 83, no. 9, pp. 1746–1748, 2003 (cit. on p. 152).

[170] W. Brandt and M. Kitagawa, "Effective stopping-power charges of swift ions in condensed matter", *Physical Review B*, vol. 25, no. 9, pp. 5631–5637, 1982 (cit. on p. 169).

Appendices

Appendix A

Briefly, for heavy ions (Z_1>2), SRIM/TRIM scale proton stopping powers using Brandt-Kitagawa theory [170]. The calculation of heavy ion electronic stopping takes the following steps[20]:

a) The relative velocity of the ion, v_{rel} is calculated with equations below depend only on the ion velocity, v_1 and the target Fermi velocity, v_F.

$$\text{For } v_1 \geq v_F : v_{\text{rel}} = v_1 \left(1 + \frac{v_F^2}{5v_1^2}\right)$$

$$\text{For } v_1 < v_F : v_{\text{rel}} = \frac{3v_F}{4}\left[1 + \frac{2v_1^2}{3v_F^2} - \frac{1}{15}\left(\frac{v_1}{v_F}\right)^4\right]$$

b) The fractional ionization of the ion, q, is calculated with

$$q = 1 - exp\left[0.803y_r^{0.3} - 1.3167y_r^{0.6} - 0.38157y_r - 0.008983y_r^2\right]$$

$$\text{with } y_r, \text{ the Effective Ion Velocty ,defined as } y_r \equiv \frac{v_{\text{rel}}}{v_0 Z_1^{2/3}}$$

c) The screening length of the ion, Λ, is calculated as a function of the ions charge state with

$$\Lambda = \frac{2a_0 N^{2/3} a}{Z_1\left[1 - \frac{N}{7Z_1}\right]} = \frac{2a_0(1-q)^{2/3} a}{Z_1^{1/3}\left[1 - \frac{1-q}{7}\right]}$$

Where a_0 = Bohr Radius = 0.529 Å and a was determined to have a length of about a_0/2; and $q = 1 - N/Z_1$.

d) The effective charge, γ , of the ion is then calculated with

$$\gamma = q + (1-q)\frac{(v_0/v_F)^2}{2}\ln\left[1 + \left(2\Lambda v_F/\left(a_0 v_0\right)\right)^2\right]$$

e) The final stopping power is then found using

$$S_{\mathrm{HI(heavy\,ion)}} = S_H \left(Z_{\mathrm{HI}}^{*}\right)^2 = S_H\, Z_{\mathrm{HI}}^2 \gamma^2$$

Where S_H is the proton equivalent stopping power.

For very low velocity ions, $v_1 < v_F/Z_1^{2/3}$, SRIM/TRIM use velocity proportional stopping except for $Z_1 < 19$ in semiconductor band-gap targets ($Z_2 = 6,\ 14$ or 32) where $S_e \propto v^{0.75}$ is used.

The major assumptions of this approach to calculating electronic stopping powers are:

- The electron density in the target varies slowly with position.
- Available electron energy levels and transition strengths of the atoms of the solid are described by those in a free electron gas.
- Target band-gap effects can be accounted for by choosing appropriate (virtual) Fermi velocity.
- The degree of ionization of the ion depends only on the velocity of the ion relative to the Fermi velocity of the target.
- For distant collisions the electronic energy loss is described by Lindhard's free electron gas theory incorporated into a local-density-approximation for the particle-solid interaction.
- For close collisions the electronic energy loss for heavy ion is corrected by Brandt and Kitagawa theory.

Appendix B

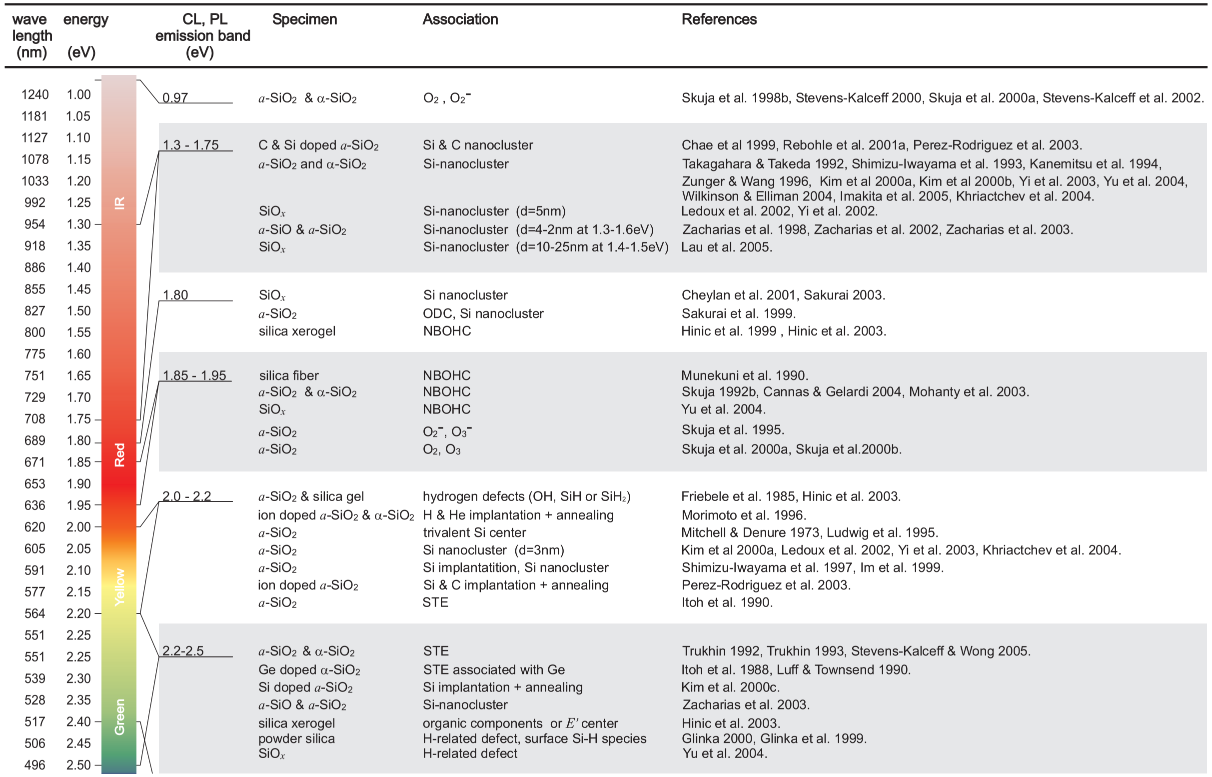

CL, PL emission band (eV)	Specimen	Association	References
0.97	a-SiO$_2$ & α-SiO$_2$	O_2, O_2^-	Skuja et al. 1998b, Stevens-Kalceff 2000, Skuja et al. 2000a, Stevens-Kalceff et al. 2002.
1.3 - 1.75	C & Si doped a-SiO$_2$	Si & C nanocluster	Chae et al 1999, Rebohle et al. 2001a, Perez-Rodriguez et al. 2003.
	a-SiO$_2$ and α-SiO$_2$	Si-nanocluster	Takagahara & Takeda 1992, Shimizu-Iwayama et al. 1993, Kanemitsu et al. 1994, Zunger & Wang 1996, Kim et al 2000a, Kim et al 2000b, Yi et al. 2003, Yu et al. 2004, Wilkinson & Elliman 2004, Imakita et al. 2005, Khriactchev et al. 2004.
	SiO$_x$	Si-nanocluster (d=5nm)	Ledoux et al. 2002, Yi et al. 2002.
	a-SiO & a-SiO$_2$	Si-nanocluster (d=4-2nm at 1.3-1.6eV)	Zacharias et al. 1998, Zacharias et al. 2002, Zacharias et al. 2003.
	SiO$_x$	Si-nanocluster (d=10-25nm at 1.4-1.5eV)	Lau et al. 2005.
1.80	SiO$_x$	Si nanocluster	Cheylan et al. 2001, Sakurai 2003.
	a-SiO$_2$	ODC, Si nanocluster	Sakurai et al. 1999.
	silica xerogel	NBOHC	Hinic et al. 1999 , Hinic et al. 2003.
1.85 - 1.95	silica fiber	NBOHC	Munekuni et al. 1990.
	a-SiO$_2$ & α-SiO$_2$	NBOHC	Skuja 1992b, Cannas & Gelardi 2004, Mohanty et al. 2003.
	SiO$_x$	NBOHC	Yu et al. 2004.
	a-SiO$_2$	O_2^-, O_3^-	Skuja et al. 1995.
	a-SiO$_2$	O_2, O_3	Skuja et al. 2000a, Skuja et al.2000b.
2.0 - 2.2	a-SiO$_2$ & silica gel	hydrogen defects (OH, SiH or SiH$_2$)	Friebele et al. 1985, Hinic et al. 2003.
	ion doped a-SiO$_2$ & α-SiO$_2$	H & He implantation + annealing	Morimoto et al. 1996.
	a-SiO$_2$	trivalent Si center	Mitchell & Denure 1973, Ludwig et al. 1995.
	a-SiO$_2$	Si nanocluster (d=3nm)	Kim et al 2000a, Ledoux et al. 2002, Yi et al. 2003, Khriactchev et al. 2004.
	a-SiO$_2$	Si implantatition, Si nanocluster	Shimizu-Iwayama et al. 1997, Im et al. 1999.
	ion doped a-SiO$_2$	Si & C implantation + annealing	Perez-Rodriguez et al. 2003.
	a-SiO$_2$	STE	Itoh et al. 1990.
2.2-2.5	a-SiO$_2$ & α-SiO$_2$	STE	Trukhin 1992, Trukhin 1993, Stevens-Kalceff & Wong 2005.
	Ge doped α-SiO$_2$	STE associated with Ge	Itoh et al. 1988, Luff & Townsend 1990.
	Si doped a-SiO$_2$	Si implantation + annealing	Kim et al. 2000c.
	a-SiO & a-SiO$_2$	Si-nanocluster	Zacharias et al. 2003.
	silica xerogel	organic components or E' center	Hinic et al. 2003.
	powder silica	H-related defect, surface Si-H species	Glinka 2000, Glinka et al. 1999.
	SiO$_x$	H-related defect	Yu et al. 2004.

FIGURE B.1: (a): Reported CL and PL luminescent bands in amorphous silicon dioxide (a-SiO$_2$) and crystalline quartz (α-SiO$_2$) and their proposed associations in IR-Green region. Figure from reference [86].

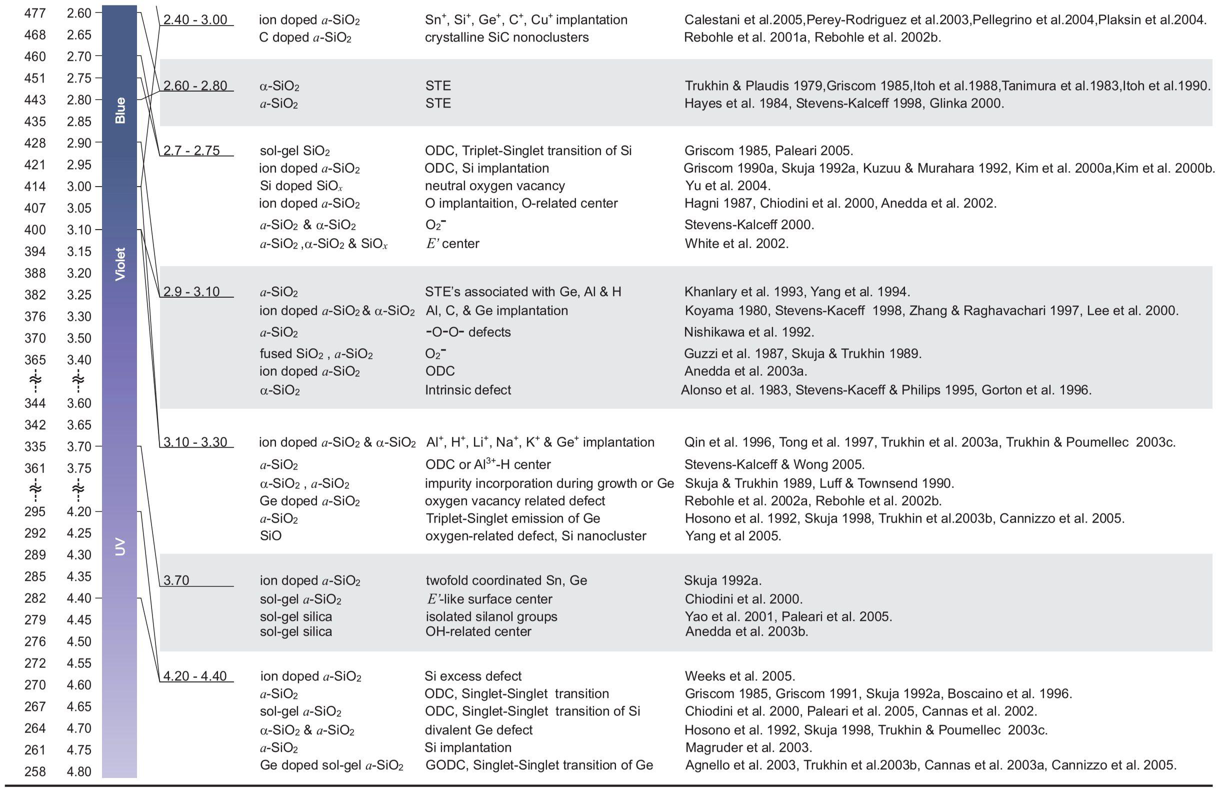

2.40 - 3.00	ion doped a-SiO$_2$	Sn$^+$, Si$^+$, Ge$^+$, C$^+$, Cu$^+$ implantation	Calestani et al.2005,Perey-Rodriguez et al.2003,Pellegrino et al.2004,Plaksin et al.2004.
	C doped a-SiO$_2$	crystalline SiC nonoclusters	Rebohle et al. 2001a, Rebohle et al. 2002b.
2.60 - 2.80	α-SiO$_2$	STE	Trukhin & Plaudis 1979,Griscom 1985,Itoh et al.1988,Tanimura et al.1983,Itoh et al.1990.
	a-SiO$_2$	STE	Hayes et al. 1984, Stevens-Kalceff 1998, Glinka 2000.
2.7 - 2.75	sol-gel SiO$_2$	ODC, Triplet-Singlet transition of Si	Griscom 1985, Paleari 2005.
	ion doped a-SiO$_2$	ODC, Si implantation	Griscom 1990a, Skuja 1992a, Kuzuu & Murahara 1992, Kim et al. 2000a,Kim et al. 2000b.
	Si doped SiO$_x$	neutral oxygen vacancy	Yu et al. 2004.
	ion doped a-SiO$_2$	O implantaition, O-related center	Hagni 1987, Chiodini et al. 2000, Anedda et al. 2002.
	a-SiO$_2$ & α-SiO$_2$	O$_2^-$	Stevens-Kalceff 2000.
	a-SiO$_2$,α-SiO$_2$ & SiO$_x$	E' center	White et al. 2002.
2.9 - 3.10	a-SiO$_2$	STE's associated with Ge, Al & H	Khanlary et al. 1993, Yang et al. 1994.
	ion doped a-SiO$_2$ & α-SiO$_2$	Al, C, & Ge implantation	Koyama 1980, Stevens-Kaceff 1998, Zhang & Raghavachari 1997, Lee et al. 2000.
	a-SiO$_2$	-O-O- defects	Nishikawa et al. 1992.
	fused SiO$_2$, a-SiO$_2$	O$_2^-$	Guzzi et al. 1987, Skuja & Trukhin 1989.
	ion doped a-SiO$_2$	ODC	Anedda et al. 2003a.
	α-SiO$_2$	Intrinsic defect	Alonso et al. 1983, Stevens-Kaceff & Philips 1995, Gorton et al. 1996.
3.10 - 3.30	ion doped a-SiO$_2$ & α-SiO$_2$	Al$^+$, H$^+$, Li$^+$, Na$^+$, K$^+$ & Ge$^+$ implantation	Qin et al. 1996, Tong et al. 1997, Trukhin et al. 2003a, Trukhin & Poumellec 2003c.
	a-SiO$_2$	ODC or Al^{3+}-H center	Stevens-Kalceff & Wong 2005.
	α-SiO$_2$, a-SiO$_2$	impurity incorporation during growth or Ge	Skuja & Trukhin 1989, Luff & Townsend 1990.
	Ge doped a-SiO$_2$	oxygen vacancy related defect	Rebohle et al. 2002a, Rebohle et al. 2002b.
	a-SiO$_2$	Triplet-Singlet emission of Ge	Hosono et al. 1992, Skuja 1998, Trukhin et al.2003b, Cannizzo et al. 2005.
	SiO	oxygen-related defect, Si nanocluster	Yang et al 2005.
3.70	ion doped a-SiO$_2$	twofold coordinated Sn, Ge	Skuja 1992a.
	sol-gel a-SiO$_2$	E'-like surface center	Chiodini et al. 2000.
	sol-gel silica	isolated silanol groups	Yao et al. 2001, Paleari et al. 2005.
	sol-gel silica	OH-related center	Anedda et al. 2003b.
4.20 - 4.40	ion doped a-SiO$_2$	Si excess defect	Weeks et al. 2005.
	a-SiO$_2$	ODC, Singlet-Singlet transition	Griscom 1985, Griscom 1991, Skuja 1992a, Boscaino et al. 1996.
	sol-gel a-SiO$_2$	ODC, Singlet-Singlet transition of Si	Chiodini et al. 2000, Paleari et al. 2005, Cannas et al. 2002.
	α-SiO$_2$ & a-SiO$_2$	divalent Ge defect	Hosono et al. 1992, Skuja 1998, Trukhin & Poumellec 2003c.
	a-SiO$_2$	Si implantation	Magruder et al. 2003.
	Ge doped sol-gel a-SiO$_2$	GODC, Singlet-Singlet transition of Ge	Agnello et al. 2003, Trukhin et al.2003b, Cannas et al. 2003a, Cannizzo et al. 2005.

FIGURE B.2: (b): Reported CL and PL luminescent bands in amorphous silicon dioxide (a-SiO$_2$) and crystalline quartz (α-SiO$_2$) and their proposed associations in Blue-UV region. Figure from reference [86]

Appendix C

Stability of the as-synthesized thin films

Humidity and temperature

To explore the influence of temperature and humidity on the synthesized IPc and ICc, we established three experimental groups. The first set of IPc and ICc were held at room temperature in a constant humidity chamber at a RH of 80%. At room temperature, the second set of IPc and ICc were immersed in a solution of 0.055 M HCl. Thirdly, we immersed the IPc and ICc in deionized water and placed them in an 40°C thermostat.

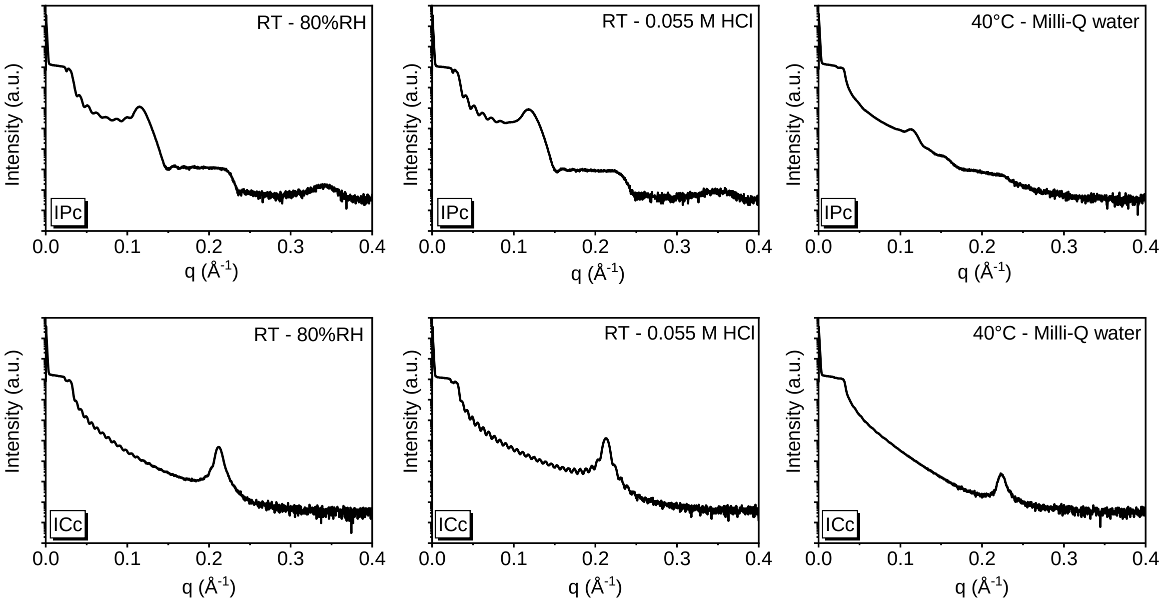

FIGURE C.1: XRR curves after three months of storage under different conditions

Three sets of samples were kept in their respective environments for three months, and the figure C.1 depict the changes in the relevant XRR measurements after the experiment.

The experimental results indicated that the experimental groups of synthetic thin film maintained a high degree of stability without significant disruption at room temperature, both in an 80 percent humidity environment and in a slightly acidic aqueous solution; however, the thin films placed in deionized water at 40 degrees were seriously impacted.

Long-term storage

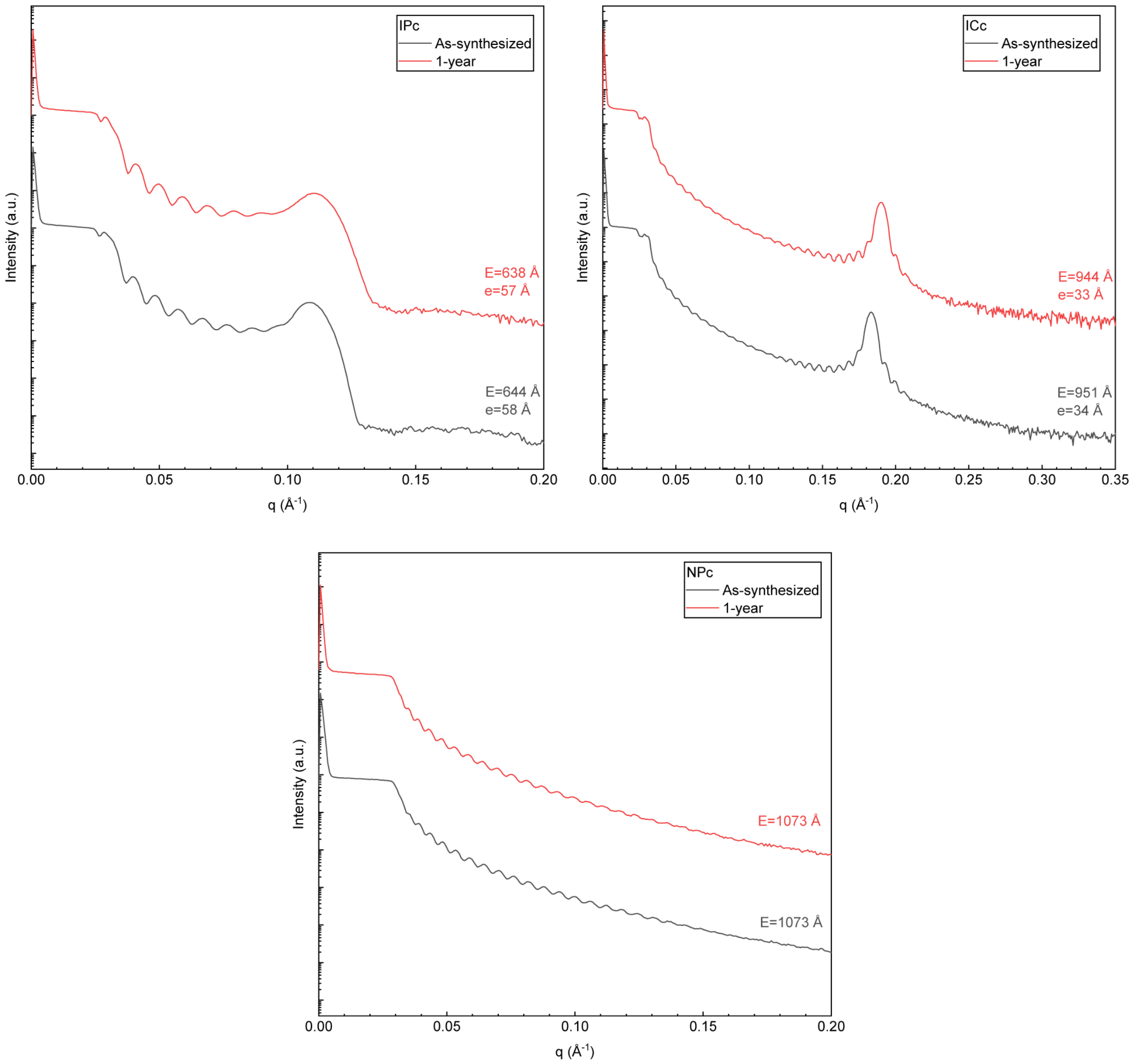

FIGURE C.2: Comparison of XRR curves of three types of silica thin films under long-term storage. The values of the thickness in the figure are calculated using the method 2 mentioned above in the page 53

The standard laboratory storage condition is to keep samples at room temperature in a desiccator. We compared samples maintained in this environment for one year, and the figure C.2 shows the corresponding XRR analysis results. The overall thickness and interlayer thickness deviations determined by XRR are less than 3%, and the intensity of the bragg peak does not alter considerably. Considering the thickness detection error of XRR is around 5%, these findings show that no observable changes occurred in the materials during long-term storage.

Follow-up analysis of the silica material over such a long duration of time validated the stability of the synthesized thin films and revealed that the damage reported in subsequent studies was indeed caused by irradiation and not by storage conditions (humidity, temperature, etc.)

Appendix D

Carbon beam irradiation

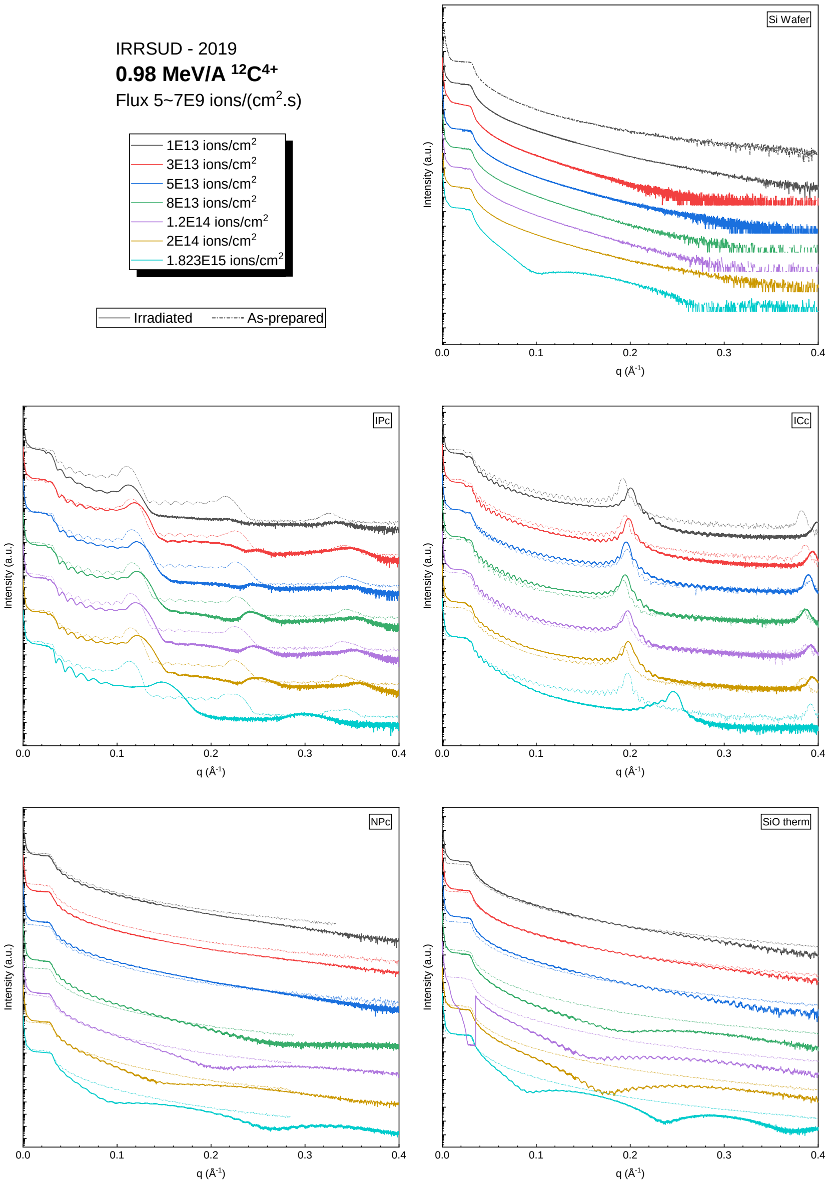

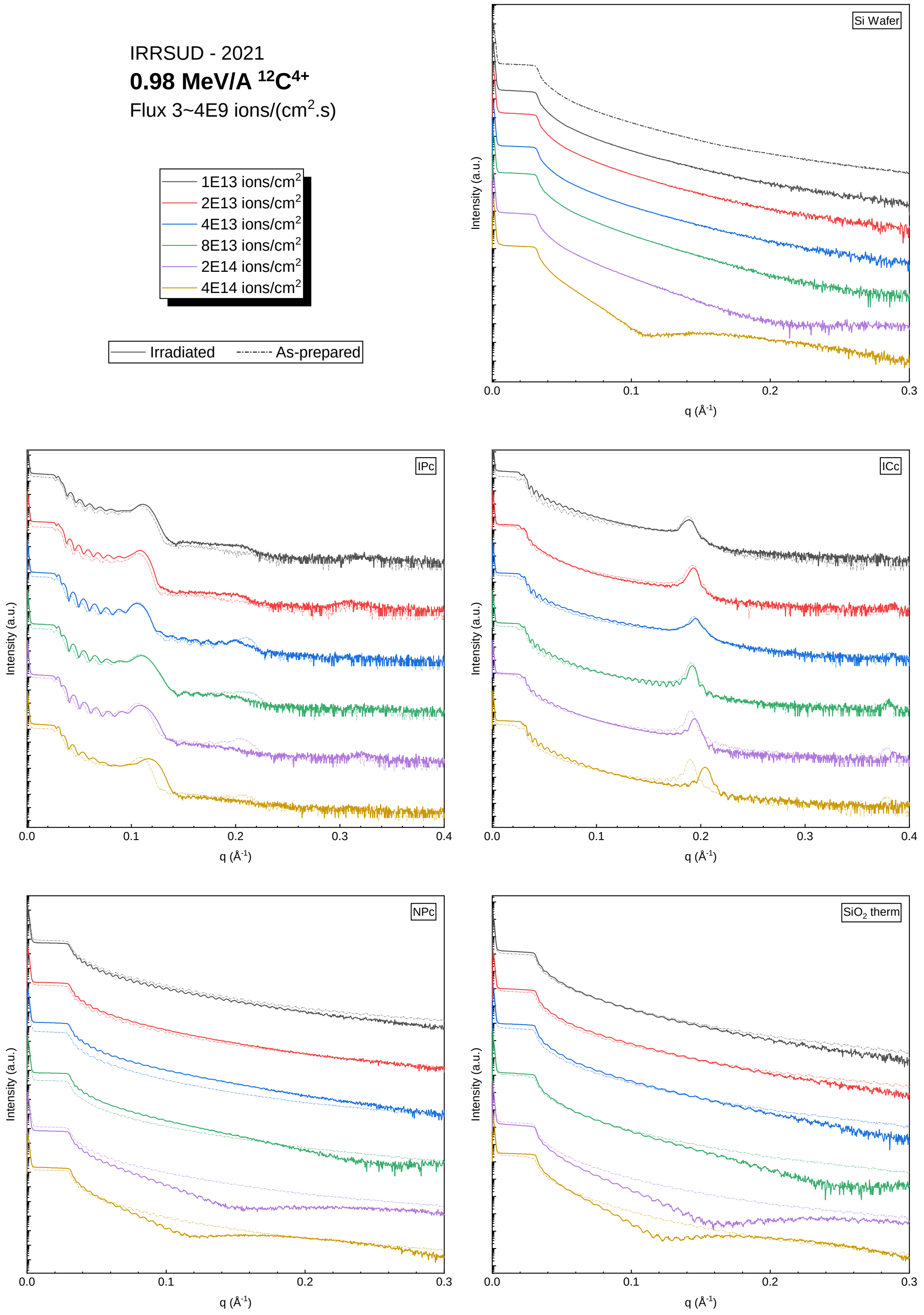
IRRSUD - 2021
0.98 MeV/A $^{12}C^{4+}$
Flux 3~4E9 ions/(cm^2.s)
1E13 ions/cm^2
2E13 ions/cm^2
4E13 ions/cm^2
8E13 ions/cm^2
2E14 ions/cm^2
4E14 ions/cm^2
Irradiated
As-prepared
Si Wafer
IPc
ICc
NPc
SiO$_2$ therm
Intensity (a.u.)
q (Å^{-1})
0.0
0.1
0.2
0.3
0.4

Calcium beam irradiation

SME - 2019
9.17 MeV/A $^{48}Ca^{18+}$
Flux 1~2E9 ions/(cm^2.s)

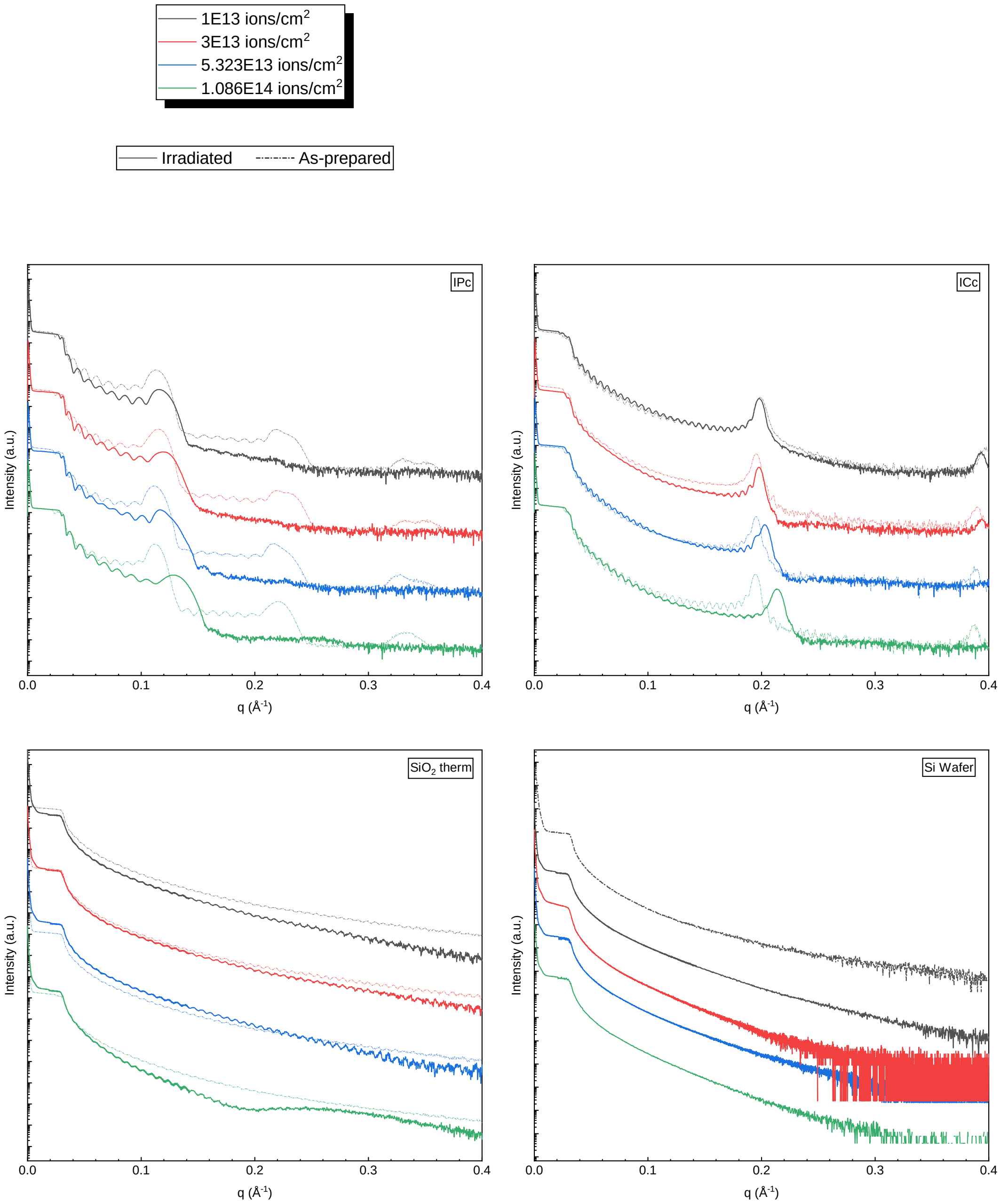

Argon beam irradiation

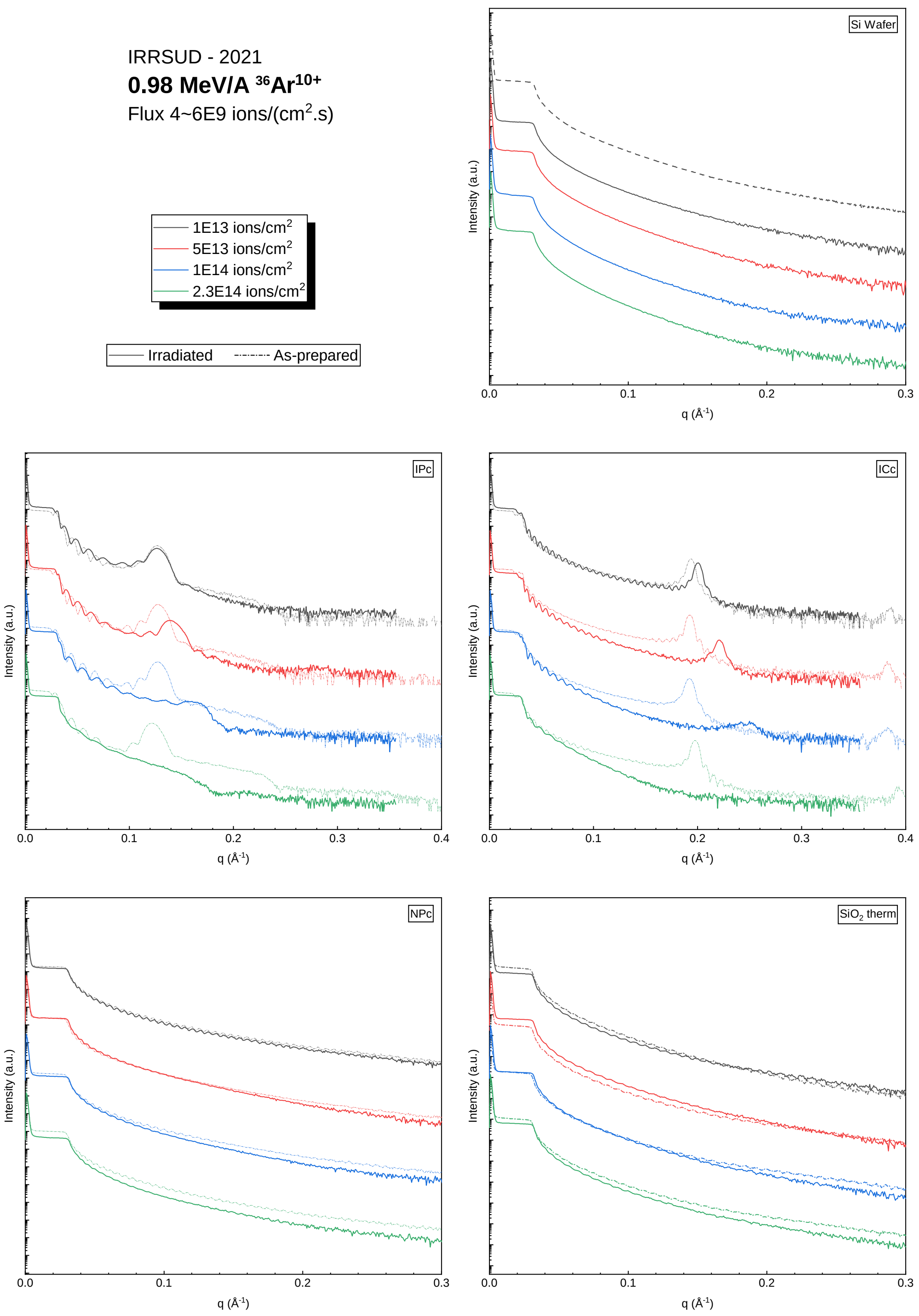

Nickel beam irradiation

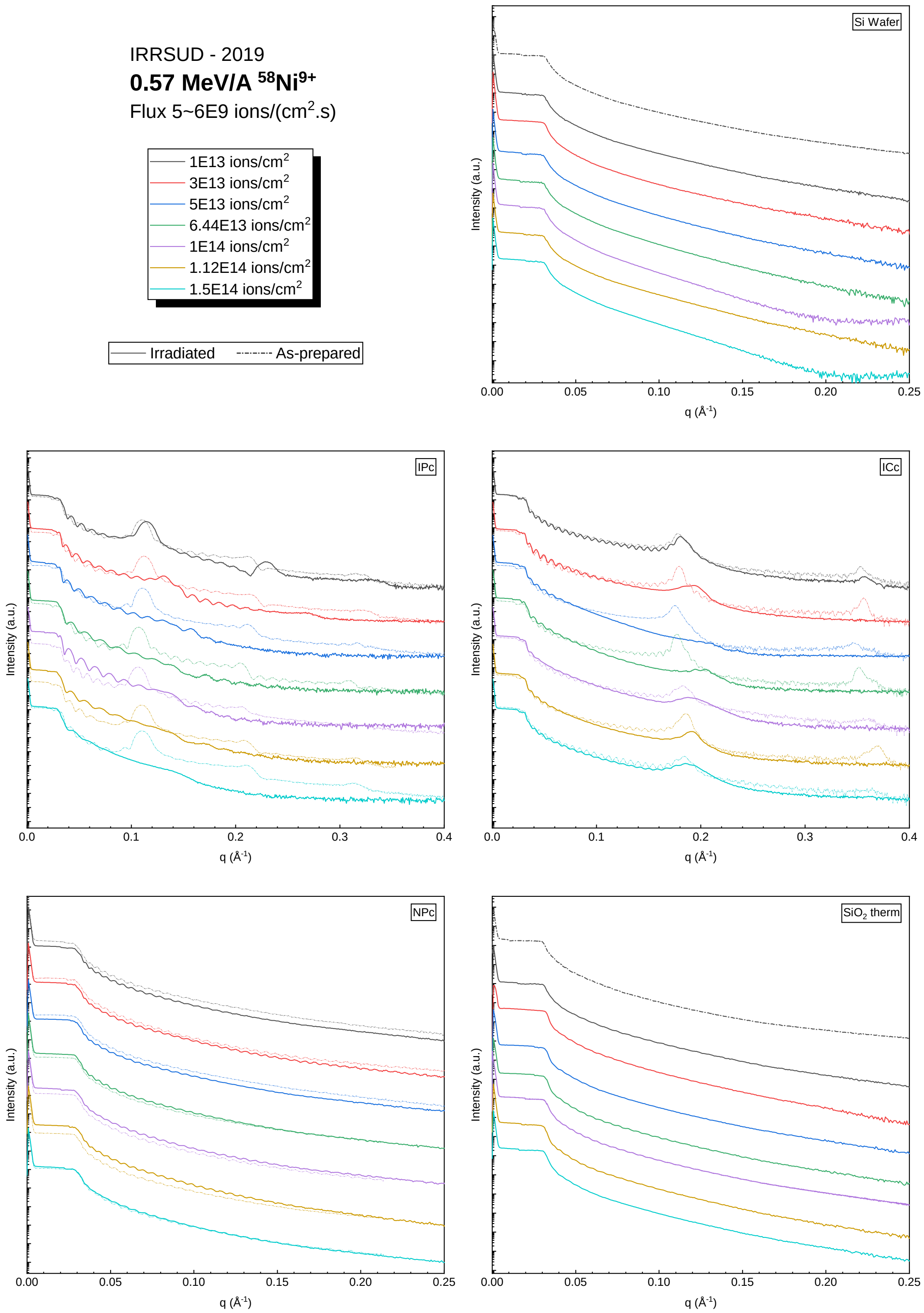

Krypton beam irradiation

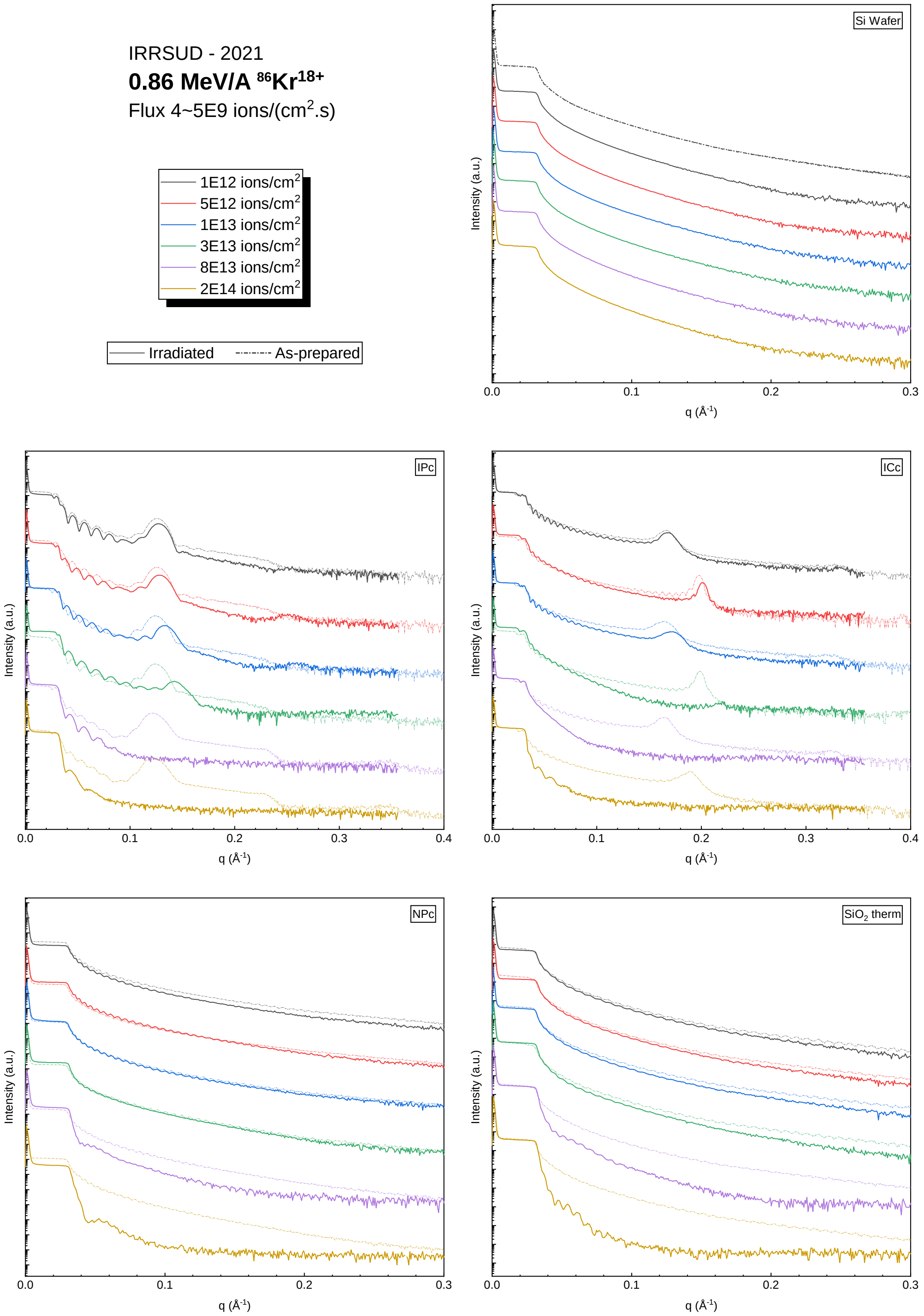

Xenon beam irradiation

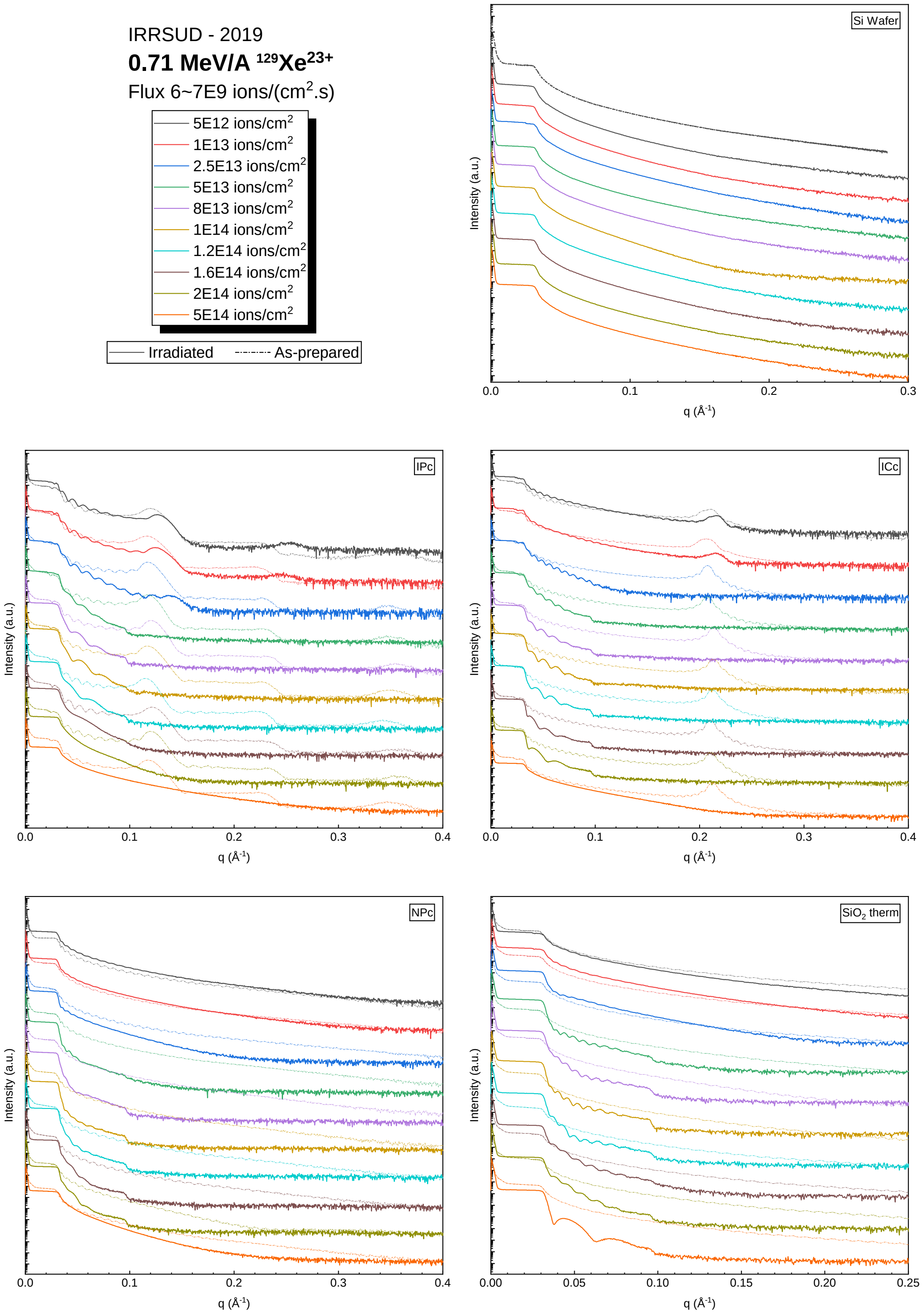

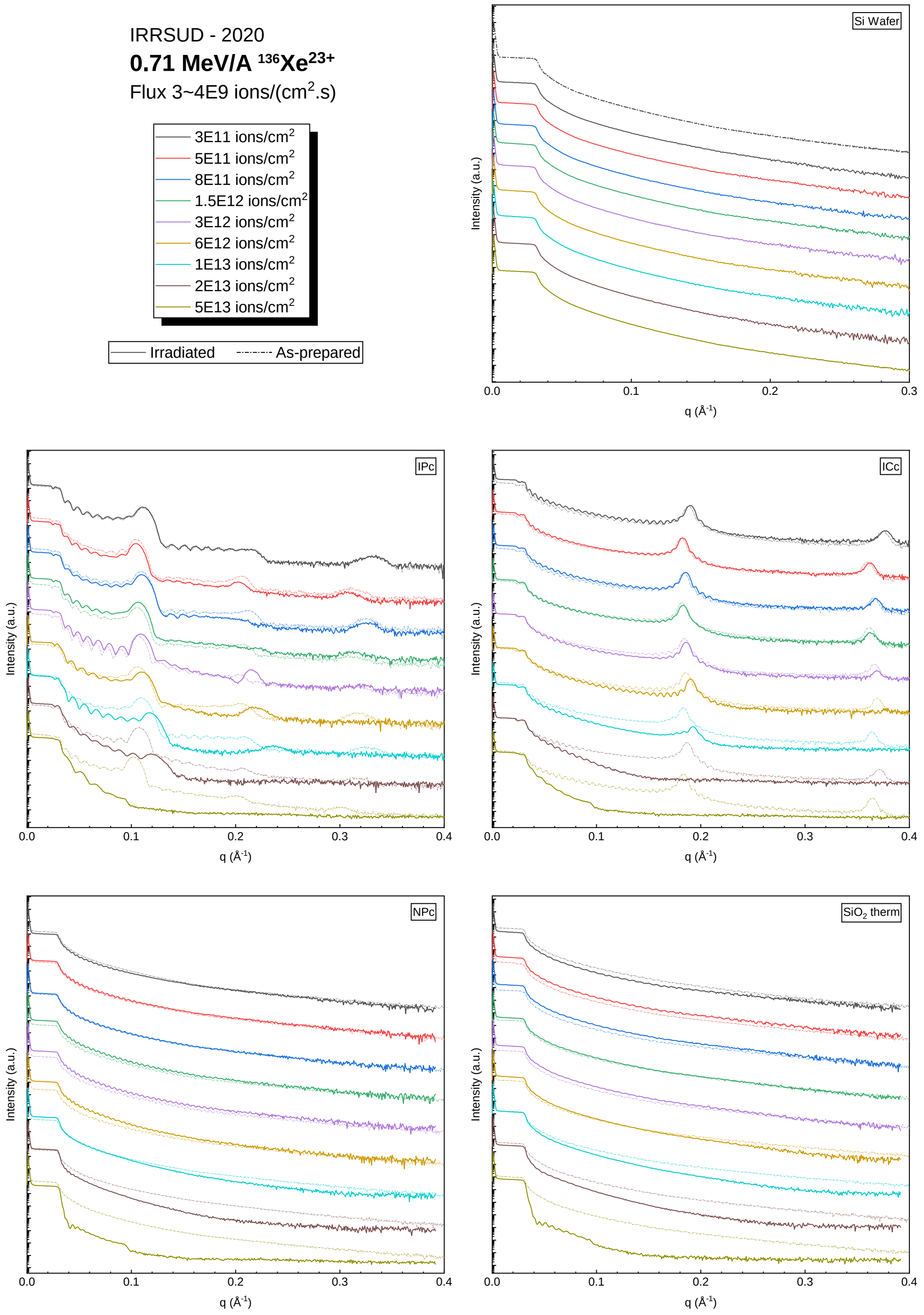
IRRSUD - 2020
0.71 MeV/A ^{136}Xe^{23+}
Flux 3~4E9 ions/(cm^2.s)
3E11 ions/cm^2
5E11 ions/cm^2
8E11 ions/cm^2
1.5E12 ions/cm^2
3E12 ions/cm^2
6E12 ions/cm^2
1E13 ions/cm^2
2E13 ions/cm^2
5E13 ions/cm^2
Irradiated
As-prepared
Si Wafer
IPc
ICc
NPc
SiO$_2$ therm
Intensity (a.u.)
q (Å^{-1})
0.0
0.1
0.2
0.3
0.4

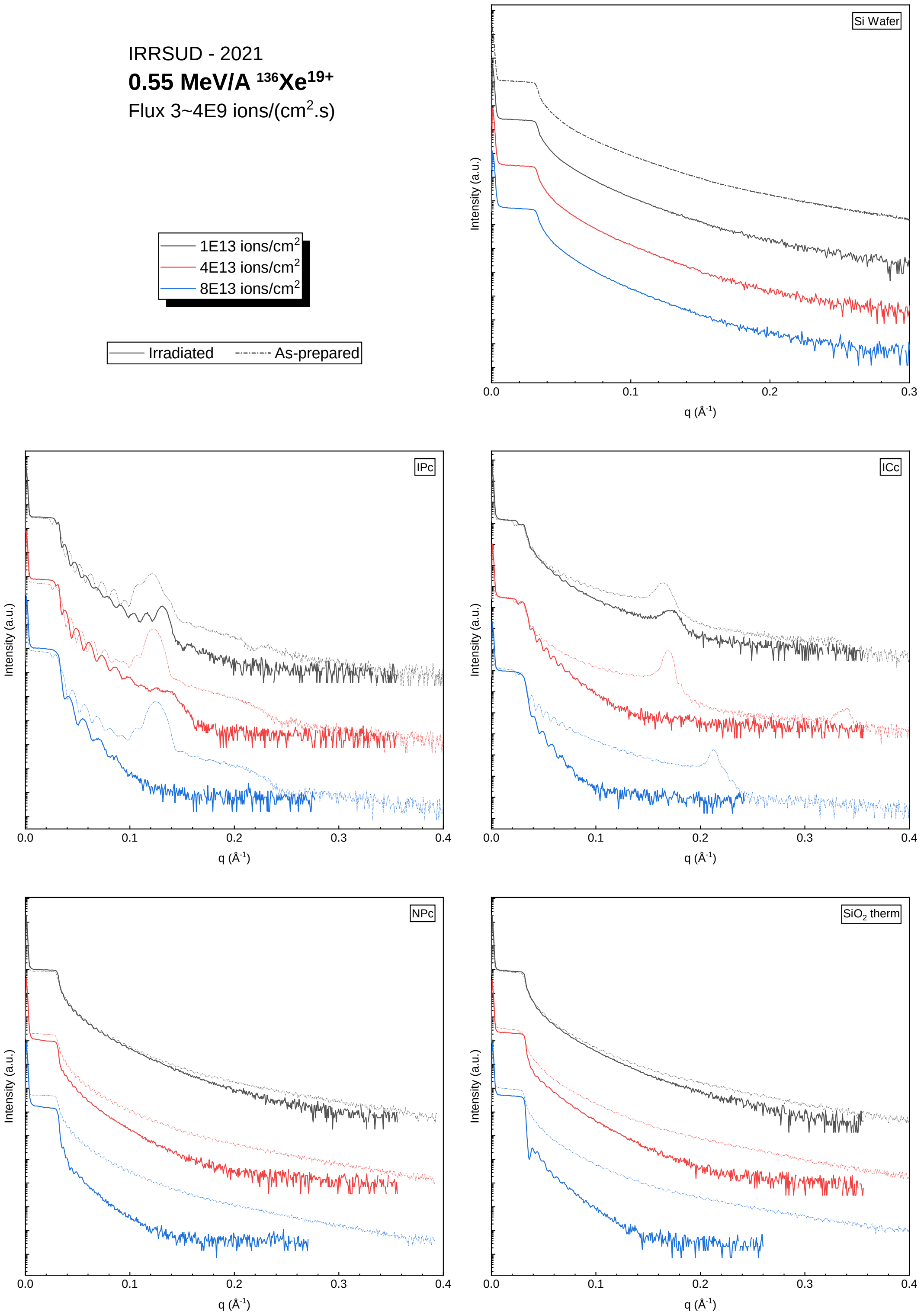
IRRSUD - 2021
0.55 MeV/A $^{136}Xe^{19+}$
Flux 3~4E9 ions/(cm^2.s)
1E13 ions/cm^2
4E13 ions/cm^2
8E13 ions/cm^2
Irradiated
As-prepared
Si Wafer
IPc
ICc
NPc
SiO_2 therm
Intensity (a.u.)
q (Å^{-1})
0.0
0.1
0.2
0.3
0.4

Appendix E

According to Dufour *et al.* [136] the $A_e\left(\overrightarrow{r},t\right)$ in 3DTS can be calculated using the following procedure.

Assume that the incident ion contacts the target parallel to the z-axis at the point (x_0, y_0) in the XY-plane. The space and time variables can be separate in such a way that $A_e\left(\overrightarrow{r},t\right) = F\left(\overrightarrow{r}\right)G(t)$. The function $G(t)$ is a time pulse with a duration of a few femtoseconds ($t_0 = 2 \times 10^{-15}s$), and is normalized so that $\int_0^{t_0} G(t)\,dt = 1$.

The function $F\left(\overrightarrow{r}\right)$ is a product $F\left(\overrightarrow{r}\right) = CS_e\left(x_0, y_0, z\right)\nu^2(x,y,z)W\left(r_\perp\right)$ with the new parameters:

$\nu(x,y,z) = \rho\text{Z}/A$, which is the parameter proportional to the electron density (ρ is the mass density, Z and A are the atomic and mass numbers of the target material);

$r_\perp(x,y,z) = \overline{\nu}\sqrt{(x-x_0)^2 + (y-y_0)^2}$ is the radial range (in g.cm^{-2}) to the ion track, weighted by the mean electron density;

$\overline{\nu} = \int_0^1 \nu\left[\xi(\vartheta), \eta(\vartheta), z\right] d\vartheta$ where $\xi(\vartheta) = x_0 + \left(x - x_0\right)\vartheta$ and $\eta(\vartheta) = y_0 + \left(y - y_0\right)\vartheta$.

Finally, $W\left(r_\perp\right) = \left(\left[1 - \left(r_\perp + R_{\min}\right)/\left(R_{\max} + R_{\min}\right)\right]^{1/\alpha}\right)/\left(r_\perp\left(r_\perp + R_{\min}\right)\right)$ is known as the radial δ-ray energy distribution. (Waligorski *et al.* [139]), where we substitute the range for homogeneous materials with our weighted range $r_\perp$. According to reference [139],$R_{\min}$, $R_{\max}$ are the ranges corresponding to the target ionization potential $E_{\min}$ and maximum energy of δ-electrons $E_{\max} = 2mc^2\beta^2/\left(1-\beta^2\right)$, β is the incident ion velocity in lightspeed units; $R = kE^\alpha$, $k = 6 \times 10^{-6}\text{g.}cm^{-2}\text{ke}V^{-\alpha}$; $\alpha = 1.079$ for $\beta < 0.03$ and $\alpha = 1.667$ for $\beta > 0.03$; $W\left(r_\perp > R_{\max}\right) = 0$.

C is a normalizing constant, so that

$$\int\int_{-\infty}^{\infty} F(x,y,z)dxdy = S_e(z)$$

Appendix F

Physical properties of air in 3DTS

Parameters	Value
Melting enthalpy (kJ)	0
Evaporation enthalpy (kJ)	0
Melting point (K)	60
Evaporation point (K)	80
Ionization potential (eV)	10
A (g/mol)	29
Solid density (g/cm^3)	0.0012
Liquid density (g/cm^3)	0.0012
Z	29
D(300K) (cm^2/s)	2
Dmin (cm^2/s)	2
Electronic concentration (cm^{-3})	2.40E+19
g_{ini}	1.00E+08
ΔT_{melt} - width of melting peak	10
ΔT_{evap}	30

T (Kelvins)	Atomic thermal conductivity K (W/cm/K)
300	2.55E-04
310	2.62E-04
340	2.84E-04
370	3.03E-04

T (Kelvins)	Atomic specific heat C (J/cm^3/K)
300	300

Appendix G

^{1}H NMR of a)SBA-15, b)MCM-41 and ^{29}Si CP NMR of c)SBA-15, d)MCM-41

a)

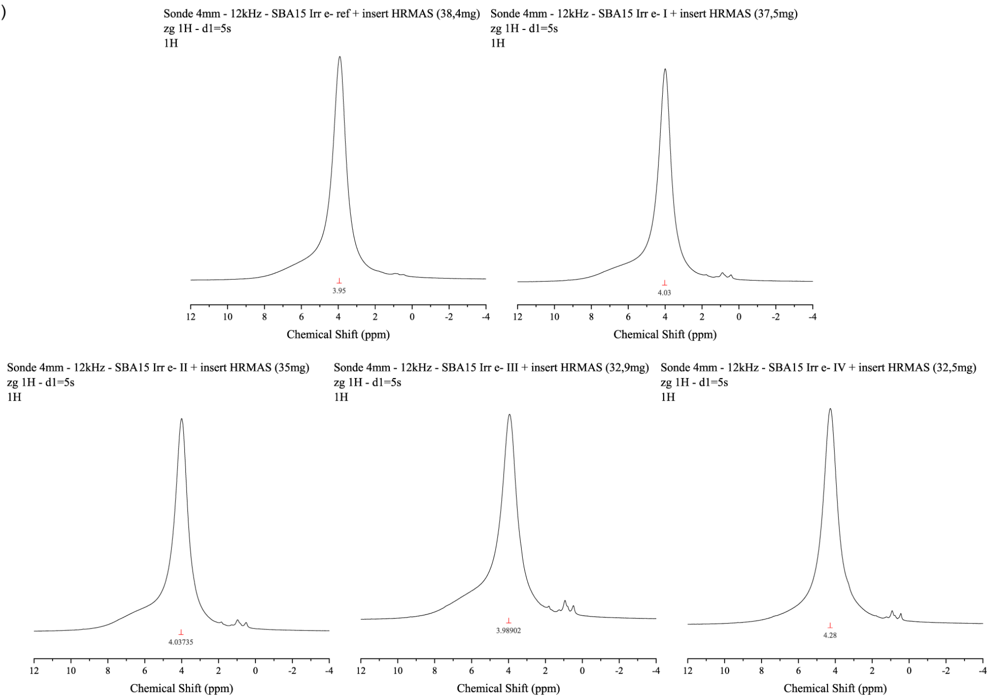

b)

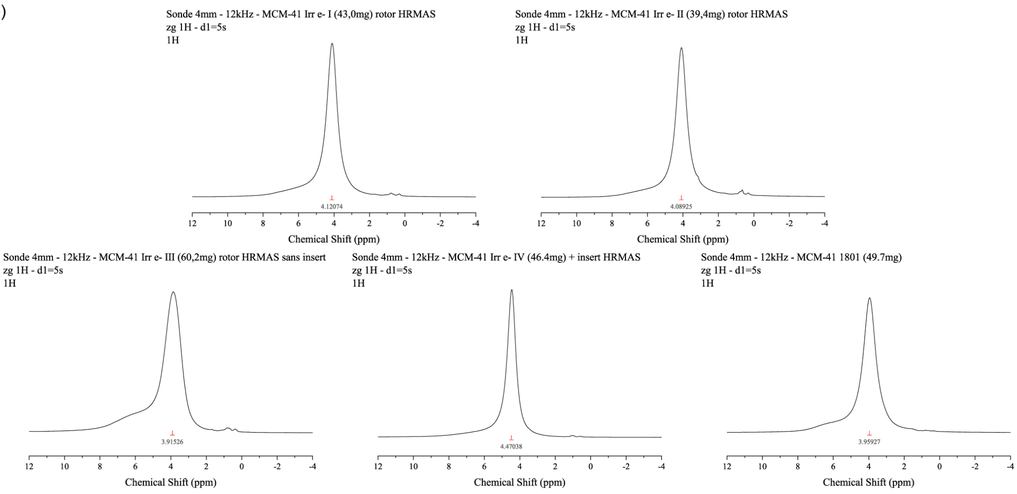

c)

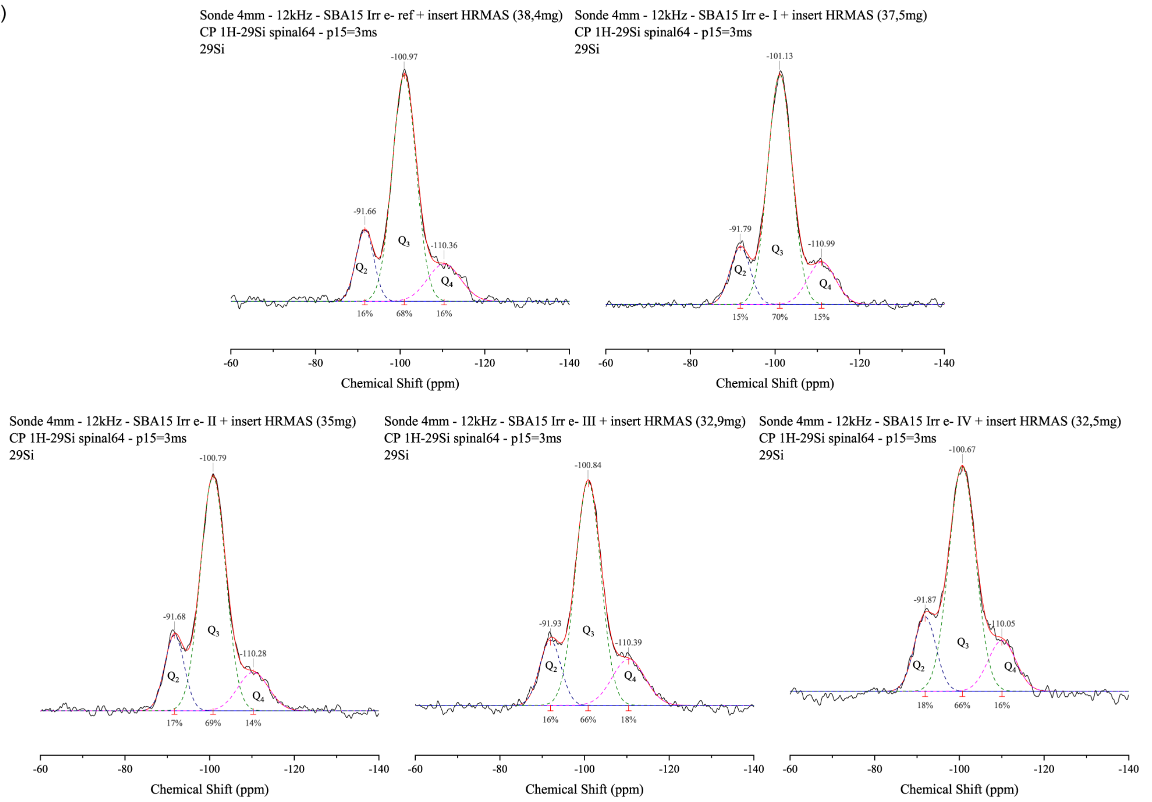
Sonde 4mm - 12kHz - SBA15 Irr e- ref + insert HRMAS (38,4mg)
CP 1H-29Si spinal64 - p15=3ms
29Si
-100.97
-91.66
-110.36
Q_2
Q_3
Q_4
16%
68%
16%
-60
-80
-100
-120
-140
Chemical Shift (ppm)
Sonde 4mm - 12kHz - SBA15 Irr e- I + insert HRMAS (37,5mg)
CP 1H-29Si spinal64 - p15=3ms
29Si
-101.13
-91.79
-110.99
Q_2
Q_3
Q_4
15%
70%
15%
-60
-80
-100
-120
-140
Chemical Shift (ppm)
Sonde 4mm - 12kHz - SBA15 Irr e- II + insert HRMAS (35mg)
CP 1H-29Si spinal64 - p15=3ms
29Si
-100.79
-91.68
-110.28
Q_2
Q_3
Q_4
17%
69%
14%
-60
-80
-100
-120
-140
Chemical Shift (ppm)
Sonde 4mm - 12kHz - SBA15 Irr e- III + insert HRMAS (32,9mg)
CP 1H-29Si spinal64 - p15=3ms
29Si
-100.84
-91.93
-110.39
Q_2
Q_3
Q_4
16%
66%
18%
-60
-80
-100
-120
-140
Chemical Shift (ppm)
Sonde 4mm - 12kHz - SBA15 Irr e- IV + insert HRMAS (32,5mg)
CP 1H-29Si spinal64 - p15=3ms
29Si
-100.67
-91.87
-110.05
Q_2
Q_3
Q_4
18%
66%
16%
-60
-80
-100
-120
-140
Chemical Shift (ppm)

d)

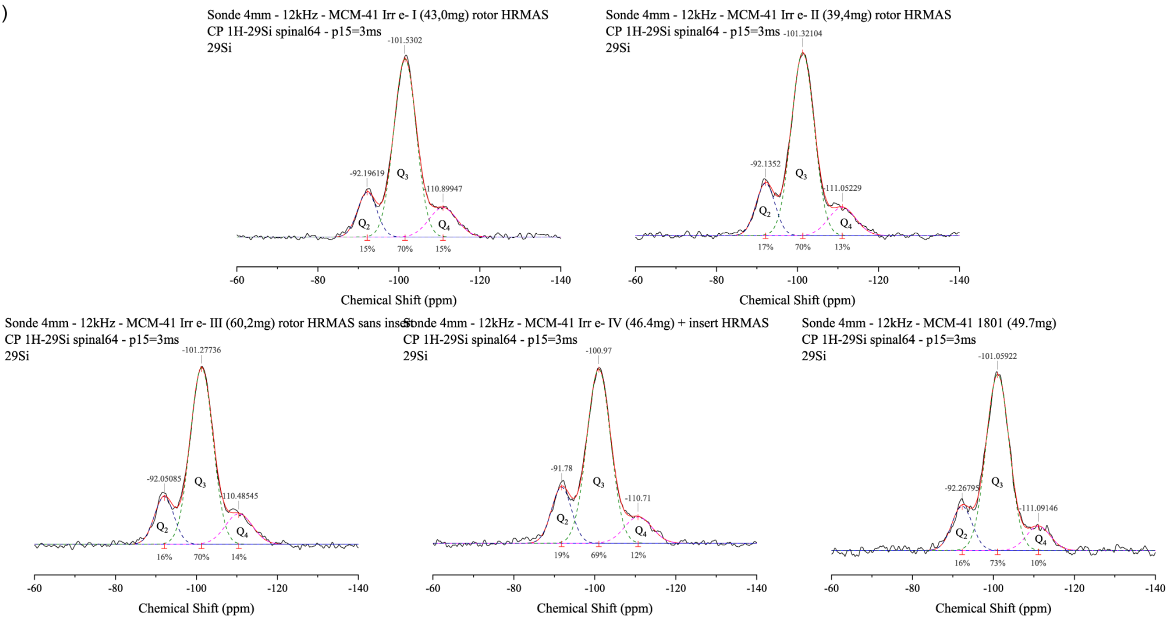
Sonde 4mm - 12kHz - MCM-41 Irr e- I (43,0mg) rotor HRMAS
CP 1H-29Si spinal64 - p15=3ms
29Si
-101.5302
-92.19619
-110.89947
Q_2
Q_3
Q_4
15%
70%
15%
-60
-80
-100
-120
-140
Chemical Shift (ppm)
Sonde 4mm - 12kHz - MCM-41 Irr e- II (39,4mg) rotor HRMAS
CP 1H-29Si spinal64 - p15=3ms
29Si
-101.32104
-92.1352
-111.05229
Q_2
Q_3
Q_4
17%
70%
13%
-60
-80
-100
-120
-140
Chemical Shift (ppm)
Sonde 4mm - 12kHz - MCM-41 Irr e- III (60,2mg) rotor HRMAS sans insert
CP 1H-29Si spinal64 - p15=3ms
29Si
-101.27736
-92.05085
-110.48545
Q_2
Q_3
Q_4
16%
70%
14%
-60
-80
-100
-120
-140
Chemical Shift (ppm)
Sonde 4mm - 12kHz - MCM-41 Irr e- IV (46.4mg) + insert HRMAS
CP 1H-29Si spinal64 - p15=3ms
29Si
-100.97
-91.78
-110.71
Q_2
Q_3
Q_4
19%
69%
12%
-60
-80
-100
-120
-140
Chemical Shift (ppm)
Sonde 4mm - 12kHz - MCM-41 1801 (49.7mg)
CP 1H-29Si spinal64 - p15=3ms
29Si
-101.05922
-92.26795
-111.09146
Q_2
Q_3
Q_4
16%
73%
10%
-60
-80
-100
-120
-140
Chemical Shift (ppm)

Dissemination and valorisation

Oral presentation:

- MRS Virtual Spring/Fall Meeting & Exhibit 2020 - Structural Behavior of Ordered Mesoporous Silica Under Swift Heavy Ions and Electrons Irradiation
- EMIRUM 2021 - Structural Behavior of Ordered Mesoporous Silica Under Swift Heavy Ions and Electrons Irradiation
- GANIL Colloque 2021 - Swift heavy ions induced modification in mesoporous silica materials

Article:

- Lin, J. *et al.* Behavior of mesoporous silica under 2 MeV electron beam irradiation. *Microporous Mesoporous Mater.* (2021), **328**, 111454. DOI:`10.1016/j.micromeso.2021.111454`.

Résumé Substantiel en Français

Les matériaux utilisés dans le nucléaire (combustible, matrice de conditionnement, matériaux de structure...) sont soumis à des contraintes importantes liées à la création de défauts d'irradiation qui modifient leurs propriétés. Plusieurs études ont montré que les interfaces peuvent agir comme un puits pour ces défauts, ce qui suggère que les nanomatériaux pourraient avoir une plus grande résistance à l'irradiation que les matériaux présentant une structure « micrométrique ». Dans ce contexte, les silices mésoporeuses constituent une classe de matériau qui peut être utilisée comme matériau modèle pour les études d'irradiation, car la taille et l'organisation de la porosité peut être facilement contrôlées lors de la synthèse. Par ailleurs, les silices mésoporeuses ont gagné en popularité ces dernières années et sont envisagées pour le traitement des effluents radioactifs (séparation, conditionnement...). Bien que de nombreuses études aient été réalisées sur le comportement de silices non poreuses sous irradiation, très peu de travaux s'intéressent à celui de la silice mésoporeuse. Ce travail a pour objectif d'étudier les modifications induites par irradiation en régime électronique des silices mésoporeuses.

Des études préalables ont mis en évidence que les changements structurels observés dans les silices mésoporeuses irradiées sont spécifiques et qu'ils ne sont pas comparables à ceux observés lors de l'application d'une autre contrainte (pression,température...). A titre d'exemple précisons que, le volume des mésopores des SBA-15 diminue et celui des micropores augmentent significativement lors de l'application d'une pression sur ce matériau. Au contraire, l'irradiation entraîne le rétrécissement des mésopores ainsi que la fermeture des micropores. De même, les résultats de RMN montrent que le traitement thermique provoque une augmentation significative du degré de polymérisation du réseau de silice, qui n'est pas observée sous irradiation.

Pour atteindre l' objectif visé, diverses conditions expérimentales d'irradiation, correspondant aux capacités des différentes installations, ont été choisies pour englober une large gamme du pouvoir d'arrêt électronique (S_e) allant de 10^{-4} keV/nm à 12 keV/nm. Ces expériences d'irradiation peuvent être classées en deux catégories : l'irradiation par faisceau d'ions (Swift Heavy Ions, SHI) et par faisceau d'électrons. Plus précisément, les énergies des ions lourds été utilisés ont été choisies afin de réduire au minimum les effets balistiques (0,98 MeV/A C, 9,17 MeV/A Ca, 0,98 MeV/A Ar, 0,57 MeV/A Ni, 0,86 MeV/A Kr et 0,55 - 0,71 MeV/A Xe). Des irradiations aux électrons d'énergie 10 - 30 - 200 kV et 0,6 MeV < E < 2,4 MeV ont respectivement été réalisées dans le microscope électronique du CIMAP, et avec l'accélérateur du LSI.

En outre, une série d'irradiation par des H^+ de 16 MeV réalisée au CEMHTI a permis de combler partiellement l'écart de pouvoir d'arrêt qui existait entre le faisceau d'ions et d'électrons. Compte tenu des différentes capacités de pénétration des particules dans les conditions expérimentales décrites ci-dessus (calcul SRIM), différents matériaux ont été irradiés pour permettre d'obtenir un profil de dépôt d'énergie relativement uniforme dans l'ensemble de l'échantillon. Deux morphologies de silice mésoporeuse ont été synthétisées : des couches minces obtenues par la méthode EISA (Evaporation Induced Self Assembly) et des pastilles de silice mésoporeuse compactée à partir de poudres de SBA-15 et MCM-41 synthétisées par voie sol-gel. Ces différents matériaux ont été irradiés par les faisceaux de particules dans les installations d'irradiation (GANIL, CEMHTI, LSI,. . .) pour les études d'irradiation externe et les caractérisations ultérieures.

Pour les couches minces, l'épaisseur totale, l'épaisseur de la couche poreuse ont été mesurée par réflectométrie des rayons X (XRR) et les caractéristiques du réseau de silices ont été obtenues par spectroscopie Infra-Rouge (IR). Les résultats XRR montrent qu'à faibles fluences, la variation de l'épaisseur totale de couche mince de silice poreuse et celle de la bi-couche sont cohérentes. Les résultats IR montrent que les pores se rétrécissent, mais que peu de dommages sont occasionnés sur le réseau de silices des murs. Une méthode de traitement des données IR qui permet de révéler les effets de l'irradiation à partir du signal global mesurée à 1080 cm^{-1} a été développée. Les volumes d'endommagement obenus sont comparables avec ceux reportés dans la littérature sur des silices non poreuse, ce qui a postériori valide la méthode de traitement. Enfin, le rayon caractéristique de la zone de silice mésoporeuse endommagée a été calculé par la formule de Marples, en utilisant les résultats du XRR et de l'IR. L'observation au microscope électronique à balayage (MEB) de lames minces de ces échantillons obtenues par FIB (Focused Ion Beam) a montré que la morphologie finale des pores endommagés variait en fonction du pouvoir d'arrêt électronique. Afin d'expliquer ce phénomène, le modèle TS3D (modèle de pointe thermique 3D) a été utilisé pour simuler le système expérimental et obtenir la variation de température du système pendant l'irradiation. En utilisant les températures d'ébullition et de fusion de la silice comme critère, les évolutions observées s'expliquent qualitativement par les effets de formation des traces et de pulvérisation.

Concernant l'irradiation du proton réalisée au CEMHTI ($S_e \sim 5 \times 10^{-3}$ keV/nm), un effet de contraction des pores induit par l'irradiation a également été observé. Cet effet a été mis en évidence par la mesure des isothermes d'adsorption-désorption d'azote.

Dans les cas d'irradiation par électrons de 0,6 - 2,4 MeV, nous avons aussi suivi l'évolution de propriétés physico-chimiques (polymérisation du réseau, création de défauts. . .) et structurales (volume poreux, diamètre et distribution des pores. . .) avec les mêmes techniques expérimentales. Les résultats montrent que les mésopores subissent une contraction induite par l’irradiation, et que les micropores ont tendance à se fermer sous l’effet de l’irradiation. Globalement le volume poreux des échantillons diminue de ~45% pour une dose de 2GGy. En même temps, il n’y a pas de changement significatif observable concernant les caractéristiques physiques de la paroi des pores. Le rayon caractéristique du volume d’endommagement associé au passage d’une particule incidente a été également calculé à partir de l’évolution du volume poreux global (Modèle de Marples).

Dans les cas de l’irradiation in situ dans le MEB (10 – 30 – 200 kV), nous avons observé la fermeture des pores et le rétrécissement de l’épaisseur de couche mince, à partir de ces résultats nous avons également calculé le rayon du volume d’endommagement.

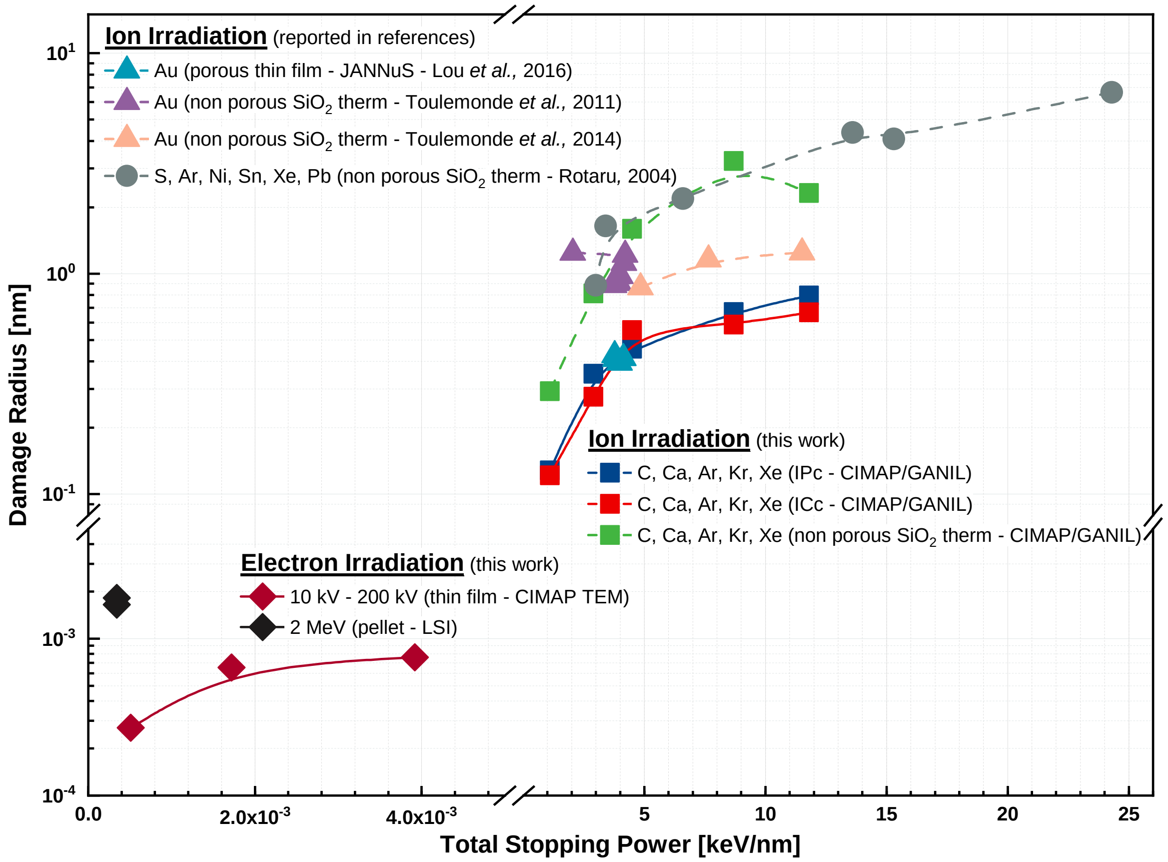

Figure α. Résumé du rayon de dommage en fonction de la puissance d’arrêt totale. Les lignes pleines indiquent les résultats obtenus à partir de la silice poreuse et les lignes pointillées les résultats obtenus à partir de la silice non poreuse. Les triangles indiquent le rayon de dommage obtenu à partir de l’irradiation par faisceau d’ions Au, dans laquelle S_n ne peut être ignoré ou même dominé par S_e.

En résumé, dans toutes les conditions d’irradiation, les résultats expérimentaux ont démontré que les structures de pores étaient soumises à un certain niveau d’endommagement induit par l'irradiation. Le volume des pores a diminué, conduisant même dans certains cas à un effondrement total de la structure. Nous avons calculé par le modèle de Marples le rayon caractéristique du volume endommagé pour chaque des conditions d'irradiation. Ces rayons sont présentés sur la figure α en fonction du pouvoir d'arrêt total. Les résultats correspondant à des études antérieures obtenus sur des silices non poreuses (Toulemonde *et al.*[1,2] et Rotaru *et al.*[3], Lou *et al.*[4] sont également reportés à titre de comparaison.

L'évolution du rayon d'endommagement des matériaux en fonction du pouvoir d'arrêt (Figure α) appelle plusieurs remarques :

- La première remarque qui peut être faite concerne le fait que, pour un même pouvoir d'arrêt total, le volume d'endommagement (rayon de dommage) de la silice non poreuse est plus important. Bien que le pouvoir d'arrêt total soit l'addition de S_n et de S_e et que les mécanismes d'irradiation par faisceau d'ions de haute énergie (dépôt d'énergie électronique principalement, formation de traces) et par faisceau d'ions Au de basse énergie (dépôt d'énergie balistique principalement) ne soient pas identiques, nous pouvons comparer deux séries de résultats deux à deux : ceux de Lou *et al.* sur la silice poreuse et de Toulemonde *et al.* sur la silice non poreuse sous irradiation Au ; et ceux de cette thèse sur la silice poreuse et non poreuse sous irradiation SHI avec les résultats pour la silice non poreuse rapportés par Rotaru *et al.* La comparaison du rayon reporté sur la figure α démontre que la présence de pores diminue de manière significative l'endommagement des matériaux. Cette conclusion est étayée par les résultats sur l'IR, qui démontrent que les modifications IR causées par l'irradiation du réseau de silice dans le matériau de silice poreux sont inférieures à celles de la silice non poreuse à la même dose.

- Comme le montre cette figure, le rayon d'endommagement augmente avec le pouvoir d'arrêt. Lorsque nous comparons les résultats de Lou *et al.* provenant de l'irradiation par faisceau d'Au, aux résultats de SHI du présent travail, nous remarquons que pour les structures poreuses, le pouvoir d'arrêt total a un effet dominant sur le rayon d'endommagement, qui semble ne pas être influencé par le régime d'irradiation (balistique ou électronique).

- Il est plus probable que la morphologie finale des matériaux poreux endommagés par des ions de haute énergie soient similaires à celle des silices non poreuses irradiées dans les

---

[1] Toulemonde, M. *et al.* Material Transformation : Interaction between Nuclear and Electronic Energy Losses. *Procedia Materials Science* **7**, 272-277 (2014).

[2] Toulemonde, M. *et al.* Synergy of nuclear and electronic energy losses in ion-irradiation processes : The case of vitreous silicon dioxide. *Physical Review B* **83** (2011).

[3] Rotaru, C. SiO_2 on silicon : behavior under heavy ion irradiation, Thesis, Université de Caen (2004).

[4] Lou, Y. Behavior of mesoporous silica under ionic irradiation, Thesis, Université Montpellier (2016).

mêmes conditions car les mêmes types de dommages sont opérants (formation de traces et pulvérisation).

- En ce qui concerne l'irradiation par faisceau d'électrons, le rayon d'endommagement causé par un faisceau d'électrons de 2 MeV est d'un ordre de grandeur supérieur à celui observé par un faisceau d'électrons de 10 kV - 200 kV. Cependant, leurs mécanismes ont été considérés comme étant les mêmes dans les études ultérieures. Cette différence peut être due à des différences dans la forme de l'échantillon et les conditions d'irradiation.

Pour conclure, les matériaux mésoporeux étudiés ont montré un rétrécissement systématique, de plus ou moins grande amplitude, du rayon des pores en fonction des irradiations. On en déduit que les matsériaux poreux tels que la silice mésoporeuse, mais peut-être aussi les MOF et d'autres matériaux poreux, sont des matrices appropriées pour le traitement des effluents contaminés provenant de l'industrie nucléaire. Comme tente de démontrer le projet ANR Automact[5], une technologie de type séparation/conditionnement tout-en-un, basée sur un matériau poreux qui permettrait la sorption et l'encapsulation d'un radionucléide (actinides, produits de fission (I, Cs...) après fermeture des pores induite par auto-irradiation semble prometteuse. De plus, cet effet de fermeture des pores assisté par irradiation, pourrait être bénéfique pour induire une auto-réparation des gels d'altération qui se forment à la surface des verres nucléaires pour le conditionnement des déchets de haute activité.

---

[5] Project-ANR-18-CE05-0016-2018, *Séparation sur solide et **AUTO**-conditionne**M**ent d'**ACT**inides provenant d'effluents contamines*, Grant, 2018